

AD-771 037

**DYNAMIC MODEL WIND TUNNEL TESTS OF A
VARIABLE-DIAMETER, TELESCOPING-BLADE
ROTOR SYSTEM (TRAC ROTOR)**

Evan A. Fradenburgh, et al

United Aircraft Corporation

Prepared for:

**Army Air Mobility Research and Development
Laboratory**

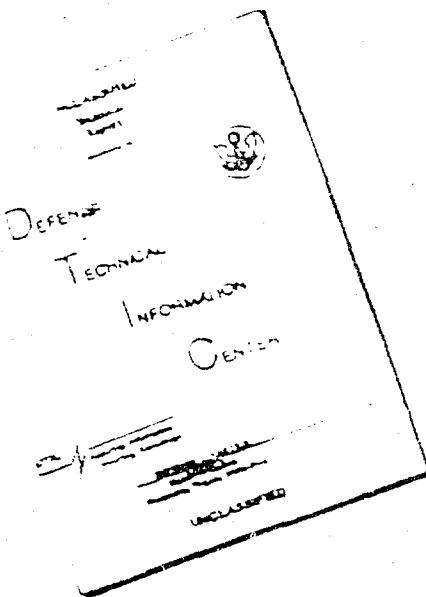
July 1973

DISTRIBUTED BY:

NTIS

**National Technical Information Service
U. S. DEPARTMENT OF COMMERCE
5285 Port Royal Road, Springfield Va. 22151**

DISCLAIMER NOTICE



THIS DOCUMENT IS BEST
QUALITY AVAILABLE. THE COPY
FURNISHED TO DTIC CONTAINED
A SIGNIFICANT NUMBER OF
PAGES WHICH DO NOT
REPRODUCE LEGIBLY.

AD 771037

AD

USAAMRDL TECHNICAL REPORT 73-32

DYNAMIC MODEL WIND TUNNEL TESTS OF A VARIABLE-DIAMETER, TELESCOPING- BLADE ROTOR SYSTEM (TRAC ROTOR)

By

Evan A. Fradenburgh
Robert J. Murrill
Edmond F. Kiely

July 1973

DDC
REF ID: A721037
DEC 20 1973

EUSTIS DIRECTORATE
U. S. ARMY AIR MOBILITY RESEARCH AND DEVELOPMENT LABORATORY
FORT EUSTIS, VIRGINIA

CONTRACT DAAJ02-68-C-0074
UNITED AIRCRAFT CORPORATION
SIKORSKY AIRCRAFT DIVISION
STRATFORD, CONNECTICUT

Approved for public release;
distribution unlimited.



Reproduced by
NATIONAL TECHNICAL
INFORMATION SERVICE
U.S. Department of Commerce
Springfield VA 22151

204

DISCLAIMERS

The findings in this report are not to be construed as an official Department of the Army position unless so designated by other authorized documents.

When Government drawings, specifications, or other data are used for any purpose other than in connection with a definitely related Government procurement operation, the United States Government thereby incurs no responsibility nor any obligation whatsoever; and the fact that the Government may have formulated, furnished, or in any way supplied the said drawings, specifications, or other data is not to be regarded by implication or otherwise as in any manner licensing the holder or any other person or corporation, or conveying any rights or permission, to manufacture, use, or sell any patented invention that may in any way be related thereto.

Trade names cited in this report do not constitute an official endorsement or approval of the use of such commercial hardware or software.

DISPOSITION INSTRUCTIONS

Destroy this report when no longer needed. Do not return it to the originator.

DISPOSITION FOR	
NTIS	White Section <input checked="" type="checkbox"/>
DDB	Buff Section <input type="checkbox"/>
UNARMED	
JUSTIFICATION.....	
BY.....	
DISTRIBUTION/AVAILABILITY U.T.C.	
DISP. 10000000000000000000	
A	

Unclassified

Security Classification

DOCUMENT CONTROL DATA - R & D

(Security classification of title, body of abstract, and indexing annotation must be entered when the overall report is classified)

1. ORIGINATING ACTIVITY (Corporate author)		2a. REPORT SECURITY CLASSIFICATION Unclassified
United Aircraft Corporation Sikorsky Aircraft Division Stratford, Connecticut		2b. GROUP
3. REPORT TITLE DYNAMIC MODEL WIND TUNNEL TESTS OF A VARIABLE-DIAMETER, TELESCOPING-BLADE ROTOR SYSTEM (TRAC ROTOR)		
4. DESCRIPTIVE NOTES (Type of report and inclusive dates) Final Report		
5. AUTHORITY (First name, middle initial, last name) Evan A. Fradenburgh Robert J. Murrill Edmond F. Kiely		
6. REPORT DATE July 1973	7a. TOTAL NO. OF PAGES 210	7b. NO. OF REFS 16
8a. CONTRACT OR GRANT NO. DAAJ02-68-C-0074	8b. ORIGINATOR'S REPORT NUMBER(S) USAAMRDI. Technical Report 73-32	
8c. PROJECT NO. Task 1F162204A13902	8d. OTHER REPORT NO(S) (Any other numbers that may be assigned this report) SER-50797	
10. DISTRIBUTION STATEMENT Approved for public release; distribution unlimited.		
11. SUPPLEMENTARY NOTES	12. SPONSORING MILITARY ACTIVITY Eustis Directorate U. S. Army Air Mobility R&D Laboratory Fort Eustis, Virginia	
13. ABSTRACT <p>An analytical and experimental program was conducted to establish feasibility and determine characteristics of the Sikorsky TRAC rotor system, which is a unique variable-diameter, telescoping-blade concept for advanced rotary-wing aircraft. The program included a preliminary design study of a full-scale blade, wind tunnel tests of a dynamically scaled rotor model in various flight modes, and correlation of experimental results with theory.</p> <p>Feasibility was established for the TRAC rotor operating both as a high-speed compound helicopter and as a stopped/stowed rotor configuration. The basic blade structural design and the retraction system were verified with the model, which was scaled for operation at full tip speeds and forward speeds. With blades extended, the rotor demonstrated lift and propulsive force capabilities comparable to those of conventional rotors over the speed range investigated in this mode, 60 to 150 knots, with satisfactory blade stresses. Diameter reductions were demonstrated at forward speeds to 150 knots with positive and rapid control and low stresses. With the rotor at minimum diameter, rotor stops and starts were demonstrated without difficulty at 150 knots forward speed, and blade indexing tests demonstrated the ease with which the blades could be folded for stowing. With the rotor at minimum diameter and remaining in the rotating, fully articulated condition, tests were conducted up to 400 knots true airspeed, demonstrating suitability for high-speed compound helicopter application. Benefits to performance, blade stresses, vibration, and gust response were demonstrated.</p>		

DD FORM 1473 REPLACES DD FORM 1473, 1 JAN 64, WHICH IS
OBSOLETE FOR ARMY USE.

Unclassified

Security Classification

Unclassified

Security Classification

14. KEY WORDS	LINK A		LINK B		LINK C	
	ROLE	WT	ROLE	WT	ROLE	WT
Helicopter TRAC rotor Variable diameter Telescoping blade Stowed rotor Compound helicopter Wind tunnel test Dynamic model Rotor performance Blade stresses						

Unclassified

Security Classification

7323-73

11a



DEPARTMENT OF THE ARMY
U. S. ARMY AIR MOBILITY RESEARCH & DEVELOPMENT LABORATORY
EUSTIS DIRECTORATE
FORT EUSTIS, VIRGINIA 23604

This report has been reviewed by the Eustis Directorate, U. S. Army Air Mobility Research and Development Laboratory and is considered to be technically sound. This program was initiated to establish the feasibility and determine the characteristics of a unique variable-diameter, telescoping-blade rotor concept for advanced rotary-wing aircraft.

The technical monitor for this contract was Mr. Patrick A. Cancro, Technology Applications Division of this Directorate.

118

Task 1F162204A13902
Contract DAAJ02-68-C-0074
USAAMRDL Technical Report 73-32
July 1973

DYNAMIC MODEL WIND TUNNEL TESTS OF
A VARIABLE-DIAMETER, TELESCOPING-
BLADE ROTOR SYSTEM (TRAC ROTOR)

Final Report

SER-50797

by

Evan A. Fradenburgh
Robert J. Murrill
Edmond F. Kiely

Prepared by

United Aircraft Corporation
Sikorsky Aircraft Division
Stratford, Connecticut

for

EUSTIS DIRECTORATE
U. S. ARMY AIR MOBILITY RESEARCH AND DEVELOPMENT LABORATORY
FORT EUSTIS, VIRGINIA

Approved for public release; distribution unlimited.

11C

SUMMARY

An analytical and experimental program was conducted to establish feasibility and determine characteristics of the Sikorsky TRAC rotor system, which is a unique variable-diameter, telescoping-blade concept for advanced rotary-wing aircraft.* The program included a preliminary design study of a full-scale blade, wind tunnel tests of a dynamically scaled rotor model in various flight modes, and correlation of experimental results with theory.

The program achieved all of its major objectives. The dynamic model rotor was successfully operated in every planned operational mode. Feasibility was established for the TRAC rotor operating both as a high-speed compound helicopter and as a stopped/stowed rotor configuration. The basic blade structural design and the retraction system were verified with the model, which was scaled for operation at full tip speeds and forward speeds. With blades extended, the rotor demonstrated lift and propulsive force capabilities comparable to those of conventional rotors over the speed range investigated in this mode, 60 to 150 knots, with satisfactory blade stresses. Diameter reductions were demonstrated at forward speeds to 150 knots with positive and rapid control and low stresses. With the rotor at minimum diameter, rotor stops and starts were demonstrated without difficulty at 150 knots forward speed, and blade indexing tests demonstrated the ease with which the blades could be folded for stowing. With the rotor at minimum diameter and remaining in the rotating, fully articulated condition, tests were conducted up to 400 knots true airspeed, demonstrating suitability for high-speed compound helicopter application.

Results of the test include rotor performance, blade stress measurements, blade motion, control loads, vibration, and stability and control derivatives. Generally, good correlation with available theoretical methods was demonstrated.

Analysis of the data confirms that the TRAC rotor offers a number of benefits relative to conventional rotor systems for compound helicopter and stowed rotor applications. Benefits for the compound include higher speed potential, better performance, lower blade stresses, lower vibration levels, reduced gust sensitivity, and reduced rotor noise. For the stowed rotor configuration, the TRAC rotor offers a feasible solution to the problem of stopping a rotor in flight; even at relatively high conversion speeds, blade aeroelastic stability problems are avoided and aircraft pitching and rolling disturbances are reduced to acceptable levels without special control devices.

The program was an effective means of evaluating an advanced rotor system concept. Feasibility of the overall system was successfully established and design improvements identified to further improve the blade for future applications.

* The name TRAC is derived from the phrase "telescoping rotor aircraft".

FOREWORD

This program was conducted for the Eustis Directorate, U. S. Army Air Mobility Research and Development Laboratory, under Contract DAAJ02-68-C-0074 (Task 1F162204A13902). Technical management for the program was provided by Mr. John L. Shipley and Mr. Patrick A. Cancro.

Mr. Evan A. Fradenburgh was the Sikorsky task manager for the overall design, development and test of the TRAC rotor system. Mr. Edmond F. Kiely was responsible for detail design and development of the model blades and other model hardware. Mr. Richard M. Segel was the principal wind tunnel test coordinator for the first two test series and Mr. Robert J. Murrill was the principal wind tunnel test coordinator for the third test series. Mr. James C. Linville and Mr. Jay M. Yarm contributed to design and development of various test hardware. Mr. John Leary was the principal instrumentation engineer. Mr. Charles F. Niebanck was responsible for the ground resonance analysis and test phase of the program. Mr. Russell R. Bergquist was responsible for most of the special mathematical analysis development utilized in this study. Several other persons contributed significantly to the success of the program.

TABLE OF CONTENTS

	<u>Page</u>
SUMMARY	iii
FOREWORD	v
LIST OF ILLUSTRATIONS	ix
LIST OF SYMBOLS	xvi
INTRODUCTION	1
ROTOR SYSTEM DESIGN	3
Description of Basic Concept.	3
Preliminary Design Study of Full-Scale Rotor.	4
Model Blade Design and Construction	6
TEST EQUIPMENT.	8
Wind Tunnel Facility.	8
Wind Tunnel Model	8
Model Control Console	9
Instrumentation and Calibration	10
Data Acquisition and Monitoring Systems	11
Data Reduction Procedures	13
TEST PLANS AND PROCEDURES	14
Definition of Test Phases	14
Pretest and Test Procedures	15
TEST RESULTS AND ANALYSIS	17
Special Considerations.	17
Helicopter Mode (Phase I)	18
Diameter Change (Phase II).	22
RPM Reduction - Articulated (Phase III)	28
RPM Reduction - Locked Hinges (Phase IV).	30
Blade Index Variations (Phase V).	32
High-Speed Compound Mode (Phase VI)	34
Rotor Head Tares (Phases VI and VIII)	39
Influence of Variable Diameter on Compound Helicopter Performance	39
General Observations and Evaluations.	42
CONCLUSIONS.	45
LITERATURE CITED	48

Preceding page blank

TABLE OF CONTENTS - Continued

	<u>Page</u>
APPENDIXES	
I. Details of Full-Scale Preliminary Design Study	171
II. Details of Model Blade Construction.	183
III. Details of Wind Tunnel Model	187
DISTRIBUTION	193

LIST OF ILLUSTRATIONS

<u>Figure</u>		<u>Page</u>
1	TRAC Rotor Blade Schematic Arrangement	54
2	TRAC Rotor Head Schematic Arrangement	55
3	Flapwise Aeroelastic Analysis for Extended Blade	56
4	Flapwise Natural Frequencies for Fully Extended TRAC Blade	57
5	Calculated Jackscrew Temperature Distribution.	58
6	TRAC Model Blade General Arrangement	59
7	Comparison of Model Spanwise Mass Distribution With Full-Scale Design	61
8	Experimentally Determined Effective Model Blade Stiffness Distribution.	62
9	United Aircraft Research Laboratories Main Wind Tunnel	63
10	Reynolds Number and Mach Number Versus Test Section Velocity	64
11	TRAC Wind Tunnel Model in UARL 18-Foot Wind Tunnel, Blades Extended	65
12	TRAC Wind Tunnel Model in UARL 8-Foot Wind Tunnel, Blades Retracted.	66
13	Model Rotor Head Components	67
14	Model Rotor in Folded Blade Configuration	68
15	Rotor Control Console	69
16	Blade Strain Gage Locations	70
17	Data Acquisition and Monitoring Equipment in Tunnel Control Room	71
18	TRAC Model Rotor Wind Tunnel Test Conditions.	72
19	Lift Envelope, TRAC Model Rotor Tests	73
20	Gust Envelope, TRAC Model Rotor Tests	74

<u>Figure</u>	<u>Page</u>
<u>Phase I - Helicopter Mode - Figures 21 thru 51</u>	
21	Measured Rotor Performance Characteristics, Full Diameter, 1375 rpm, $V = 60$ Knots 75
22	Measured Rotor Performance Characteristics, Full Diameter, 1375 rpm, $V = 90$ Knots 76
23	Measured Rotor Performance Characteristics, Full Diameter, 1375 rpm, $V = 120$ Knots 77
24	Measured Rotor Performance Characteristics, Full Diameter, 1375 rpm, $V = 150$ Knots 78
25	Measured Blade Flapping, Full Diameter, 1375 rpm, $V = 60$ Knots 79
26	Measured Blade Flapping, Full Diameter, 1375 rpm, $V = 90$ Knots 80
27	Measured Blade Flapping, Full Diameter, 1375 rpm, $V = 120$ Knots. 81
28	Measured Blade Flapping, Full Diameter, 1375 rpm, $V = 150$ Knots 82
29	Theoretical Rotor Performance Characteristics, Full Diameter, 1375 rpm, $V = 90$ Knots 83
30	Theoretical Rotor Performance Characteristics, Full Diameter, 1375 rpm, $V = 150$ Knots 84
31	Theoretical Blade Flapping, Full Diameter, 1375 rpm, $V = 90$ Knots 85
32	Theoretical Blade Flapping, Full Diameter, 1375 rpm, $V = 150$ Knots. 86
33	Rotor Performance Correlation, Full Diameter, 1375 rpm, $V = 90$ Knots 87
34	Rotor Performance Correlation, Full Diameter, 1375 rpm, $V = 150$ Knots. 88
35	Measured Azimuthal Variation of Blade Stresses and Motion, Full Diameter, 1375 rpm, $V = 90$ Knots, $\alpha_s = -12^\circ$. . 89
36	Measured Azimuthal Variation of Blade Stresses and Motion, Full Diameter, 1375 rpm, $V = 150$ Knots, $\alpha_s = -8^\circ$ 91

<u>Figure</u>	<u>Page</u>
37 Flapwise Vibratory Stress Distributions, Full Diameter, 1375 rpm, V = 60 Knots	93
38 Edgewise Vibratory Stress Distributions, Full Diameter, 1375 rpm, V = 60 Knots	94
39 Torsional Vibratory Stress Distributions, Full Diameter, 1375 rpm, V = 60 Knots	95
40 Flapwise Vibratory Stress Distributions, Full Diameter, 1375 rpm, V = 150 Knots	96
41 Edgewise Vibratory Stress Distributions, Full Diameter, 1375 rpm, V = 150 Knots	97
42 Torsional Vibratory Stress Distributions, Full Diameter, 1375 rpm, V = 150 Knots	98
43 Mean Blade Stress Distributions, Full Diameter, 1375 rpm, V = 150 Knots, $\alpha_s = 45^\circ$	99
44 Effect of Rotor Operation Conditions on Root Flapwise Vibratory Stress, Full Diameter, 1375 rpm, V = 60 Knots . .	100
45 Effect of Rotor Operating Conditions on Outer Blade Flapwise Vibratory Stress, Full Diameter, 1375 rpm, V = 60 Knots	101
46 Flapwise Vibratory Blade Stress - Correlation With Theory, Full Diameter, 1375 rpm, V = 90 Knots	102
47 Flapwise Vibratory Blade Stress - Correlation With Theory, Full Diameter, 1375 rpm, V = 150 Knots	103
48 Azimuthal Variation of Root Flapwise Stress - Correlation With Theory, Full Diameter, 1375 rpm, V = 90 Knots $\alpha_s = -12^\circ$	104
49 Azimuthal Variation of Outer Blade Flapwise Stress - Correlation With Theory, Full Diameter, 1375 rpm, V = 90 Knots $\alpha_s = -12^\circ$	105
50 Azimuthal Variation of Root Flapwise Stress - Correlation With Theory, Full Diameter, 1375 rpm, V = 150 Knots, $\alpha_s = -8^\circ$	106
51 Azimuthal Variation of Outer Blade Flapwise Stress - Correlation With Theory, Full Diameter, 1375 rpm, V = 150 Knots, $\alpha_s = -8^\circ$	107

Phase II - Diameter Change - Figures 52 thru 62

52	Diameter Change Time History, 1185 rpm, $V = 120$ Knots, $a_g = 0^\circ, \theta_c = 0^\circ$	108
53	Diameter Change Time History, 1375 rpm, $V = 150$ Knots, $a_g = 0^\circ, \theta_c = 0^\circ$	109
54	Diameter Change Time History, 1375 rpm, $V = 150$ Knots, Gust Condition, $a_g = 2^\circ, \theta_c = 0^\circ$	111
55	Blade Vibratory Stresses During Retraction, 1375 rpm, $V = 150$ Knots, $a_g = 0^\circ, \theta_c = 0^\circ$	113
56	Blade Flapping Motion During Retraction, 1375 rpm, $V = 150$ Knots, $a_g = 2^\circ, \theta_c = 0^\circ$	114
57	Influence of Rotor Diameter on Performance Parameters, 1375 rpm, $V = 150$ Knots, $\theta_c = 0^\circ$	115
58	Variation of Rotor Lift With Incremental Angular Inputs, 1375 rpm, $V = 150$ Knots	116
59	Influence of Rotor Diameter on Stability and Control Derivatives, 1375 rpm, $V = 150$ Knots	117
60	Effect of Diameter and Simulated Gust on Flapwise Stress Distributions, 1375 rpm, $V = 150$ Knots, $\theta_c = 0^\circ$	118
61	Effect of Diameter, RPM, and Collective Pitch on Flapwise Stress Distributions, $V = 150$ Knots, $a_g = 0^\circ$	119
62	Effect of Diameter on Model Vibration Levels, 1375 rpm, $V = 150$ Knots, $a_g = 0^\circ, \theta_c = 0^\circ$	120

Phase III - RPM Change, Articulated - Figures 63 thru 67

63	Blade Vibratory Response During RPM Reduction, 62.5% Diameter, $V = 150$ Knots, $a_g = 0^\circ, \theta_c = 0^\circ$	121
64	Effect of RPM on Performance Parameters, 60.8% Diameter, $V = 150$ Knots, $a_g = 0^\circ$	123
65	Effect of RPM on Blade Flapwise Stress Distribution, 60.8% Diameter, $V = 150$ Knots, $a_g = 0^\circ$	124
66	Effect of RPM and Gusts on Torque Tube Flapwise Stress Distribution, 60.5% Diameter, $V = 150$ Knots, $\theta_c = 0^\circ$	125

<u>Figure</u>	<u>Page</u>
67 Effect of RPM on Torque Tube Stress Measured at the 15% Station, 60.5% Diameter, $V = 150$ Knots	126
<u>Phase IV - RPM Change, Locked Hinge - Figures 68 thru 75</u>	
68 Typical Time History of Stop-Start Sequence, 60.8% Diameter, $V = 150$ Knots, $\alpha_s = 0^\circ$, $\theta_c = 0^\circ$	127
69 Rotor Vibratory Loads During Typical Rotor Stop, 60.8% Diameter, $V = 150$ Knots, $\alpha_s = 0^\circ$, $\theta_c = 0^\circ$	131
70 Calculated Natural Frequencies for 60.8% Diameter Conditions	133
71 Effect of Cyclic Pitch and Gusts on Blade Flapwise Stress Distribution, Locked Hinge, 60.8% Diameter, 740 rpm, $V = 150$ Knots, $\theta_c = 0^\circ$	134
72 Effect of Cyclic Pitch and Gusts on Blade Flapwise Stress Distribution, Locked Hinge, 60.8% Diameter, 290 rpm, $V = 150$ Knots, $\theta_c = 0^\circ$	135
73 Variation of Blade Stress With RPM and Collective Pitch, 60.8% Diameter, $V = 150$ Knots, $\alpha_s = 0^\circ$	136
74 Variation of Rotor Performance Parameters With RPM, Locked Hinge, 60.8% Diameter, $V = 150$ Knots, $\alpha_s = 0^\circ$. . .	137
75 Variation of Stability Derivatives With RPM for Locked Hinge Configuration, 60.8% Diameter, $V = 150$ Knots.	138
<u>Phase V - Blade Index Variations - Figures 76 thru 79</u>	
76 Variation of Blade Root Bending Stress With Azimuth Position, 60.8% Diameter, Stopped Rotor, $V = 150$ Knots, $\theta_c = 0^\circ$	139
77 Effect of Fore-and-Aft Folding on Blade Root Bending Stress Measured at the 15% Radial Station, 60.8% Diameter, $V = 150$ Knots, $\theta_c = 0^\circ$	140
78 Effect of Rotor Index Position and Folding on Rotor Forces, 60.8% Diameter, $V = 150$ Knots, $\theta_c = 0^\circ$	141
79 Stability and Control Derivatives for Stopped Rotor, 60.8% Diameter, $V = 150$ Knots	142

<u>Figure</u>	<u>Page</u>
<u>Phase VII - High Speed Compound Mode - Figures 80 thru 92</u>	
80 Rotor Performance Parameters at High Forward Speeds, 60.8% Diameter	143
81 Rotor Equivalent Drag at High Forward Speeds, 60.8% Diameter, $\theta_c = 0^\circ$	144
82 Blade Flapping at High Forward Speeds, 60.8% Diameter	145
83 Stability and Control Derivatives at High Forward Speeds, 60.8% Diameter, 1184 rpm	146
84 Gust Response Characteristics at High Forward Speeds	147
85 Effect of Forward Speed on Flapwise Vibratory Stress Distributions, 60.8% Diameter	148
86 Variation of Torque Tube 15% Station Flapwise Vibratory Stress With Forward Speed, 60.8% Diameter	149
87 Variation of Outer Blade 79% Station Flapwise Vibratory Stress With Forward Speed, 60.8% Diameter	150
88 Variation of Edgewise Vibratory Stress With Forward Speed, 60.8% Diameter	151
89 Variation of Torsional Vibratory Stress With Forward Speed, 60.8% Diameter	152
90 Variation of Pushrod Load With Forward Speed, 60.8% Diameter	153
91 Measured Azimuthal Variation of Blade Stresses and Motion, 60.8% Diameter, 1184 rpm, V = 250 Knots, $\alpha_s = 0^\circ$, $\theta_c = 0^\circ$, $A_{ls} = -2.6^\circ$, $B_{ls} = -0.6^\circ$	154
92 Measured Azimuthal Variation of Blade Stresses and Motion, 60.8% Diameter, 1184 rpm, V = 350 Knots, $\alpha_s = 0^\circ$, $\theta_c = 0^\circ$, $A_{ls} = -3.9^\circ$, $B_{ls} = -1.0^\circ$	155
<u>Phases VI and VIII - Rotor Head Tares - Figures 93 and 94</u>	
93 Typical Total Rotor Head Tares (Aerodynamic Plus Gravity)	156
94 Rotor Head Drag Tare at High Forward Speeds, $\alpha_s = 0^\circ$	157

<u>Figure</u>		<u>Page</u>
95	Assumed Rotor Lift Schedule and Wing Profile Drag	158
96	General Arrangement of Typical Compound Helicopter with TRAC Rotor	159
97	Power Required for Compound Helicopter at Sea Level	161
98	Power Required for Compound Helicopter at 10,000 Feet Altitude	162
99	Power Required for Compound Helicopter at 20,000 Feet Altitude	163
100	Effect of Wing Area on Performance at 10,000 Feet Altitude.	164
101	Effect of 20 Percent Drag Reduction on Performance at 10,000 Feet Altitude.	165
102	Weight Savings due to Power Reduction With TRAC Rotor, Sea Level	166
103	Blade Vibratory Stress Comparison	167
104	Airframe Vibration Comparison	168
105	Aircraft Gust Response Comparison at Sea Level.	169
106	Rotor Advancing Tip Mach Number/Noise Comparison.	170
107	Full-Scale Preliminary Design - TRAC Rotor Head and Retraction Mechanism	175
108	Full-Scale Preliminary Design - TRAC Blade General Arrangement	177
109	Full-Scale Preliminary Design - Torque Tube and Spar.	179
110	Mass Distribution for Full-Scale Blade Design	181
111	Centrifugal Force Distribution for Full-Scale Blade Design	182
112	Model Blade Spar Assembly	186
113	Fuselage With Outer Shell Partially Removed	190
114	Model Support Strut System in 18-Foot Wind Tunnel	191
115	Model Fuselage and Strut Configurations Utilized in First Two Test Series	192

LIST OF SYMBOLS

A_{1s}	first harmonic lateral cyclic pitch angle with respect to the shaft axis
AR	aspect ratio
a_o	rotor coning angle
a_1	first harmonic longitudinal flapping angle with respect to the control axis
a_{1s}	first harmonic longitudinal flapping angle with respect to the shaft axis
B_{1s}	first harmonic longitudinal cyclic pitch angle with respect to the shaft axis
b	number of rotor blades
b_1	first harmonic lateral flapping angle with respect to the control axis
b_{1s}	first harmonic lateral flapping angle with respect to the shaft axis
C_D^*	rotor drag coefficient, $\frac{D}{\pi R^2 \rho (\Omega R)^2}$
C_{Di}	wing induced drag coefficient, $\frac{C_{Lw}^2}{\pi ARe}$
C_{Do}	wing profile drag coefficient, $\frac{\text{Profile Drag}}{\frac{1}{2} \rho V^2 S}$
C_L^*	rotor lift coefficient, $\frac{L}{\pi R^2 \rho (\Omega R)^2}$
C_{Lw}	wing lift coefficient, $\frac{L_w}{\frac{1}{2} \rho V^2 S}$
C_M^*	rotor pitching moment coefficient, $\frac{PM}{\pi R^2 \rho (\Omega R)^2 R}$
C_Q^*	rotor torque coefficient, $\frac{Q}{\pi R^2 \rho (\Omega R)^2 R}$
C_R^*	rotor rolling moment coefficient, $\frac{RM}{\pi R^2 \rho (\Omega R)^2 R}$
c	rotor blade chord

\bar{c}	mean chord, $\frac{\int_0^R cr^2 dr}{\int_0^R r^2 dr}$
D	rotor drag
E	Young's modulus
f	parasite area, $Drag/\frac{1}{2}\rho V^2$
GJ	section torsional stiffness
I_{XX}	flapwise area moment of inertia about the neutral axis
I_{YY}	edgewise area moment of inertia about the neutral axis
L	rotor lift
L_w	wing lift
M	Mach number at the advancing blade tip
N	rotor rotational speed
PM	rotor pitching moment
Q	rotor torque
R	rotor radius
RM	rotor rolling moment
r	distance from center of rotation to spanwise station
S	wing area
V	forward speed
W	aircraft gross weight
α_s	rotor shaft angle of attack
α_{TPP}	rotor angle of attack, (tip path plane), $= \alpha_s + \alpha_{ls}$
β	rotor blade flapping angle relative to shaft, $= \alpha_0 - \alpha_{ls} \cos \psi - \beta_{ls} \sin \psi - \alpha_{2s} \cos 2\psi - \beta_{2s} \sin 2\psi - \dots$
δ_3	pitch-flap coupling angle

ϵ wing span efficiency factor
 θ blade pitch, $= \theta_c - A_{ls} \cos \psi - B_{ls} \sin \psi - \beta \tan \delta_3$
 θ_c collective pitch
 ρ air density
 σ rotor solidity, $\frac{bC}{\pi R}$, .095 for extended diameter
 ψ blade azimuth angle (measured from downwind position in direction of rotation)
 Ω rotor shaft angular velocity

NOTE: Asterisk (*) indicates rotor coefficients nondimensionalized by full diameter and tip speed values even though test data may be obtained at reduced diameter and tip speed.

INTRODUCTION

The TRAC rotor system concept was oriented initially to the problems associated with a stowed-rotor aircraft configuration, wherein the aircraft converts from a helicopter to a conventional fixed-wing aircraft in flight.* The problems of stopping or starting a rotor in forward flight are extreme with blades of conventional length and flexibility. Although the rotor design may be compromised to aid the solution, by increasing disk loading to reduce blade length and by increasing blade stiffness substantially by means of increased structural thickness and weight, significant problems remain. The difficulties include excessive blade root bending moments, blade aeroelastic stability limitations, aircraft stability and control problems resulting from large rotor pitching and rolling moments, and design compromises forced by the necessity of keeping conversion flight speeds low. The problems can be eliminated or minimized with a variable-diameter rotor wherein the diameter is substantially reduced prior to stopping the rotor. The TRAC rotor is designed to allow a decrease in rotor diameter from 100 percent to approximately 60 percent while turning at full rotational speed. By reducing the effective blade area and the moment arm from the center of rotation, the problems of rotor stops and starts in forward flight are greatly diminished. This approach permits use of lower disk loadings and higher conversion flight speeds than would otherwise be possible.

In addition to the stowed-rotor application, the potential advantages of variable diameter to the high-speed compound helicopter configuration were also investigated. Improved performance was predicted due to reduced rotor system drag in cruise flight, and it was also anticipated that there would be beneficial reductions in blade vibratory loadings, rotor gust response, and improved blade flapping stability.

Development of the TRAC rotor was initiated under Sikorsky Aircraft's Independent Research and Development program. Preliminary design studies were conducted and special analyses were developed to determine the blade aeroelastic properties and the heat dissipation characteristics associated with the retraction mechanism within the blade. The dynamically scaled model rotor utilized in the present investigation was designed and fabricated as a part of this effort. Some of this work is described in Reference 1. The hovering efficiency and vertical drag effects due to the unusual blade planform shape were evaluated with small-scale model hover tests sponsored by the U. S. Air Force and the U. S. Army. These investigations were reported in References 2 and 3.

Testing of the dynamically scaled model rotor in the program reported herein was conducted under the sponsorship of the Eustis Directorate, U. S. Army Air Mobility Research and Development Laboratory, Fort Eustis, Virginia. This program was initiated in 1968 and was aimed originally at evaluation of the rotor as a stopped/stowed-rotor configuration. In 1969 the scope of the program was increased to include evaluation of the rotor

* The name TRAC is derived from the phrase "telescoping rotor aircraft".

in the high-speed compound helicopter mode, wherein the rotor continues to rotate, operating at minimum diameter, at forward speeds as high as 400 knots. Some of the advantages of the TRAC rotor in the high-speed compound mode are described in Reference 4.

The first wind tunnel test program of the dynamically scaled blades was conducted in 1969. It was terminated by two accidents which damaged two sets of blades beyond repair. The first accident was caused by an inadequate safety lock which allowed the rotor head to lift off the shaft at a high lift condition in forward flight, and the second was caused by a ground resonance type instability during a preliminary static whirl run with the second set of blades. It was believed that this instability would be cured by a more rigid mount, and a new fuselage with a stiffer internal structure was adapted to the system. A second test series, conducted in 1970, was also terminated by a form of ground resonance instability which occurred suddenly during a test run. Detailed records of the instability were obtained which demonstrated that the TRAC rotor blades were operating at perfectly acceptable stress conditions and that the problem was a classical ground resonance type of phenomenon in which the motion of the blades about the lag hinge coupled with lateral translation of the model on the support strut. Previous Sikorsky tests of other rotor systems on similar supports had always been conducted with reduced tip speeds (blades constructed to provide proper aeroelastic scaling at one-half tip speeds and forward speeds). The TRAC rotor model was designed to operate at full tip speeds and forward speeds, so that the rotational kinetic energy was much higher than for previous tests, and the potential ground resonance problem correspondingly more severe. It was finally evident that the test program would have to be interrupted to incorporate major revisions to the model support system, and the scope of the program was increased to accomplish these changes. Results of this phase of the contract program are reported in Reference 5 and are summarized briefly in this report. The problem was corrected, and it was demonstrated that the ground resonance behavior of the TRAC blades is essentially identical to that of conventional blades.

The basic tests of the TRAC rotor were completed in a straightforward manner in the third test series in 1972, including low-speed tests in the United Aircraft Research Laboratories (UARL) 18-foot wind tunnel and high-speed tests in the UARL 8-foot wind tunnel. The objectives of the test, which were to establish feasibility of the rotor system and to determine the aerodynamic, dynamic, and aeroelastic characteristics, were accomplished.

ROTOR SYSTEM DESIGN

DESCRIPTION OF BASIC CONCEPT

A schematic arrangement of the TRAC rotor blade is shown in Figure 1. The basic retraction mechanism is a jackscrew which serves as a primary tension member of the blade. Rotation of this screw imparts a linear retraction or extension motion to the retention nut and, through tension straps, to the outboard half of the blade which is the main lifting member. A torque tube, which is a streamlined ellipse in cross section, encloses the jackscrew, transmits blade pitch control motion to the outboard blade, and carries bending moments across the sliding joint. When the rotor diameter is reduced, the outboard blade slides over and encloses the torque tube. The outboard blade, with a full airfoil cross section, comprises the outer half of the radius when the blade is extended. The blade planform is unusual in that the effective root cutout is very large; however, even on a conventional blade the outboard half typically produces 90 percent of the total lift in hover, and the large root cutout produces only a few percent loss in hover efficiency (References 2 and 3).

The means for actuating the blade jackscrew is shown schematically in Figure 2. The heart of the mechanism is a differential gear set contained within the rotor head. The differential consists of upper and lower bevel gears and one bevel pinion connected to each blade jackscrew through a universal joint. The upper and lower bevel gears are each connected by coaxial shafts to a clutch or brake at the bottom of the transmission. Stopping the lower bevel gear with respect to the fuselage, while the rotor is turning, forces the pinions of the differential to roll around the bevel gear and thus turn the jackscrews and retract the blades. Braking the upper bevel gear reverses the motion and extends the blades. With both clutches released, there is no relative motion and the rotor diameter remains fixed. The basic mechanism is as simple and reliable as an automobile differential. The gears are fully engaged at all times and the blades are completely synchronized. No separate power supply is required, as the system is driven in both directions by rotation of the main shaft. The rotor diameter is under direct control of the pilot, or test operator, and is not influenced by aerodynamic forces or torques. It is mandatory that the clutches be released when the blades reach the limit of extension or retraction; however, there are a number of means of providing for automatic limitation of travel and redundant safety features.

Selection of Basic Concept

Early in the design study, numerous schemes were evaluated for their potential in achieving a variable-diameter rotor system. These included use of cables, rack-and-pinion devices, hydraulic and pneumatic systems, elastic schemes, and jackscrews (both conventional and antifriction types). A conventional type of jackscrew was selected as the best choice because of the following advantages: it has a high load capacity for its size and weight, it is simple and reliable, it is self-storing in the blade, and its efficiency can be adjusted to a desired value by selection of thread pitch and lubricants. A very high efficiency is neither needed nor particularly

desirable, because the rotor would tend to speed up when the blades are retracted. When operating at an overall mechanical efficiency of 50 percent, the rotational kinetic energy of the blades is dissipated at just the rate required for retraction at constant rpm in the absence of any external aerodynamic torque. A self-locking system results if the static efficiency is less than 50 percent. The jackscrew serves as a heat sink during diameter changes, and can be cooled conveniently with centrifugally pumped air. The jackscrew, in combination with the rotor head differential, provides positive synchronization between blades, with no requirement for ratchets, pawls, or gear-shifting devices. The jackscrew/tension strap combination can be made structurally redundant for high structural reliability. In addition to being self-storing, the mass of the jackscrew contributes substantially to blade flapping stability at minimum diameter, allowing operation at very high advance ratio.

The blade planform arrangement, wherein the outer blade slides over and encloses the torque tube, was selected over the alternate arrangement in which the outer blade slides into an airfoil-shaped sleeve. The sleeve configuration results in more blade surface area exposed after retraction and has a severe problem related to carrying the blade bending moments, particularly chordwise moments, across the sliding joint. The selected configuration greatly diminishes the problems of the sliding joint and, despite the large root cutout, has a hovering efficiency nearly as high as a blade with conventional planform.

PRELIMINARY DESIGN STUDY OF FULL-SCALE ROTOR

Design Criteria

Prior to the design and fabrication of the dynamic model blades for the wind tunnel investigation, a preliminary design study was conducted for a full-scale rotor system. It was decided that the study would be based on a relatively large helicopter. This ground rule results in a more severe test of the concept than would basing it on a small aircraft, because of the square-cube tendency for the weight fraction of the rotor system to increase with increasing size. Accordingly, a 72-foot-diameter rotor and a gross weight of 10,000 pounds were selected. This is the same diameter and approximately the same gross weight as for the CH-53 and CH-54 helicopters. Resulting disk loading is 10 pounds per square foot. A wing and auxiliary propulsion were assumed to be provided for cruise flight; thus the lift and propulsive force requirements of the rotor are reduced relative to a high-performance pure helicopter. It was assumed that the TRAC rotor would be required to provide full lift and propulsive force up to a forward speed of 100 knots, but that above this speed the lifting requirement (rotor blades extended) would be reduced in a linear fashion to 50 percent of gross weight at 150 knots, and that the propulsive force requirement would be reduced to zero at 150 knots. Diameter reduction was assumed to take place at 150 knots forward speed. This conversion speed is relatively high in order to permit complete unloading of the rotor during conversion with a wing sized for efficient cruise, so that the excessive wing size that would be required for a low-speed conversion is avoided.

A performance analysis indicated that the rotor lift and propulsive force criteria could be satisfied with a four-bladed rotor having a chord dimension of the outboard blades of 3.0 feet, corresponding to a weighted rotor solidity of 0.095, for a tip speed in the range of 650 to 700 feet per second (conventional Sikorsky Aircraft practice).

Additional design criteria included a rotor overspeed condition (tip speed up to 840 feet per second), vertical gust conditions (± 30 feet per second) and, with the rotor stopped at minimum diameter, maximum lift coefficient along the entire exposed blade length at 150 knots.

Analytical Methods

Because of the unusual blade structural arrangement, it was necessary to develop analytical design tools for the blade prior to the actual design. Two aeroelastic analyses, shown schematically in Figure 3, were developed by Sikorsky to assist in the design process. The first analysis considered only two major structural elements; the inboard element representing the combination of the torque tube and the jackscrew, and the outboard blade in compression. The tension strap was represented mathematically as a weightless string. The analysis represented the structural elements as eight finite length segments with lumped masses and equivalent springs representing elastic stiffness. Aerodynamic forces were treated in a conventional strip theory procedure utilizing two-dimensional airfoil data, including stall and Mach number effects. The analysis provided blade flapwise aeroelastic time histories and was also used to determine natural frequencies and mode shapes. This analysis was used in a parametric investigation in which a large number of different structural combinations were studied in order to establish a satisfactory design. The second analysis, with four structural elements, was developed to refine the design study by treatment of the internal components as well as the external ones. The general mathematical approach was the same, but 30 mathematical segments were used.

Flapwise bending natural frequencies calculated with the two-element aeroelastic analysis are shown in Figure 4 (from Reference 1) along with a comparison of the frequencies calculated by conventional analysis (outer blade in tension rather than in compression). This calculation corresponds to the full-scale blade design at full diameter, and demonstrates the effects of compression in the outer blade. At a tip speed above 1000 feet per second (well above design overspeed condition), compressive buckling would occur with a drop in the first mode natural frequency to zero. In the normal operating range, the natural frequencies are quite similar to those of current production blade designs.

More recently, the aeroelastic analysis has been extended to include chordwise and torsional degrees of freedom as well as any desired condition of retraction or extension. This work, performed with support from the U. S. Army and reported in Reference 6, will permit additional refinements in future design studies.

Another analytical method developed prior to the blade design was a heat transfer analysis developed to calculate temperature distributions within

the jackscrew caused by frictional heat generated during diameter changes.

In order to evaluate these temperatures it was necessary to develop a special analysis. Classical heat transfer problems usually involve a specified temperature boundary, whereas in this case the temperatures are unknown and the rate of heat generation at the contact surface is the known quantity. Consequently, the boundary condition at the contact surface is a temperature gradient which is dependent on the material conductivity properties, contact area, friction coefficient, centrifugal load, and retraction rate. A step-by-step numerical integration technique was programmed to solve the problem, and the computer program prints out a map of isotherms at specified time intervals. Figure 5 from Reference 1 shows the calculated temperature distribution within the jackscrew for the mid-point and the last instant of the passage of the nut over a particular point. The maximum contact temperature of approximately 500°F over ambient, calculated for the full-scale blade design, is within acceptable limits for the materials used.

Full-Scale Rotor Hardware Design

The preliminary design study included a brief investigation of the main rotor hub and diameter change actuation mechanism, and a study of the blade design in sufficient depth to obtain a reasonably accurate determination of dimensional characteristics and weight breakdown.

The study was based on the design conditions previously listed under the heading Design Criteria. Details of the design, derived from Reference 7, are presented in Appendix I.

MODEL BLADE DESIGN AND CONSTRUCTION

Design Criteria

A diameter of 9 feet (extended) was selected as a convenient size to test in the UARL 18-foot wind tunnel. This makes the model a one-eighth scale of the 72-foot rotor described in the preceding section and Appendix I. The model was dynamically scaled to provide aeroelastic similarity to the full-scale design when operated at full-scale tip speeds and forward speeds; thus, the model also provides full-scale Mach number scaling. A replica technique was used in designing the model, where, insofar as possible, the model structure was based on the same materials as the full-scale design and the dimensions were one-eighth those of the full-scale design. This technique automatically provides the aeroelastic similarity desired in flapwise, edgewise, and torsional degrees of freedom. A general discussion of the dynamic scaling techniques utilized is presented in Reference 8.

Full-speed and Mach-number scaling, rather than reduced-speed scaling, was selected because it was felt that the evaluation of structural dynamics of the concept would be the most important output of the program. Reduced-speed scaling is more easily achieved and entails lower risks because of reduced forces, moments and stresses, but does not provide a realistic

evaluation of the structural concepts involved. Furthermore, the total thermal energy generated by friction between the nut and screw would be greatly reduced. With full tip speeds, the thermal energy generated is properly scaled relative to the model mass; however, even in this case it should be noted that the heat transfer properties do not scale correctly, so that while the average jackscrew temperature due to the thermal impulse from a diameter change cycle is correct, the transient temperature distribution within the threads and body of the jackscrew is incorrect. Evaluation of this characteristic was beyond the scope of the contract study.

Description of Model Rotor

A general arrangement of the model blade including the inboard flapping mass is shown in Figure 6 in both the fully extended and retracted positions. The outer section of the blade has a chord of 4.50 inches and an NACA 63,A016 airfoil contour. The torque tube has an elliptical cross section with a chord of 1.50 inches and a thickness of 0.52 inch. The torque tube incorporates an integral cuff at the root end which is mechanically fastened to the sleeve-spindle assembly. No attempt was made to scale this assembly accurately because of the lack of availability of suitably sized bearings having the required load capacities, and as a result the sleeve-spindle assembly is substantially heavier than a dynamically scaled unit would be.

The major components of the blade consist of the outer blade, torque tube, bearing blocks, and the internal retraction mechanism (jackscrew, nut and tension straps). Details of the model blade construction are presented in Appendix II.

Model Rotor Specifications

Specifications for the TRAC model rotor are given in Table I. A comparison of the spanwise distribution of blade weight with that of the full-scale design (scaled down to the model size) is presented in Figure 7. Elastic stiffness properties, determined by static deflection tests, are presented in Figure 8.

TEST EQUIPMENT

WIND TUNNEL FACILITY

The United Aircraft Research Laboratories Main Wind Tunnel located in East Hartford, Connecticut, and shown in Figure 9 was used for the TRAC test. This tunnel is an atmospheric total-pressure, single-return, closed test section type. Both the low-speed and high-speed test sections are octagonal in shape. The low-speed section, which is 18 feet across the flats, is capable of speeds of approximately 170 knots. The high-speed insert, referred to as the 8-foot test section, is 7.75 feet across the flats and is capable of speeds approaching sonic velocity. Remotely controlled air exchangers located in the low-velocity section of the circuit are employed to maintain tunnel stagnation temperature at desired values. The large area of the exchangers insures that tunnel stagnation pressure is atmospheric. The tunnel fan is driven by a 9000-horsepower motor.

Velocity in the low-speed test section was measured with static pressure taps located along the sidewalls of the section. A calculated blockage correction of 1% was applied to tunnel speed for the low-speed tests. No angle-of-attack corrections were applied.

Velocity measurement in the high-speed test section involved a different procedure. Prior to rotor testing, a velocity calibration was performed with the tunnel cleared, using a Pitot-static tube and a rigidly mounted miniature airfoil section equipped with chordwise static pressure taps mounted at the front of the test section. The relationship between the airfoil minimum static pressure and tunnel velocity as measured by the Pitot tube was determined. The calibrated static pressure measurements on the airfoil were then used for setting tunnel velocity with the model installed and the Pitot tube removed. A 5% correction to tunnel velocity due to blockage was determined using static pressures measured on the test section sidewalls at stations adjacent to and upstream of the model. No angle-of-attack corrections were made.

The test section Reynolds number per foot and Mach number as a function of velocity are shown in Figure 10. Selection of full-scale Mach number testing minimized inaccuracies in blade loading and resultant stress distributions due to premature flow separation associated with subcritical Reynolds number on the outer blade. However, the Reynolds numbers were still only one-eighth of full scale, and corresponding aerodynamic effects are to be expected. The inboard portions of the torque tube, for example, normally operated at subcritical Reynolds number and presumably had an excessive drag coefficient as a result.

WIND TUNNEL MODEL

The TRAC wind tunnel model with blades fully extended is shown installed in the 18-foot low-speed section of the United Aircraft Research Laboratories Main Wind Tunnel in Figure 11. Figure 12 shows the model installed in the 8-foot section of the tunnel for the high-speed portion of the test, with blades in the retracted position.

The four-bladed model rotor head is of conventional design with the addition of a differential gear set and universal joints to permit extension and retraction of the telescoping rotor blades. A photograph of the rotor-head partially disassembled is shown in Figure 13. The fully articulated head has coincident flap and lag hinges located at the 3.0-inch radial station, corresponding to an offset ratio of .0555 with blades fully extended. Rotary viscous dampers are provided for each lag hinge. A 3:1 ratio mechanical linkage joins the rotary damper shaft and hinge (this linkage is disconnected in Figure 13). A pitch-flap coupling ratio of -0.5 (0.5 degree of down pitch per degree of up flapping) was provided for articulated portions of the test program. Rigid locking blocks were used to eliminate the flap and lag freedoms during the fully retracted low-rpm slowed-rotor and stopped-rotor phases of the test. The locking blocks also had provision for holding the blades in the partially folded and fully folded configurations appropriate for a stowed-rotor aircraft, as shown in Figure 14.

Additional details of the model, including the diameter change and measurement systems, blade pitch control system, rotor drive and gimbal mounting systems, and fuselage and support struts, are presented in Appendix III.

MODEL CONTROL CONSOLE

Three of the model operating parameters (forward speed, rotor rpm and fuselage angle of attack) were controlled from the wind tunnel facility control console in a standard manner. The remainder of the model controls, including blade pitch and rotor diameter controls, were centralized in a special console shown in Figure 15. The three blade pitch settings were independently controlled by three-position, spring-centered toggle switches. The impressed blade pitch angles (which can differ from actual angles because of the pitch-flap coupling) were displayed in digital form immediately above the corresponding toggle switches. These display meters were calibrated in degrees with a readout accuracy of .01 degree. The blade cyclic controls were frequently used in conjunction with the flapping resolver meters located higher up on the control console. Longitudinal and lateral tip path plane tilt were independently displayed.

The diameter control lever and readout meter were located near the top of the console. The diameter control lever was spring-centered to a neutral position and was moved to the left or right to retract or extend the blades as desired. Limit lights at both ends of the travel were activated by limit switches in the mechanized portion of the diameter measurement system contained within the model fuselage. These limit switches also controlled the diameter change clutch actuator as described in Appendix III.

Warning lights at the top of the console were wired to signal various types of information, such as drive motor temperature over limits, loss of drive motor power or control system power, gearbox chip detection, etc.

INSTRUMENTATION AND CALIBRATION

The measurements listed below were recorded during the wind tunnel test program. Several were included strictly for monitoring the safe operation of the model and are not presented in this report. Slipring capacity limited the number of simultaneous rotating measurements to eleven strain gage bridges in addition to the instrumented blade flap and lag motions. Several combinations of strain gages were selected for recording during the various phases of the test program. Strain gage data from the outer blade, jackscrew, and straps could not be recorded during the extension and retraction cycles. A small number of blade measurements were lost intermittently as the test progressed due primarily to failure of the strain gage wiring at connectors and solder joints.

The overall instrumentation list was as follows:

1. Fourteen rotor blade strain gage bridges were incorporated on the instrumented blade, including five flapwise, three edgewise, three torsion, jackscrew root flapwise and edgewise bending, and strap differential tension. Locations selected for strain gaging are shown in Figure 16. They were chosen to insure adequate definition of the radial distribution of stress and to include the stations where maximum stress was calculated with the aeroelastic analysis. The edgewise torque tube strain gages were mounted inside the elliptical tube to avoid interference with the sliding joints during diameter changes. Flapwise and torsion bridges on the outside of the torque tube were covered with a thin mylar and stainless steel bandage to prevent grounding of the gages when the outer blade covered the section. All strain gage bridges were assembled using four active arms to provide maximum transducer output, temperature compensation, and most complete cancellation of centrifugal strain.
2. Instrumented blade flap and lag motions were measured using film potentiometers.
3. Pushrod axial load was measured for the instrumented blade.
4. Rotor diameter was measured using a special mechanism driving a potentiometer.
5. Cyclic and collective pitch inputs were measured with potentiometers.
6. Six components of force and moment were measured on a Task Corporation 2.50 Mk XXIII strain gage balance.
7. Ten accelerometers were used for monitoring pitch and roll of the internal model, pitch and yaw of the fuselage structure, and lateral and longitudinal motions of the wind tunnel mounting struts.

8. Motor, gearbox, and clutch temperatures were monitored. Motor power, water, hydraulic, and oil system pressure, gearbox chip detection, clutch servo controller position and dynamic system elapsed time readouts were also available.
9. Timing signals for blade azimuthal reference were provided by photoelectric means producing a 1/rev and 72/rev pulse train. A 60-cps reference clock was also used.
10. Fundamental model operating conditions such as shaft angle of attack, and wind tunnel velocity, pressure, and temperature were determined using the wind tunnel facilities monitoring system.

Calibration of the model rotor blade strain gages was conducted with precision weights in a special fixture which applied pure moments along the length of the blades. Separate calibrations were conducted for the external and internal components of the blade. All physical calibrations were referenced to readings obtained by installing a precision series calibration resistor in the bridge circuit. A post-test calibration of the blade strain gages was conducted which verified that the values had remained constant.

The six-component strain gage balance was calibrated by applying known pure moments and forces in the shaft axis system at the rotorhead. A post-test verification calibration of the balance was also conducted.

The control system was calibrated using an inclinometer attached to a blade tip with an airfoil template which provided a flat surface parallel to the chordline.

Rotor shaft angle was controlled by the wind tunnel pitching strut which attached to the aft part of the fuselage. Shaft angle was calibrated using an inclinometer attached to the fuselage keel structure. Actual rotorshaft angle of attack varied by a negligible amount from these values due to deflections of the gimbal caused by airloads and gravity.

The instrumented blade flap and lag position transducers were calibrated prior to each test run using fixtures which held the blade in prescribed orientations.

DATA ACQUISITION AND MONITORING SYSTEMS

The principal data recording device used for the test program was a 14-track AMPEX AR200 FM tape deck. The recording system used narrow-band FM multiplex with standard subcarrier oscillators for IRIG channels 7 thru 16, allowing ten channels of data to be recorded on each track. Five direct-record tracks were used, allowing all dynamic measurements to be recorded simultaneously to provide proper time correlation of the signals. Channel allocation on each track was selected to insure high resolution of the retrieved harmonic blade strain traces to a minimum of 300 Hz. Additionally, one track was used for audio comments, one track

for rotor azimuth reference, and one track for a 60-Hz standard time reference. All signal conditioning and tape control functions were accomplished using Sikorsky-designed electronic modules. The data acquisition and monitoring system is shown installed in the wind tunnel control room in Figure 17.

In addition to the primary FM data acquisition system, which recorded 5-second data bursts at each test point, a second tape deck was provided to record continuously whenever the rotor system was turning. Normally, after the conclusion of a test run the magnetic tape from this unit was degaussed and reinstalled in preparation for the next phase of the test program. However, in the event that anything unusual had happened during the previous run which had not been recorded on the primary data tape, the backup tape could be interrogated for immediate inspection of the time history of the occurrence and could be retained for later detailed analysis.

Rotor performance information as measured by the strain gage balance was displayed on-line using the Sikorsky-developed Balance Axis Converter. This unit contains a small analog computer which performs the matrix manipulation to convert the measured strain gage outputs to pure forces and moments in the shaft axis coordinate system at the rotorhead. The unit utilizes third-order Butterworth filters to obtain pure steady readings. Resultant force and moment outputs in engineering units (pounds and foot-pounds) are displayed on six digital meters. A 70-mm camera was used to obtain a permanent record of the meter readings at each point.

Critical transducers were monitored continuously during the test runs. The instrumented blade flap and lag motions were displayed on oscilloscopes. Any FM channel could be displayed on-line for study of amplitude, wave form or signal quality. Sixteen channels of dynamic data were presented continuously on-line in a Sikorsky-developed console which detected average and one-half peak-to-peak signal content and presented these readings on vertically mounted meters, yielding a bar graph type presentation. Pre-determined redline operational limits were affixed to each of the meters. The system provided a quick-scan determination of overall model stress and vibration condition as well as rapid detection of excessive loading on any of the 16 channels.

An electronic resolver was provided for monitoring the first harmonic components of the instrumented blade flapping response. Nominal trimmed flight was considered achieved when first harmonic flapping as displayed on the two resolver output meters reached zero. Thus the tip path plane was trimmed perpendicular to the rotorshaft axis. Second or higher harmonics of flapping did not influence the resolver readings, but could be observed, when present, on the oscilloscope trace of flapping motion.

Portions of the test program completed in the first and second test series used data acquisition and monitoring systems similar to those described above with the exception of the Balance Axis Converter and stress monitor console. In the first test series the balance data was recorded by the

United Aircraft Research Laboratories STADAS II Static Data Acquisition System. The system included a computer link which provided on-line data reduction to coefficient form. In both test series, direct-writing oscillographs were used for monitoring multiple strain gage outputs.

DATA REDUCTION PROCEDURES

The dynamic test data tapes were processed using standard Sikorsky equipment and procedures. Each tape track was played back into a bank of narrow-band FM discriminators which decoded the multiplexed signals. The analog signals were then filtered at specified frequencies and recorded on permanent record oscillograph paper.

The order of the test points in each test run was similar, to facilitate data reduction procedures. Three points were recorded prior to and following each set of test points to provide the calibration constants of the strain gages and other transducers for that test run. Additionally, a nonrotating static test point provided the unloaded (except gravity load) position of all transducers, and a full rpm, zero velocity and collective pitch point provided the nominal zero strain output under centrifugal load alone.

All oscillograph records produced from the FM tapes were scanned. Significant data were read in engineering units with scale cards developed from the average pre- and post-run calibration values. (These values generally agreed within 2 percent). Conversion of calibrated bending moment to stress was made with the properties listed in Table I.

Repeatability and accuracy of the blade strain gage data are considered very good. Manual readings of the calibrations and data signals are estimated to involve inaccuracies no greater than 3% for highly loaded transducers and approximately 5% for moderately loaded flapwise and edge-wise bridges. Repeatability of strain gage data was very good, as demonstrated by duplicate test points in many of the figures.

The Balance Axis Converter data was manually read from the photographic records and was processed on a UNIVAC 1108 computer to correct the loads for gravity tares and rotorhead tares (rotorhead-alone airloads). Lift and drag in the wind axis system were then calculated, as well as the nondimensionalized performance coefficients.

Characteristic repeatability of the force and moment outputs is also good as shown by duplicate test points in many figures. Repeatability of post-run static force and moment readings was generally within 1 pound and 1 foot-pound respectively.

TEST PLANS AND PROCEDURES

DEFINITION OF TEST PHASES

The wind tunnel test plan was divided into eight phases as follows:

Phase I - Helicopter Mode - evaluation of rotor performance and stresses at conventional helicopter tip speed and forward speeds, over a range of lift and propulsive force conditions.

Phase II - Diameter Change - evaluation of stresses and dynamic behavior during blade retractions and extensions and at intermediate fixed diameter conditions at speeds up to 150 knots.

Phase III - RPM Change, Articulated - evaluation of rotor behavior at minimum diameter at rotor rpm values between 50 percent and 100 percent of normal, with blades fully articulated.

Phase IV - RPM Change, Locked Hinges - evaluation of rotor behavior at minimum diameter with hinges locked, at rpm values between 0 and 50 percent, simulating conversion to a stopped-rotor configuration.

Phase V - Blade Index Variations - investigation of rotor characteristics as blades were indexed to various positions, simulating folding the blades preparatory to stowing for a stowed-rotor configuration.

Phase VI - Low-Speed Hub Tares - measurement of hub forces and moments with blades removed at conditions corresponding to Phases I - V.

Phase VII - High-Speed Compound Mode - evaluation of rotor characteristics in the minimum diameter, fully articulated configuration in the speed range from 150 to 400 knots.

Phase VIII - High-Speed Hub Tares - measurement of hub forces and moments with blades removed at conditions corresponding to Phase VII.

The first six test phases were conducted in the UARL 18-foot wind tunnel, and the last two in the UARL 8-foot wind tunnel. The above-listed phases do not include the normal pretest activities or ground resonance investigations described briefly in a following section.

The rotor operating conditions corresponding to the various test phases are illustrated in Figure 18, which shows the rotor tip speed/forward speed combinations of the test. Lines of advance ratio (ratio of forward speed to tip speed) are shown, and one line of advancing tip Mach number for a standard day condition is also shown. Each circle in Figure 18 represents

a number of test points taken at that condition, and the size of the circle is intended to correspond to the rotor diameter. Not shown on the chart are a number of preliminary diameter change trials conducted at forward speeds below 150 knots.

PRETEST AND TEST PROCEDURES

Ground Resonance Checkout

An extensive pretest checkout of the model installed on the wind tunnel struts was conducted to insure that ground resonance type instabilities would not be encountered. This work, described in detail in Reference 5, is summarized briefly below.

A 100-lb-capacity electromagnetic shaker was mounted in the wind tunnel at the level of the blade hinges. A strain gage load cell connected the shaker to the rotorhead. The shaker was operated at several force amplitudes through a range of frequencies to determine rotor hub lateral and longitudinal impedance characteristics and nonlinearities with forcing amplitude. Tuning of the gimbal and support structure by varying damping outputs and spring constants was conducted to provide maximum stability margins.

The shaker was then mounted on a pedestal below the model to permit forcing of the internal model with the rotor operating and with the wind on. Nontelescoping dynamically scaled 9-foot-diameter model rotor blades were installed. Testing was conducted with the rotor operating in hover, through a wide range of rotor rpm values, at various shaker amplitudes and frequencies. Instrumented blade lag motions were monitored continuously to detect any increase in subharmonic inplane response. A repeat of this hover testing, with the extended TRAC blades installed, verified that the TRAC blades and standard nontelescoping blades had similar response characteristics. Final validation of the gimbal and strut system was accomplished by operating the nontelescoping blades at forward speeds to 170 knots, again using the shaker to provide variable-frequency vibratory inputs. Satisfactory response characteristics were found throughout the flight test envelope.

The adequacy of the high-speed test section mounting struts was also experimentally verified. Lateral and longitudinal hub impedance characteristics were again determined by applying vibratory inputs to the rotorhead. Margins of safety were found to be large, and no additional validation was conducted other than the operational vibratory check described below.

An operational check of the overall system response was conducted prior to each test run and at each new flight regime during testing with the telescoping blades. Operation of a variable-speed mass-imbalance vibrator through a range of frequencies produced a characteristic amplitude and frequency response. The response was checked regularly for any signs of decrement in the performance of the dampers, or failure of gimbal or strut components leading to increased response amplitude or lowered natural frequency. No difficulty was encountered with ground resonance in any part

of the program with the new model mounting system.

Normal Run Procedure

Prior to each test run a series of electrical instrumentation calibrations were conducted to provide the calibration constants in the subsequent data reduction process. Blade flap and lag motions (for articulated test phases) were calibrated by physically positioning the blades in prescribed positions. Model angle of attack was then positioned to each of the angles planned for the test run in order to establish gravity tares (effect of the weight of the metric portion of the model on strain gage balance output). The angle of attack was then returned to zero and the rotor brought up to the rpm value planned for the initial test conditions, at zero blade pitch values, and a "dynamic zero" test point recorded for reference. The wind velocity in the tunnel was increased from zero to the desired value with the model at a nominal zero lift condition, while blade stresses and other parameters were monitored and tip path plane tilt was kept approximately at zero by cyclic pitch inputs. After the desired wind speed was reached, the planned test envelope was investigated while continuously monitoring stress and vibration levels. In some cases stress levels reached prescribed limits before all planned test points were obtained. In these cases half increments in the parameter being varied were utilized to define the stress buildup and to obtain the desired number of test conditions. On other occasions additional test points were added to the test plan to more fully explore moderate load flight regimes.

At the completion of each test run, the wind tunnel was shut down with the model returned to the nominal zero lift condition and the rotor rpm maintained. A repeat "dynamic zero" point was followed by shutting down the rotor and then obtaining final electrical calibration points to verify the initial calibrations.

TEST RESULTS AND ANALYSIS

SPECIAL CONSIDERATIONS

Because the rotor diameter is a variable in this program, it is necessary to adopt certain conventions in presenting the data. Identification of strain gage locations, for example, is based on the radial position, expressed in percent, of the gage location when the blade is fully extended. The same identification labels are utilized when the blade is partially or fully retracted.

Interpretation of rotor force measurements requires an unconventional means of data presentation. It is conventional helicopter practice to present nondimensional force coefficients by dividing rotor forces by the factor $\pi R^2 \rho (\Omega R)^2 c$. However, with radius R decreased, solidity c increased, and in some cases rotational speed Ω decreased, the nondimensional coefficients for the rotor at reduced diameter cannot be compared directly with those for the rotor at full diameter. A similar situation exists for rotor moments. In order to provide a common base, in most cases rotor forces and moments are presented in pounds and foot-pounds, respectively, or are nondimensionalized by the extended values of R and c and by full rotational speed (1375 rpm), even though the values differ from actual test conditions. In these cases an asterisk is utilized to denote that this convention has been used. In some plots multiple ordinate scales are utilized to provide rapid conversion from one convention to the other. The advantage of using a common base for the data is that direct comparisons of the extended conditions (low-forward-speed helicopter mode) and retracted conditions (higher speed modes) may be made. Such comparisons are an important consideration in the present program. For reference purposes, the nominal lift of the model rotor is 625 pounds. This number is derived from the full-scale design study gross weight of 40,000 pounds, divided by the model scale factor squared: $40,000 / (8)^2 = 625$.

A summary of the maximum range of rotor lift encountered in the test program is presented in Figure 19. This plot illustrates the use of the convention described above. It should be noted that the rotor lift coefficient-solidity ratios, based on actual dimensions and tip speed, are much higher at high forward speeds than the values shown (by a factor varying from 4 to 10 depending on rotor rpm).

In some phases of the test program, simulated vertical gusts were investigated by means of increasing or decreasing model angle of attack with all rotor controls held fixed. The relation between the angle of attack change and simulated gust velocity is $\Delta\alpha = \tan^{-1} \frac{\Delta V}{V} \text{ gust}$. The range of gust

velocities investigated as a function of forward speed is presented in Figure 20. These gusts are unrelieved because there is no relieving vertical acceleration as in free flight; also the simulated gust in the wind tunnel lasts much longer than a real gust because the model angle of attack changes slowly and must be held in the gust condition long enough to record data.

HELICOPTER MODE (Phase I)

The objectives of the Phase I portion of the test program were to demonstrate satisfactory performance and blade stress characteristics for the TRAC rotor in the conventional helicopter flight regime. The model was tested through a range of angle of attack and collective pitch at forward velocities of 60, 90, 120, and 150 knots to establish maps of rotor flight conditions encompassing low-power descent, cruise and climb. Full rotor diameter and tip speed were maintained throughout this phase of the test. First harmonic blade flapping (tip path plane tilt) with respect to the rotor shaft was trimmed to zero by means of cyclic pitch for all test points.

At each velocity and rotor shaft angle, testing was begun at an unloaded rotor condition. Test points were then recorded at increasing collective pitch values until limitations of available power or blade stress were encountered. A repeat data point was then taken at the unloaded collective pitch value before the rotor shaft angle was changed for the next series of data points.

Rotor Performance Characteristics

Figures 21 thru 24 present the fundamental rotor performance test data results at velocities of 60, 90, 120 and 150 knots respectively. The data form a consistent family of curves of conventional appearance for a rotor with pitch-flap coupling. Repeat data points are also indicated on these figures. The lack of repeatability for some of these points was due to a difference in the cyclic control position used to trim the rotor within the $\pm 0.2^\circ$ tip path plane tilt tolerance. Lift, drag, and torque values agreed very closely for points which were retrimmed at identical cyclic pitch values.

The range of lift and propulsive force values investigated exceeded the minimum requirements discussed in the section entitled Preliminary Design Study of Full-Scale Rotor. At 60 and 90 knots the maximum lift was higher than the scaled gross weight value (625 lb for the one-eighth scale model) and at 120 and 150 knots the maximum lift was higher than the assumed rotor lift schedule, which decreased linearly from 100% rotor lift at 100 knots to 50% rotor lift at 150 knots. Similarly, the propulsive force requirements called for in the design study were exceeded throughout the speed range. At 60 and 90 knots, the maximum propulsive force conditions reached correspond to a rate of climb of approximately 1000 feet per minute without auxiliary propulsion. The maximum rotor power reached was at 60 knots; the single test point shown in Figure 21 at a collective pitch of 16 degrees corresponded to a blade stall condition, and the drive motor horsepower at this point was approximately 50 percent above nominal rated capacity.

One unanticipated result is that measured rotor lift is negative at the nominal zero lift condition (zero angle of attack and zero collective pitch). In previous test programs of other rotor systems, positive lift usually occurred at this condition due to aerodynamic interference of the fuselage or support system below the rotor. The large root cutout of the TRAC blade planform may account for this apparent reversed interference effect. The

magnitude of the negative lift measured is equivalent to a collective pitch increment of approximately 1 degree.

The first harmonic coefficients of blade flapping in the control axis system are presented in Figures 25 thru 28 corresponding to 60, 90, 120- and 150-knot forward velocities. The coefficients were obtained from the cyclic control inputs required to trim flapping relative to the shaft, in accordance with the following relationships: $a_1 = a_{1s} + B_{1s}$, $b_1 = b_{1s} - A_{1s}$.

For the Phase I tests, $a_{1s} = b_{1s} = 0$ because the rotor tip path plane was trimmed perpendicular to the rotor shaft axis. Curves were faired through the constant collective pitch points. Scatter in the data (generally less than 0.3°) is due primarily to the tolerance on the trimmed flapping.

Blade flapping motion is typical for articulated rotors. Longitudinal flapping increases with forward speed, collective pitch, and shaft angle in a manner similar to rotor lift. Lateral flapping also increases with collective pitch, but the incremental change for a given change in collective decreases with increasing forward speeds.

Theoretical rotor performance characteristics were calculated with the Sikorsky Generalized Rotor Performance method for correlation with test data. The computer program is the same as that utilized in preparing the performance charts of Reference 14, except that different airfoil section data were used as appropriate. Calculated data are presented in Figures 29 and 30 for forward speeds of 90 and 150 knots respectively. As can be seen by a comparison with Figures 22 and 24, the qualitative agreement with test data is excellent. The primary difference between theoretical and experimental data is the apparent increment to collective pitch previously noted for the test data.

Predicted blade flapping responses from the Generalized Rotor Performance program are presented in Figures 31 and 32 at 90 and 150 knots respectively. By comparing these results with test data shown in Figures 26 and 28 it is apparent that longitudinal blade flapping correlates well. Lateral flapping response is not as accurately predicted, with the experimental data showing larger values than the theoretical results.

A more succinct comparison between predicted and experimentally determined rotor performance is shown in Figures 33 and 34 for 90 and 150 knots respectively. These cross-plots present the primary parameters of rotor lift, drag and torque and eliminate angle of attack and blade pitch angles as variables. The correlation at 90 knots is quite good. At high lift and high propulsive force, rotor torque is underpredicted by approximately 10%, but as the propulsive force is reduced the calculated value approaches the experimental data. At 150 knots the calculated torque values were generally above those found experimentally for a given lift and propulsive force. Differences between theory and experiment are presumed to be due at least partially to the airfoil characteristics assumed, which were derived from various sources to represent full-scale TRAC blade sections. Experimental airfoil data corresponding to the model blade sections were not available.

The azimuthal variations of several model blade strain gage and blade motion signals are presented in Figures 35 and 36 for 90 and 150 knots respectively. The harmonic content of these traces is representative of that found throughout Phase I. Also included in these figures is jackscrew flapwise bending moment, which was of small magnitude. Jackscrew edgewise moment and strap differential tension were not recorded in Phase I.

Typical blade vibratory bending moment and stress data are presented in Figures 37 thru 42. Figures 37 thru 39 respectively present radial distributions of flapwise, edgewise, and torsional vibratory moments (one-half peak-to-peak values) for a test speed of 60 knots. Figures 40 thru 42 present similar data obtained at 150 knots. Each figure contains the maximum and minimum vibratory loading encountered at each of three rotor shaft angles of attack, covering the helicopter mode test envelope. Blade vibratory bending moment is used as the primary ordinate scale because of the continuous character of the moment loading across the sliding joint of the blade. Blade stresses are not continuous across the joint because the structural section properties on the torque tube and outer blade are different. Separate stress scales are shown for these two components on the right and left of each plot. The actual moment at the end of each section of the blade must go to zero in the overlap region approximately as indicated by the dotted lines in Figure 37 for $\alpha_{TPP} = +4^\circ$. In all cases, tip loading must go to zero.

No root end restraint exists in the flapwise direction; therefore, these moments go to zero at the hinge ($r/R = .055$). Edgewise motion is partially restrained by the lag damper, and therefore the edgewise vibratory moment is not zero at the hinge. Torsional moments also do not go to zero at the blade root, but are transferred across the hinge by the pushrods and control horn. Repeat data points indicate that repeatability of the stress measurements is very good.

Flapwise moments and stresses are shown in Figures 37 and 40 for 60 and 150 knots respectively. Stress levels on the torque tube were low throughout this phase of the test. Maximum stress on the torque tube was always measured at the root end (15% radial station) and reached values of approximately 3000 psi. This stress level is higher than would be experienced full scale due to the over-scale root flapping mass. The outer blade, which is under a compressive centrifugal load, experiences maximum stress near its midpoint, as measured by the strain gage at the 79% radial station. The vibratory bending stresses increase with rotor lift and were normally limited to approximately 8000 psi. Because of the steady centrifugal compression load, allowable stresses should be higher than for a blade in tension. It should also be possible to reduce outer blade stresses by increased flapwise stiffness.

Edgewise bending moments and stresses are presented in Figures 38 and 41. Two separate ordinate scales are shown on the right of each plot for edgewise stresses on the outer blade; one scale for leading-edge stress and one scale for trailing-edge stress. The stresses on leading and trailing edges are different for a given edgewise moment because of the differing distance from the blade elastic axis and because of the differing moduli

of elasticity of the two materials used. Vibratory edgewise stresses on the torque tube were found to be well within material limits, with maximums of less than 3000 psi. Stress levels on the outer blade leading edge were small, and the levels on the magnesium trailing edge were well within allowable limits.

Model blade edgewise stresses are believed to be somewhat higher than would be experienced full scale, due to an edgewise frequency for the fully extended blade which was close to the model drive motor 1/rev frequency. The drive motor was known to have a slight unbalance, and the gearbox reduction ratio would convert this to a 3.25/rev frequency with respect to the rotor. This exact frequency was prominent in the blade edgewise stresses.

Torsional blade vibratory moments and stresses as shown in Figures 39 and 42 were small on both the torque tube and outer blade. Torsional vibratory stress was essentially constant along the length of the torque tube, with the maximum values encountered being approximately 1600 psi. The vibratory torsional moment dropped significantly outboard of the sliding joint and then reduced gradually to satisfy the zero boundary condition at the tip end. Maximum outer blade torsional stress in the spar was less than 1000 psi.

Although vibratory stresses are of primary concern, the steady or mean components of stress on the blade are also of interest. Figure 43 is a representative plot of the range of mean moment and stress values encountered during Phase I testing. The mean stresses presented are due to aero-elastic bending and do not include steady centrifugal stress loadings. As before, maximum and minimum rotor loading conditions are presented which correspond to the uppermost plots of Figures 40, 41, and 42. The flapwise mean moment on the outer blade was found to change significantly as the rotor loadings increased. The shape of the mean flapwise loading curve, with the torque tube bending up and the outer blade bending down, is typical.

Edgewise mean bending moments increased only slightly at high rotor loadings. Maximum edgewise mean moment and stress occurs inboard of the location of maximum vibratory stress, at about the 50% radial station. Torsional mean loadings were very low and were not significantly affected by the increase in rotor lift.

The effects of variation of rotor shaft angle and collective pitch on the maximum flapwise vibratory stress on the torque tube and outer blade, for the fully extended blade, are presented in Figures 44 and 45 for a test speed of 60 knots. The fact that well-defined families of curves were found is indicative of the sensitivity and repeatability of the stress measurements. The flapwise 15% station shown in Figure 44 was found to be relatively insensitive to changes in shaft angle and collective pitch except at the highest collective values tested. The flapwise 79% station shown in Figure 45, on the other hand, indicates a strong relationship. Outer blade flapwise stress increased with collective pitch and increased with increasing shaft angle at least to $\alpha_{Tpp} = +40^\circ$.

The four-element aeroelastic analysis discussed in ROTOR SYSTEM DESIGN was used to calculate stresses for correlation with test data. The calculated rotor conditions were matched to the actual model rotor lift at the same tip path plane angle and forward speed. The program iterated to a trimmed flapping solution. Calculated cyclic pitch, rotor drag and rotor torque for the converged solutions agreed closely with actual model values; however calculated collective pitch was about 2 degrees lower than experimental values. Figures 46 and 47 present blade vibratory moment and stress correlation results at 90 and 150 knots respectively. The aeroelastic analysis results predicted the general character of the radial distribution of vibratory moment. The calculated loading on the torque tube agreed closely with that found experimentally except at the inboard end. The outer blade stress was significantly underpredicted. One factor that tends to account for this discrepancy is that uniform rotor inflow was assumed in the calculations, whereas both the rotor wake vortex structure and the fuselage interference effects will result in nonuniform inflow, known to influence blade aeroelastic behavior. A reduction in vibratory bending moment in the blade overlap area was predicted by the analysis. This is not confirmed by the test data except possibly for the case shown in Figure 47 at $\alpha_{TPP} = 0^\circ$.

Theoretical and experimental time histories of blade bending moment and stress for one rotor revolution are compared in Figures 48 thru 51. The flapwise 15% station measurement at 90 knots is shown in Figure 48. The predicted average and peak-to-peak values are reasonably similar to the test values; however, the time history differs considerably due to the higher frequency content in the experimental data. Experimental and computed time histories of flapwise 79% station moment are presented in Figure 49 for the same test condition. The waveform characteristics of the two traces are similar. The mean experimental stress values indicate more tip-down bending than the calculated result, and the vibratory amplitude is approximately 60% higher than the predicted value. In addition, a general phase shift of the traces in which the experimental peaks lag the predicted peaks by approximately 40° is noted.

The predicted bending moment at the 15% flapwise station at 150 knots is shown in Figure 50. As at the lower speed, prediction of waveform is relatively poor. Figure 51 presents the flapwise 79% station data at 150 knots. Theory and experiment show good waveform agreement, although the average and peak-to-peak values are underpredicted by the analysis and the previously noted phase shift is evident.

DIAMETER CHANGE (Phase II)

This test phase included continuous (dynamic) diameter changes (retractions and extensions) as well as tests at constant, intermediate-diameter conditions. Simulated vertical gusts were included at various test conditions, and also rotor stability and control derivatives were established over a range of diameters.

Initial continuous diameter changes were investigated at reduced tip speeds

and forward speeds, building up toward full rotational speed and the nominal forward-flight conversion speed of 150 knots. Another safety consideration dictated the use of travel margins for both retractions and extensions. As the model did not incorporate redundant physical stops that would be designed into a full-scale system, and also because of the very rapid change in diameter for the model (full travel in approximately 4 seconds at full rpm), which made fine manual positioning difficult, a margin for error of 2 to 3 percent radius was incorporated in the electrical feedback system described in Appendix III. Thus, the continuous diameter changes do not cover the full range of 100 to 60 percent, but in most cases from approximately 97.5 to 62.5 percent. The fixed-diameter conditions in the other test phases, however, did cover the full diameter range.

Continuous Diameter Changes

A total of 16 diameter changes were demonstrated during the test program, as listed in Table II. Because of the large amount of data obtained, only typical cases can be presented; however, all of the data support the general conclusions drawn.

A time history of diameter change at 120 knots forward speed and 1185 rpm is presented in Figure 52. This data trace, obtained in the second series of model tests (1970), shows a diameter reduction followed by a diameter increase. The model was initially trimmed to zero tip-path-plane tilt, and the pitch controls were held fixed during the diameter reduction and subsequent extension. The oscillograph record presentation suggests that the extension occurred within a few seconds of the retraction; actually there were several minutes between these two records while rotor forces, etc., were recorded.

A number of pertinent facts can be observed by examination of Figure 52. The top trace in the figure is the rotor diameter signal, and (in this figure only) an upward slope to the line indicates that the diameter is decreasing. The abrupt changes in slope at the initiation and completion of the diameter changes indicate that the clutch did not slip appreciably during engagement or disengagement. The second trace indicates that the flapping angle responded significantly during the initial portion of the blade retraction, with a maximum tip-path-plane tilt of approximately 1.3 degrees. More will be said about this response subsequently. The third trace is blade lag angle, which shows that during retraction the blade leads forward from the initial position by about 1 degree and that it lags backward about the same amount during the subsequent extension. This is a simple Coriolis effect that is to be expected from the radial motion of the outer blade mass.

The fourth trace is the torsion measurement at the root end of the torque tube (17% station). This measurement indicated a noticeable nose-down torsional moment on the blade which slightly preceded the actual diameter change. It is explained by consideration of the torque which the blade jackscrew must exert on the nut during retraction. This torque on the nut is reacted by the blade torque tube, and is responsible for the shift

in the torsional stress. As the blade has a finite torsional stiffness, this torque physically twists the blade a slight amount, with the result that the rotor ends up with a small negative increment in collective pitch. This pitch change causes the flapping response shown. As the blade is retracted, the nut moves from the outer end of the torque tube toward the root end, and the centrifugal force of the outer blade is reduced. This results in a smaller reaction torque and a shorter length of the blade over which the torque is applied, so that the blade pitch change and hence the flapping response is reduced as the diameter is reduced.

The blade twist resulting from the nut torque also produced a negative lift on the rotor during retraction. The magnitude of this lift change was not measured because it was a transient phenomenon and only steady-state rotor loads were measured. The lift increment would correspond approximately to the change in coning angle, which was determined to be approximately 0.4 degree. The lift and flapping responses are considered to be undesirable side effects to the blade retraction. These effects could be alleviated or eliminated by one or more of the following means: (1) a smoother, slipping clutch engagement, (2) increasing collective pitch during engagement of the retraction clutch in such a way as to cancel the twisting effect, or (3) provision for an internal, secondary torque tube to react the nut torque without transmitting it to the outer main torque tube.

During blade extension, there is essentially no nut torque reaction; this is evidenced by the fact that the 17 percent station torsion measurement shows a very small response and the flapping also shows essentially no change on clutch engagement.

The remainder of the oscillograph traces in Figure 52 are three flapwise stress stations on the torque tube, pushrod load, an edgewise stress station on the torque tube, and the one-per-revolution reference signal at the bottom of the figure. Stresses on the outer blade could not be recorded during continuous diameter changes because of the problem of getting instrumentation signals across the sliding joint. The measured stresses were all low throughout the time history; the maximum vibratory stress was only about 2500 psi, less than half of allowable values. Despite the fact that as blade length changes there must have been a number of resonant conditions (blade natural frequency in some mode equal to an integral number times the rotational frequency), there was no sign of any important amplification of stresses. This result is probably due both to the rapid change of blade length, so that no resonant condition existed very long, and to adequate damping and lack of strong aerodynamic excitation at the resonant frequencies. The traces do show some undulations in the mean stress values; for example, the flapwise 32% station trace shows a wave-like disturbance part way through the retraction cycle. These disturbances correlate with the location of the bearing block on the root end of the outboard blade; when the bearing block slides close by a strain gage station on the torque tube, there is a local stress redistribution which shows up in the oscillograph record.

The pushrod load trace in Figure 52 shows the same shift in steady value as the torsion 17% station, for the same reason. However, the higher ratio of vibratory to steady load in the pushrod signal indicates that the feathering inertia of the root end mass and/or the friction force in the feathering bearings are relatively high; otherwise, this measurement would have a signature essentially identical to that of the torsion measurement.

Two more time histories of diameter changes are presented in Figures 53 and 54 for 150 knots forward speed and 1375 rpm. The first case corresponds to an initial trim condition (zero tip-path-plane tilt) at zero collective pitch and zero shaft angle of attack. The second case is a simulated gust condition, with an incremental angle of attack of +2.0 degrees, corresponding to an unrelieved vertical gust velocity of approximately 9 feet per second. Results are generally similar to those of Figure 52, although certain differences should be noted. The rotor diameter signal has been reversed relative to Figure 52 so that a positive slope corresponds to a diameter increase; also, the diameter signal is displayed twice. An additional edgewise bending station is shown, and the outputs of the six individual force elements of the strain gage balance are shown for reference.

One difference between the time histories shown in Figures 53 and 54 and that shown in Figure 52 is that the clutch was engaged much more gradually, resulting in somewhat rounded curves on the diameter trace at the start of the records and correspondingly more gradual changes on some of the other signals.

In the simulated gust case (Figure 54), the diameter change lever on the control console was not returned to neutral position until the limit switch in the diameter control system, described in Appendix III, was contacted. Under these circumstances the diameter control circuit automatically drives the diameter in the opposite direction as soon as the control lever is released. This behavior is evidenced both in the retraction cycle and the subsequent extension cycle by the slight reversal in the diameter trace at the completion of the blade travel. The disturbance caused by this reversal at the end of the retraction cycle is minimal, but at the end of the extension cycle, when the rotor goes automatically into the retract mode for about three rotor revolutions, a greater disturbance was noted, because of the higher internal reaction torque involved.

The time history of the vibratory (one-half peak-to-peak) blade stresses during a typical retraction at 150 knots is shown in Figure 55. These data were derived from the oscillograph record of Figure 53. The abscissa of Figure 55 is time from the start of retraction; also shown is rotor diameter, which is slightly nonlinear with time because of the gradual clutch engagement. As can be seen, all of the vibratory stresses reduce as the rotor is reduced in diameter from maximum to minimum, although there are small amplifications indicated at various points. Again, all measured stresses are well below allowable limits throughout the cycle.

The time history of rotor coning and tip-path-plane tilt for the gust case, derived from an expanded time scale version of the oscillograph record shown in Figure 54, is shown in Figure 56. The diameter reduction is accompanied, near the start of the cycle, by a decrease in coning angle of about 0.5 degree and an incremental forward tip-path-plane tilt of about 2.0 degrees. This response is caused by the effective negative blade collective pitch induced by the nut torque. The lateral tip-path-plane tilt is not influenced appreciably. As the diameter was reduced to the minimum value, the flapping response decreased. At the end of the cycle, when the clutch was released and the torque became nonexistent, the blade flapping had an impulse in the opposite sense as at the start of the cycle, but of smaller magnitude. The longitudinal tip-path-plane tilt was farther from trim than before the start of the retraction; this is merely an indication that different cyclic pitch values are required to trim the rotor at different diameters.

Constant-Diameter Conditions

Performance parameters measured with the rotor at various fixed diameters are presented in Figure 57. As explained at the beginning of the TEST RESULTS AND ANALYSIS section, the nondimensional performance coefficients shown are based on full diameter and tip speed even though actual diameter and tip speed are variables on the plot. Results are shown for the rotor at nominal zero lift ($\alpha_s = \theta_c = 0^\circ$, flapping trimmed to zero) and for two gust cases. As noted in the discussion on Phase I, there was a significant negative lift at full diameter at the nominal zero lift setting, attributed to an airframe aerodynamic interference effect. After the diameter is reduced, the lift does become nearly zero, at least at this forward speed. (As noted under Phase VII, the lift interference reverses and becomes strongly positive at high forward speeds.) The gust conditions were simulated at each diameter by increasing and decreasing model angle of attack from the trimmed condition, holding rotor pitch controls fixed. As can be seen, the magnitude of the lift change due to the gust decreases substantially as diameter is reduced.

Reduction in diameter produces large reductions in both drag and torque, as indicated in Figure 57. At minimum diameter the rotor drag is less than 1 percent of the 625-pound lift value that corresponds to the design gross weight of the assumed aircraft. The simulated gusts have relatively little effect on the drag and torque parameters.

Part of the investigation of the TRAC rotor was to determine how the various operational modes of the rotor influenced static stability and control derivatives. These derivatives were established by means of incrementally varying angle of attack and blade pitch control settings, one at a time, from an initial trim condition and recording the changes in rotor lift and hub moment. For each angular parameter, both positive and negative increments of 1 or 2 degrees were utilized in order to have at least three points on the curve of output force or moment versus input angle. A typical plot of this type is shown in Figure 58, which presents rotor lift as a function of each of the four angles, for three diameter conditions. As can be seen, the relationships are linear; the partial

derivatives of interest are the slopes of these lines. Similar plots were made for rotor pitching and rolling moment; 12 derivatives were established in this manner for each initial trim condition.

The measured derivatives are presented in Figure 59 as a function of rotor diameter. Unflagged symbols and faired curves represent the experimental data; flagged symbols are theoretical values. The lift derivatives all decrease substantially in magnitude as diameter is decreased. The derivative of lift with respect to lateral cyclic pitch is small at all diameters. Note that the partial derivative of lift with respect to shaft angle, $\partial L/\partial a_s$, is approximately equal and opposite to the derivative with respect to longitudinal cyclic pitch, $\partial L/\partial B_{1s}$; this equivalency is normal for articulated rotors. It should be noted that all of the a_s derivatives, in addition to being longitudinal stability derivatives, also represent the rotor response to a vertical gust that produces a 1-degree angle-of-attack change.

The pitching moment derivatives also decrease in magnitude with decreasing diameter, but not to the same extent as the lift derivatives. The maximum moments are not excessive in any case because of the articulation. For example, the maximum longitudinal cyclic derivative shown (-20 ft-lb/deg) represents a moment per degree equivalent to a shift in aircraft center of gravity of only 0.7 percent of the extended rotor radius. Unlike the lift derivatives, the pitching moment produced by shaft angle of attack variation is not equivalent to the variation with longitudinal cyclic pitch; this stems from the fact that the hub moment for an articulated rotor is primarily a function of tip-path-plane tilt relative to the shaft. At 150 knots flight speed, 1 degree B_{1s} produces substantially more flapping relative to the shaft than does 1 degree change in shaft angle of attack.

The derivative of pitching moment with lateral cyclic pitch is nonlinear with rotor diameter. Normally this derivative would be expected to be much smaller than the longitudinal cyclic derivative, but there is a significant cross-coupling in the A_{1s} and B_{1s} controls because of the pitch-flap coupling. For an articulated rotor with zero hinge offset, pitch-flap coupling reduces the phase angle (angle between input blade pitch and maximum flapping response) from 90 degrees to 90 degrees minus the "delta three" angle. For the pitch-flap coupling used in this program the "delta three" angle is 26.5 degrees, so that the phase angle for zero hinge offset would be 63.5 degrees. With a finite hinge offset, the phase angle is further reduced by a few percent. As rotor diameter is reduced, the percent hinge offset is increased with additional reduction of phase angle; this effect is believed to be responsible for the nonlinear variation noted. At minimum diameter, the A_{1s} and B_{1s} derivatives are approximately equal in magnitude. In a flight vehicle design, of course, most of this cross coupling can be eliminated simply by reorienting the phase of the swash plate input controls; this is standard helicopter practice.

The rolling moment derivatives shown at the bottom of Figure 59 show additional evidence of the cross coupling induced by the pitch-flap coupling, similar to the case for pitching moment. The derivatives with

respect to collective pitch and shaft angle actually increase slightly as diameter is reduced, but are small in magnitude.

The theoretical stability and control derivatives (flagged symbols) were calculated for maximum and minimum diameter conditions, using the same Generalized Rotor Performance method as was used in the Phase I performance correlations. Correlation with experiment is very good, with all of the major trends predicted quite accurately.

The influence of rotor diameter on the radial distribution of blade flap-wise vibratory moments at 150 knots is shown in Figures 60 and 61. Figure 60 presents data for a trimmed flapping case at $\alpha_s = 0 = 0^\circ$ and two gust cases. Figure 61 presents the same trimmed flapping case plus data for two collective pitch cases at reduced rpm. At reduced diameters, the curve for the outer blade vibratory moment is moved to the left, corresponding to the actual radial position of the outboard blade. The primary ordinate scale is vibratory moment, as in previous plots of this type; separate stress scales are shown for the torque tube and outer blade. Reduction in diameter results in a 2:1 reduction in the vibratory stresses on the outboard blade. Torque tube stresses are also reduced, except that only a very small reduction occurs at the inboard end where the stresses are highest (approximately 3000 psi, well below allowable values). The gust conditions produce slight increases in stresses at maximum diameter but negligible changes at minimum diameter. Reduction in rotor speed from 1375 to 1184 rpm (Figure 61) shows slight reductions in stresses at full diameter but no significant effect at minimum diameter.

Reduction in diameter not only reduces blade stresses, but, as was anticipated, also provides significant reductions in vibratory loads transmitted to the airframe. Although the test was not designed to measure vibration levels and the model fuselage structure bears no resemblance to an actual aircraft structure, the accelerometers installed at various points could be used to establish the general trends. In particular, an accelerometer sensitive to gimbal pitch motion showed the most distinct 4/rev signal corresponding to rotor vibratory airloads that would be transmitted to the stationary system by a four-bladed rotor. Data from this accelerometer are presented in Figure 62 as a function of rotor diameter, normalized to the measured value with the fully extended blade. Reduction in diameter produces a large drop in vibration with the value at minimum diameter only one-third of the fully extended value.

RPM REDUCTION - ARTICULATED (Phase III)

This phase was concerned with rotor behavior at minimum diameter as the rotational speed was reduced from the normal helicopter mode value to about half of that, simulating part of the rotor stopping cycle for the stowed-rotor configuration. Previous studies have indicated that the first half of the rpm reduction in the stopping sequence should be conducted with the hinges free in order to keep stresses low in a gust environment and to minimize possible impact loads when the hinges are locked prior to final stopping. The articulated case was investigated

down to 592 rpm, at 150 knots, whereas the locked-hinge case (Phase IV) was explored between 740 and 0 rpm. Thus, there was a range of rpm, between 740 and 592, where both configurations were tested. Test conditions at which rpm changes were made, for both Phases III and IV, are listed in Table III.

Model response during rpm reduction was completely satisfactory, with small increases in flapping and lag, a general reduction in vibratory stress, and no significant resonant blade response. Figure 63, from the third test series, presents typical one-half peak-to-peak vibratory transducer readings as a function of rpm as rpm was continuously reduced from 1375 to approximately 700. In this figure, increasing time is from right to left. The rpm reduction was performed over a time period of approximately 10 seconds (over 150 rotor revolutions), insuring that any increased response would have time to develop for any resonant rpm value. At the start of the rpm reduction, the rotor was trimmed to zero flapping. No adjustment of cyclic pitch was made as rotational speed was lowered; thus, the rotor gradually went out of flapping trim at low rpm values. Flapwise vibratory stresses increased very slightly as rpm was lowered to 1100, then decreased continuously. Maximum stress values were measured at the 15 percent flapwise radial station and did not exceed 3000 psi. Edge-wise and torsional stresses remained low.

The variations in lift, drag, and torque with rotor rpm are presented in Figure 64. All points were obtained at constant rpm under trimmed blade flapping conditions. No significant effect of reduced rpm on lift or drag is noted, but rotor torque is further reduced. The flagged symbols represent theoretical values for zero collective pitch. Rotor drag is underpredicted, but calculated torque is quite accurate.

Radial distributions of flapwise vibratory stress are shown in Figure 65 for the same rpm cases as Figure 64. Stresses are slightly lower than shown in Figure 63 for rpm values below 1375 because the flapping has been trimmed.

A more detailed survey of torque tube vibratory stress over the range of rpm, including the effects of simulated gusts, was obtained in the first test series. Radial distributions of torque tube stress for several rpm values are presented in Figure 66. The torque tube stress scale presents the measured strains in terms of stress in aluminum, to be consistent with previous figures, although steel was actually used for the torque tube in the first series. This conversion is legitimate as long as the two blade constructions were dynamically scaled to each other. The wall thickness was adjusted to compensate for the different materials except that space limitations did not allow for full compensation at the inboard and outboard extremities of the aluminum tube, as discussed in Appendix II.

The curves in Figure 66 are faired through the circles which correspond to the trimmed flapping cases. Positive 30 ft/sec simulated gusts ($\Delta\alpha_s = 6.8^\circ$), indicated by the square symbols, were found to significantly increase the blade root stress in some cases, although the largest stress measured did not exceed 6500 psi.

Maximum blade stress, measured at the 15 percent flapwise station, is shown as a function of rotor rpm in Figure 67 for 0° and 2° of collective pitch both at the trimmed flapping condition and with a 30 ft/sec positive gust. The 2° increment in collective pitch does not significantly increase root flapwise stress. The gust does significantly increase stress, but vibratory levels remain within acceptable limits. Flapwise stress decreases continuously with reduction in rpm for trimmed flapping conditions, except for an increased response at 1330 rpm. This amplification was not noted during the third test series as presented in Figure 63 although general stress levels were found to be slightly higher. The difference noted in the stiffness of the root end of the torque tube is believed to account for the difference in stress.

RPM REDUCTION - LOCKED HINGES (Phase IV)

This phase of the program was concerned with evaluation of the rotor in the final part of the stopping sequence for the stopped/stowed rotor configuration. The blade flap and lag degrees of freedom were locked out for the entire phase, because the blade motion stability resulting from centrifugal force vanishes as the rpm drops to zero. The model was not built to provide a locking capability during a test run; locking blocks were affixed to the blades and to the rotor head before the start of this phase of the test. Thus, the rotor head configuration was somewhat different in this phase compared to the previous phases; however, the hub tare runs included this configuration so that proper tares were subtracted from the test data.

This phase included several rotor stops and starts, for which continuous time histories were recorded, and several steady-state conditions at various fixed rpm values. A listing of the stops and starts performed is given in Table III.

A typical time history of a rotor stop and start at 150 knots flight speed is shown in Figure 68. This was a nominal zero lift condition ($\alpha_s = \theta = 0$) with cyclic pitch adjusted to minimize blade stresses at the initial value of rotor speed, 740 rpm. The actual lift was not zero but rather was slightly negative because of airframe interference effects. The pitch controls were not touched during the rotor stop or during the subsequent start. The largest response occurred in flapwise bending, with the highest stresses located at the inboard end of the torque tube (15% station), as might be anticipated. The edgewise and torsion stresses and pushrod load were small throughout the test condition. The rotor start condition appeared to be essentially a mirror image of the stop. All of several stop/start cycles investigated were very smooth, with no visual indication of blade flapping response or vibration of any kind.

The time histories of the vibratory components (one-half peak-to-peak values) of various parameters, derived from Figure 68, are presented in Figure 69 for the rotor stop sequence. The basic abscissa chosen for this plot was rotor rpm; therefore, the time scale is nonlinear and reads from right to left. The flapwise vibratory stresses all increase initially as rotor speed is reduced from 740 rpm, reaching the highest values in the

approximate 200-300 rpm range, and then dropping to near zero (not exactly zero because of wind tunnel and model-generated air turbulence) at 0 rpm. A number of resonant peaks can be observed which were identified as the first cantilever flapwise bending mode frequency coinciding with various multiples of rotor rpm. The two-, three-, and four-per-rev resonant peaks are quite distinct. Measured stresses at all stations were quite low except for the flapwise 15 percent measurement, which approached 10,000 psi vibratory for a few cycles. In another test condition, a simulated gust with an angle of attack increment of 2 degrees, the maximum momentary vibratory stress at this station was approximately 12,000 psi. Although this may be acceptable because of the few cycles involved, it indicates that local stiffening at the very root end of the torque tube would be desirable to reduce stress levels in a gust environment. As previously indicated, the full-scale preliminary design called for an increased thickness wall at this point. This increased thickness was provided in the steel torque tubes utilized in the first series of wind tunnel tests, but a corresponding increase could not be provided in the aluminum tubes used during most of the program, including the Phase IV rotor stops and starts.

Calculated blade natural frequencies for the fully retracted condition are shown in Figure 70. The Sikorsky normal modes analysis, described in Reference 15, was used to develop natural frequencies for both the fully articulated and locked hinge cases. This analysis is applied only to fully retracted blade conditions where the centrifugal compressive loads on the outer blade are comparatively small and the blade can reasonably be assumed to act elastically as a conventional blade in tension. Predicted nonarticulated first flapwise bending resonant frequencies correspond closely to the resonant peaks discussed in Figure 69.

Flapwise vibratory bending moment and stress were found to be strongly dependent on cyclic pitch position, as expected for the rigid-rotor configuration. The variations in radial stress distribution due to cyclic pitch change and simulated vertical gusts are shown in Figures 71 and 72 for two rpm values. In Figure 71, at 150 knots and 740 rpm, a 60 percent reduction in root flapwise stress was found when cyclic pitch was optimized for minimum stress (dashed lines in upper plot in Figure 71) as opposed to the initial $A_{1s} = 0$, $B_{1s} = 0$ position (solid lines in upper plot). Application of 2-degree (9° ft/sec) simulated gusts (bottom plot) significantly increased root stress from the minimum stress condition to approximately 7500 psi. Outer blade stresses also increased but remained far below allowable material limits.

Blade stresses as predicted by the normal modes analysis, with cyclic pitch set at the position found experimentally to produce minimum stress, are also shown in Figure 71 as flagged symbols. The input shaft angle for the analysis was set at 1 degree to attempt to partially account for airframe interference. Predicted stress levels were found to fall within the range of experimental data for model angle of attack between zero and 2 degrees.

Figure 72 presents similar test results at 296 rpm. The cyclic pitch values for the dashed line in the upper half of the figure are the same as those which gave minimum stress at 740 rpm (Figure 71). These presumably are not the optimum values for the lower rpm, as only a slight reduction in stress is noted compared to the zero cyclic pitch results (solid line). Gust conditions, shown in the lower half of Figure 72, again caused a significant increase in stress.

Stress data at two blade stations, obtained at various collective pitch values over a range of rpm, are presented in Figure 73. The solid lines correspond to data obtained with zero cyclic pitch. The curves were faired through the experimental points with peaks corresponding to the 2-, 3-, and 4-per-rev resonant rpm values for the first flapwise bending mode. The dashed lines in Figure 73, reproduced from Figure 69, are for a continuous rpm reduction with cyclic pitch held constant at the values which minimized stress at 740 rpm. The fairing of the zero cyclic pitch data, obtained at discrete rpm values, is consistent with the continuous rpm reduction data. It can be seen that as rpm is reduced, the stress increment due to a given collective pitch increment is reduced. It is also apparent that the optimum cyclic pitch for minimum stress at high rpm is not optimum at lower values; the dashed curve crosses over the zero cyclic curve at low rpm values. Presumably the vibratory moments could be reduced in the 200-300 rpm range with some other cyclic pitch combination, but this was not explored in the test program.

Rotor lift, drag, and torque data for the locked hinge configuration for each of the discrete rpm values is shown in Figure 74. Lift and torque are reduced substantially as rpm is lowered. Drag remains essentially constant. All values are extremely small compared to the full-diameter helicopter mode flight conditions.

Stability and control derivatives for the locked hinge flight condition were determined at 740 and 296 rpm and are presented in Figure 75. Although locking the hinges increases the moment that can be generated by the rotor, the derivatives are small compared to the major derivatives in the normal helicopter mode (fully extended, articulated blades at high rpm). Comparison of the data of Figure 75 with those of Figure 59 demonstrates that although the cross coupling between longitudinal and lateral cyclic pitch increases when the hinges are locked, the small diameter limits the magnitude of the derivatives to values that should not cause difficulty in a stopped/stowed-rotor aircraft configuration. The largest derivative with locked hinges is the rolling moment per degree of collective pitch. This is the only hub moment derivative which does not reduce in magnitude substantially when rpm is reduced.

BLADE INDEX VARIATIONS (Phase V)

This test phase was designed to evaluate some of the problems that might be encountered when folding the blades fore and aft, preparatory to stowing in the top of the fuselage of a stowed-rotor configuration. Included are rotor index position variations with the blades equally spaced and with

two blades folded forward and two blades folded aft. The full fore-and-aft fold position is shown in Figure 14.

The highest stress measured on the blade during this test phase was always the flapwise measurement at the root end of the torque tube (15% station). The variation of the steady or mean component of stress at this station with blade azimuth, with blades equally spaced, is shown in Figure 76 for three angle-of-attack conditions. It should be noted that the vibratory stresses in this phase were very small and were due only to air turbulence. At zero degrees azimuth (downstream position) there was a download on the blade at all angles of attack, resulting from the flow field around the pylon and rotor head. The maximum up-bending on the blade at positive angle of attack occurred at $\psi = 225$ degrees. This result is in general agreement with a previous investigation of slowed/stopped-rotor characteristics reported in Reference 13, and is attributed to the aeroelastic behavior of the blade, with flapwise bending and torsional deformations combining to increase the aerodynamic loading at that azimuth. The maximum stresses were well within allowable steady stress values for the conditions investigated, but could become excessive at higher angles of attack.

Theoretical predictions of blade root bending moment, based on an aerodynamic analysis neglecting elastic effects, are also shown in Figure 76 for the up-gust condition. The general character of the variation with azimuth is predicted correctly, but the calculated value at 0 degrees azimuth (downstream position) is incorrect because the theory neglects the apparent strong influence of the airframe and rotor head on the air-flow in this area.

The highest measured flapwise bending moment on the outboard blade was only one-half to one-third of that carried by the root end of the torque tube, and relative stresses were even smaller. Blade edgewise and torsional stresses were all very low.

Steady stresses measured at the root end of the torque tube (15% station) during simulated fore-and-aft blade folding at 150 knots are shown in Figure 77. The left-hand plot in Figure 77 presents measured bending moment and stress as a function of shaft angle of attack for each of the four blade locations when the rotor is positioned with blades equally spaced and 45 degrees to the longitudinal axis. The center plot presents the same information when the blades are in an intermediate fore-and-aft fold position (each blade repositioned by 22 $\frac{1}{2}$ degrees using the lag hinge as a fold axis). The right-hand plot presents data measured with full fore-and-aft folding (each blade folded 45 degrees about the lag hinge). It can be seen that as the blades are folded the stresses on the forward blades are reduced, corresponding to the reduction in lift that occurs on the blade as a result of the high sweep angles of the blade span axis relative to the wind. The lift and bending stress of the aft blades go increasingly negative during folding, and become essentially independent of shaft angle of attack.

Measured rotor lift and drag forces are presented in Figure 78 as a function of angle of attack for two conditions with blades equally spaced

and for the partial and fully folded conditions. Rotor lift slope is reduced when blades are folded and there are shifts in the angle for zero lift. It should be noted, however, that rotor lift is very small at all points compared to the model force equivalent to aircraft gross weight (625 pounds). The drag is also reduced as the blades are folded; a negative drag is shown for the full-fold condition, mainly indicating that hub drag is reduced in this condition (same hub tares applied as for the unfolded cases). If the hub drag could be kept low enough by suitable fairings, the fore-and-aft folded rotor might represent an attractive concept without the final stowing operation.

Control power derivatives were measured for the stopped-rotor configuration with equally spaced blades. Results are shown in Figure 79 as a function of azimuth position. Only one-quarter of a revolution is shown because the curves repeat every 90 degrees. In the stopped condition the various rotor controls behave very differently than they do under conventional conditions of rotation. Collective pitch is totally ineffective as a lift control, but does provide rolling moment control. Longitudinal cyclic B₁ provides a small amount of lift control at all azimuths, and some longitudinal pitching moment with the blades at 45° azimuth. Lateral cyclic pitch A₁ produces no measurable effect of any kind. With the TRAC rotor at minimum diameter, the moments produced with the rotor stopped are small in any case, and should not interfere with the fixed-wing aircraft type of controls that would be provided for this configuration. Thus, it appears that for a TRAC stopped/stowed-rotor configuration, it may not be necessary to disconnect rotor controls from the aircraft controls during the stopping or folding sequence.

HIGH-SPEED COMPOUND MODE (Phase VII)

Test Phases III, IV, and V were concerned with evaluation of the TRAC rotor as a stopped/stowed-rotor configuration. Phase VII is concerned with a different application: the high-speed compound helicopter configuration for which the rotor is reduced in diameter but remains exposed and rotating. With centrifugal force to provide flapping stability, the benefits of articulation can be retained; both flap and lag hinges remained free throughout the speed range. Phase VII overlaps Phase III to some extent, but was conducted in the high-speed 8-foot test section of the wind tunnel rather than in the 18-foot test section. The blades were not quite in the minimum-diameter condition for this phase, because intermittent electrical grounding of solder joints was experienced with the flapwise 15% strain gage station when the blade was fully retracted, despite the protective bandage applied to the area. To avoid this problem the blades were left extended approximately 0.2 inch, or less than $\frac{1}{4}$ percent of the extended radius.

Rotor Performance

At high forward speeds and advance ratios, the TRAC rotor, as well as any conventional rotor system, has a relatively small lifting capacity. This is unimportant in a compound helicopter configuration because the fixed wing of the compound is an efficient device with a lift capacity that

increases rapidly with forward speed. The most important rotor performance parameters for the compound helicopter configuration at high speeds are rotor drag and power, not lift or lift-drag ratio. Thus, there was no attempt to obtain detailed maps of rotor performance in this test phase like those obtained in the pure helicopter mode (Phase I).

Rotor performance parameters for the range of test conditions explored in Phase VII are presented in Figure 80. Force and moment results are plotted in pounds and foot-pounds respectively and, as discussed at the beginning of TEST RESULTS AND ANALYSIS, in terms of dimensionless coefficients based on helicopter mode operating conditions (full radius and tip speed) to permit direct comparison with results of other test phases. Blade flapping was trimmed (zero tip-path-plane tilt relative to the shaft) for all points in Figure 80.

The rotor lift data in Figure 80 indicate that, at nominal zero lift conditions ($\alpha = 0^\circ = 0$), there is actually a substantial increase in lift with forward speed. At 1184 rpm, the lift increases from zero at 130 knots to over 90 pounds at 350 knots, corresponding to approximately 15 percent of nominal aircraft gross weight. Other rpm and collective pitch conditions indicate similar trends. At $\alpha = -2^\circ$, the lift at 1184 rpm and $\alpha = 0$ is reduced substantially but is still positive. One known contributing factor is that rotor drag tends to increase shaft angle of attack because of the deflection of the internal gimbal system about its pitching axis. However, the calculated deflection based on measured rotor drag (including hub tares) and the measured stiffness properties of the gimbal indicate that this factor accounts for less than 25 percent of the observed effect at 350 knots. The reason for the lift increase with forward speed is presumed to be a fuselage aerodynamic interference effect, possibly related to free-stream Mach number, which reaches 0.6 at 400 knots. The shape of the rotor pylon between the fuselage and rotor probably is an important parameter in determining the magnitude of the interference. The shaft incidence relative to the fuselage centerline (zero for the test model) may also be important.

Another phenomenon which can be discerned from the lift results shown in Figure 80 is that at high forward speeds an increase in collective pitch results in a decrease in lift. For example, at 888 rpm and 250 to 300 knots, rotor lift is substantially less at +1 deg collective pitch (lower dashed line) than the lift at zero collective pitch (upper dashed line). This result applies only when cyclic pitch is used to trim flapping, i.e., to maintain zero tip-path-plane tilt relative to the shaft. This phenomenon has previously been observed for rotors operating at advance ratios near unity or higher, as reported in Reference 16. The partial derivative of lift with respect to collective pitch (without cyclic pitch adjustment) remains positive, as will be shown in a following figure.

Rotor drag, shown in the center plot of Figure 80, exhibits a general increase with forward speed. This increase follows approximately the increase of free-stream dynamic pressure; other parameters are relatively unimportant. Rotor torque, shown in the bottom plot, remains low at all conditions up to about 300 knots but increases rapidly at higher

osphere, particularly for 1375 rpm at 350 knots and for 1184 rpm at 400 knots, where advancing tip Mach number is approximately 0.91.

The most important rotor performance parameter in the high-speed compound mode is rotor equivalent drag, which is the sum of the actual drag and the drag equivalent of the rotor shaft power: $D_e = D + 550 \text{ HP/V}$, where HP is horsepower and V is forward speed in feet per second. Equivalent drag for the TRAC rotor is presented as a function of forward speed in Figure 81. The upper plot in this figure shows the effect of rotor rpm for zero collective pitch and zero shaft angle of attack (except for flagged symbols which are at -2 degrees angle of attack). Up to 300 knots, there is little benefit from reducing rotational speed below 1375 rpm, which is the full value used in the low-speed helicopter flight mode. Above 300 knots, there is a significant benefit from reduced rpm. At 400 knots, rotor equivalent drag is 70 pounds, or 11% percent of the nominal aircraft gross weight (629 pounds for the model scale). This value would be higher if the wind tunnel static pressure, rather than the total pressure, were atmospheric (at 400 knots the equivalent altitude in the wind tunnel is nearly 9000 feet because of this factor). A rotor equivalent drag of over 10 percent of gross weight is probably unacceptable from an overall aircraft efficiency standpoint at these high forward speeds. Up to 300 knots, equivalent drag for the TRAC rotor is less than 5 percent of gross weight; at higher speeds drag could be reduced for an actual aircraft by operation at higher altitudes.

The lower plot in Figure 81 shows a comparison of measured equivalent drag with theoretical values calculated with the Generalized Rotor Performance method. Also shown separately are the drag equivalents of the rotor shaft power as measured and calculated. Actual rotor drag force is the difference between upper and lower curves. The agreement between theory and experiment is quite acceptable.

First harmonic blade flapping angles relative to the control axis (equal in magnitude to cyclic pitch values required to trim flapping relative to the shaft as discussed in Phase I) are presented in Figure 82. The highest measured value is less than 4 degrees, indicating that flapping trim is easily controlled despite the high advance ratio. In fact, blade flapping was very stable and tip-path-plane tilt was very easy to control throughout the speed range up to and including 400 knots. Also shown in Figure 82 are theoretical calculations of blade flapping, based on the normal modes analysis used to predict blade stresses at high forward speeds. The theoretical curve corresponds to the same lift as for the experimental curve shown for 1184 rpm and $\alpha_s = \theta_c = 0$, except that in the theory a shaft angle of attack of +1 degree was used to approximate airframe interference and collective pitch was adjusted until the lift, with trimmed flapping, equaled the measured lift. As can be seen, the predicted longitudinal flapping, α_1 , follows the trend of the experimental data although with a bias of up to 14 degrees. The error in predicted lateral flapping is somewhat greater. Again, it is probable that the airframe interference effect, which produces a nonuniform inflow velocity in the plane of the rotor, causes a large part of the observed discrepancy.

Stability and Control Derivatives

Stability and control derivatives were established in the manner previously described at the intermediate rpm value (1184) of the high-speed portion of the test program. Results are shown in Figure 83 as a function of forward speed. Lift and pitching moment derivatives all increase with increasing speed, whereas the rolling moment derivatives stay relatively constant. Theoretical predictions of derivatives, based on the Generalized Rotor Performance method, are shown at 350 knots by the flagged symbols. Agreement with experimental values is very good, indicating that even at this high flight speed, conventional theory can be used with confidence in predicting the stability and control characteristics of the rotor system. It should be noted that despite the increase with speed, the maximum values of the derivatives are comparable to those of the fully extended blades at 150 knots, shown in Figure 59. The control power of the TRAC rotor at high speed will be relatively small compared to the control power of the fixed-wing type control surfaces on a compound helicopter airframe.

The partial derivative of rotor lift with respect to angle of attack can be interpreted as a gust response. The experimental derivatives from Figure 83 have been converted to lift response in a gust in Figure 84. Results are normalized to a 10-foot-per-second vertical gust, which corresponds to an incremental angle of attack varying from approximately 2.3 degrees at 150 knots down to 1.0 degree at 350 knots. The lift response increases with speed as shown, but even at 350 knots the value is less than the point shown for the extended rotor at 150 knots, which in turn is only about one-half of the value that would be obtained for a conventional rotor without pitch-flap coupling. Thus, the gust response of the TRAC rotor in the high-speed compound mode is small compared to that of current helicopters.

Also shown in Figure 84 is the experimental rotor flapping response, normalized to a 10-foot-per-second gust. This response has not been divided into longitudinal and lateral components but rather is the total tip-path-plane tilt measured. As can be seen, the rotor is extremely stable, with a total response of only about 1 degree throughout the speed range, despite the fact that the advance ratio is well beyond that at which a conventional rotor would experience catastrophic divergent flapping. This characteristic results from the very low Lock number of the blades in the minimum-diameter condition, achieved without the large weight penalty that would be required to provide the same Lock number at the full diameter.

Blade Vibratory Loads

Blade stresses were all very low at 150 knots but increased steadily with forward speed. The radial distribution of flapwise vibratory bending moment and stress at 150, 250, and 350 knots is shown in Figure 85. The data bands shown for each forward speed encompass all of the test conditions encountered. Maximum bending moments occurred on the outer blades at all speeds, but maximum stress, at least at high forward speeds, occurred at the root end of the torque tube (15 percent station).

The variation of the flapwise 15 percent station stress with forward speed is shown in Figure 86. In the upper plot, data for various rpm and collective pitch settings are presented, and in the lower plot the effect of simulated gusts at 1184 rpm is shown. As can be seen, the sensitivity of stress to gust disturbances is high at high speed; at 350 knots a $\frac{1}{4}$ -degree simulated gust produces a larger stress increment than 1 degree at 300 knots. The lowest stresses at high speed occur at test points corresponding to the lowest rotor lift conditions. As can be seen in Figure 80, nearly all of the test points at high speed correspond to relatively high lift conditions; thus it is presumed that if the rotor is trimmed closer to zero lift at high speeds the stress levels would be generally lower.

Also shown in the top half of Figure 86 are theoretical stress calculations for the flapwise 15 percent station, based on the normal modes analysis, with assumptions as previously discussed in connection with prediction of blade flapping angles (Figure 82). The theory, calculated for lift values measured for the 1184 rpm, $\alpha = 0 = 0$ curve, shows a trend similar to the experimental curve but underpredicts the stress at high speed. This may be a result of the presumably unrealistic uniform inflow assumption or may result from the fact that the normal modes analysis used does not represent the internal blade components or the outer blade compressive loading. The more recent analysis developed for the TRAC rotor (Reference 6) was not available when the present correlation study was conducted.

Variation of flapwise vibratory stress on the outer blade (79 percent station) is presented in Figure 87. The range of conditions is the same as for Figure 86. The outer blade stress appears to be somewhat more sensitive to variations in rpm and collective pitch than the torque tube stress, but exhibits less sensitivity to gusts.

Variation of edgewise vibratory moments with test speed is presented in Figure 88. The upper plot is for the torque tube 30 percent station, and the lower plot is for the outer blade 70 percent station. The data bands shown cover all of the recorded test conditions. Similar data for torsional stresses (torque tube 17 percent station and outer blade 70 percent station) are shown in Figure 89.

Vibratory pushrod load data are presented in Figure 90. Results indicate a gradual increase in load up to 350 knots and a large increase at 400 knots. As is the case for blade stresses, minimum pushrod loads at high speeds correspond to the minimum rotor lift conditions.

Typical oscillograph records obtained during this phase of the test are presented in Figures 91 and 92 for 250 and 350 knots respectively. Jack-screw flapwise and edgewise bending moments shown in these figures are well within the nominal prescribed limit of ± 50 inch-pounds. At 400 knots, however, the jackscrew edgewise bending was approximately equal to this limit. Differential strap tension results are not shown because of excessive electrical noise for these test points; however, measured values were generally less than 1 percent of the strap static tensile strength.

ROTOR HEAD TARES (Phases VI and VIII)

Typical rotor head tare characteristics are presented in Figure 93. Rotor blades were removed at the juncture of the torque tube and sleeve-spindle assembly, dummy blade cuffs were attached, and metric system forces and moments were recorded through the same range of forward speed, angle of attack, and rpm as for the test conditions with blades installed. The resultant tares were subtracted from the forces and moments recorded with blades installed. When test phases required modifications to rotor head hardware, such as the hinge locking blocks, separate tare runs were conducted. The tares shown in Figure 93 include gravity effects due to the weight of the metric portion of the model as well as aerodynamic effects. The dashed curves, obtained at zero wind speed, show the gravity effects only; the differences between these lines and the others show the aerodynamic effects.

The most important aerodynamic tare, and the only one of appreciable magnitude, is drag of the rotor head. The drag tare obtained in the high-speed portion of the test is presented in Figure 94. These tares reach a sizeable magnitude at high speed; rotor head drag is significantly higher than the rotor blade drag forces shown in Figure 80. It should be noted that there was no attempt to design a minimum-size rotor head for the model or to fair the head in any way; obviously, an actual high-speed compound helicopter would require a relatively low-drag head design.

INFLUENCE OF VARIABLE DIAMETER ON COMPOUND HELICOPTER PERFORMANCE

In accordance with contract requirements, a brief analysis was conducted to determine the influence of the TRAC rotor on the design of a high-speed compound helicopter. Variables considered include design speed, wing loading, operational altitude, and airframe parasite drag area. Only one design gross weight (40,000 pounds) and one rotor configuration (extended diameter 72 feet, solidity .095) was considered, in order to keep the analysis compatible with the rotor preliminary design study of this report. A conventional rotor compound was also included in the analysis in order to establish the differences caused by the variation of blade area and tip speed which result when the TRAC rotor is reduced to minimum diameter.

The assumptions utilized in the performance calculations are presented in Table IV and Figure 95. Although the TRAC rotor has demonstrated a significant lifting capability up to 400 knots, it was assumed that vibration and stress considerations would make zero rotor lift desirable at 300 knots or above. The variation of lift assumed for conventional rotors is based on previous Sikorsky studies of compound helicopter designs, and is also reduced to zero at 300 knots. The TRAC rotor at minimum diameter, with less exposed area and lower tip speeds, has a lower lift capacity than the conventional rotor and thus is penalized in the performance comparison by higher wing induced drag values. There is also a parasite drag penalty added to allow for the probability that the TRAC rotor head will have a slightly larger frontal area to allow for the internal differential gears required. Except for these differences, the same assumptions were made for the two types of rotor systems in the calculated performances. A

simplified three-view drawing of the compound helicopters represented in this study is shown in Figure 96. Variable-pitch cruise fans are shown for propulsion at high speeds, but conventional propellers could also be used.

The calculated cruise power required as a function of forward speed is presented in Figure 97 for compound helicopters with the medium size wing (400 square feet) and operating at sea level. Two rpm values, 100 and 80 percent, are shown for each rotor system. The corresponding tip speeds are 700 and 560 ft/sec for the conventional rotor, and 420 and 336 ft/sec for the TRAC rotor (diameter reduced to 60 percent of the extended value). Lines of constant installed power (sea level static military ratings) are also shown; the power at any point on the line represents the normal rated power available at that speed and altitude condition, based on typical shaft turbine engine power characteristics. Tick marks are shown on the power-required curves for advancing tip Mach number conditions of 0.90 and 0.95.

The curves indicate that a conventional rotor operating at full rpm value is not suitable for a compound helicopter at speeds much above 200 knots. The total power required is high because of the high rotor equivalent drag, and the advancing tip Mach number is also excessive. Not only is rotor performance penalized by high Mach numbers, but vibration, control loads, and noise also would be adversely affected. Generally it is desirable to keep the maximum Mach number to 0.9 or less. Reducing rotor rpm by 20 percent improves the performance substantially and also moves the Mach number limits to higher forward speeds. Additional rpm reduction would be desirable from a performance standpoint, but severe problems will result from excessive slowing. The problems include increased blade vibratory stresses, excessive sensitivity of flapping motion to control inputs or gusts, high levels of rotor-induced airframe vibrations, and the necessity for a two-speed gearbox to avoid inefficient engine operation. Some of these factors are discussed in References 4 and 9. It is believed that the 80 percent rpm value represents approximately the practical minimum for most conventional rotor systems.

The TRAC rotor provides a substantial performance improvement over the conventional rotor without the necessity for reduced rpm. Less power is required over the range of forward speeds considered despite the higher assumed wing induced drag and parasite drag, because of the large reduction in rotor equivalent drag. An additional small improvement is available by reducing rpm to 80 percent. The advancing tip Mach number is below 0.9 for the TRAC rotor throughout the range of speeds considered in Figure 97 for both rpm values.

Because the conventional rotor requires an rpm reduction, whereas the TRAC rotor shows little additional benefit from rpm reduction, the remainder of the comparisons are restricted to the conventional rotor at 80 percent rpm and the TRAC rotor at 100 percent rpm. The influence of altitude on the performance comparison is shown in Figures 98 and 99 for altitudes of 10,000 feet and 20,000 feet respectively. Operating at altitude reduces the power required primarily because of reduced parasite drag values.

Because of the reduction in speed of sound at altitude, the advancing tip Mach numbers are increased at any given forward speed, and the forward speed at which the nominal Mach number limits are encountered is reduced. For the conventional rotor at 80 percent rpm, the forward speed at which an advancing tip Mach number of 0.9 is encountered is reduced from 264 knots at sea level to 243 knots at 10,000 feet and to 221 knots at 20,000 feet. The corresponding figures for the TRAC rotor at 100 percent rpm are 347 knots at sea level, 326 knots at 10,000 feet, and 304 knots at 20,000 feet (all calculations based on standard day conditions).

Operating at altitude rather than at sea level tends to increase the speed advantage afforded by the TRAC rotor at any given installed power level. Also, because of the effect of altitude on Mach number, the conventional rotor compound is not able to utilize as high a level of installed power at altitude as it is at sea level, unlike conventional fixed-wing airplanes. For example, with 12,000 horsepower installed (sea level static military rating) it would be possible to fly the conventional compound at 281 knots at sea level, with the advancing tip Mach number equal to approximately 0.92. At 20,000 feet, restricting the advancing tip Mach number to 0.95 would result in a maximum forward speed of 252 knots, utilizing less than 11,000 installed horsepower. The TRAC rotor would not be so restricted, and with the same installed power the cruise speed would stay essentially constant: 305 knots at sea level and 304 knots at 20,000 feet.

The influence of wing size on power required is presented in Figure 100 for an altitude of 10,000 feet. Although fairly large changes were investigated (plus 50 percent and minus 33 percent from the basic 400-square-foot area), the effect on power is not pronounced for either rotor system, except that at the lower speeds, use of the small wing results in a power penalty because of higher induced drag. Similar calculations at sea level showed less effect, and at 20,000 feet the differences were somewhat greater. It was concluded that the 400-square-foot wing size (gross weight divided by wing area equal to 100 pounds per square foot) was the best choice for either rotor system.

The influence of parasite drag on power required is shown in Figure 101 for an altitude of 10,000 feet. A 20-percent reduction in parasite drag area was taken as a reasonable variation from initially assumed values. At a given forward speed, the reduction in power required is virtually identical for the two different rotor systems. However, for a given installed power level, the speed increase resulting from the parasite drag reduction is substantially larger for the TRAC rotor than for the conventional rotor. For example, with an installed power level of 10,000 horsepower, the drag savings results in a speed increase of 11 knots for the conventional rotor, from 264 to 275 knots. With the TRAC rotor the speed increment is 18 knots, from 287 to 305 knots. Thus the TRAC rotor, because of its low rotor drag, increases the benefits to be obtained from other devices to reduce drag.

The reduction in power required provided by the TRAC rotor can be translated into savings in propulsion system weight and mission fuel. These savings are illustrated in Figure 102, derived from the power-required curves in Figure 97 for the conventional rotor at 80 percent rpm and the

TRAC rotor at 100 percent rpm. For example, if the mission calls for a 300-knot dash speed capability and a 2-hour endurance at a cruise speed of 250 knots, the total weight reduction of engines, propellers, and fuel amounts to more than 6 percent of the gross weight, or more than 2400 pounds for the 40,000-pound gross weight assumed.

GENERAL OBSERVATIONS AND EVALUATIONS

Full evaluation of the results of this program requires some additional comparisons of the telescoping rotor system with conventional systems. The TRAC rotor shows a potential for improved reliability over conventional rotors despite the increased complexity in the blades, because of reduced stresses in high-speed cruise. This is illustrated in Figure 103, which compares maximum blade stress data obtained on the NH-3A research aircraft, Reference 10, with that obtained on the TRAC blade at minimum diameter. The NH-3A exhibited reduction in stress in the compound helicopter mode compared to the pure helicopter mode of operation, and, with additional lift unloading by the wing and additional auxiliary propulsive force, further improvements could probably be obtained. The TRAC rotor, in the same speed range, exhibited much lower vibratory stresses with the same structural material (aluminum). Above 300 knots, the maximum stresses on the TRAC blades become higher than desirable (6000 psi is a commonly used criterion for long life), but several factors contributing to these stresses should be noted. First, the maximum stress in the retracted blade condition was measured at the root end of the torque tube where local beefup could be utilized to reduce stresses with a minor weight penalty. Second, the blade root mass for the model is excessive because of the difficulties of obtaining feathering bearings with adequate load capacity in small sizes. This factor is known to contribute to blade root vibratory stresses. Third, it appears that the TRAC blade stresses are approximately proportional to flight dynamic pressure (note similarity between the stress curve and test dynamic pressure curve in Figure 103), and it is anticipated that stress will be reduced at increased altitude. Operation at altitude at high speeds will be required in most cases for another reason: to reduce the airframe parasite drag to satisfactory levels for performance requirements. Thus, there is good reason to believe that satisfactory blade stress levels can be achieved in a full-scale aircraft application throughout the speed range to 400 knots.

Another comparison with NH-3A test data is presented in Figure 104, which shows the general behavior of airframe vibration as a function of forward speed. Because there was no attempt to design the wind tunnel model fuselage structure to represent a realistic aircraft structure, it is not possible to make a direct comparison of the model and full-scale vibrations, and the comparison shown must be considered qualitative. Typical vibration data measured on the NH-3A aircraft (cockpit vertical acceleration) are shown relative to the mean measured value at 120 knots flight speed. These data indicate that vibration levels increase rapidly with forward speed, resulting from increased blade vibratory airloads. The TRAC model vibration data are based on an accelerometer mounted on the internal gimbal, sensitive to gimbal pitch motion. This accelerometer was selected because it gave the most distinct "N per rev" signal and should respond to the same

vibratory force inputs at the rotor head that would produce vertical acceleration in the cockpit. The model data were also normalized relative to the 120-knot condition for the TRAC rotor at full diameter and at high lift. If it can be assumed that it is possible to achieve the same vibration level with a TRAC rotor operating in the helicopter mode as with a conventional rotor system at the same speed, then the comparison shown in Figure 104 will be valid. At minimum diameter, the blade vibratory loadings are greatly reduced and the overall airframe vibration will be correspondingly reduced. As was the case for blade vibratory stresses, the vibration levels measured for the TRAC model are approximately proportional to test dynamic pressure, and it is to be expected that operation at altitude will further reduce vibration levels.

Another advantage of the TRAC rotor is its low gust response at high speeds. The response in terms of incremental load factor for a specified gust condition (10 ft/sec unrelieved vertical gust) is presented in Figure 105 for a number of aircraft configurations. Because comparable test data are not available for these configurations, the comparisons shown are calculated. The pure helicopter response calculation assumed full tip speed (700 feet per second) and no pitch-flap coupling. The conventional compound was assumed to operate at 80 percent tip speed, with a pitch-flap coupling ratio of -0.5 incorporated to reduce the response, and was also assumed to have a 400-square-foot wing for a gross weight of 40,000 pounds (W/S = 100 pounds per square foot). The wing adds its own gust response to that of the rotor, but at moderate forward speeds the overall response is comparable to the pure helicopter. The TRAC compound, with the same wing, is less sensitive to gusts than the conventional compound because of the lower rotor response. It should be noted that the dashed curve in Figure 105, identified as test data for the TRAC rotor, does not include a wing. The curve for the TRAC stowed-rotor aircraft represents the response of the wing alone, and has the lowest gust sensitivity of the configurations considered. Typical high-performance fixed-wing airplanes have lower wing loadings because of takeoff and landing considerations, and for this reason have a higher gust response. Airplane wing loadings vary over a large range, of course, and the gust sensitivity is inversely proportional to wing loading. Two examples in the approximate gross weight category considered are the Grumman Gulfstream II, with a wing loading approximately equal to the 67 psf value indicated in Figure 105, and the DHC-5 Buffalo, which has a wing loading under 50 psf and a correspondingly higher gust response at any given speed and altitude. The TRAC stowed-rotor aircraft does not require as large a wing as the fixed-wing airplane because of its high allowable conversion speed. Both the TRAC compound and TRAC stowed-rotor aircraft offer improved gust response characteristics over other aircraft types.

Another consideration of importance relates to rotor-induced noise characteristics. Although no attempt was made to measure noise in the current program, it is well known that advancing tip Mach number is one of the important factors in rotor noise generation in forward flight. In particular, rotor impulsive noise ("blade slap") is sensitive to this factor. Although airfoil section, tip aerodynamic load distribution, etc., are very important, as a general rule rotors having advancing tip Mach

numbers of 0.9 or higher are apt to be annoyingly loud, whereas with Mach numbers of 0.8 or less it is possible to have a relatively quiet rotor. This relationship is shown in Figure 106, which presents advancing tip Mach number as a function of forward speed, altitude and percent rpm for a conventional rotor and the TRAC rotor. Because of reduced tip speeds, it is evident that the TRAC rotor offers the potential of substantial reductions in rotor noise in spite of increased forward speeds.

Thus, there appears to be a substantial number of benefits to be derived from the TRAC rotor, including better performance and lower stresses, vibration, gust sensitivity, and noise than for conventional rotors. The TRAC rotor also offers the distinct option of stopping and stowing the rotor in flight, with further substantial improvements in all of the above items. In a general sense the benefits are attributable to the use of variable geometry, which has long been used in fixed-wing aircraft (notably high-lift flaps) but not in helicopters.

Variable geometry is not achieved without increased weight, cost, and complexity of the particular component in question, but when properly used it can offer positive attributes of considerable importance. When the overall aircraft is considered, variable geometry sometimes offers decreased weight, cost, and complexity. The TRAC variable-diameter rotor is believed to have the potential system benefits required to make it economically attractive. The TRAC rotor blades, with conventional materials, will be heavier than conventional blades by a few percent of gross weight, and there is additional mechanism in the rotor head and gearbox. It is anticipated that the blade weight penalty can be reduced substantially through use of advanced composite materials. The corresponding potential for weight reduction of conventional blades is not as great, partly because coning angle limitations dictate a minimum allowable weight.

The investment in achieving a variable diameter capability provides a number of simplification and weight reduction items in the rest of the aircraft. For example, a single-speed gearbox is adequate, whereas for a conventional rotor compound a two-speed gearbox may be required if engine efficiency compromises are to be avoided. The weight of vibration control devices, which can amount to a significant penalty, will be reduced substantially with the TRAC rotor, both because of lower input vibratory forces and a smaller design operating rpm range. The retraction clutch of the TRAC rotor can also serve as a rotor brake for stopping the rotor on the ground, eliminating this conventional item. A blade folding system, if required, involves a substantial weight penalty for conventional rotors, but for the TRAC rotor the blades are easily folded fore and aft about the lag hinge, using the dampers as hydraulic servos, so that this penalty is avoided. As previously discussed, for a given design speed the performance benefits of the TRAC rotor can save a significant amount of engine weight and mission fuel. Thus, there are reasons to believe that the TRAC rotor, because of its variable-geometry feature, can be developed into a cost-effective device for improving performance and extending the capabilities of rotary-wing aircraft.

CONCLUSIONS

An analytical and experimental program was conducted to establish feasibility and determine characteristics of the Sikorsky TRAC rotor, a variable-diameter, telescoping-blade, fully articulated rotor system. The program included a preliminary design study of a full-scale blade, wind tunnel tests of a dynamically scaled rotor model in various flight modes, and correlation of experimental results with theory.

Major conclusions and recommendations resulting from this investigation are as follows:

1. The TRAC rotor was established as a feasible rotor system for both the stopped/stowed-rotor aircraft configuration and for the high-speed compound helicopter.
2. The basic blade structural design and the retraction system were verified by tests of the dynamically scaled model, which operated at full-scale tip speeds and forward speeds.
3. Rotor performance characteristics in the low-speed helicopter mode with fully extended blades are comparable to those of conventional helicopters. Experimental lift and propulsive force values over the speed range from 60 to 150 knots were more than adequate for the assumed stopped/stowed rotor or compound helicopter flight envelopes.
4. Diameter changes, demonstrated at forward speeds up to 150 knots and at rotational speeds up to full rpm, were rapid, with positive control and low blade stresses. Diameter changes could be stopped or reversed at any point in the cycle. Despite the variation in blade length with consequent change in blade natural frequencies, there was no significant amplification of stresses during diameter changes. Test data obtained at constant, intermediate diameter values also showed no evidence of serious resonance conditions.
5. At the initiation of the blade retraction cycle there was a blade flapping response which corresponded to a forward tip-path-plane tilt of approximately 2 degrees, and a negative rotor lift increment, as a result of the internal torque in the blade retraction system which caused a slight blade twist. This is not a serious problem, but the response would have to be counteracted in flight to eliminate the disturbance to aircraft trim. Possible means of minimizing or eliminating this response were identified.
6. Rotor stops and starts, demonstrated at 150 knots true airspeed, with hinges locked below approximately 50 percent rpm, were very smooth and rotor forces and moments were low, indicating minimum disturbance to aircraft stability and control. Stresses were low except at the root end of the torque tube at very low rpm values; local beefup of the blade in this area (in accordance with details of the full-scale blade preliminary design study not incorporated in the model) would be desirable.

7. Indexing the blades to various positions about the lag hinge axis, with the rotor stopped at 150 knots true airspeed, demonstrated that fore-and-aft blade folding for the stopped/stowed-rotor configuration is easily achieved, with low forces and moments. Special fold hinges are not required.

8. In the high-speed compound helicopter mode, with blades retracted but fully articulated, tests were conducted at true forward speeds up to 400 knots and at advance ratios up to 2.0. Blade flapping was very stable and easily controlled throughout the speed range. Rotor equivalent drag was less than 5 percent of the value representing aircraft gross weight at forward speeds up to more than 300 knots, even at full rpm. Drag increased significantly at higher forward speeds, to more than 8 percent of gross weight at 350 knots at full rpm, but could be reduced by reducing rpm. Further reductions in drag would result from operation at increased altitude.

9. Blade stresses in the high-speed compound mode were very low at minimum speeds but increased with forward speed. Maximum stress, at the root end of the torque tube, became excessive at the highest speeds tested, partly because of a significant rotor lift at most test conditions due to airframe aerodynamic interference. The local strengthening of this portion of the blade, recommended in conclusion 6, should also serve to reduce stresses in the high-speed compound mode. Blade stresses were approximately proportional to flight dynamic pressure, so that lower stresses should result from operation at increased altitude.

10. Correlation of experimentally determined performance with theory was generally good throughout the test range of forward speeds.

11. Stability and control power derivatives obtained in the various operating modes show that stability and control problems will be minimal for TRAC rotor aircraft. The derivatives reduce in magnitude when diameter is reduced, and then increase in the high-speed compound mode; at 350 knots the magnitudes are comparable to those of the extended blades at 150 knots. For the locked hinge configuration the control phase relationships are altered, but the magnitudes of the derivatives are small at 150 knots, and there should be little difficulty controlling a stopped/stowed-rotor aircraft configuration with conventional control surfaces throughout the conversion cycle. Theoretical values of stability and control derivatives agreed very well with experimental values.

12. Vibration levels measured on the model showed a large reduction as the diameter was reduced. Vibration increased with speed in the high-speed compound mode, but comparison with published flight data for a compound helicopter indicates that the TRAC rotor will have lower vibration levels at high forward speeds than a conventional rotor.

13. Theoretical predictions of blade stresses for the various flight modes, using existing methods and assuming uniform inflow in the plane of the rotor, showed qualitative agreement with experiment but generally underpredicted the magnitude. A more recent aeroelastic analysis, developed

specifically for the TRAC blade under another contract with USAAMRDL, has been correlated with test data in a separate report (Reference 6).

14. A brief performance evaluation of the TRAC rotor in a compound helicopter application indicates significant advantages, relative to a conventional rotor. Higher cruise speeds are achieved for a given installed power, or less power is required for a given speed, without the necessity for the RPM reduction required for the conventional rotor. The relative advantage of the TRAC rotor increases with altitude or with reduction in airframe parasite drag. The power reduction provided by the TRAC rotor can be translated into significant reductions in fuel weight and installed propulsion system weight.

15. Other advantages demonstrated for the TRAC rotor in the high-speed compound mode, relative to conventional rotors, include reduced blade stresses, reduced vibration, and lower gust sensitivity. Because of lower advancing tip Mach numbers, the TRAC rotor will also be quieter at high speeds.

16. For the stopped-or stowed-rotor configuration, the TRAC rotor eliminates or greatly reduces the serious problems of blade stresses, aeroelastic instabilities, and stability and control difficulties encountered with conventional rotors, without compromising hover disk loading or requiring special control devices. A high conversion flight speed permits utilization of a relatively small wing sized for cruise.

17. Ground resonance difficulties encountered early in the model test program were due to model support strut characteristics and were unrelated to the TRAC blade structure. A revised model support structure corrected the problem, and special tests demonstrated that the ground resonance characteristics of the TRAC blades are essentially identical to those of conventional blades.

LITERATURE CITED

1. Segel, R. M., and Fradenburgh, E. A., DEVELOPMENT OF THE TRAC VARIABLE DIAMETER ROTOR CONCEPT, Paper presented at the AIAA/AHS VTOL Research, Design, and Operations Meeting, Georgia Institute of Technology, Atlanta, Georgia, February 17-19, 1969. AIAA paper No. 69-221.
2. Cassarino, S. J., EFFECT OF ROOT CUTOUT ON HOVER PERFORMANCE, U. S. Air Force Flight Dynamics Laboratory Technical Report AFFDL-TR-70-70, June 1970.
3. Cassarino, S. J., EFFECT OF BLADE ROOT CUTOUT ON VERTICAL DRAG, USAAVLABS Technical Report 70-59, U. S. Army Aviation Material Laboratories, Fort Eustis, Virginia, October 1970, AD877174.
4. Fradenburgh, E. A., EXTENSION OF COMPOUND HELICOPTER PERFORMANCE BY MEANS OF THE TELESCOPING ROTOR, Paper presented at the Air Force V/STOL Technology and Planning Conference, Las Vegas, Nevada, September 23-25, 1969.
5. Niebanck, C. F., DEVELOPMENT OF A MODEL ROTOR SUPPORT TO PREVENT GROUND RFSONANCE INSTABILITY, Sikorsky Aircraft Report SER-50826, February 1973.
6. Carlson, R. G., and Cassarino, S. J., AEROELASTIC ANALYSIS OF A TELESCOPING ROTOR BLADE, USAAMRDL Technical Report 73-48, U. S. Army Air Mobility R&D Laboratory, Fort Eustis, Virginia, 1973.
7. Carlin, J. M., Stepkovich, A., and Reinfelder, W., FEASIBILITY STUDY, VARIABLE DIAMETER STOWED ROTOR (TRAC), Sikorsky Aircraft Report SEM-8359, May 1967.
8. Fradenburgh, E. A., and Kiely, E. F., DEVELOPMENT OF DYNAMIC MODEL ROTOR BLADES FOR HIGH SPEED HELICOPTER RESEARCH, Paper presented at the Symposium on Aeroelastic and Dynamic Modeling Technology, Wright-Patterson Air Force Base, Ohio, September 23-25, 1963.
9. Bergquist, R. R., and Tanner, W. H., SOME PROBLEMS OF DESIGN AND OPERATION OF A 250-KNOT COMPOUND HELICOPTER ROTOR, Journal of Aircraft, Vol. 1 No. 5, September-October 1964.
10. Segel, R. M., Jenney, D. S., Gerdes, W., et al, Final Report-NH-3A (Sikorsky S-61F) Flight Test Program, Sikorsky Aircraft Report SER-611344, March 1969.
11. Linville, J. C., AN EXPERIMENTAL INVESTIGATION OF HIGH-SPEED ROTOR-CRAFT DRAG, USAAMRDL Technical Report 71-46, U. S. Army Air Mobility R&D Laboratory, Fort Eustis, Virginia, February 1972, AD 740771.

12. Bain, L. J., and Landgrave, A. J., INVESTIGATION OF COMPOUND HELICOPTER AERODYNAMIC INTERFERENCE EFFECTS, USAAVLABS Technical Report 67-44, U. S. Army Aviation Materiel Laboratories, Fort Rucker, Virginia, November 1967, AD 663427.
13. Fradenburgh, E. A., and Flint, D. F., AN EXPERIMENTAL INVESTIGATION OF SLOWED/STOPPED MOTORS, Sikorsky Aircraft Report AER 30457, January 1967.
14. Tanner, W. H., CHARTS FOR ESTIMATING ROTARY WING PERFORMANCE IN HOVER AND AT HIGH FORWARD SPEEDS, NASA Contractor Report CR-114, November 1964.
15. Arvidiacono, P. J., PREDICTION OF ROTOR INSTABILITY AT HIGH FORWARD SPEEDS, Volume I, Steady Flight Differential Equations of Motion for A Flexible Helicopter Blade With Chordwise Mass Unbalance, USAAVLABS Technical Report 68-18A, U. S. Army Aviation Materiel Laboratories, Fort Rucker, Virginia, February 1969, AD 689060.
16. Fradenburgh, E. A., and Begel, R. N., MODELS AND FULL SCALE COMPOUND HELICOPTER RESEARCH, Paper presented at the A. H. S. 21st Annual National Forum, Washington D. C., May 1965.

TABLE I. THAC MODEL ROTOR SPECIFICATIONS

Number of blades	4				
Diameter	9 feet (extended) 5.4 feet (retracted)				
Chord	4.90 inches (outer blade) 1.50 inches (torque tube)				
Length of outer blade	95 inches				
Airfoil	NACA 63,4016 (outer blade) 34% ellipair (torque tube)				
Solidity	.095 (extended) .177 (retracted)				
Hinge offset	3.0 inches				
Twist	0 degree				
Link Number	5.8 (extended) 2.2 (retracted)				
Component \ Section Properties	EI_{xx} , LB-IN ²	EI_{yy} , LB-IN ²	QJ	$(\frac{I}{C})_{xx}$	$(\frac{I}{C})_{yy}$
Torque Tube	4.27×10^4	2.74×10^5	5.06×10^4	.0164	.0365
Outer Blade	9.12×10^4	10.02×10^5	9.66×10^4	.0254	.0390 (L.E.)
Jackscrew (min. section)	1.17×10^4	1.17×10^4	0.94×10^4	.00237	.00237

TABLE II. CONTINUOUS DIAMETER CHANON TEST CONDITIONS

Point	Forward Speed, V, Kt	Motor RPM	Diameter, Percent	Shaft Angle, α_s , deg	Collective Pitch, θ_c , deg	Cyclic Pitch/Flapping Trim
1	60	592	96 + 66	0	0	Flapping trim at max diameter
2	60	592	66 + 96	0	0	Same cyclic as pt 1
3	90	888	96 + 66	0	0	Flapping trim at max diameter
4	90	888	66 + 96	0	0	Same cyclic as pt 3
5	120	1184	96 + 66	0	0	Flapping trim at max diameter
6	120	1184	66 + 96	0	0	Same cyclic as pt 5
7	90	888	97.5 + 62.5	0	0	Flapping trim at max diameter
8	90	888	62.5 + 97.5	0	0	Same cyclic as pt 7
9	150	1184	97.5 + 62.5	0	0	Flapping trim at max diameter
10	150	1184	62.5 + 97.5	0	0	Same cyclic as pt 9
11	150	1375	97.5 + 62.5	0	0	Flapping trim at max diameter
12	150	1375	62.5 + 97.5	0	0	Same cyclic as pt 11
13	150	1375	97.5 + 62.5	2	0	Simulated gust- Same cyclic as pt 11
14	150	1375	62.5 + 97.5	2	0	Simulated gust- Same cyclic as pt 11
15	150	1375	97.5 + 62.5	0	2	Flapping trim at max diameter
16	150	1375	62.5 + 97.5	0	2	Same cyclic as pt 15

Points 1 - 6 obtained in second wind tunnel test series

Points 7 - 16 obtained in third wind tunnel test series

TABLE III. CONTINUOUS RPM CHANGE TEST CONDITIONS

Point	Forward Speed, V, Kt	Rotor RPM	Shaft Angle, α_s , deg	Collective Pitch θ_c , deg	Cyclic Pitch/Flapping Trim
<u>Articulated - Phase III</u>					
1	150	1480 \rightarrow 740	0	0	Flapping trim at starting rpm
2	150	740 \rightarrow 1480	0	0	Same cyclic as pt 1
3	150	1480 \rightarrow 740	6.8	0	Simulated gust - Same cyclic as pt 1
4	150	740 \rightarrow 1480	6.8	0	Simulated gust - Same cyclic as pt 1
5	150	1375 \rightarrow 700	0	0	Flapping trim at starting rpm
6	150	700 \rightarrow 1375	0	0	Same cyclic as pt 5
7	150	1375 \rightarrow 700	2	0	Simulated gust - Same cyclic as pt 5
8	150	700 \rightarrow 1375	2	0	Simulated gust - Same cyclic as pt 5
<u>Locked Hinges - Phase IV</u>					
9	90	740 \rightarrow 0	0	0	Cyclic for min stress at starting rpm
10	90	0 \rightarrow 740	0	0	Same cyclic as pt 9
11	150	740 \rightarrow 0	0	0	Cyclic for min stress at starting rpm
12	150	0 \rightarrow 740	0	0	Same cyclic as pt 11
13	150	740 \rightarrow 0	2	0	Simulated gust - Same cyclic as pt 11
14	150	0 \rightarrow 740	2	0	Simulated gust - Same cyclic as pt 11
15	150	740 \rightarrow 0	2	0	Cyclic for min stress at starting rpm
16	150	0 \rightarrow 740	2	0	Same cyclic as pt 15
17	150	740 \rightarrow 0	0	1	Cyclic for min stress at starting rpm
18	150	0 \rightarrow 740	0	1	Same cyclic as pt 17
Points 1 - 4 obtained in first wind tunnel test series Points 5 - 18 obtained in third wind tunnel test series All points with rotor at or near minimum diameter.					

TABLE IV. ASSUMPTIONS USED IN PERFORMANCE COMPARISONS FOR COMPOUND HELICOPTERS

Weights and Dimensions

$W = 40,000$ lb	
Diameter	72 ft (Conventional Rotor)
	72 ft (TRAC-extended)
	43.2 ft (TRAC-retracted)
Solidity	.095 (Conventional and TRAC-extended)
Hover tip speed	700 ft/sec
Wing area	400 ft ²
Wing span	49 ft
Aspect ratio	6.0

Other dimensions as shown in Figure 96.

Rotor Lift Variation

Rotor lift in cruise at sea level as shown in Figure 95.
Rotor lift at altitude proportional to density ratio.

Parasite Drag Area

$$f = .02(W)^{2/3} = 23.5 \text{ ft}^2 \text{ (Conventional Rotor)}$$

$$f = 25 \text{ ft}^2 \text{ } (\Delta f = 1.5 \text{ ft}^2) \text{ (TRAC Rotor)}$$

Parasite drag includes rotor head drag but does not include wing drag.

Wing Aerodynamic Characteristics

Variation of wing profile drag with lift coefficient as shown in Figure 95.

Wing induced drag based on span efficiency factor of 0.8:

$$C_{D_i} = \frac{C_{LW}^2}{\pi AR \epsilon} \text{ where } AR = 6.0, \epsilon = 0.8$$

Wing maximum lift/drag ratio = 19.4 @ $C_{LW} = 0.4$

Propulsion System

Propulsion efficiency of 80 percent assumed for all conditions (applies to rotor shaft power as well as propeller/fan power). Tail fan assumed shut down in cruise (zero tail fan power).

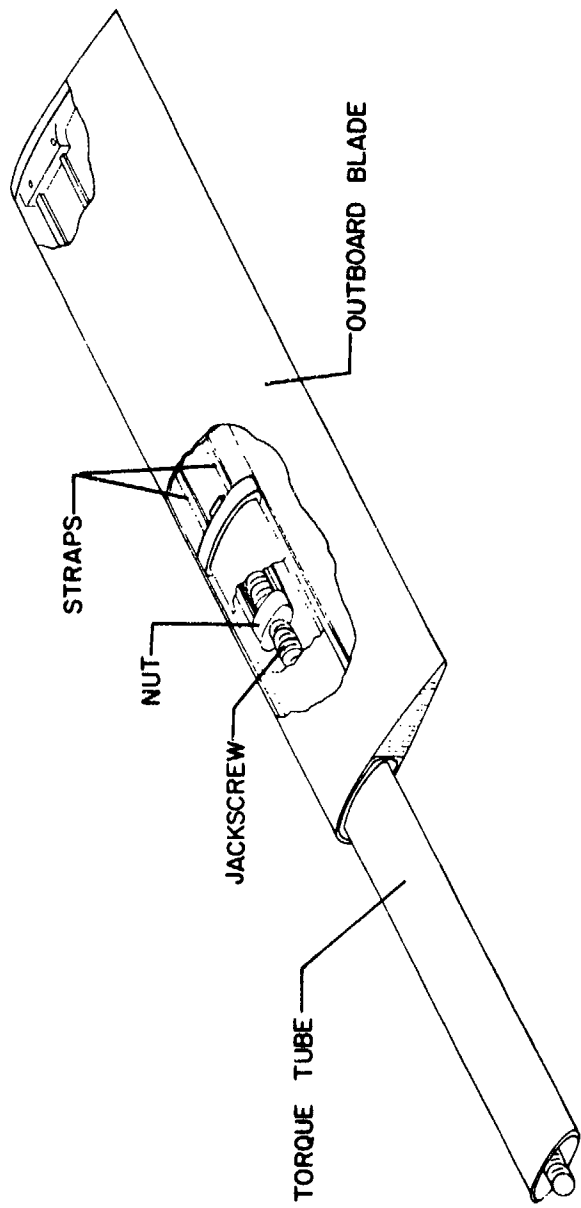


Figure 1. TRAC Rotor Blade Schematic Arrangement.

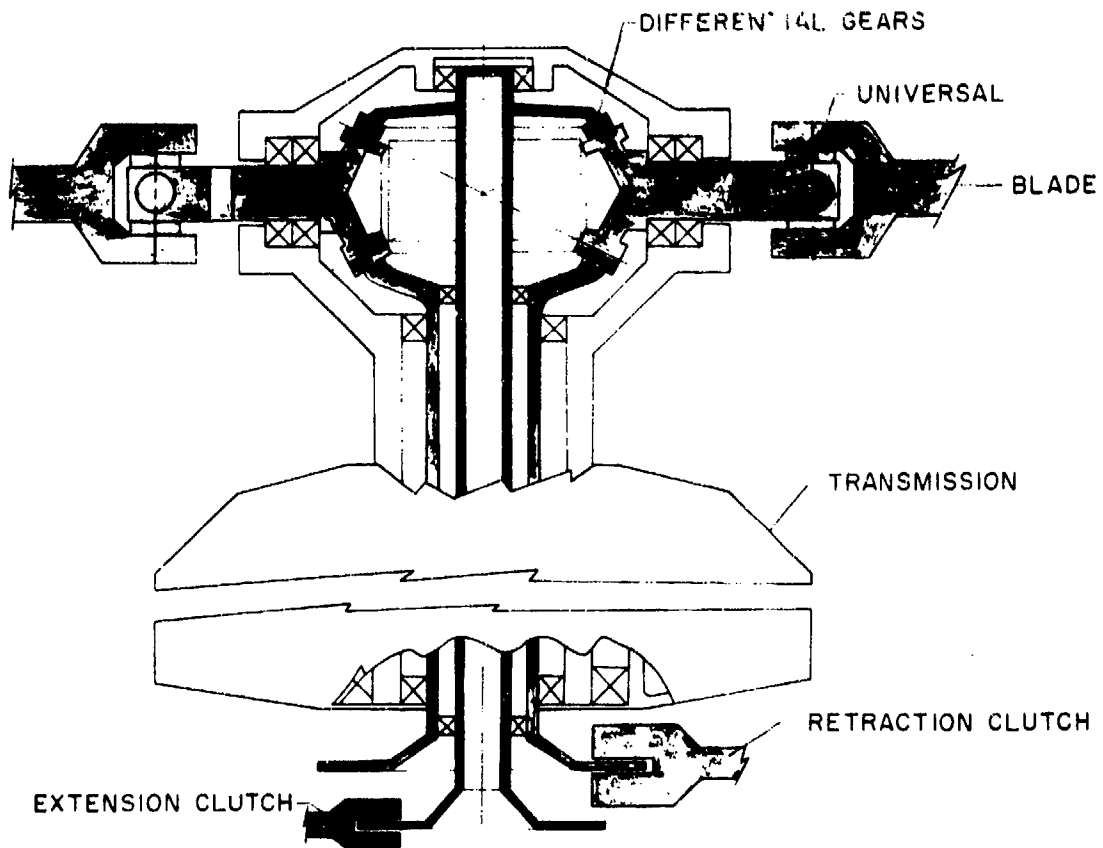
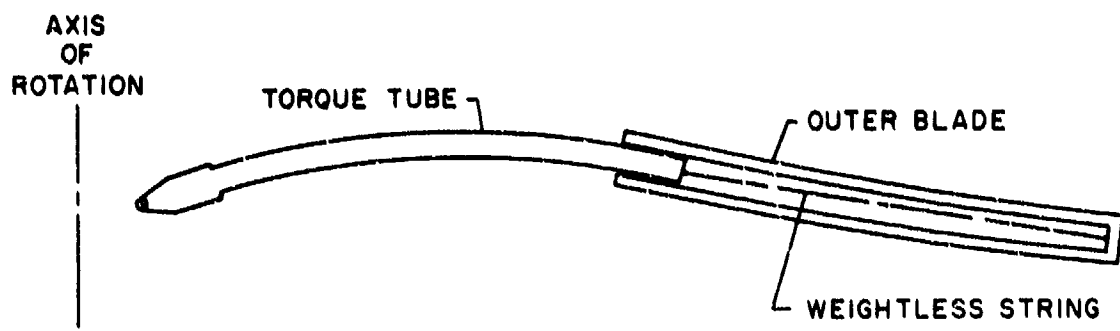
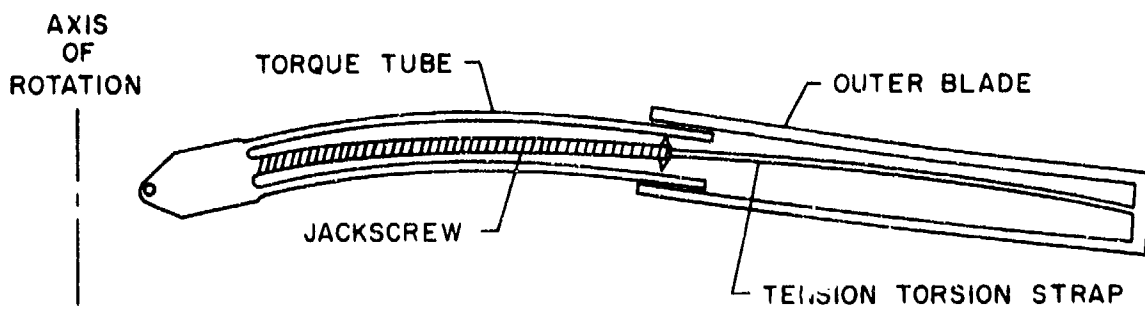


Figure 2. TRAC Rotor Head Schematic Arrangement.



(a) TWO-ELEMENT ANALYSIS



(b) FOUR-ELEMENT ANALYSIS

Figure 3. Flapwise Aeroelastic Analysis for Extended Blade.

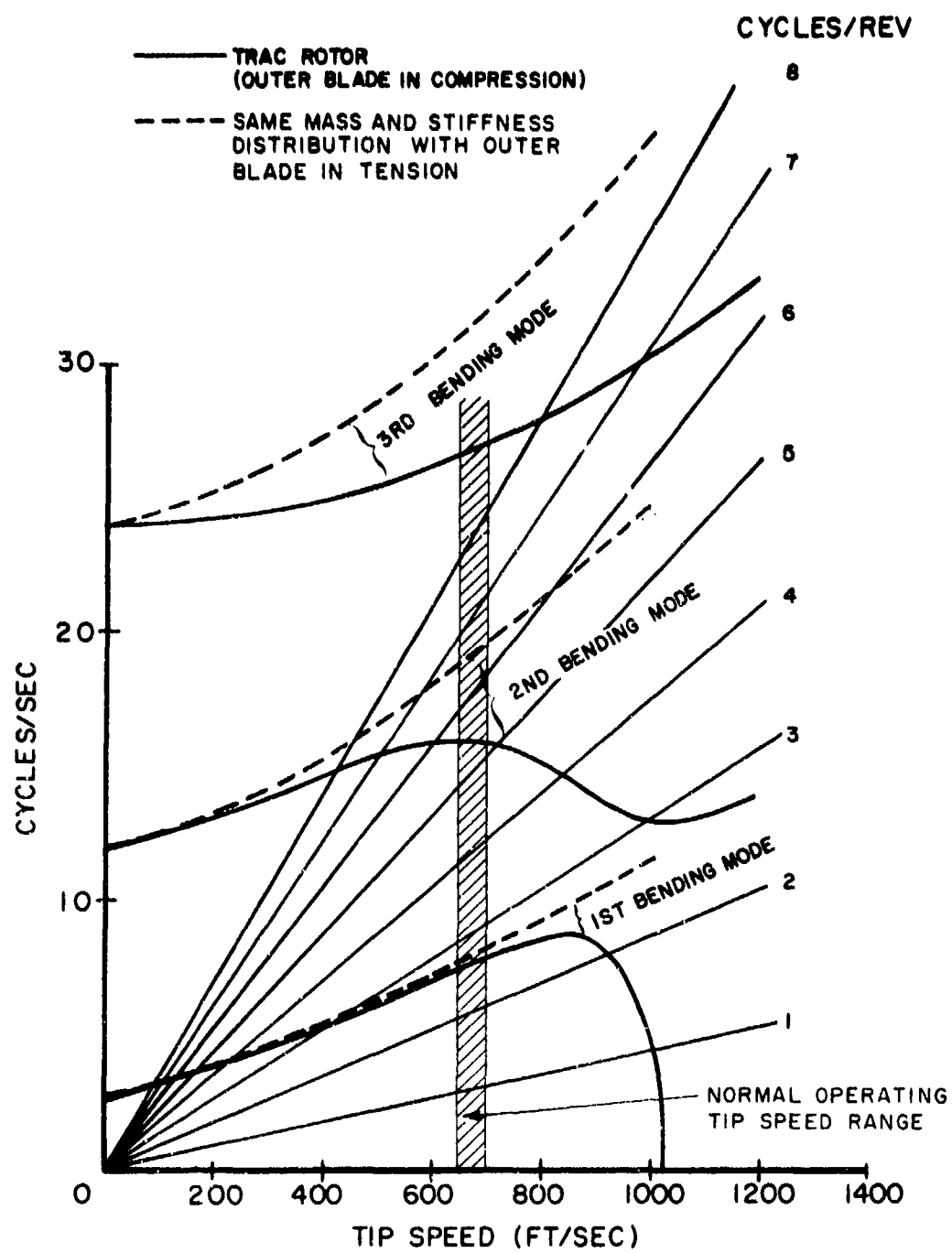
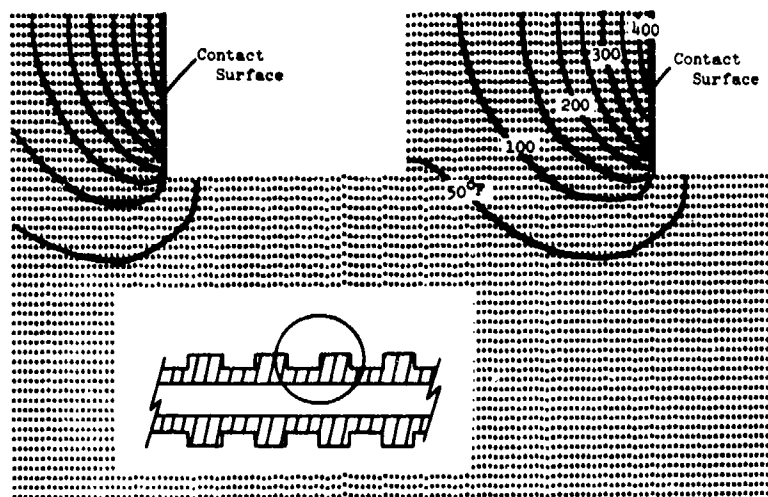
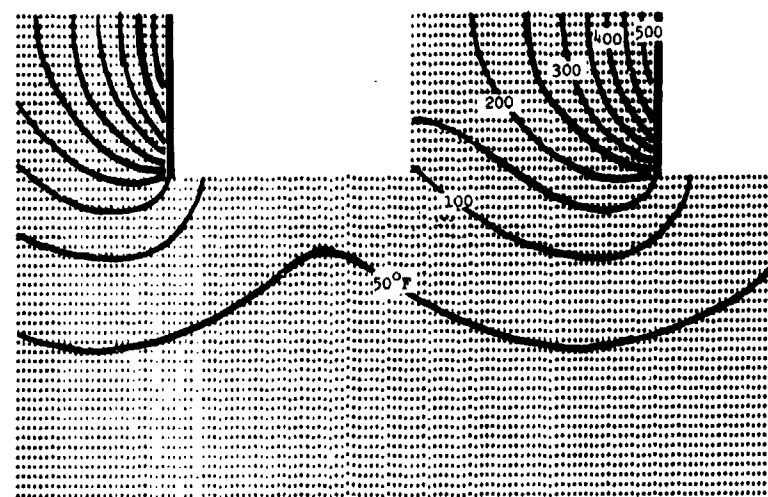


Figure 4. Flapwise Natural Frequencies for Fully Extended TRAC Blade.



a. Midway through passage of nut



b. End of passage of nut

Figure 5. Calculated Jackscrew Temperature Distribution.

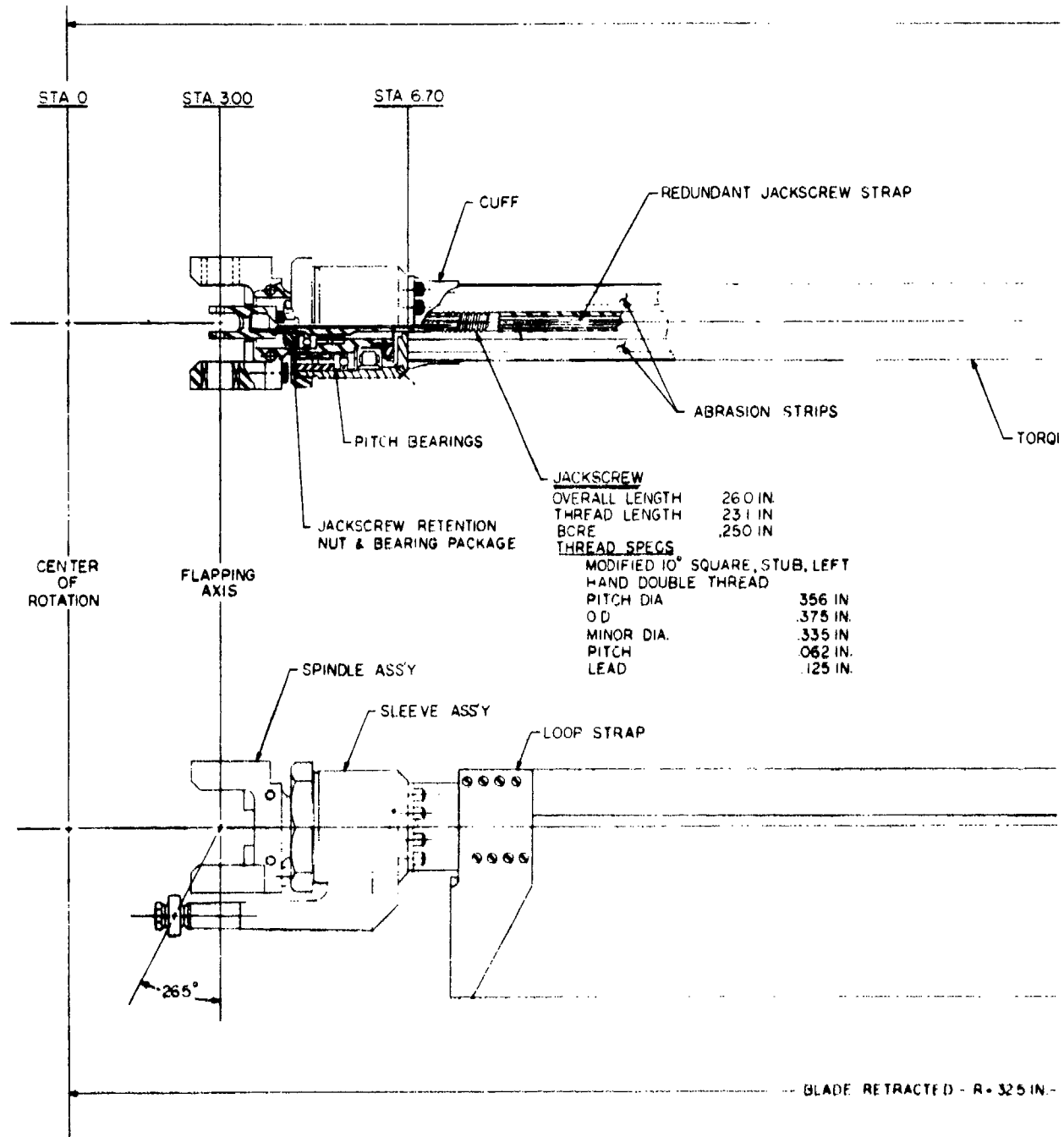
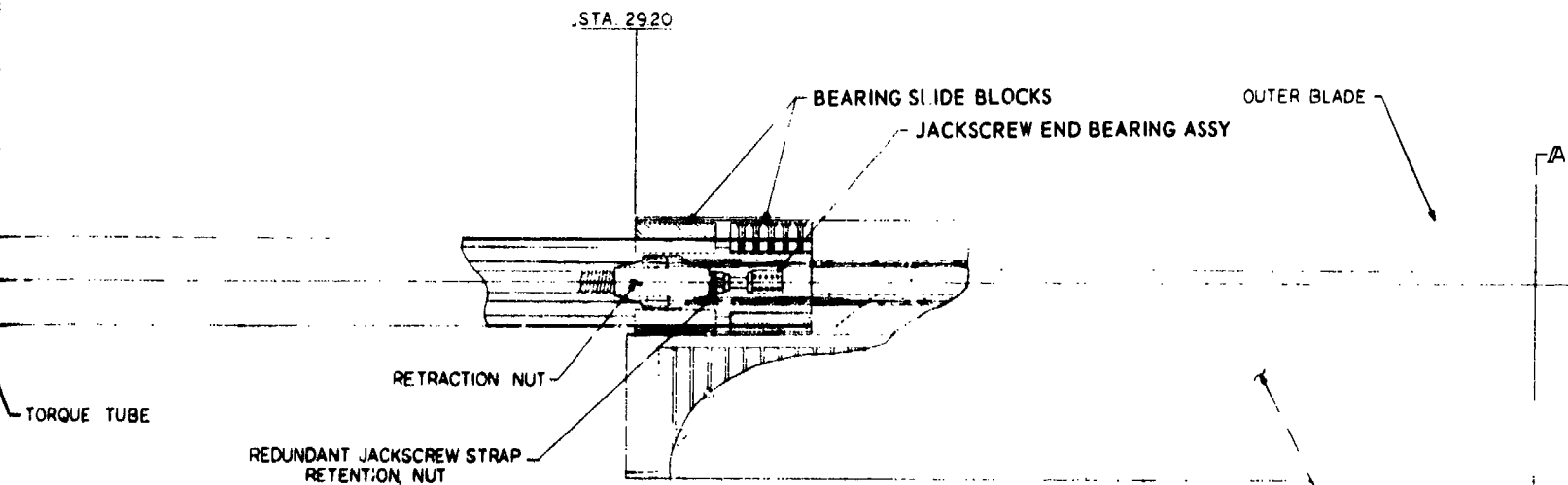
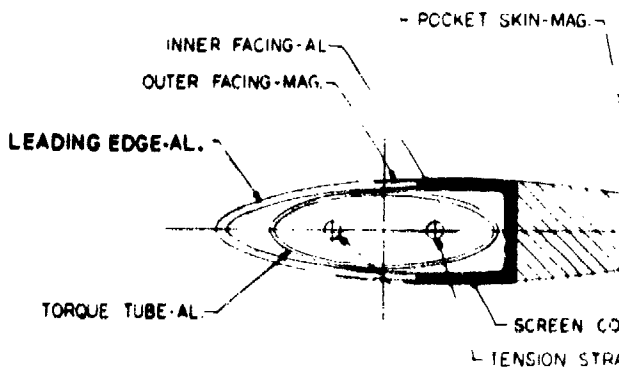


Figure 6. TRAC Model Blade General Arrangement.

BLADE EXTENDED - R= 540 IN.



STA 325

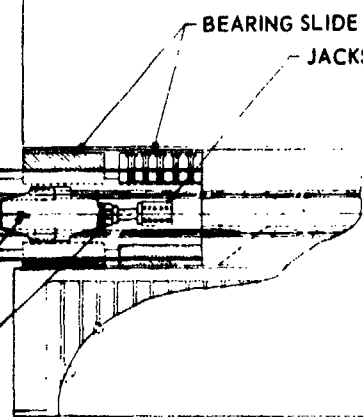


325 IN.

IN.

.2920

STA 5400



OUTER BLADE

BEARING SLIDE BLOCKS

JACKSCREW END BEARING ASSY

TIP BLOCK ASS'Y

TENSION STRAPS

A

A

STA 325

- POCKET SKIN-MAG. -

BALSA WOOD CORE

INNER FACING-AL

OUTER FACING-MAG. -

LEADING EDGE-AL.

TORQUE TUBE-AL

SCREEN CORE-AL

- TENSION STRAPS-STEEL

A-A TYPICAL CROSS SECTION

AIRFOIL 63, AO16
CHORD 450 IN

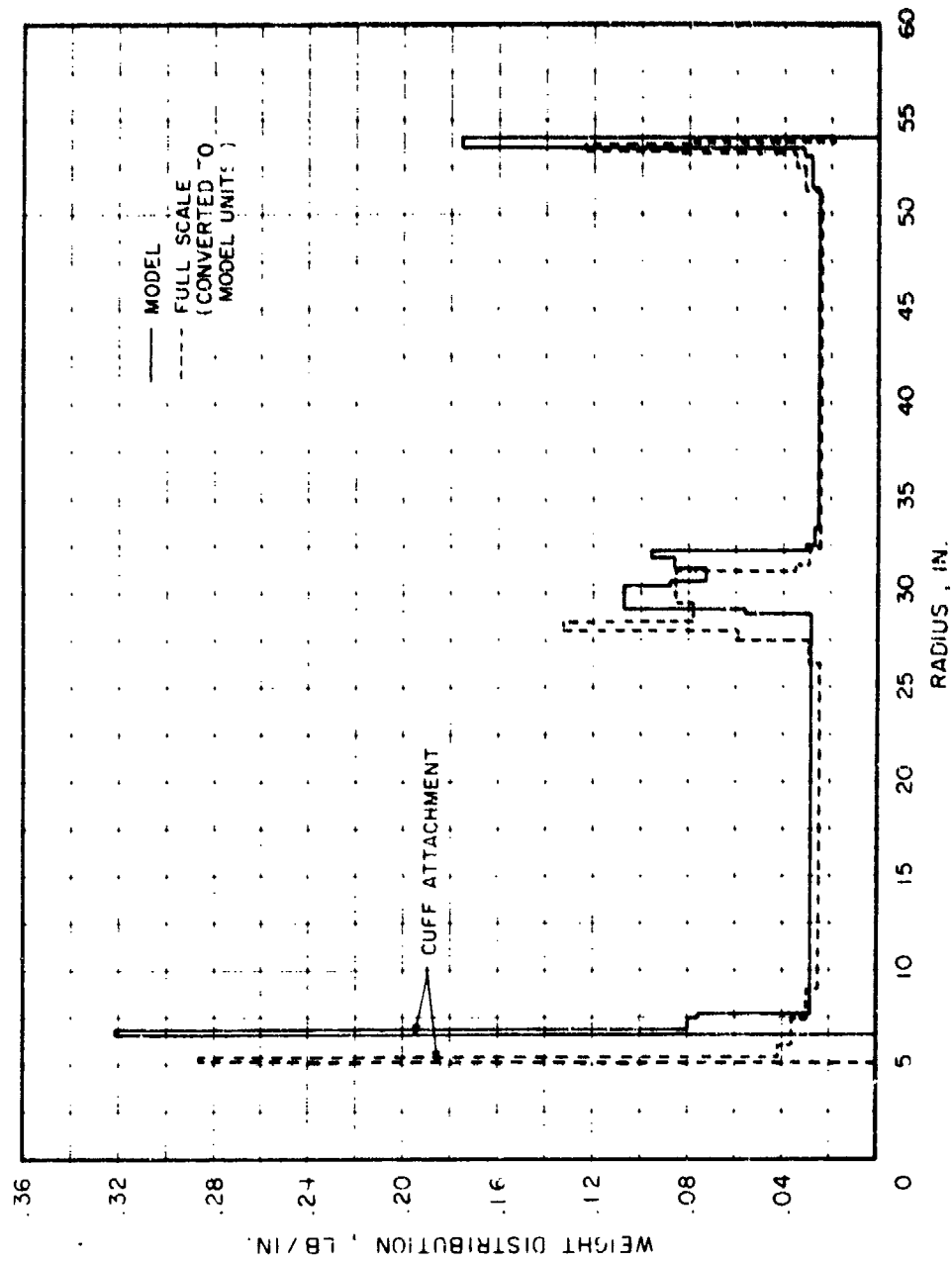


Figure 7. Comparison of Model Spanwise Mass Distribution with Full-Scale Design.

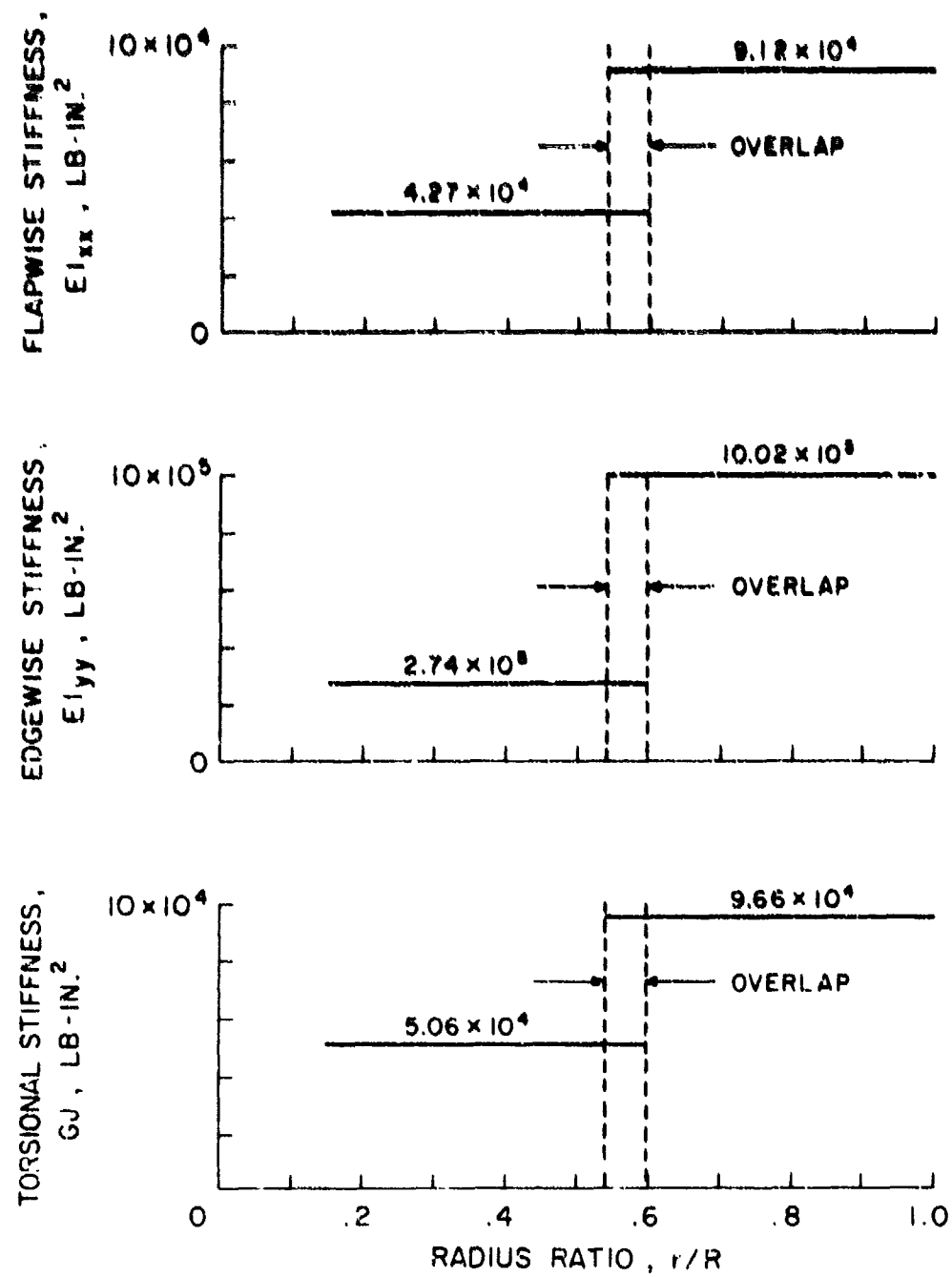


Figure 8. Experimentally Determined Effective Model Blade Stiffness Distribution.

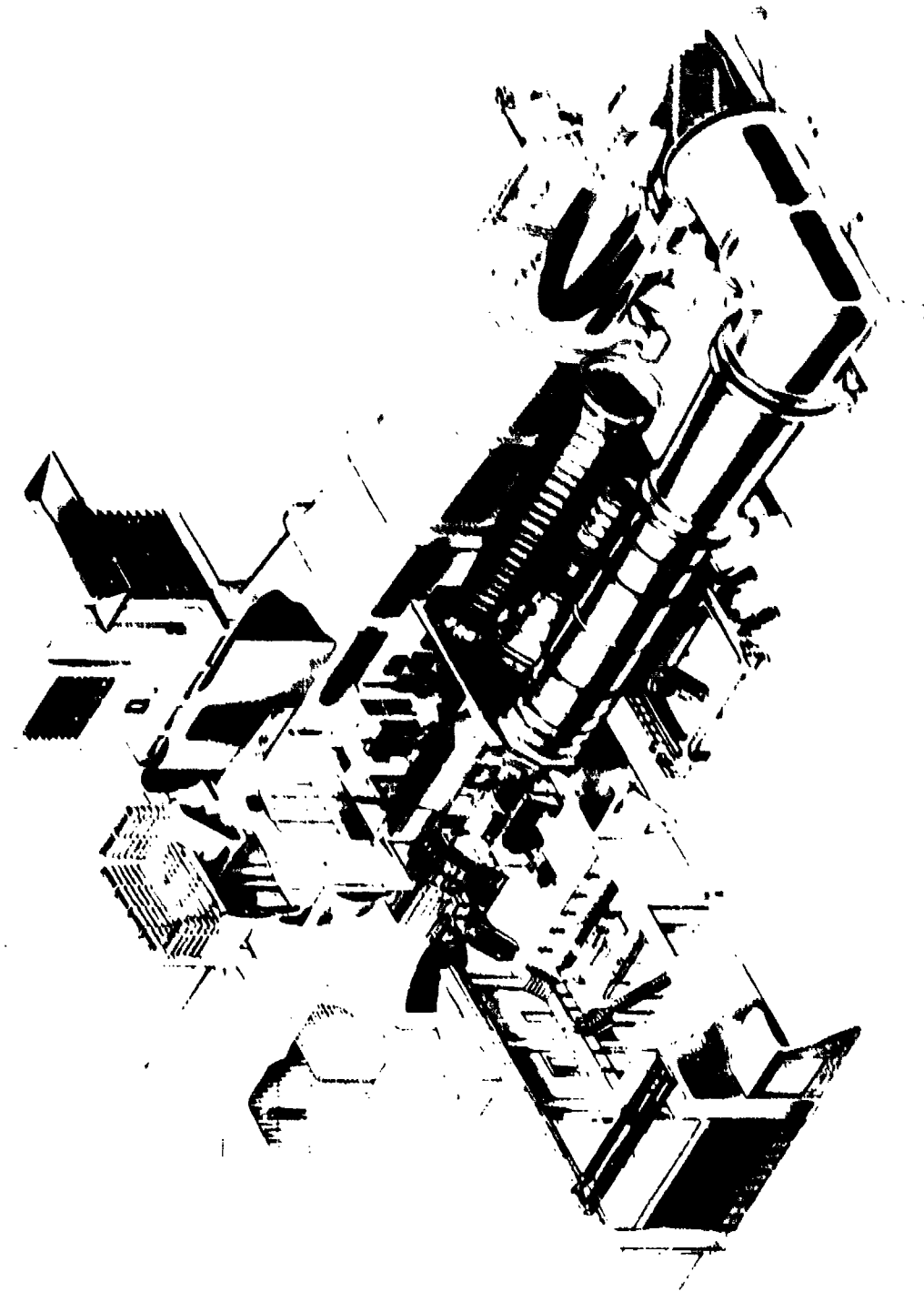


Figure 3. Unloaded Marquette Research Instrumentation Model 1000.

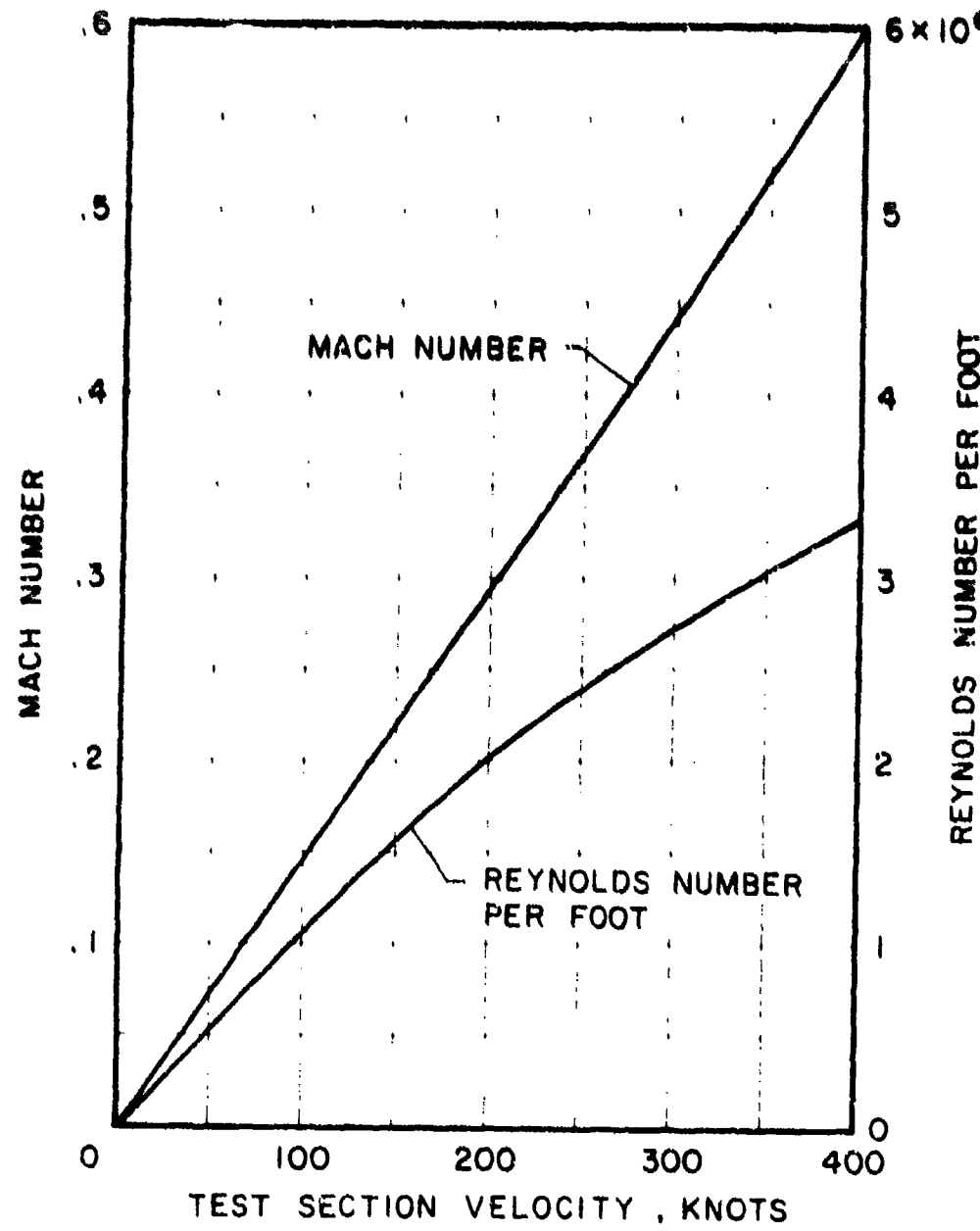


Figure 10. Reynolds Number and Mach Number Versus Test Section Velocity.



Figure 10. Hand search of interior of vehicle. (See Fig. 12 for identification, Figure 42 for
comparison.)

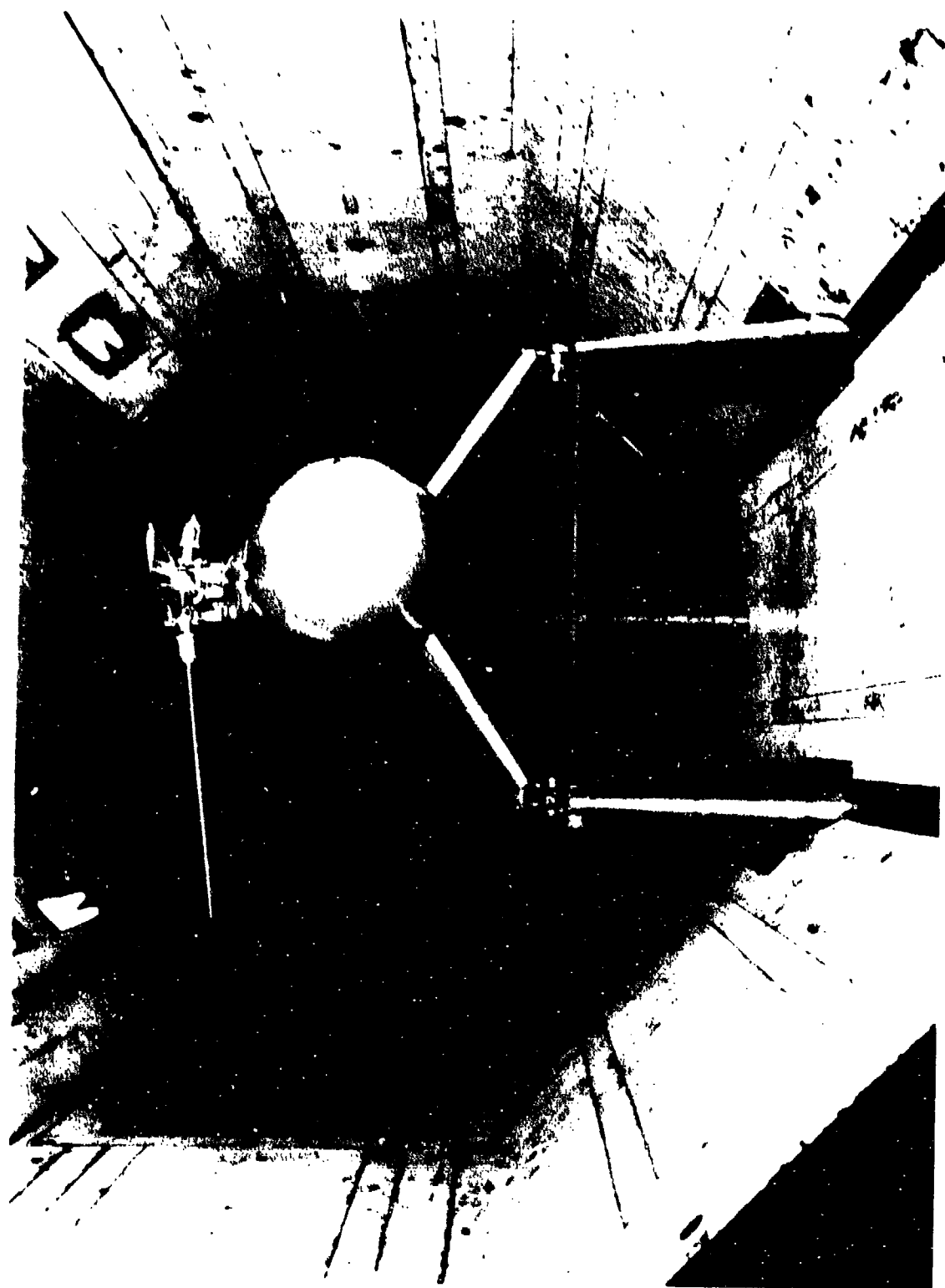


Figure 1. A high-contrast, black-and-white photograph of a person in a dark suit and hat, holding a briefcase, walking away from the camera. The image is framed by a thick black border.

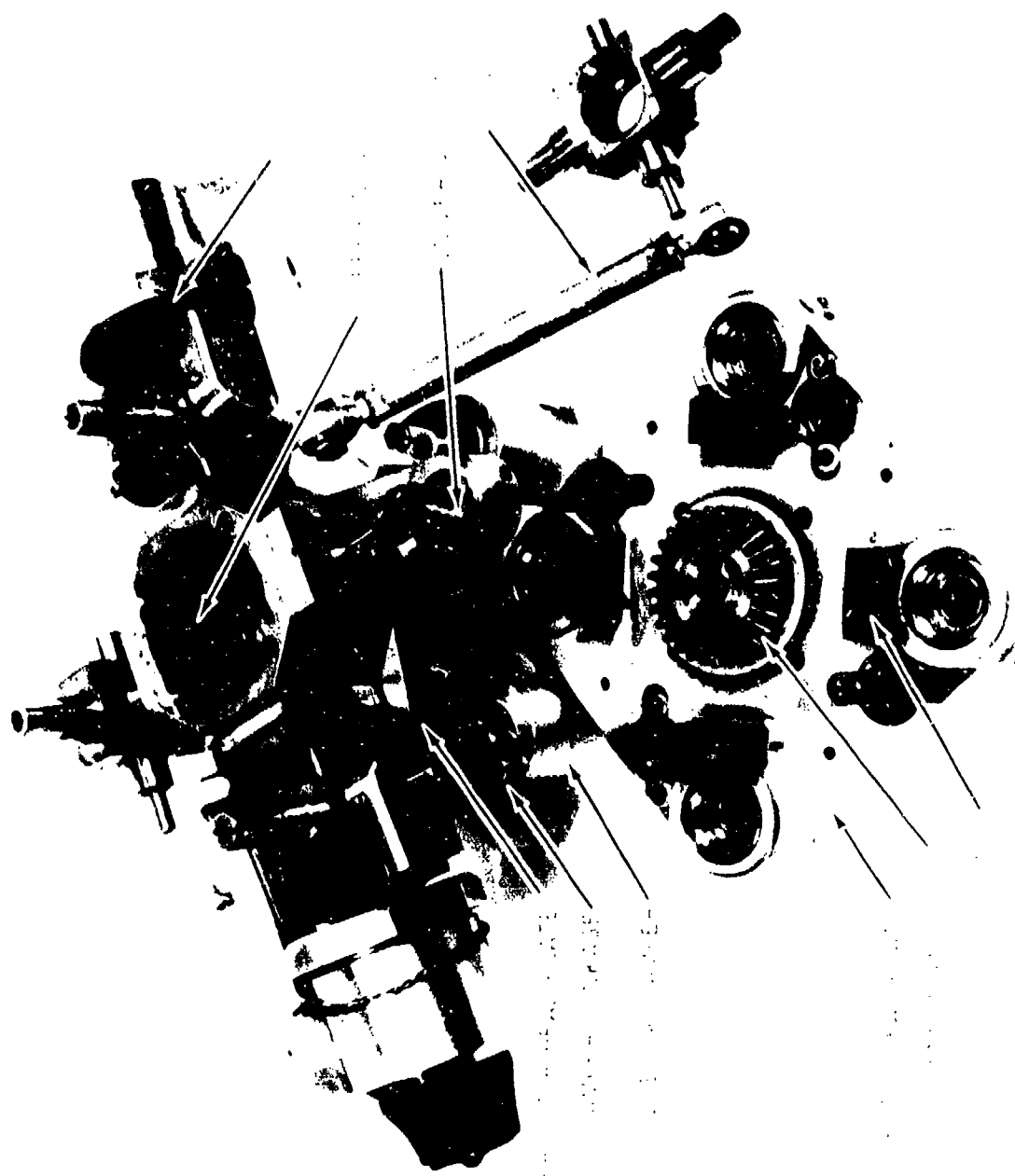


Figure 1. A heavily modified transmission.



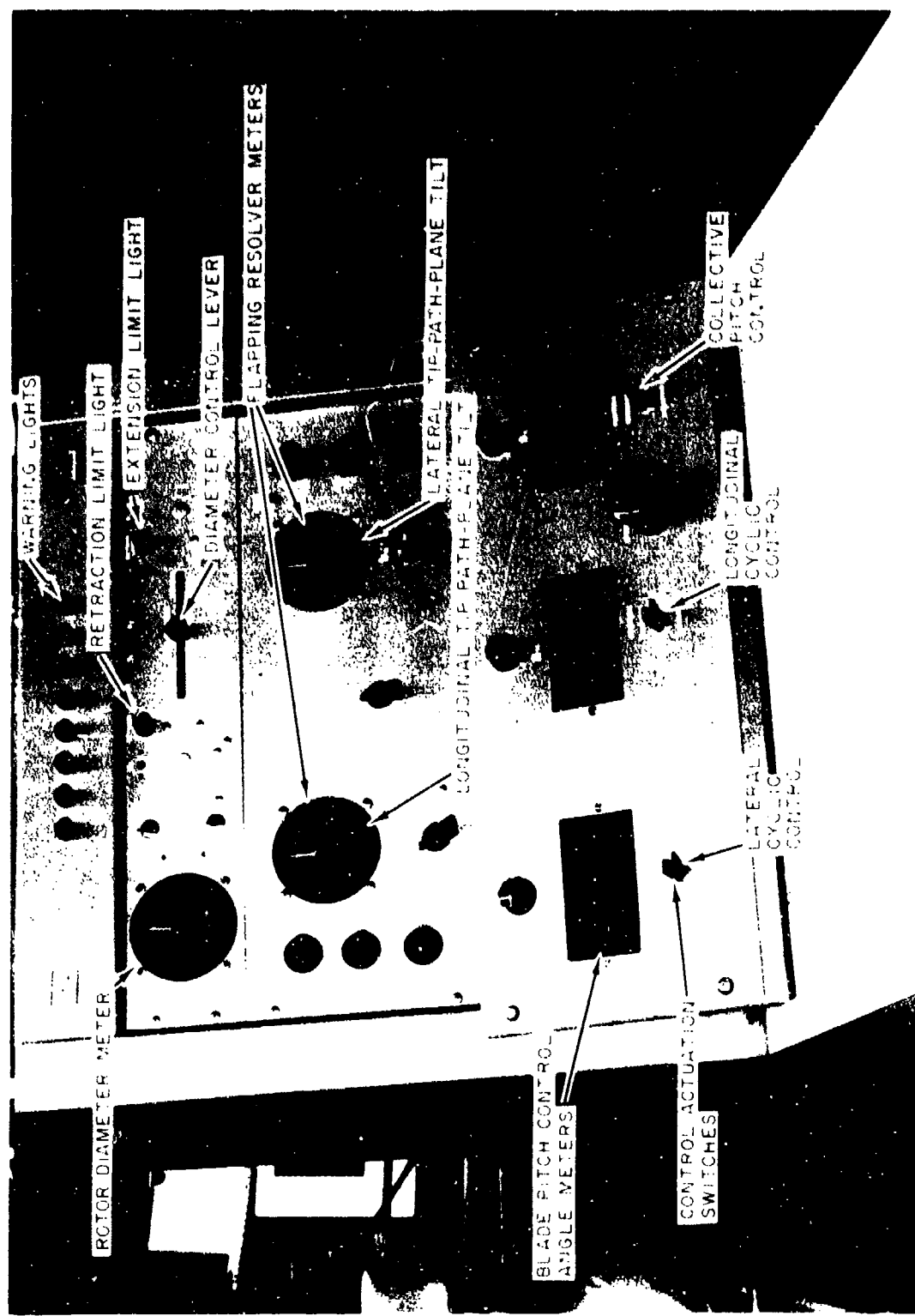


FIGURE 15. ROTOR CONTROL CONSOLE.

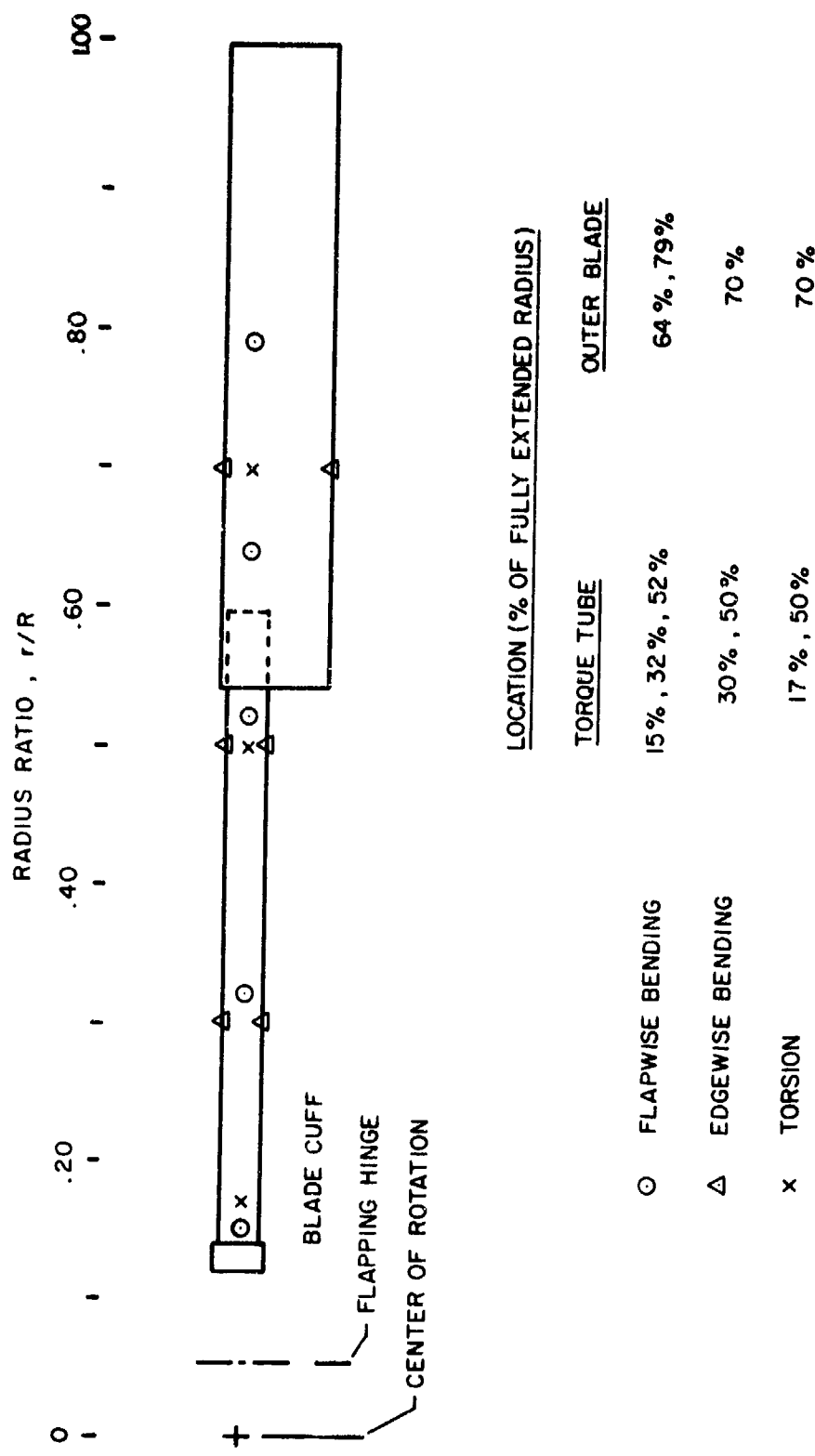


Figure 16. Blade Strain Gage Locations.



Figure 17. Data Acquisition and Monitoring Equipment in Tunnel Control Room.

PHASE I HELICOPTER MODE
 PHASE II DIAMETER CHANGE
 PHASE III RPM CHANGE, ARTICULATED
 PHASE IV RPM CHANGE, LOCKED HINGES
 PHASE V BLADE INDEX VARIATIONS
 PHASE VII HIGH SPEED COMPOUND MODE

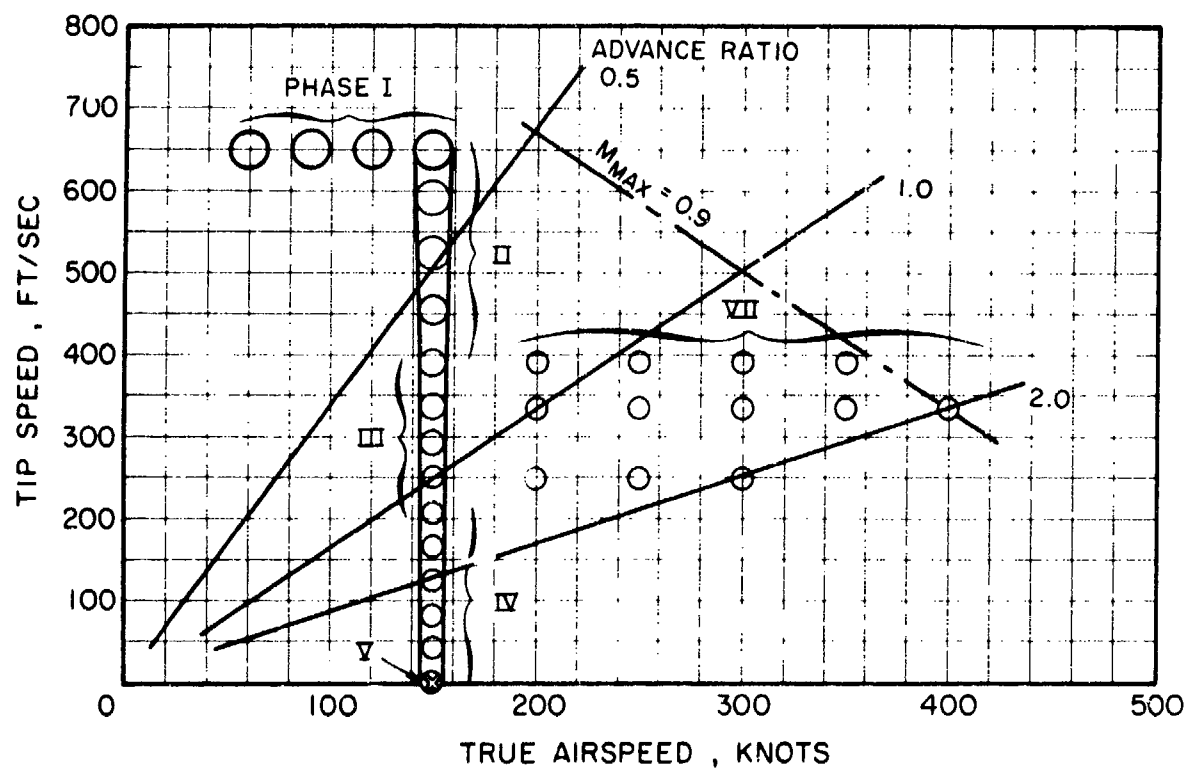


Figure 18. TRAC Model Rotor Wind Tunnel Test Conditions.

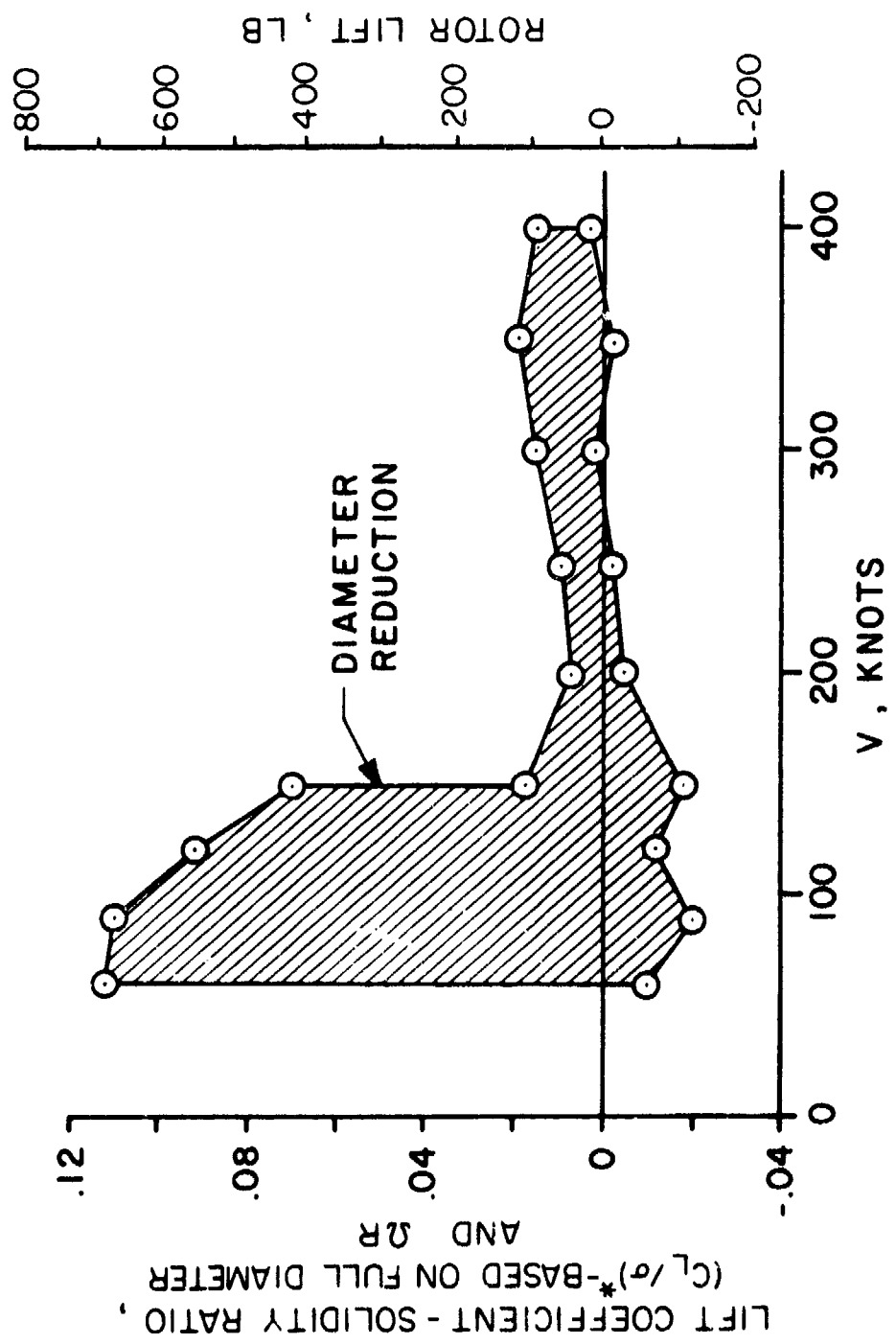


Figure 19. Lift Envelope, TRAC Model Rotor Tests.

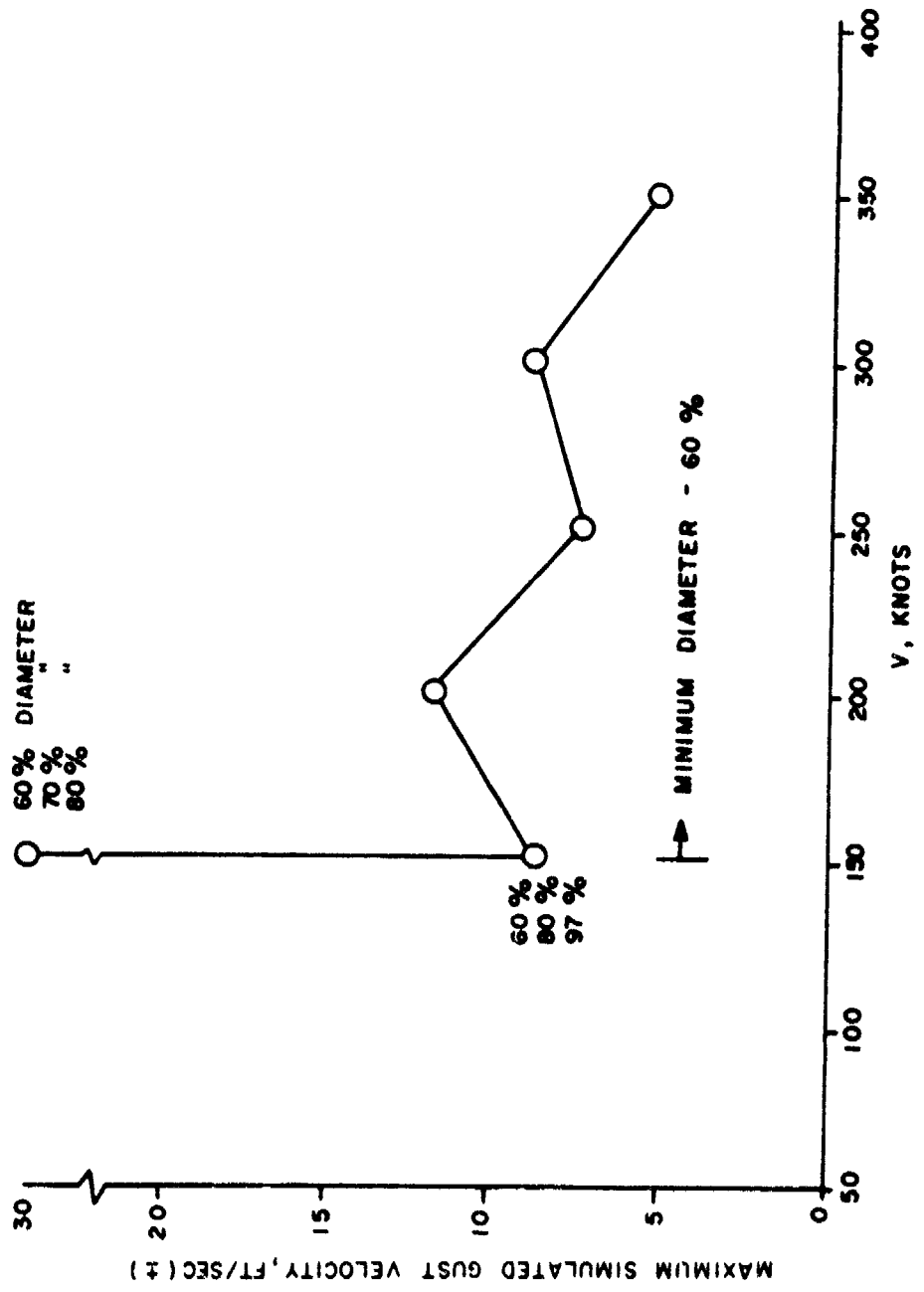


Figure 20. Gust Envelope, TRAC Model Rotor Tests.

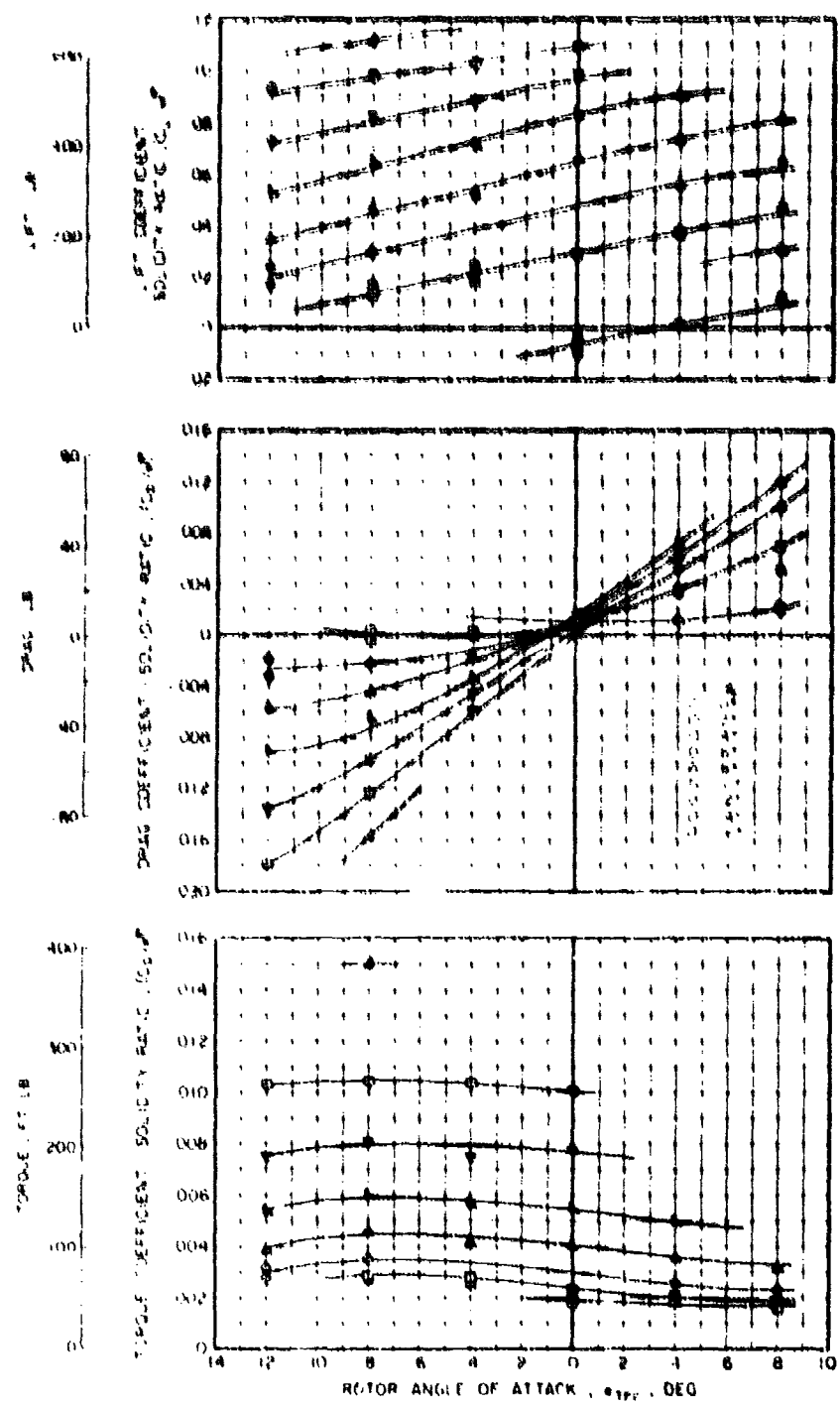


Figure 21. Measured Rotor Performance Characteristics,
Full Diameter, 1375 rpm, $V = 60$ Knots.

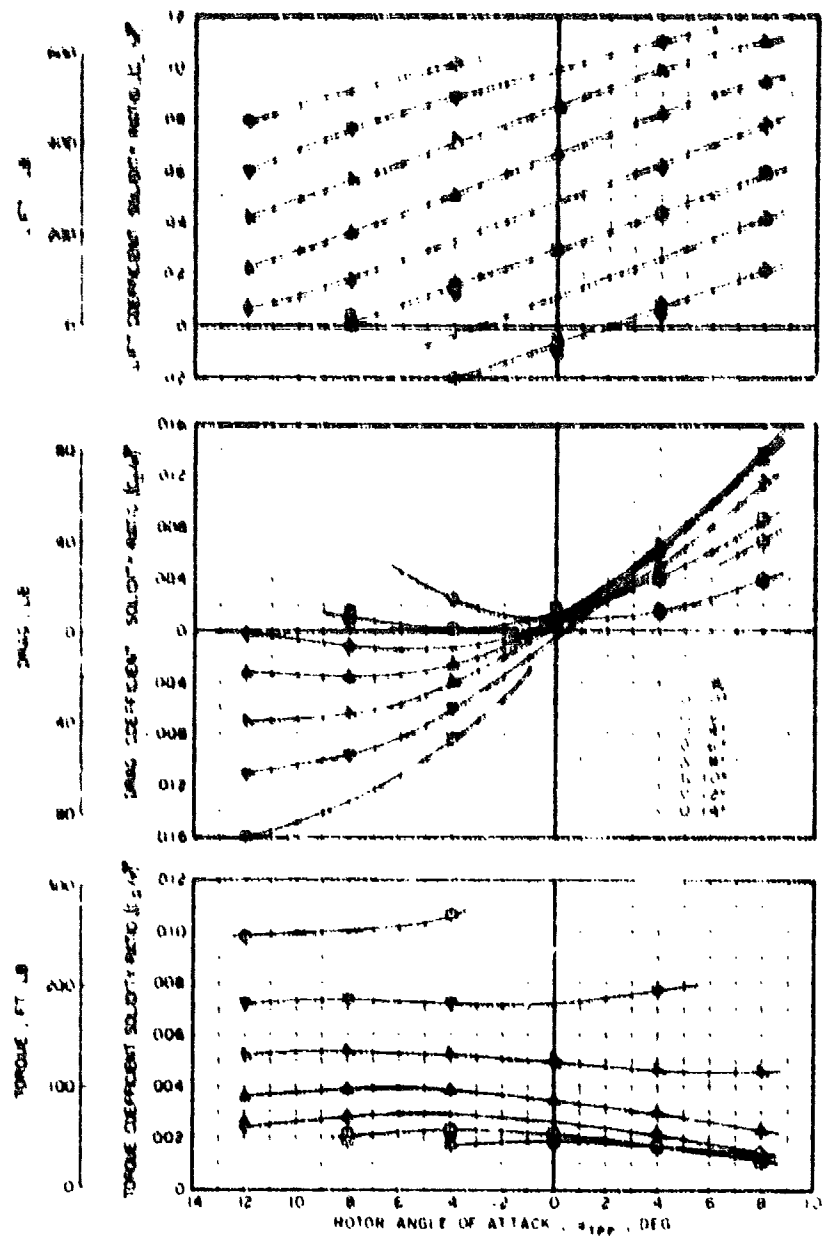


Figure 22. Measured Rotor Performance Characteristics,
Full Diameter, 1375 rpm, $V = 90$ Knots.

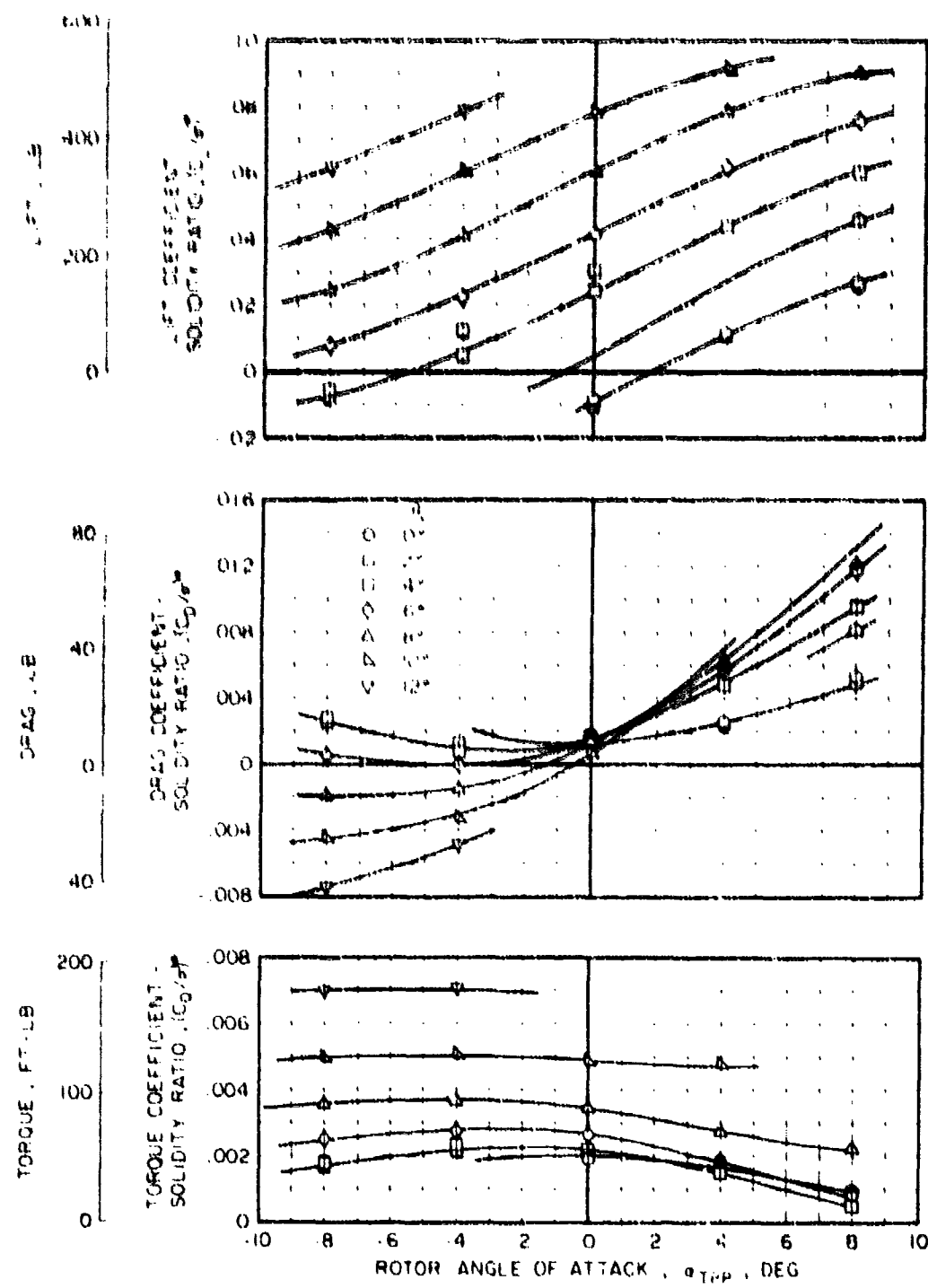


Figure 23. Measured Rotor Performance Characteristics, Full Diameter, 1375 rpm, $V = 120$ Knots.

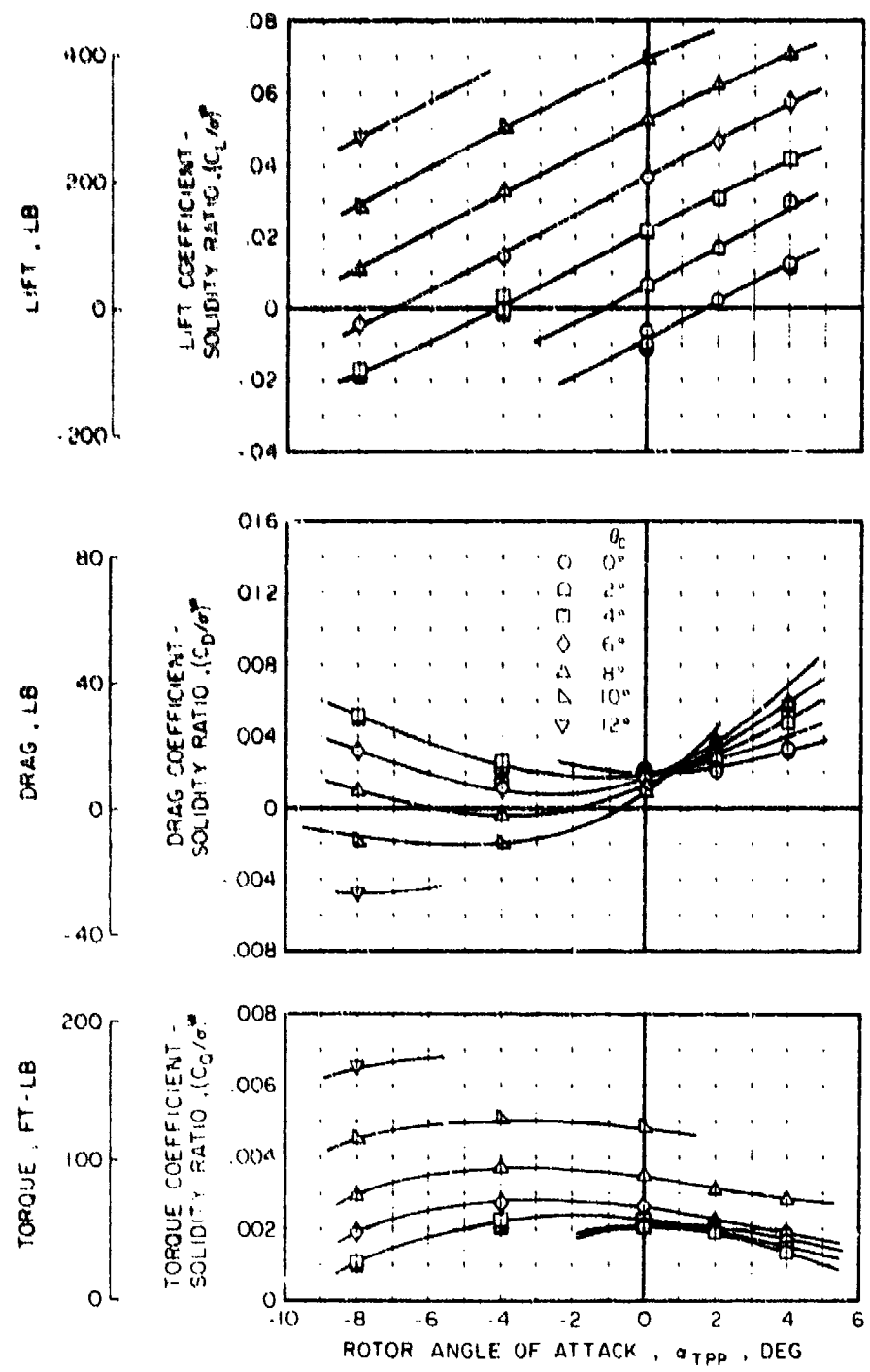


Figure 24. Measured Rotor Performance Characteristics,
Full Diameter, 1375 rpm, $V = 150$ Knots.

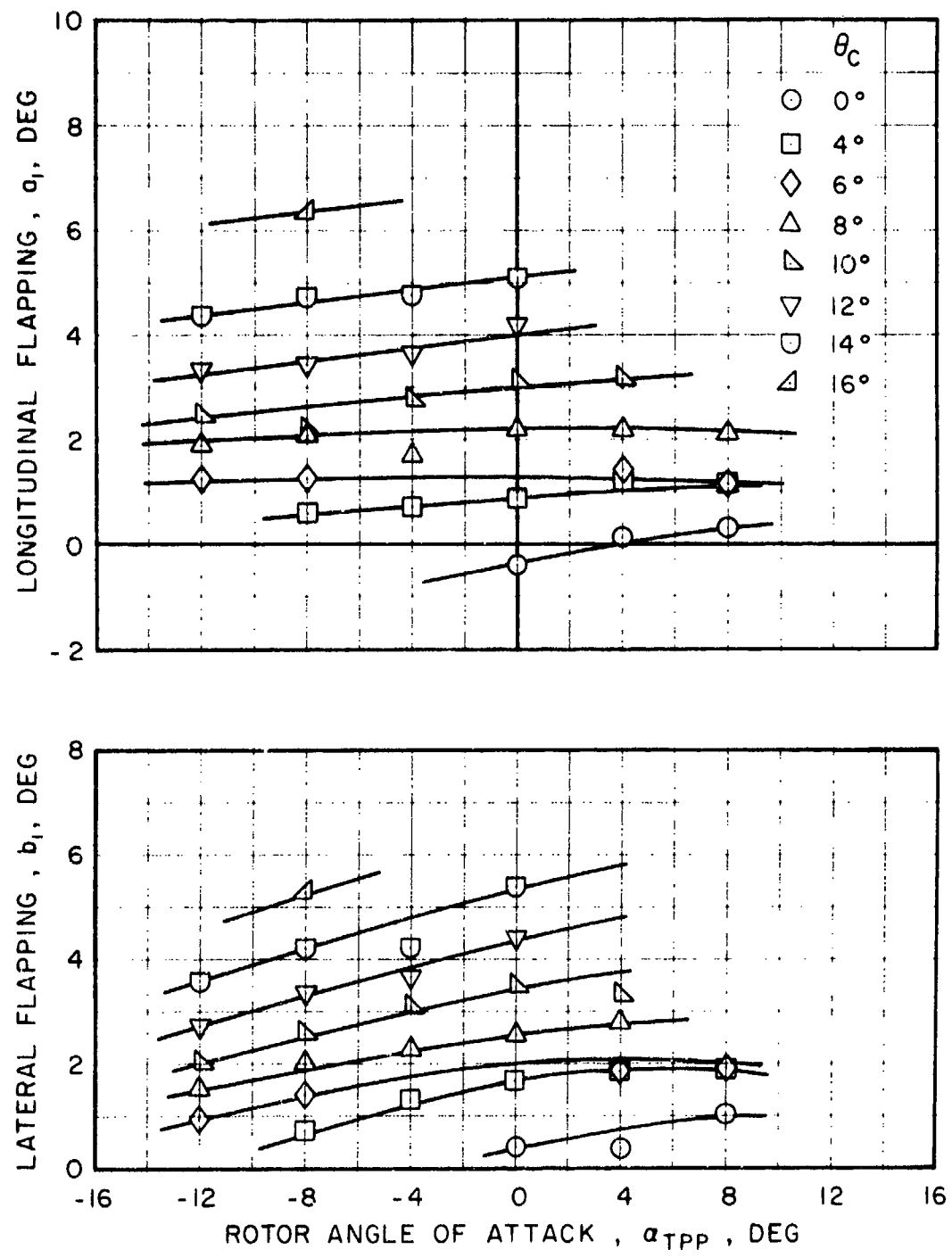


Figure 25. Measured Blade Flapping, Full Diameter,
1375 rpm, $V = 60$ Knots.

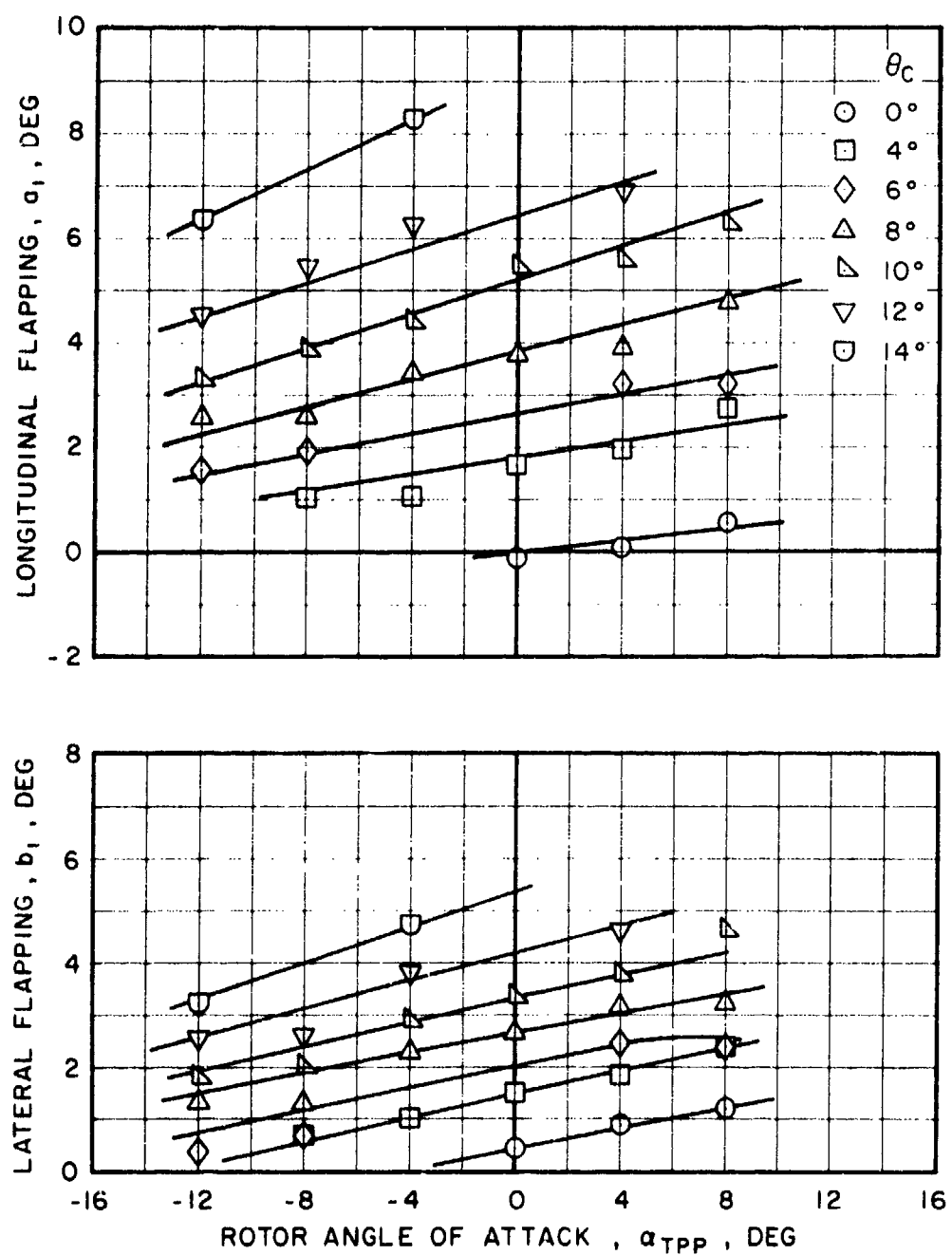


Figure 26. Measured Blade Flapping, Full Diameter, 1375 rpm,
 $V = 90$ Knots.

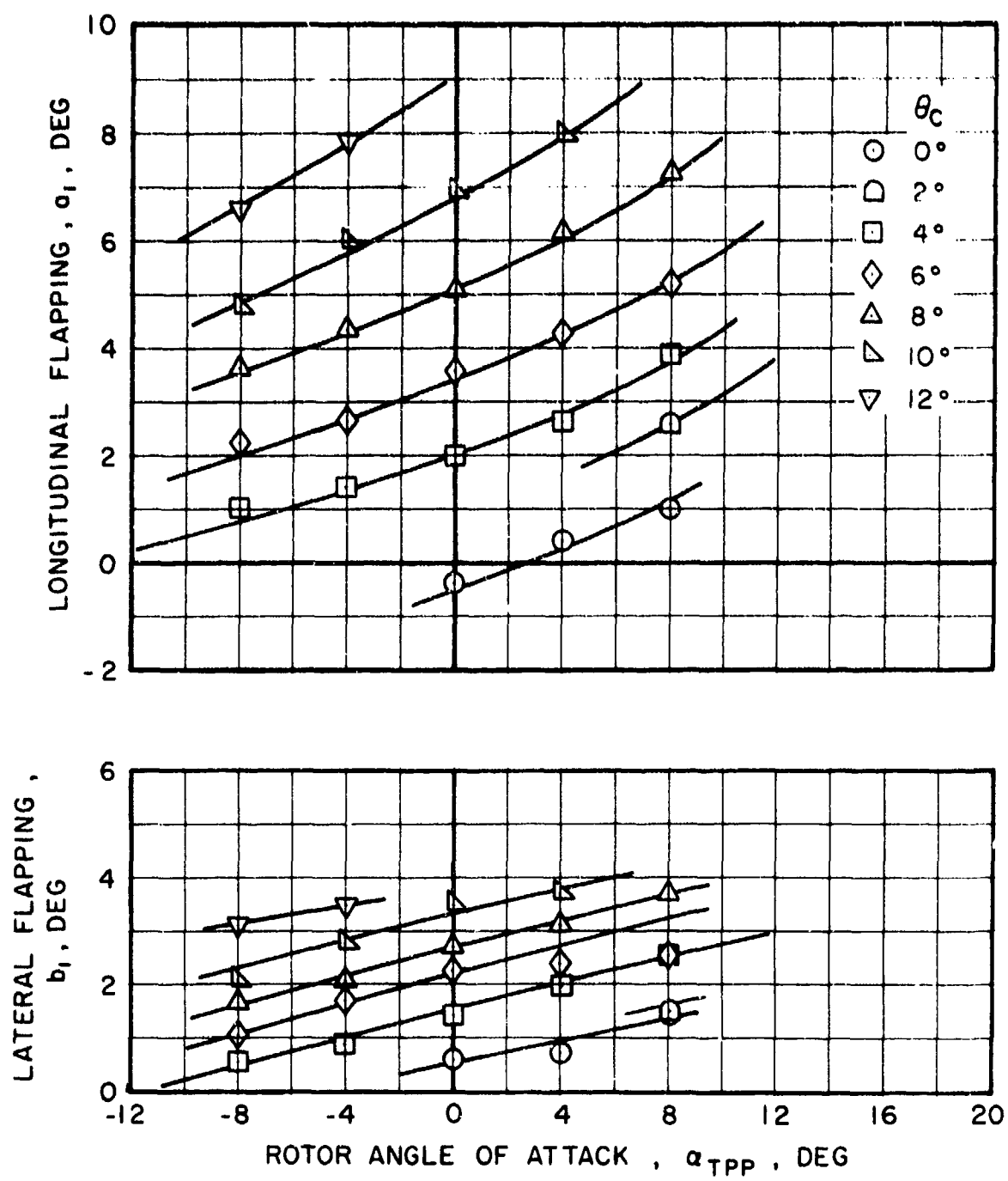


Figure 27. Measured Blade Flapping, Full Diameter,
1375 rpm, $V = 120$ Knots.

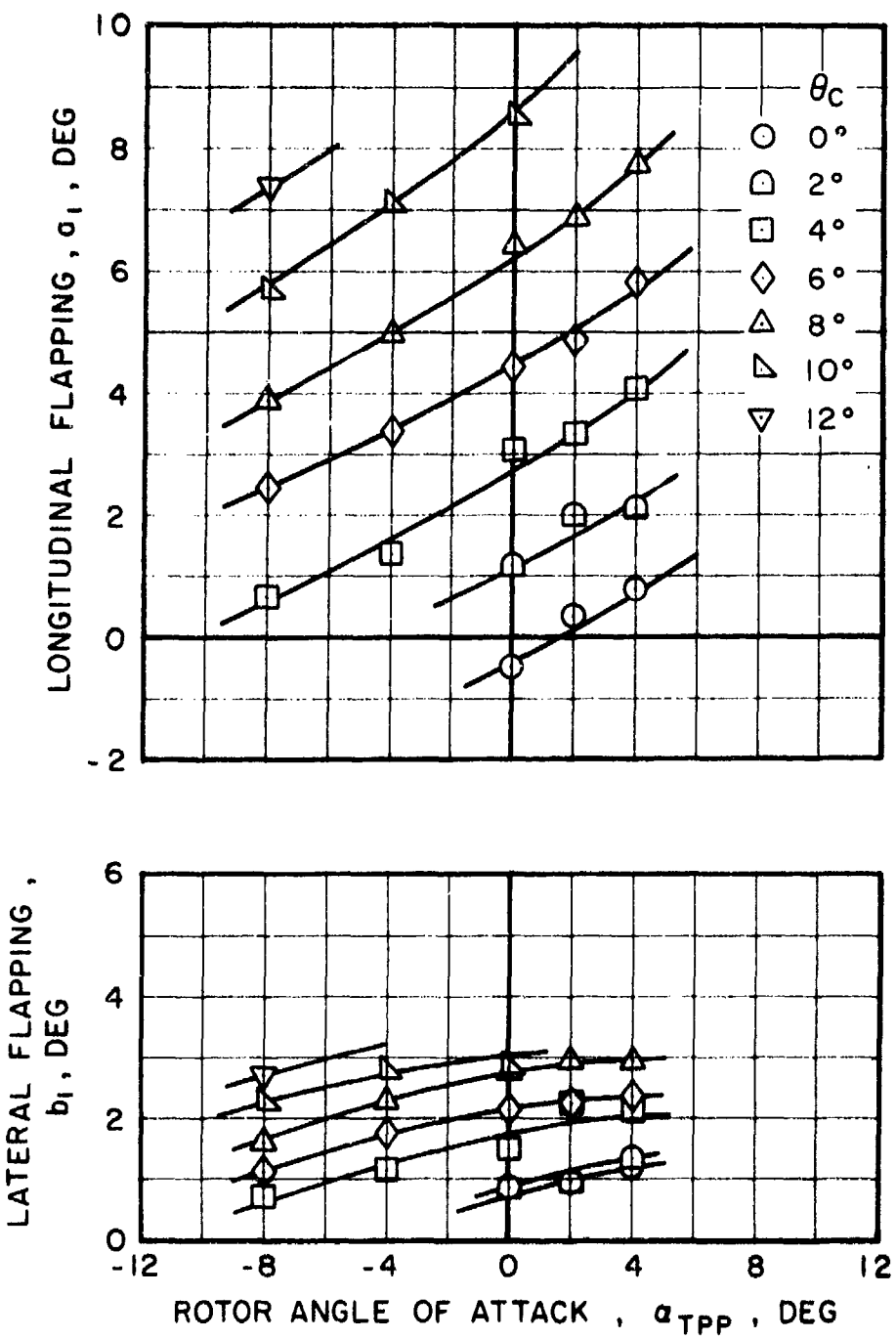


Figure 28. Measured Blade Flapping, Full Diameter, 1375 rpm,
 $V = 150$ Knots.

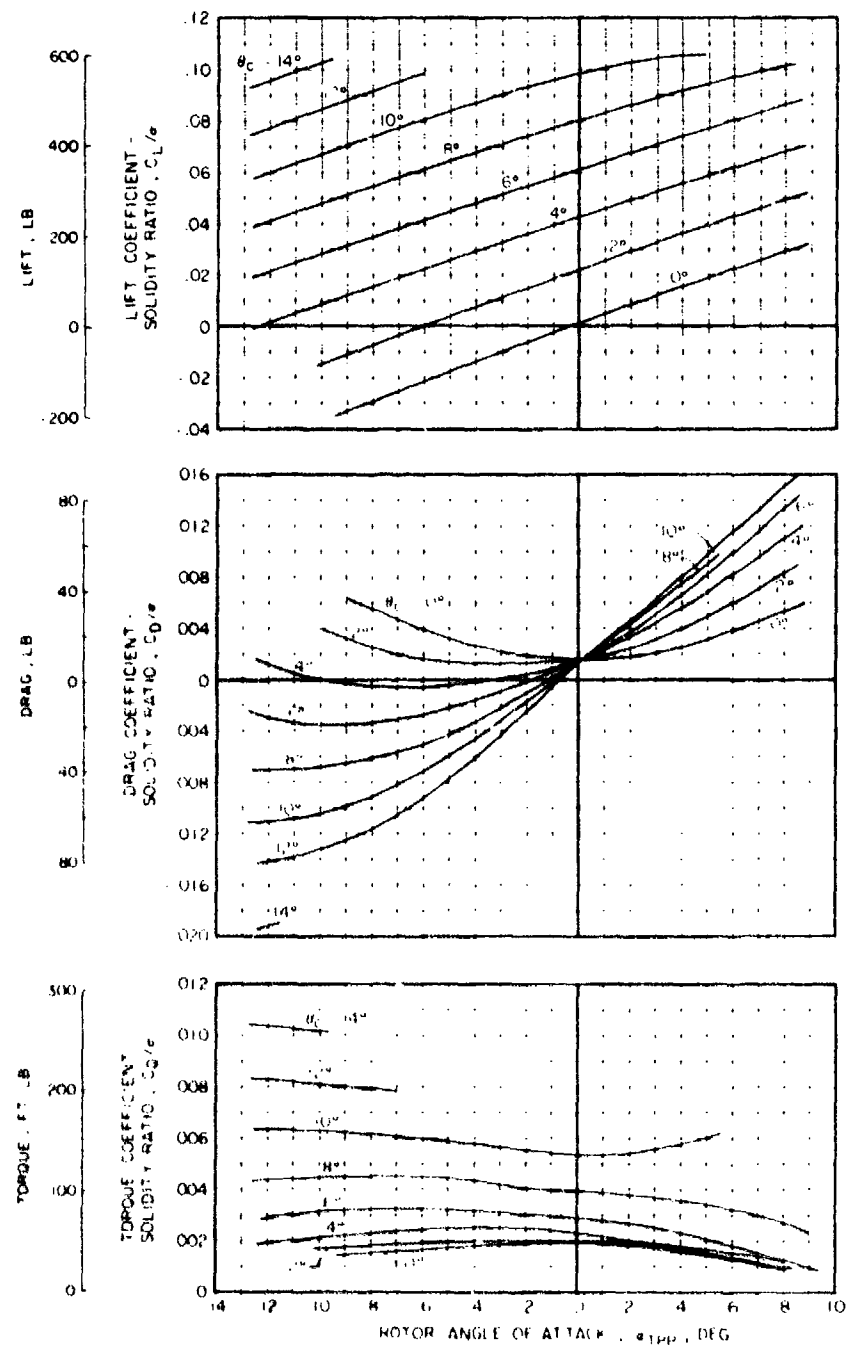


Figure 29. Theoretical Rotor Performance Characteristics, Full Diameter, 1375 rpm, $V = 90$ Knots.

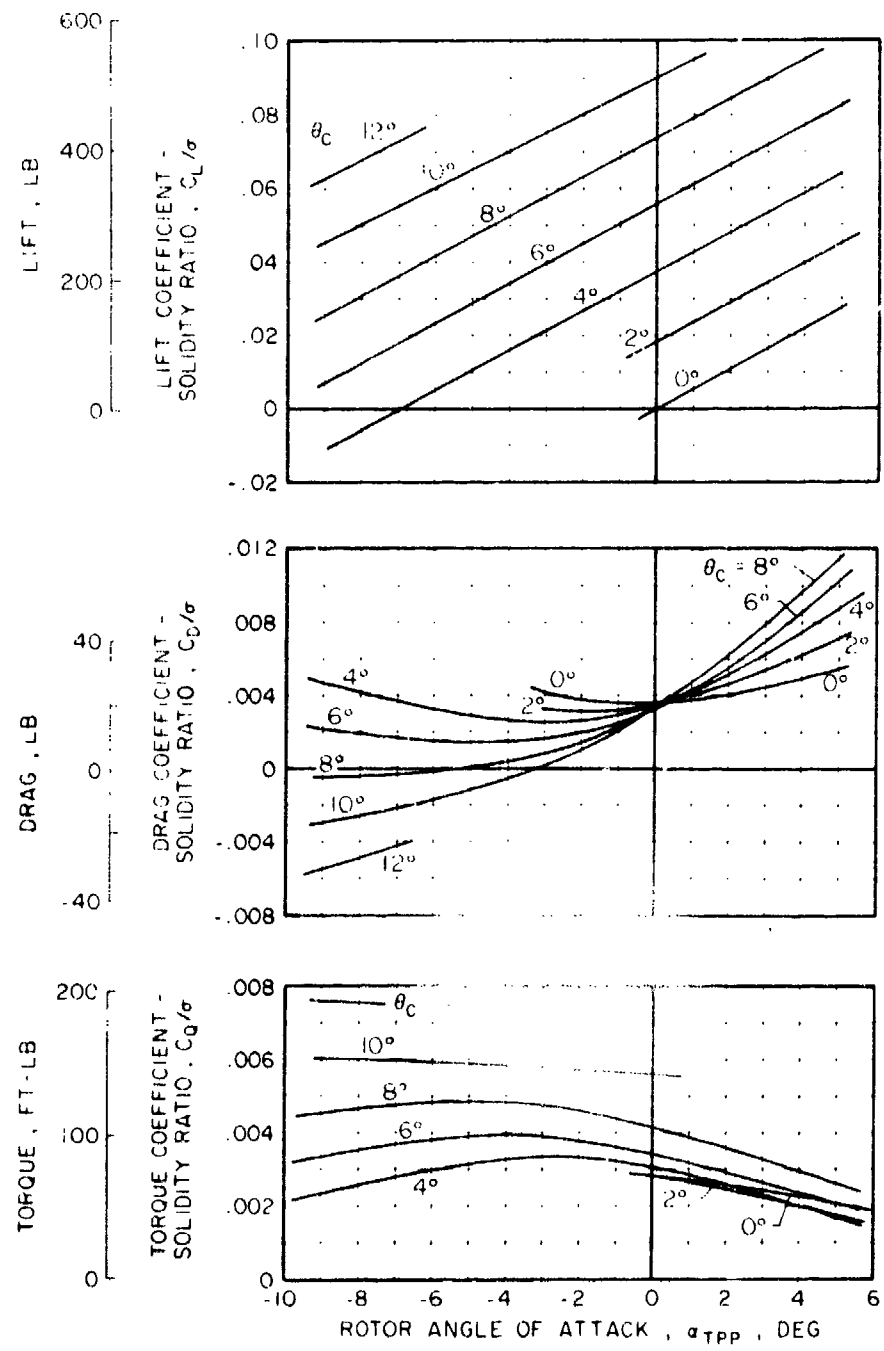


Figure 30. Theoretical Rotor Performance Characteristics, Full Diameter, 1375 rpm, $V = 150$ Knots.

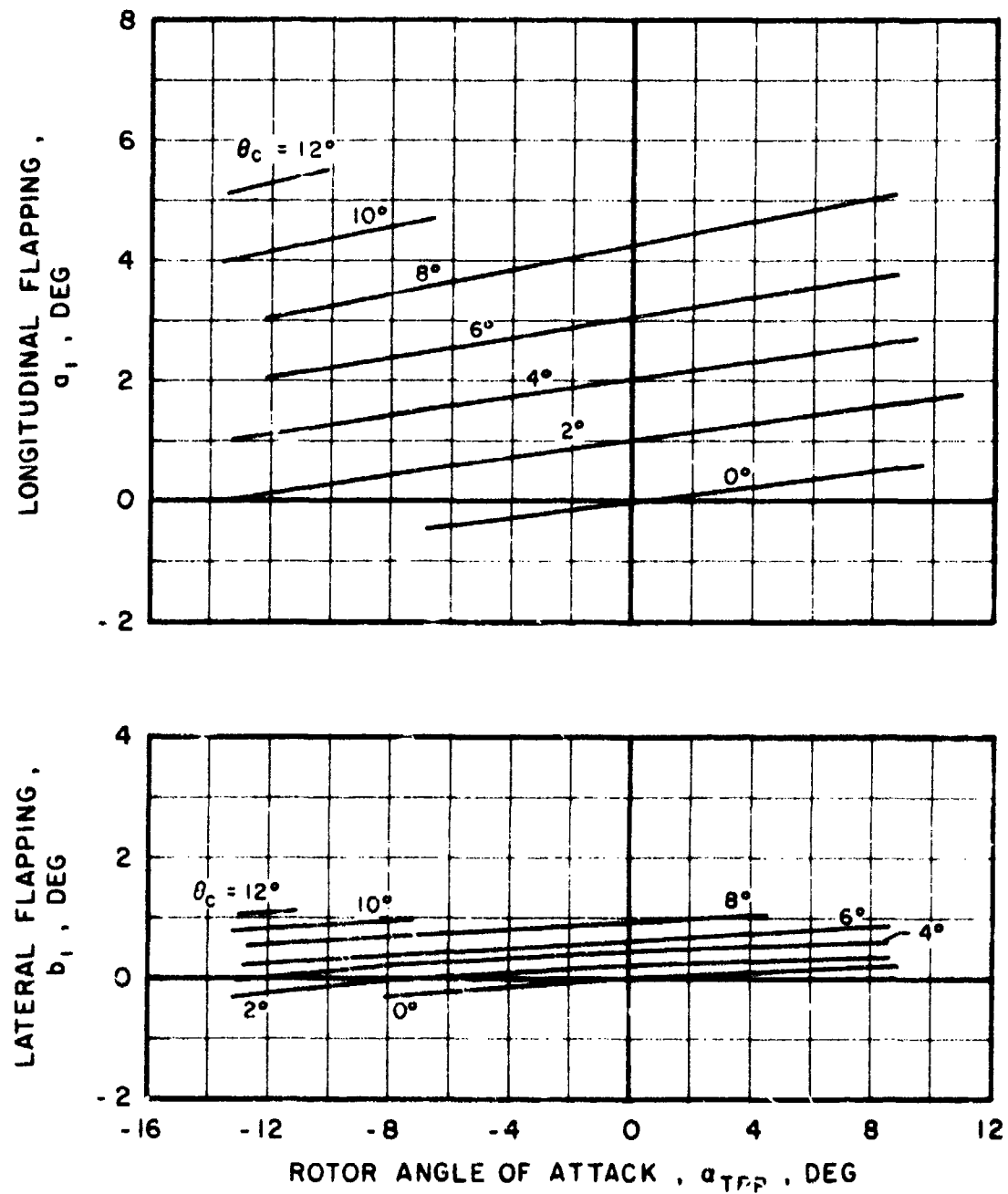


Figure 31. Theoretical Blade Flapping, Full Diameter,
1375 rpm, $V = 90$ Knots.

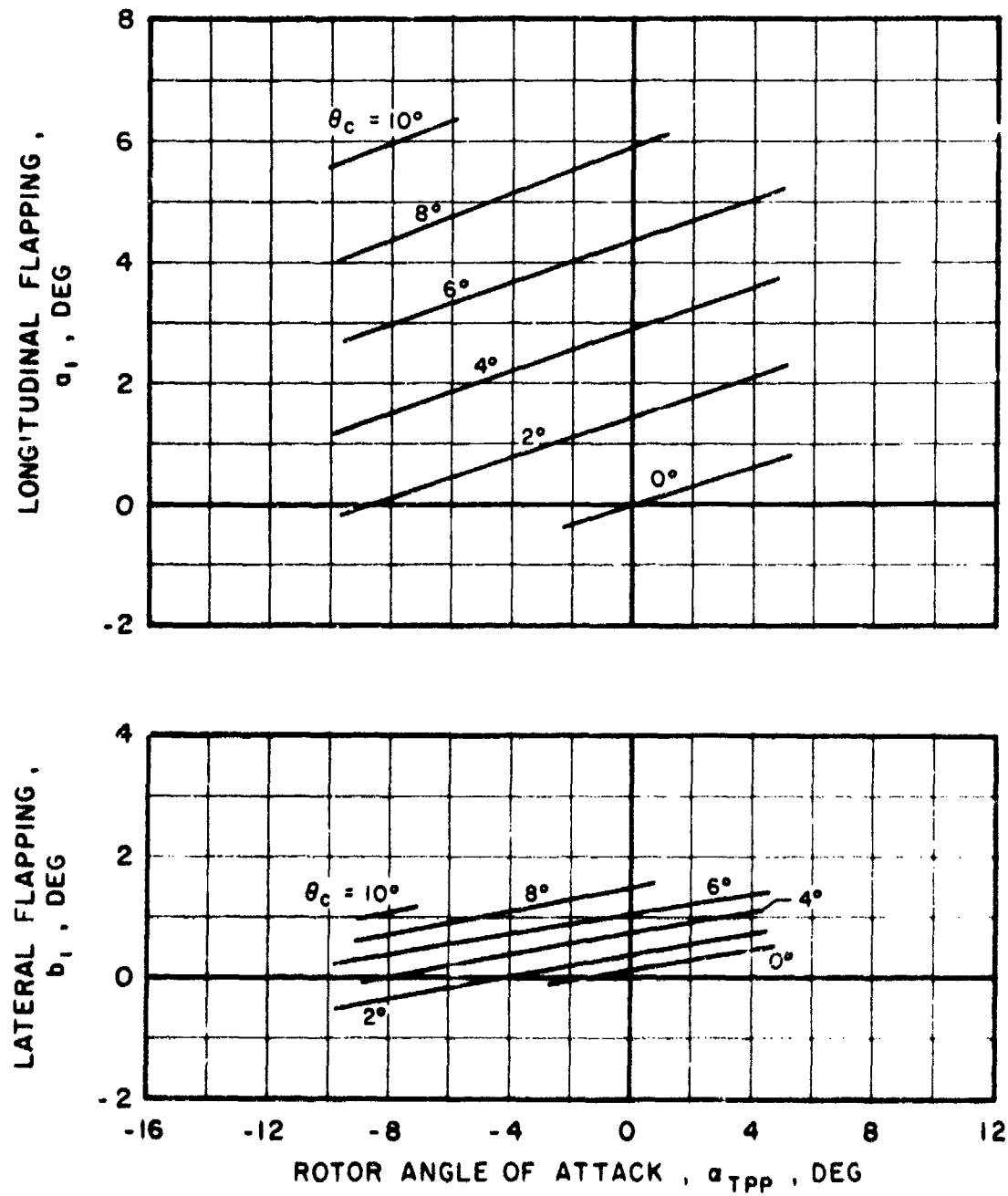


Figure 32. Theoretical Blade Flapping, Full Diameter,
1375 rpm, $V = 150$ Knots.

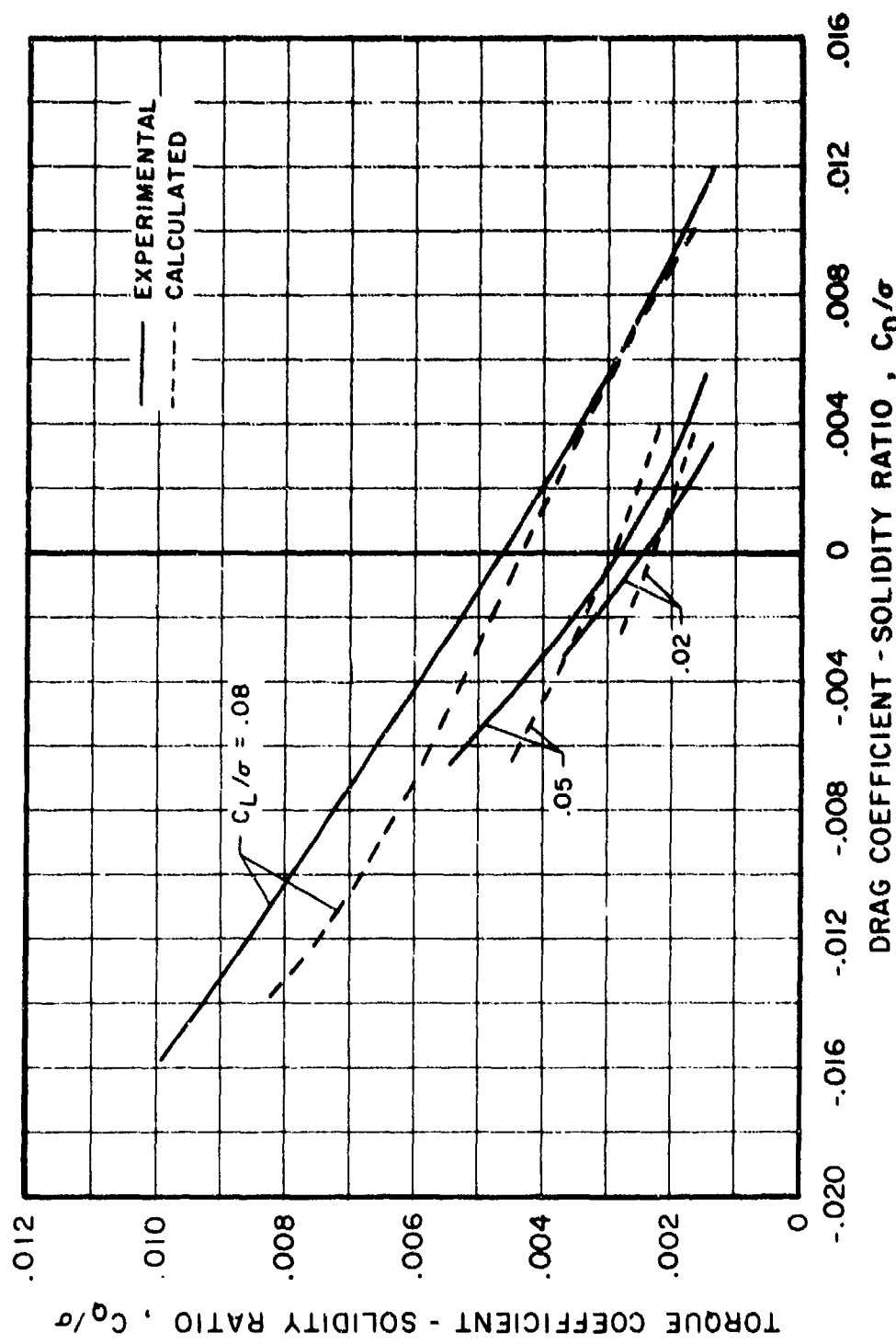


Figure 33. Rotor Performance Correlation, Full Diameter, 1375 rpm, $V = 90$ Knots.

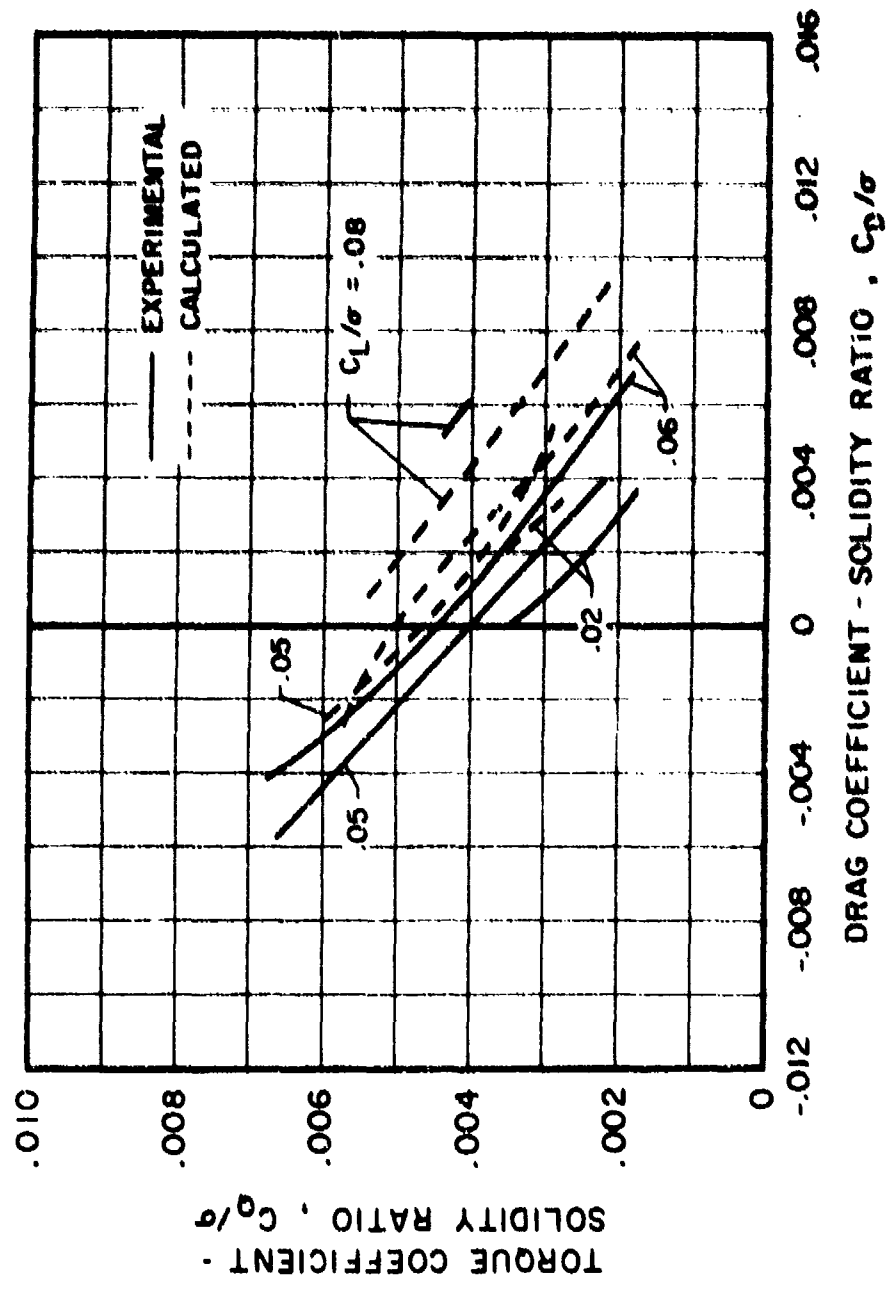


Figure 34. Rotor Performance Correlation, Full Diameter, 1375 rpm, $T = 150$ roots.

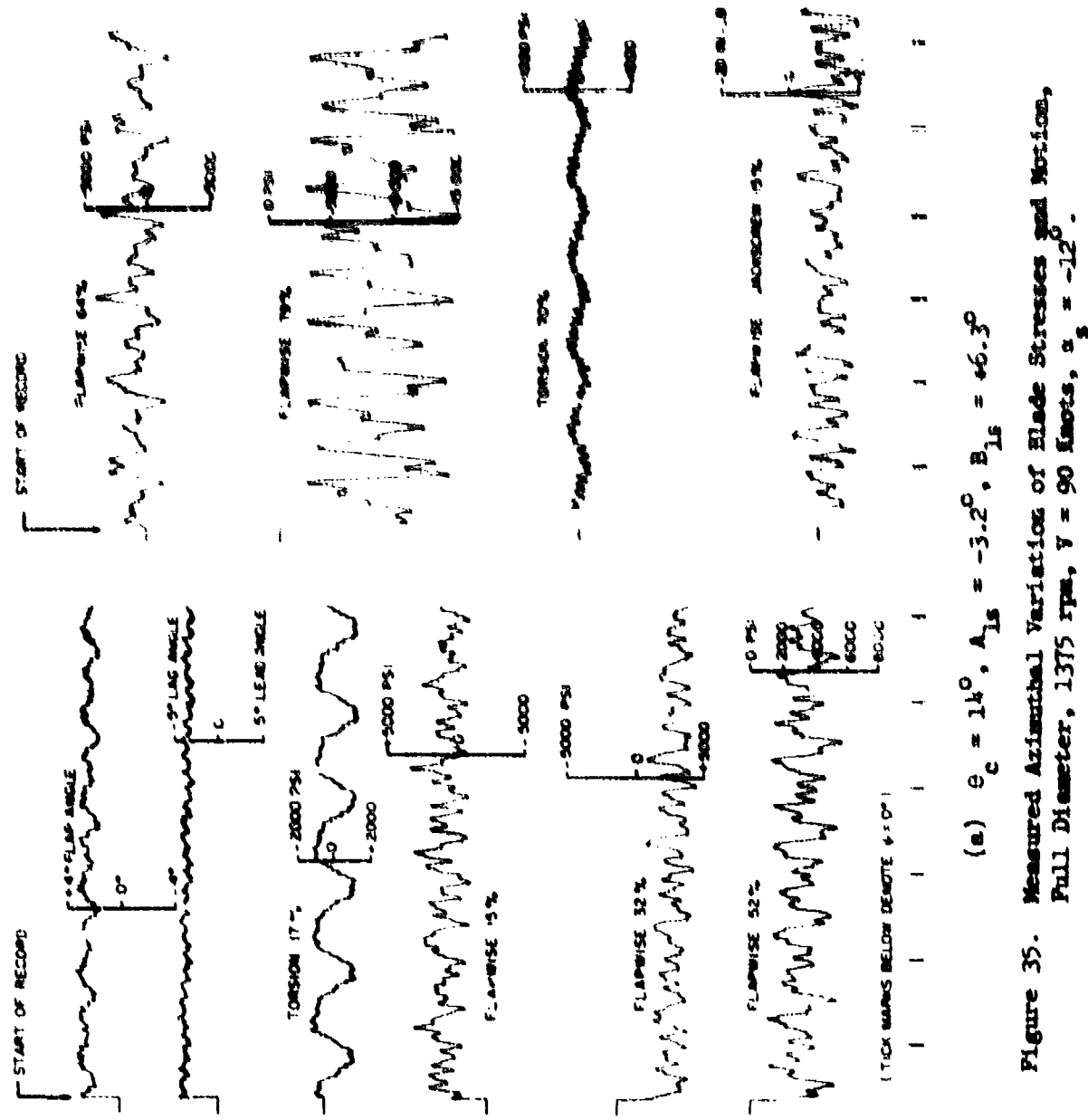
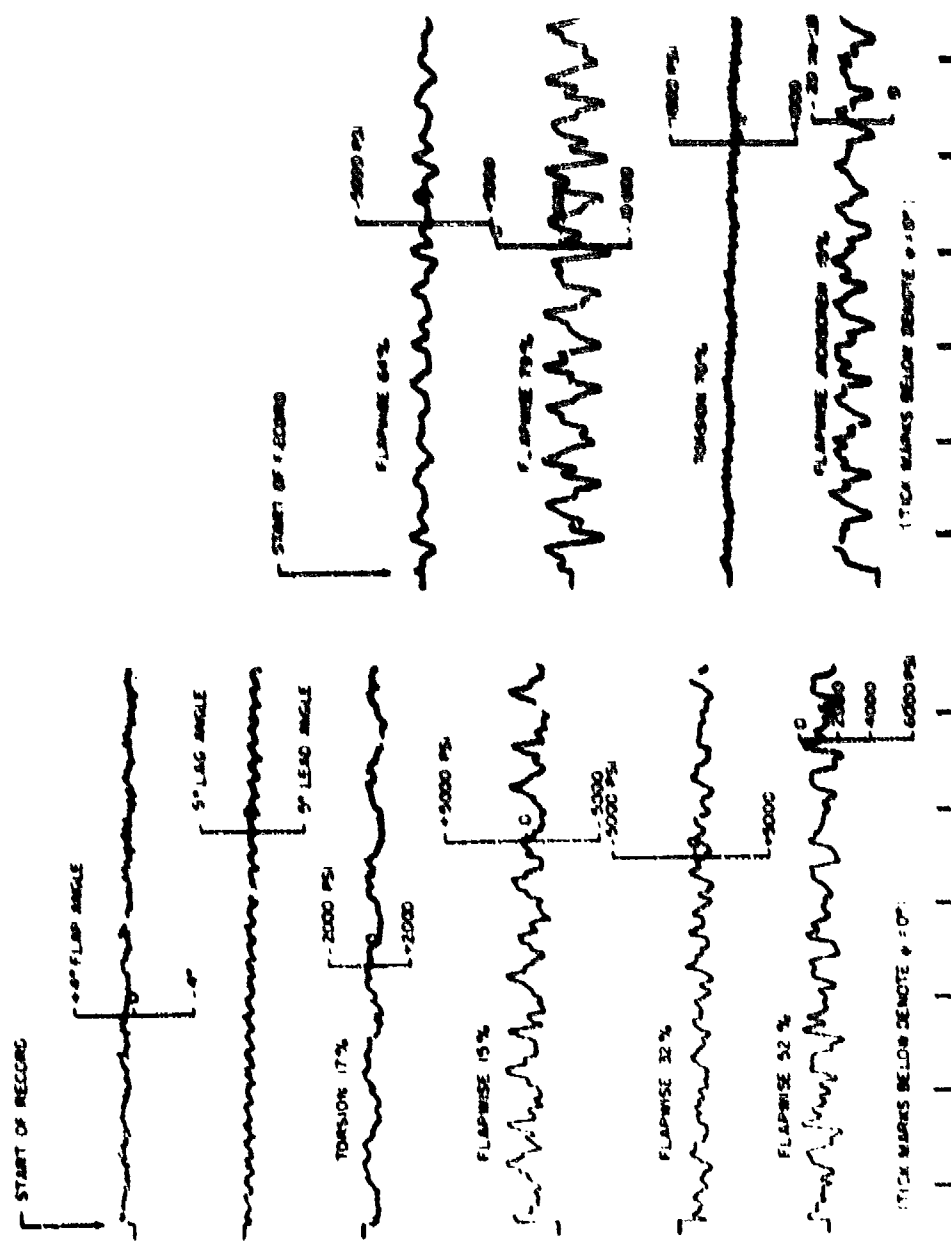
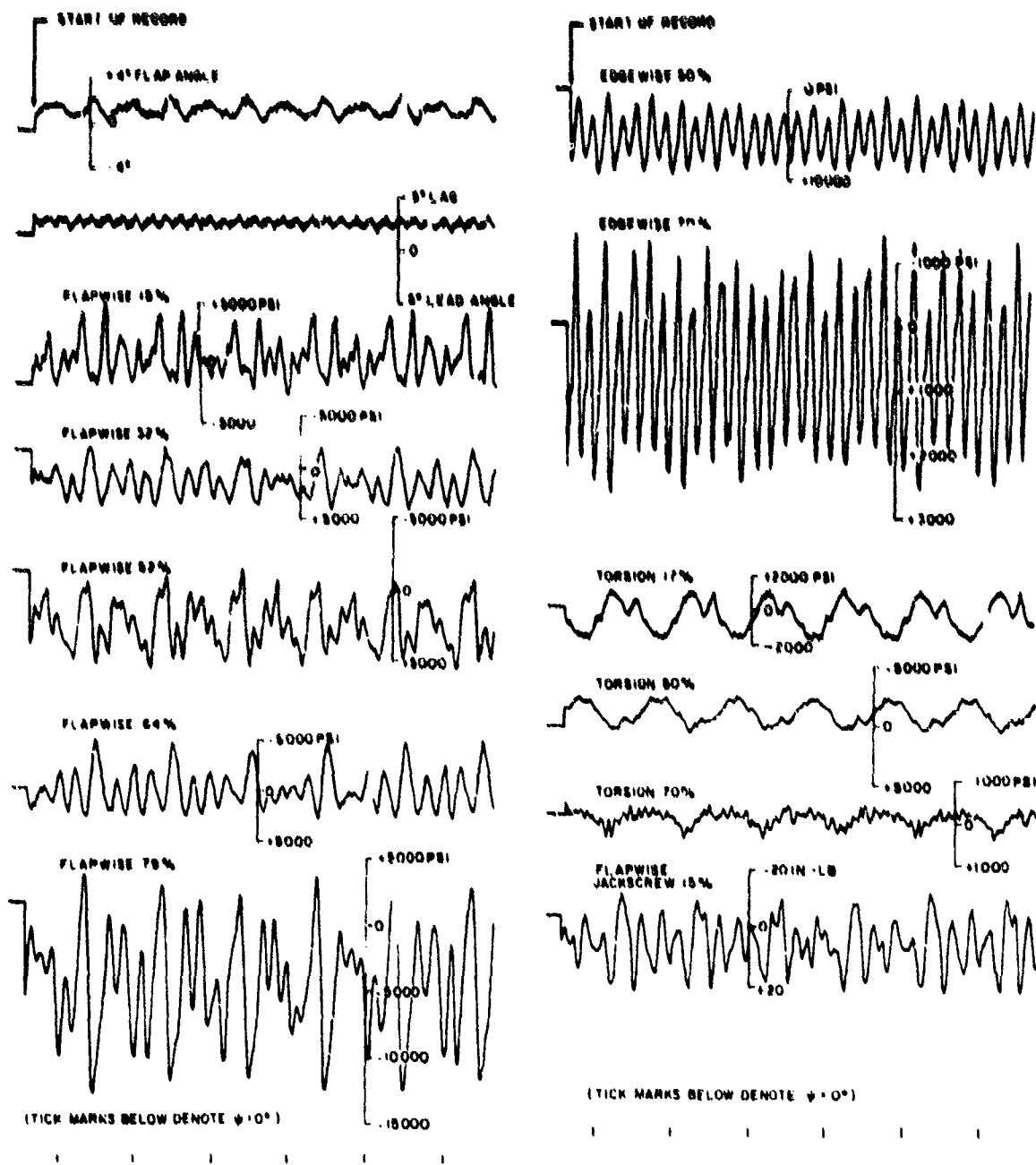


Figure 35. Measured Azimuthal Variations of Blade Stresses and Motion, Full Diameter, 1375 rpm, $\gamma = 90$ degrees, $s_s = -12^\circ$.



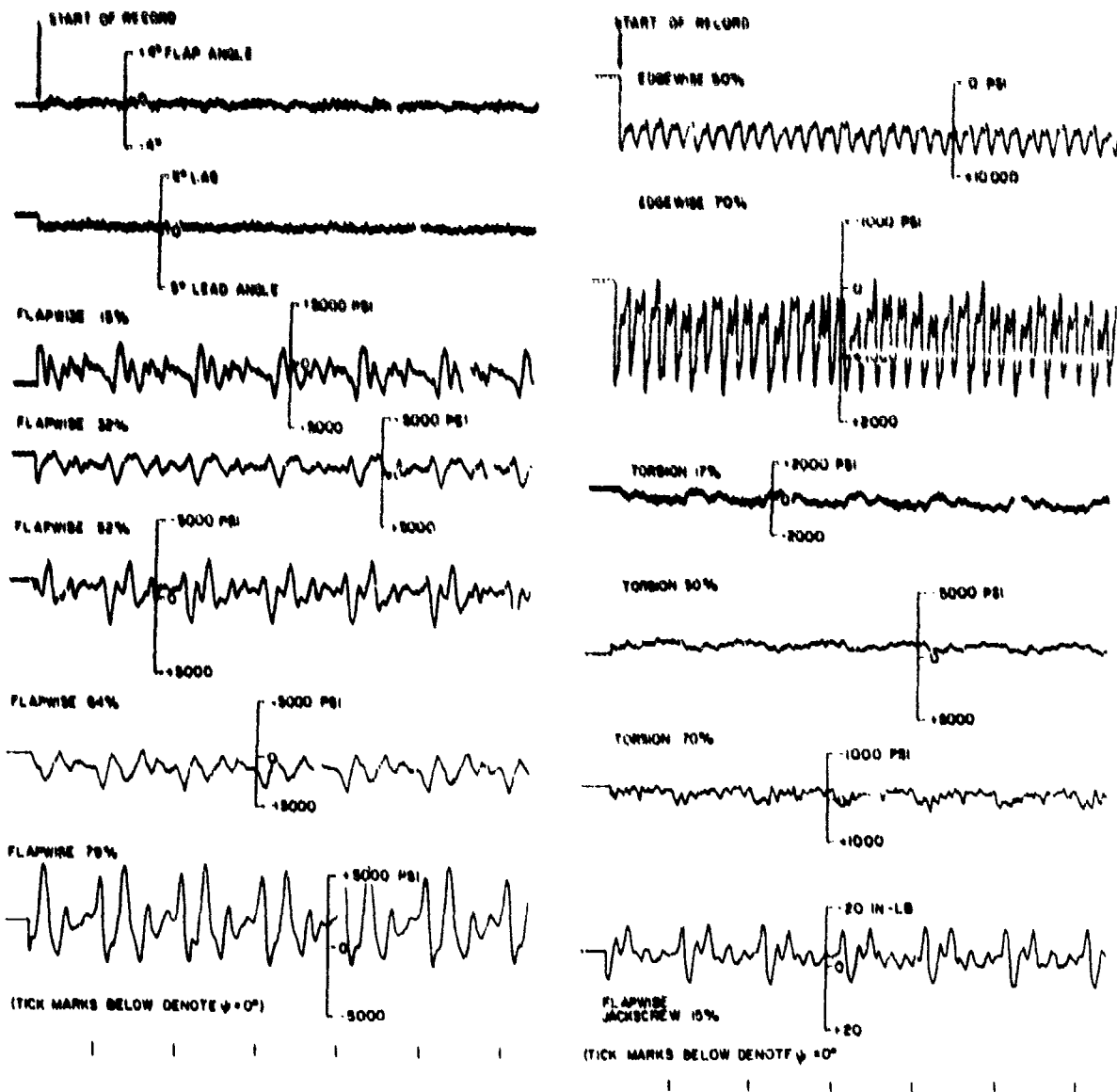
(b) $\theta_c = 6^\circ$, $\theta_{LS} = -0.8^\circ$, $\beta_{LS} = +1.7^\circ$

Figure 35. Concluded.



$$(a) \theta_c = 12^\circ, A_{ls} = -2.7^\circ, B_{ls} = +7.4^\circ$$

Figure 36. Measured Azimuthal Variation of Blade Stresses and Motion, Full Diameter, 1375 rpm, $V = 150$ Knots, $\alpha_s = -8^\circ$.



$$(b) \quad \theta_c = 4^\circ, A_{1s} = -0.8^\circ, B_{1s} = +1.2^\circ$$

Figure 36. Concluded.

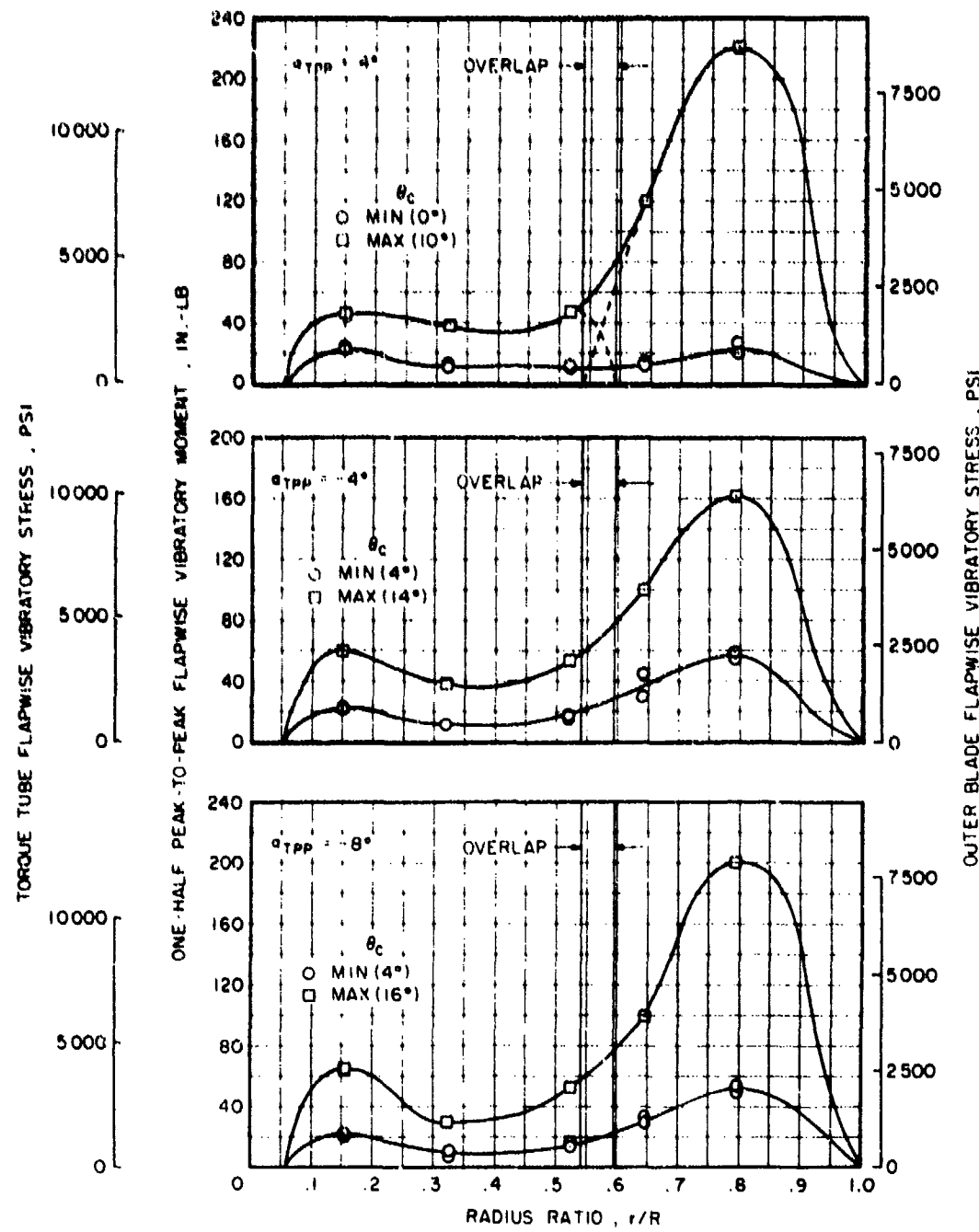


Figure 37. Flapwise Vibratory Stress Distributions, Full Diameter, 1375 rpm, $V = 60$ Knots.

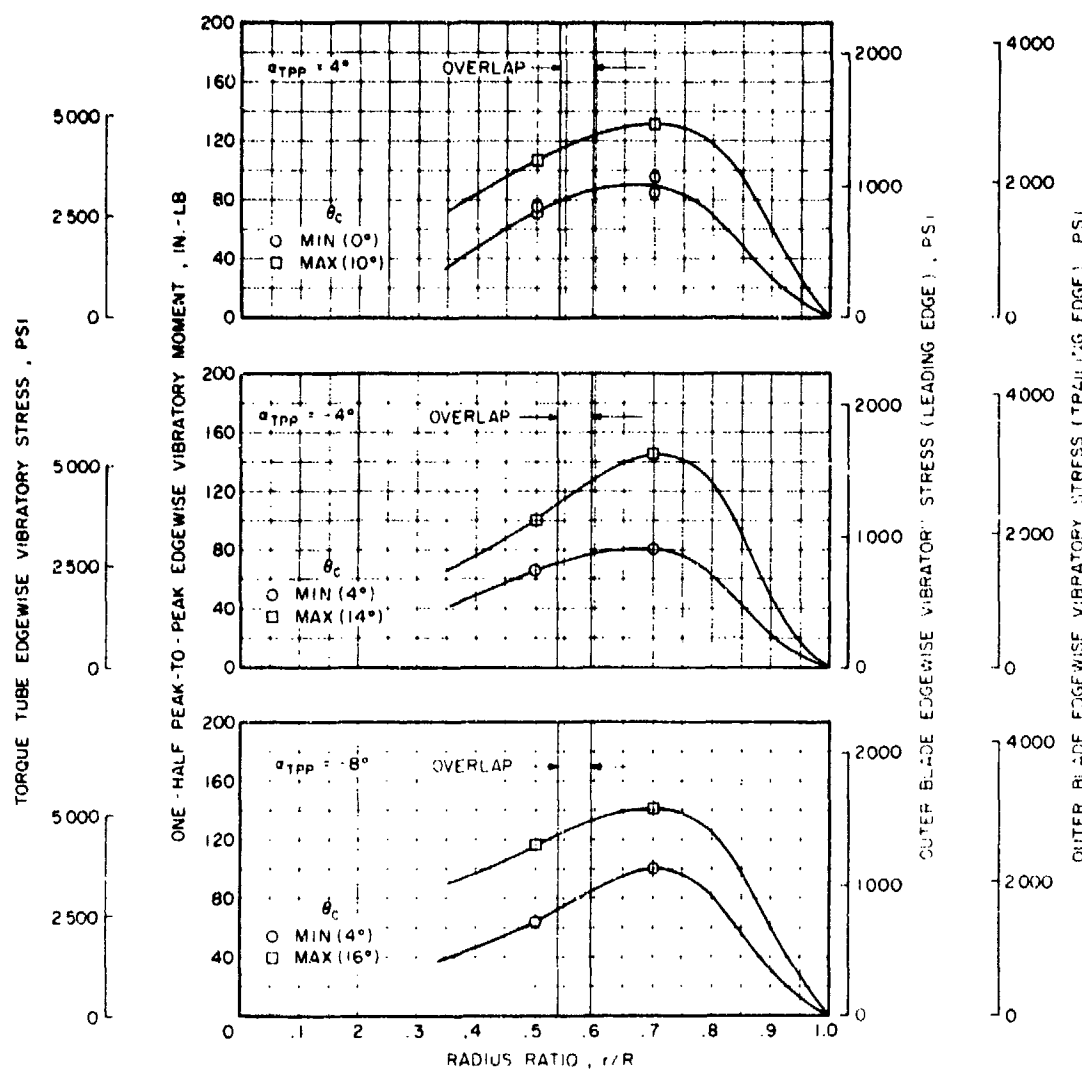


Figure 38. Edgewise Vibratory Stress Distributions, Full Diameter, 1375 rpm, $V = 60$ Knots.

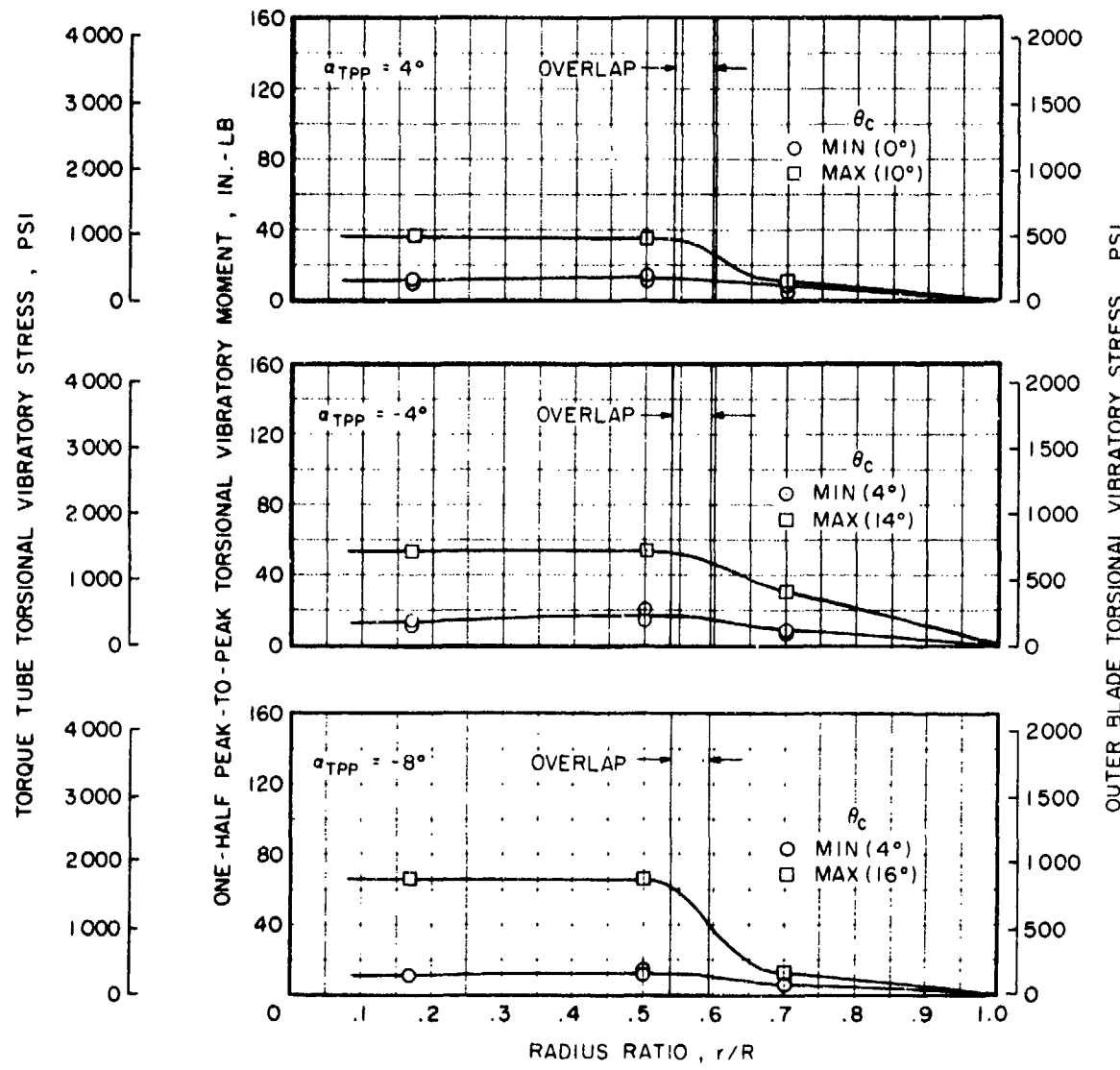


Figure 39. Torsional Vibratory Stress Distributions, Full Diameter, 1375 rpm, $V = 60$ Knots.

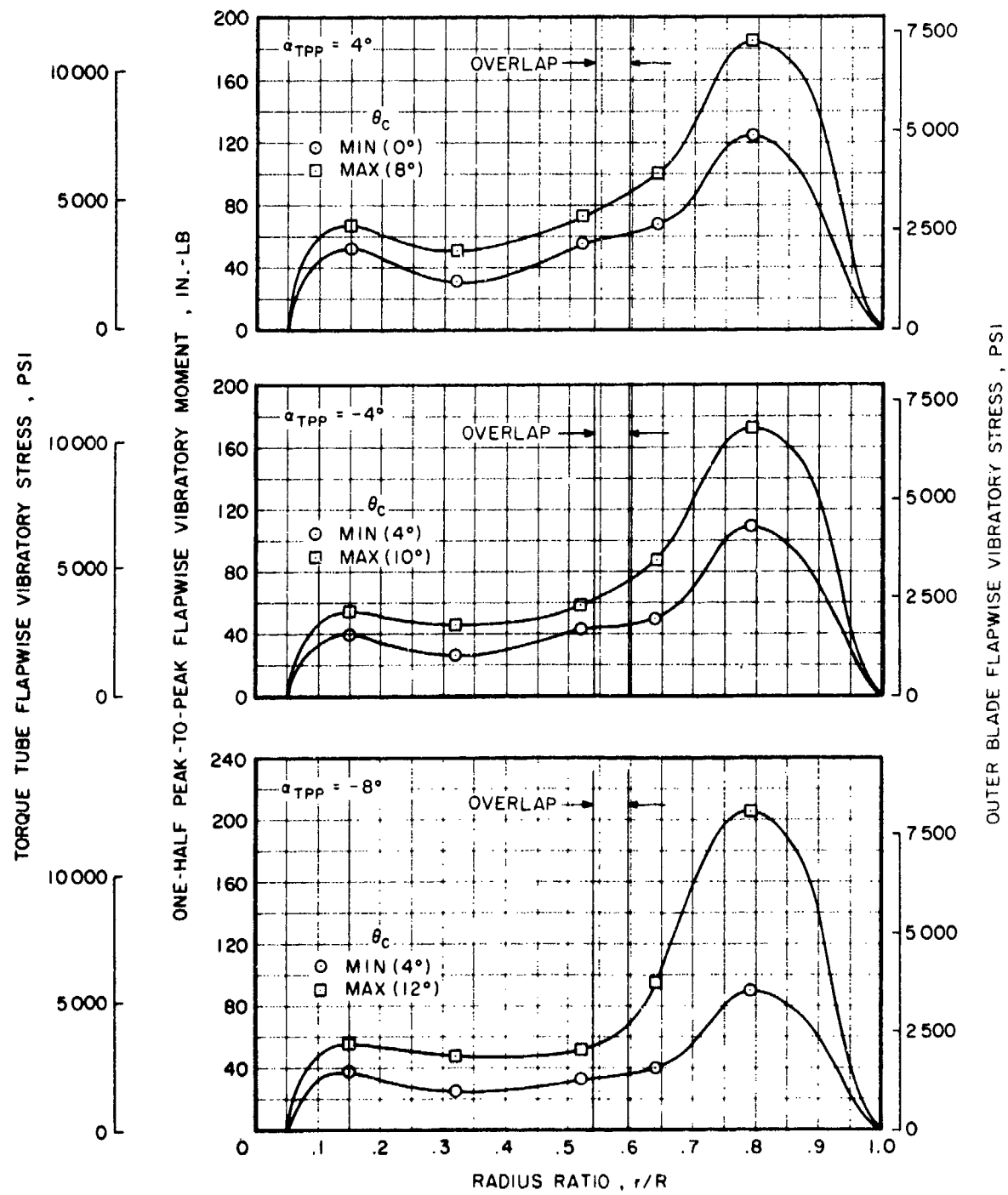


Figure 40. Flapwise Vibratory Stress Distributions, Full Diameter, 1375 rpm, $V = 150$ Knots.

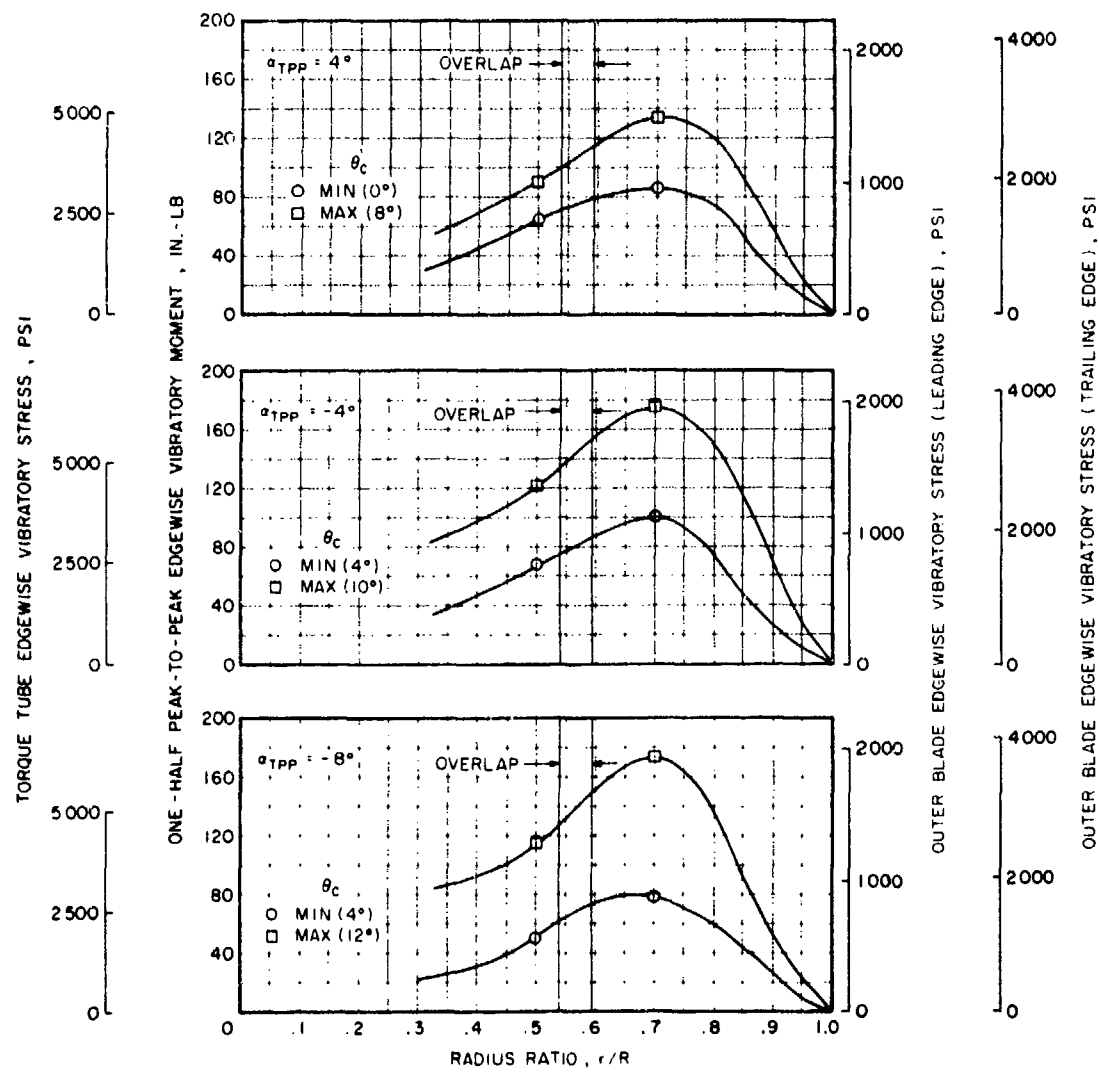


Figure 41. Edgewise Vibratory Stress Distributions, Full Diameter, 1375 rpm, $V = 150$ Knots.

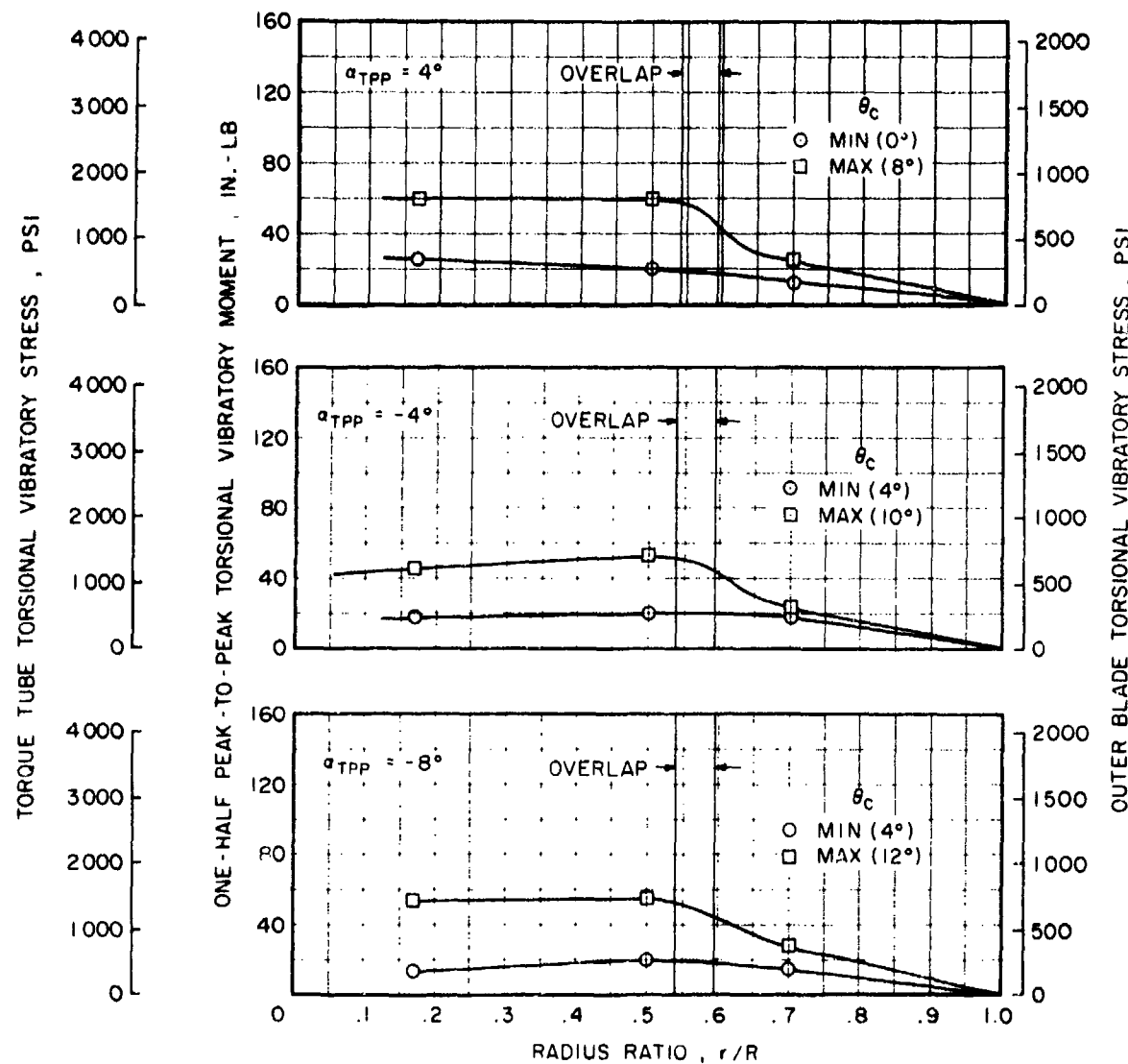


Figure 42. Torsional Vibratory Stress Distributions,
Full Diameter, 1375 rpm, $V = 150$ Knots.

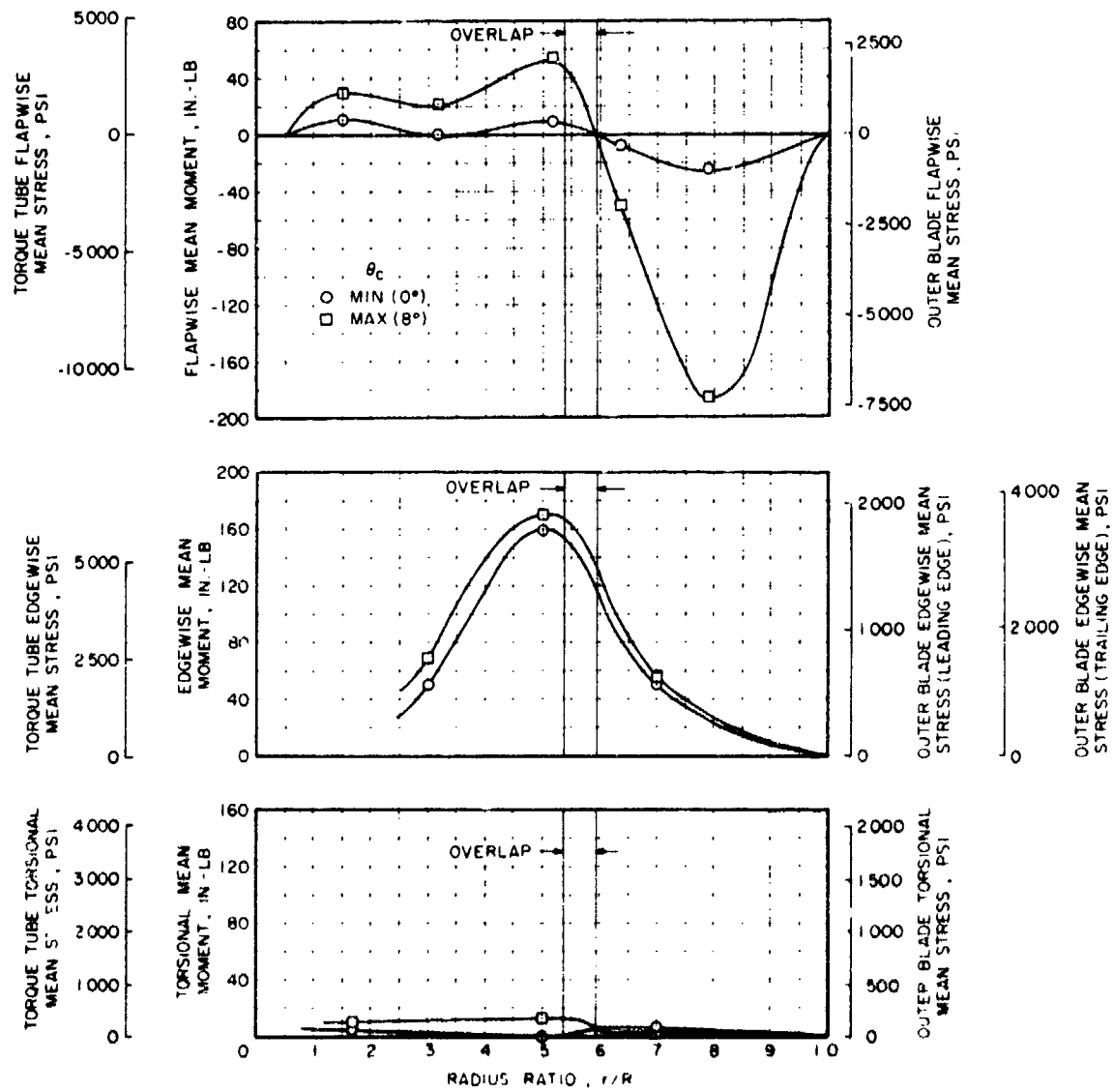


Figure 43. Mean Blade Stress Distributions, Full Diameter, 1375 rpm, $V = 150$ Knots, $\alpha_s = 4^\circ$.

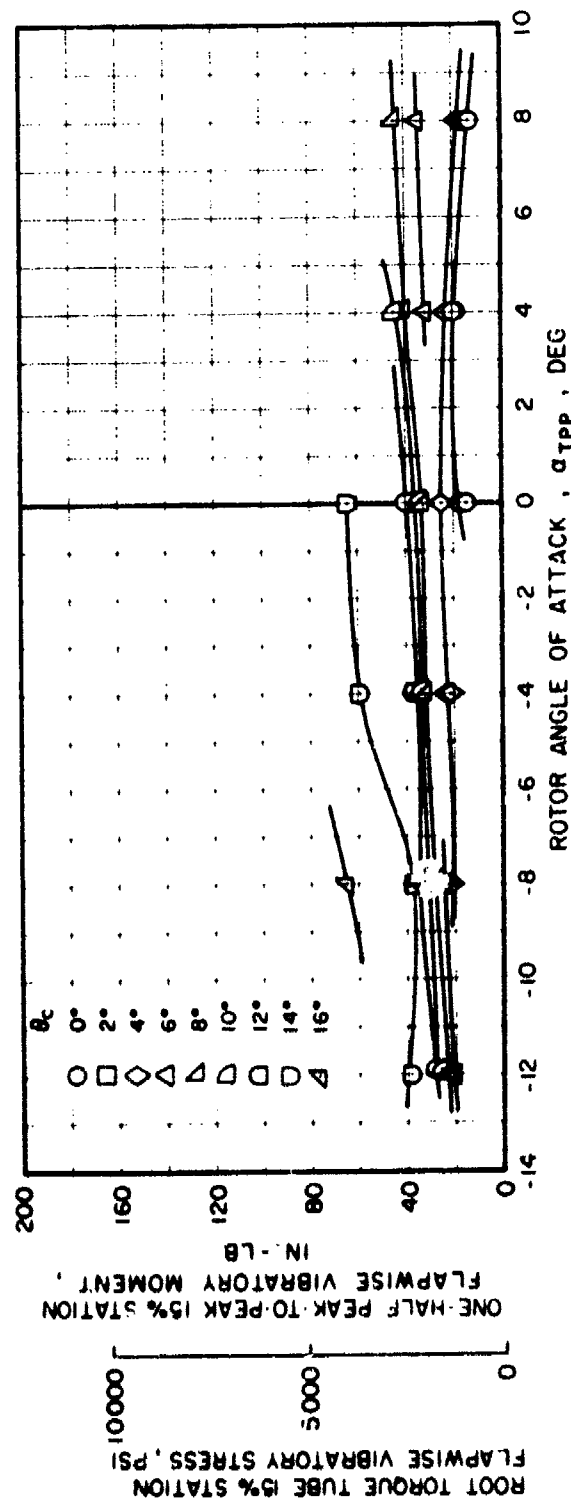


Figure 44. Effect of Rotor Operation Conditions on Root Flapwise Vibratory Stress, Full Diameter, 1375 rpm, $V = 60$ Knots.

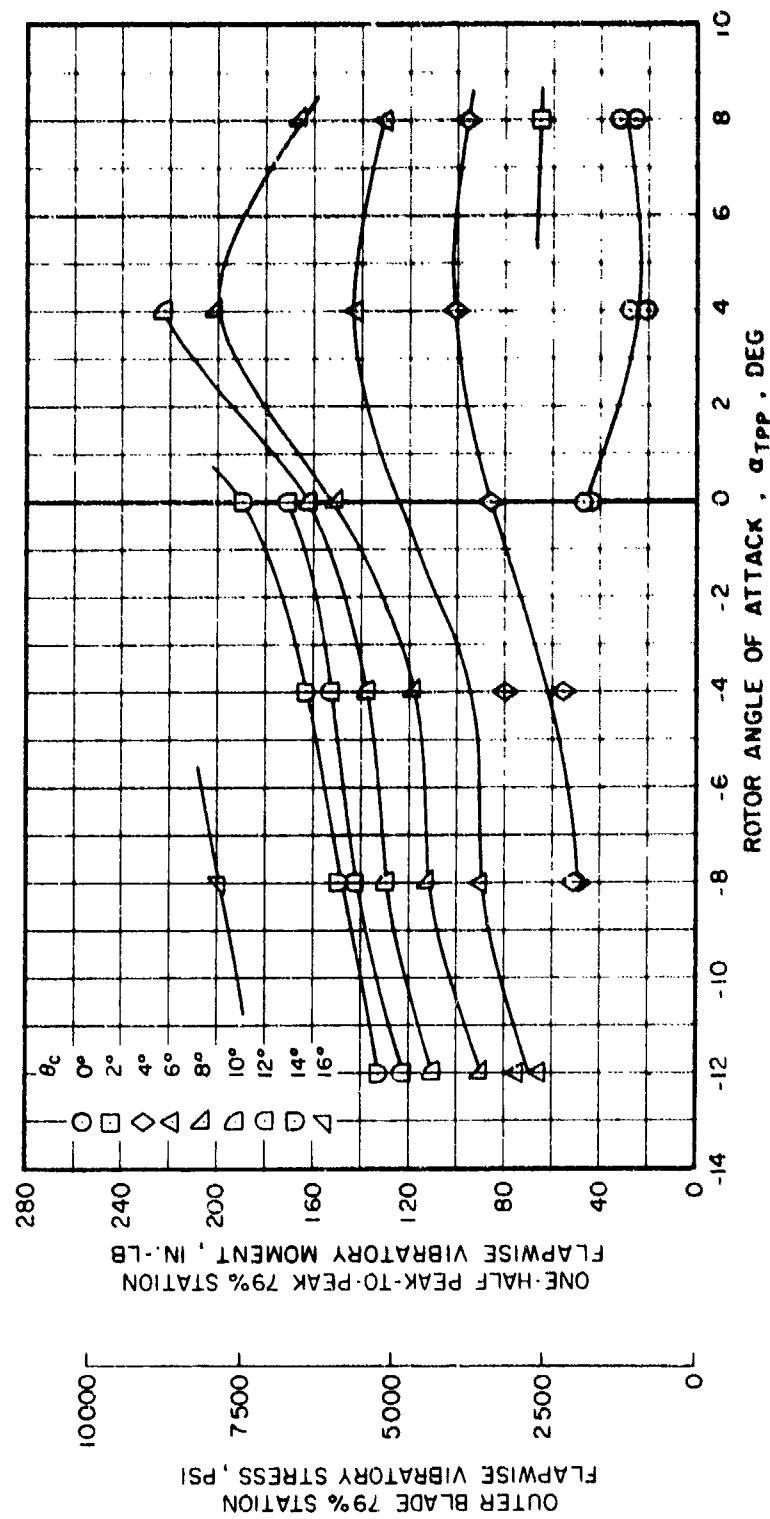


Figure 45. Effect of Rotor Operating Conditions on Outer Blade Flapwise Vibratory Stress. Full Diameter, 1375 rpm, $V = 60$ Knots.

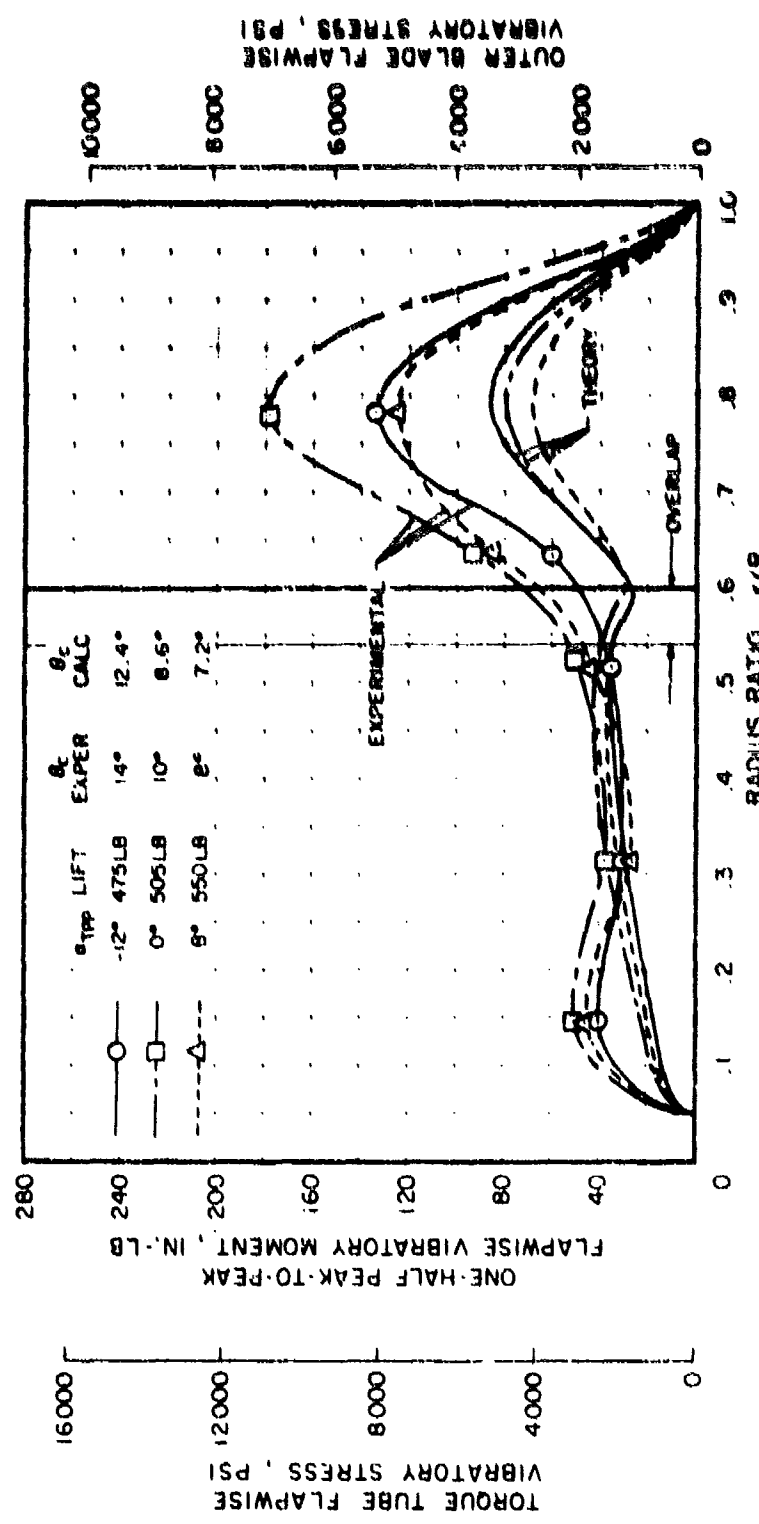


Figure 46. Flapwise Vibratory Blade Stress - Correlation With Theory.
Full Diameter, 1375 rpm, $\gamma = 90$ Knots.

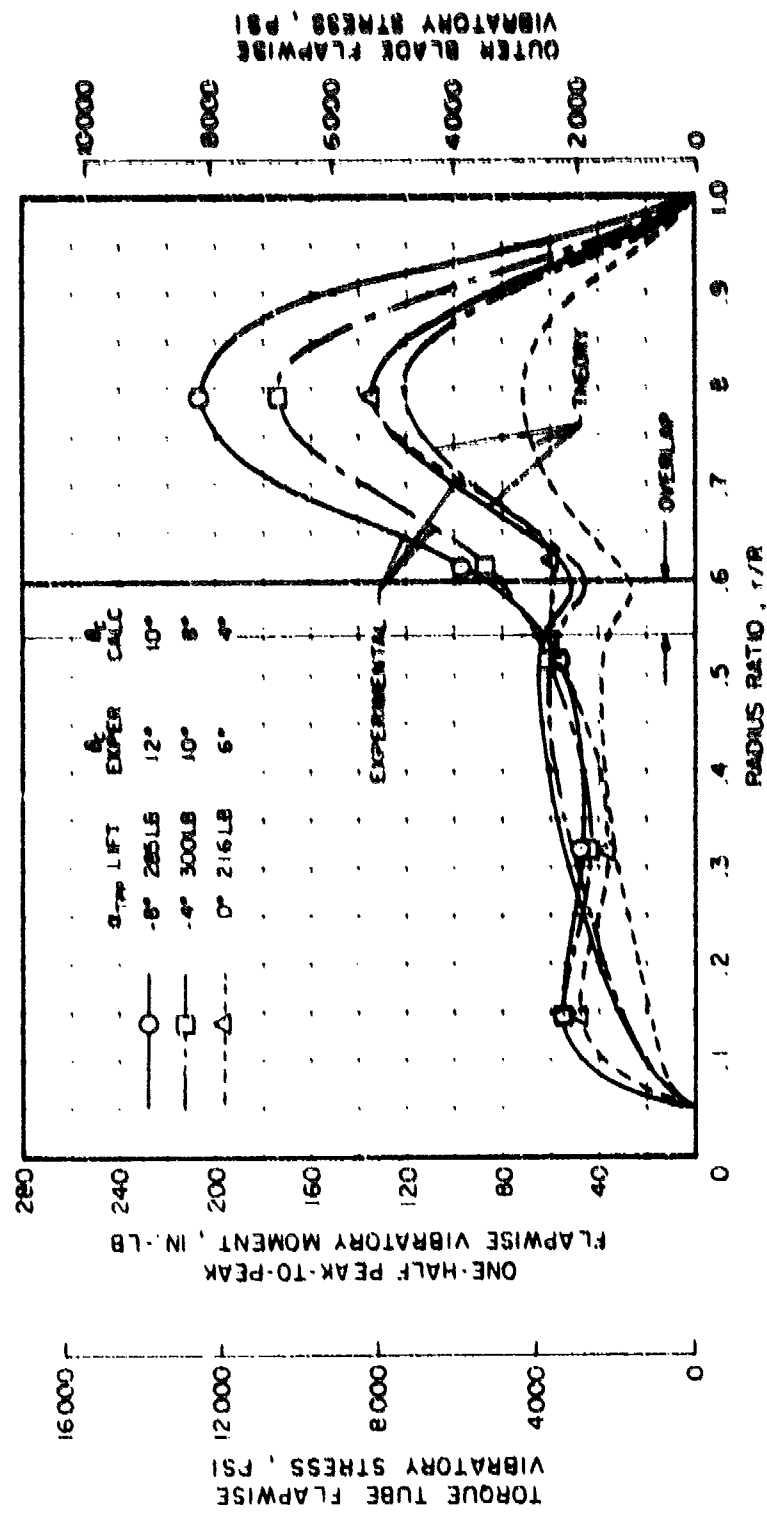


Figure 47. Flapwise Vibratory Blade Stress - Correlations with Theory.
 Full Diameter, 1375 rpm, $V = 150$ Knots.

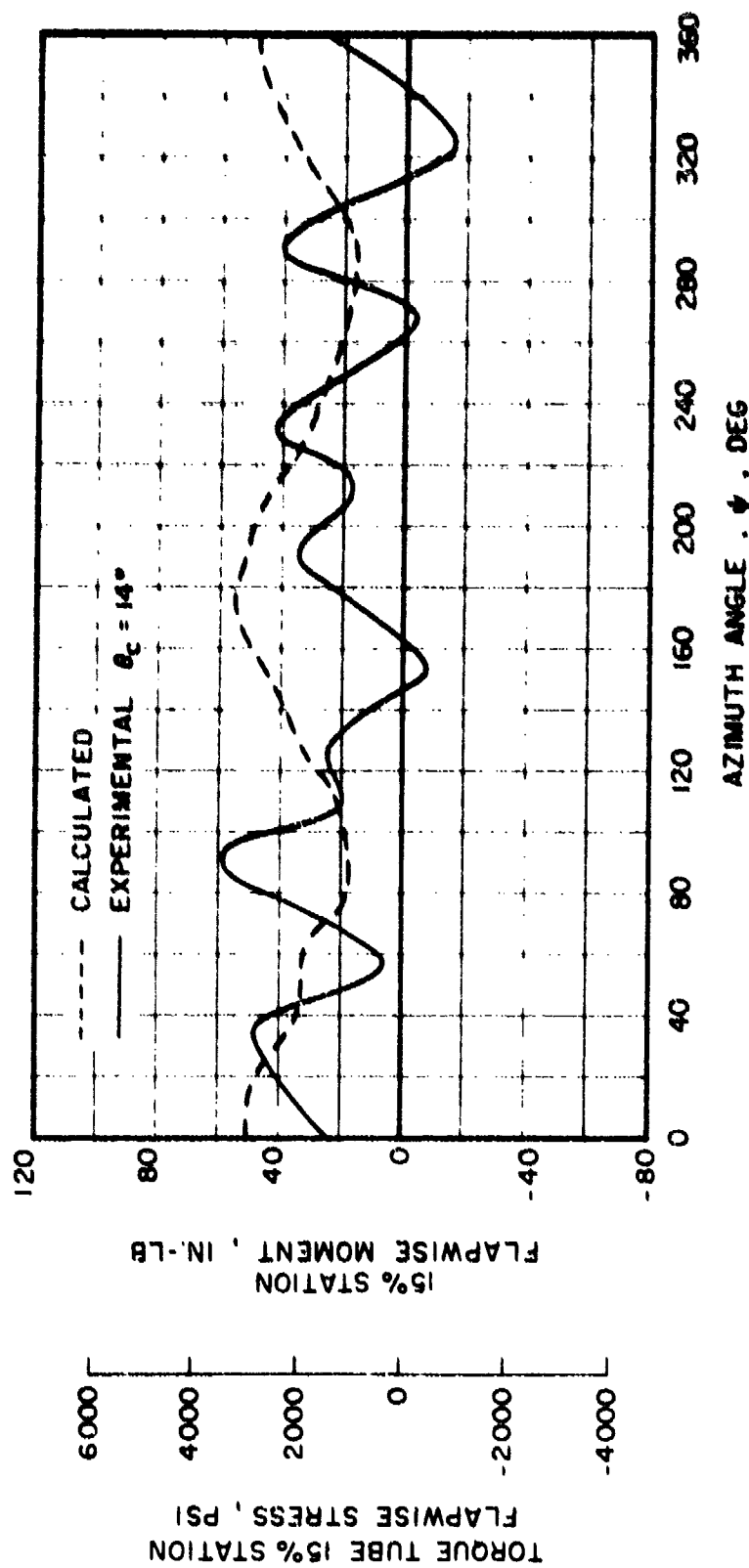


Figure 48. Azimuthal Variation of Root Flapwise Stress - Correlation With Theory, Full Diameter, 1375 rpm, $V = 90$ Knots, $\alpha_s = -12^\circ$.

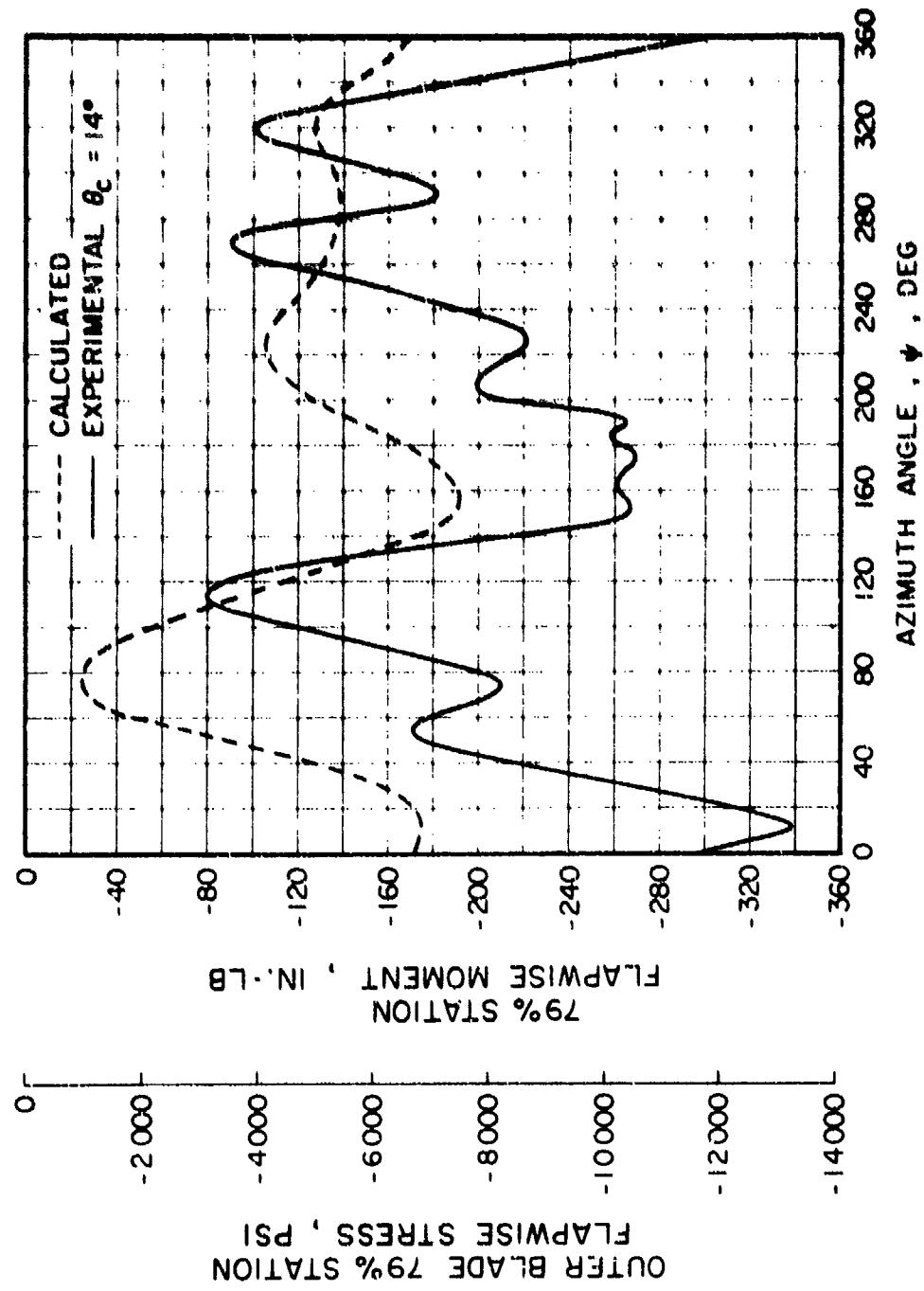


Figure 49. Azimuthal Variation of Outer Blade Flapwise Stress - Correlation With Theory, Full Diameter, 1375 rpm, $V = 90$ fpm, $a_s = -12^\circ$.

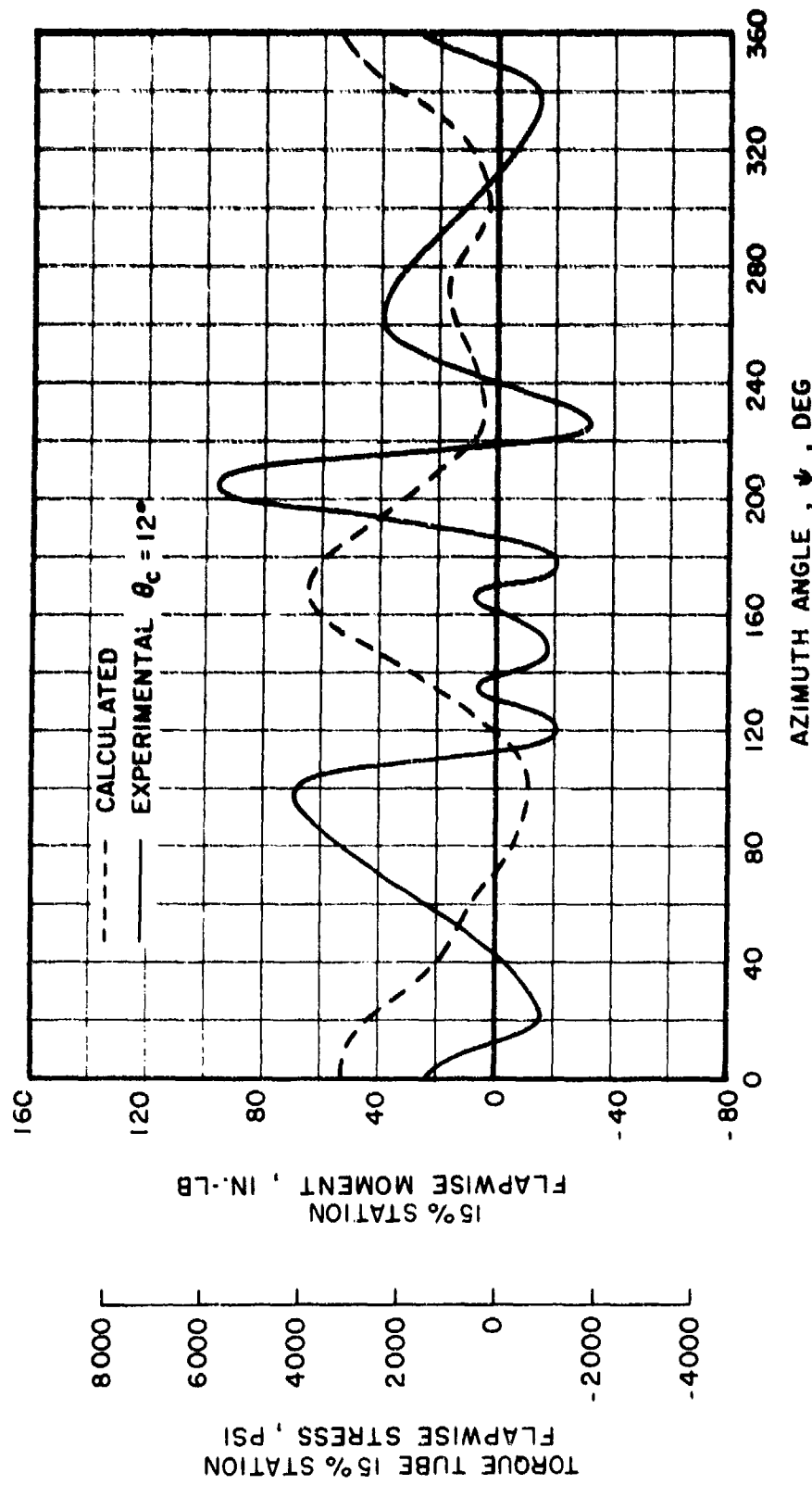


Figure 50. Azimuthal Variation of Root Flapwise Stress - Correlation With Theory, Full Diameter, 1375 rpm, $V = 150$ Knots, $\alpha_s = -8^\circ$.

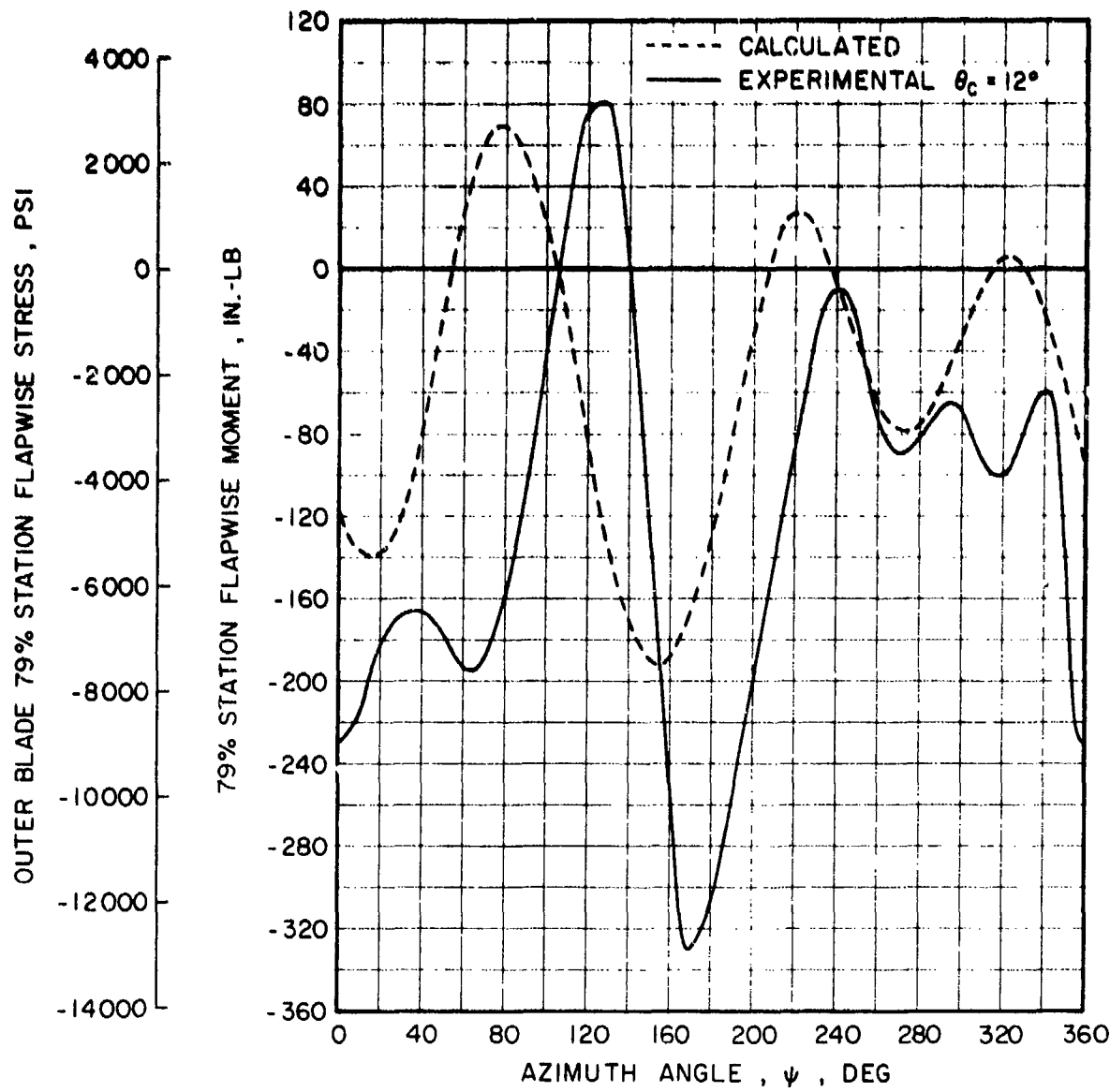


Figure 51. Azimuthal Variation of Outer Blade Flapwise Stress - Correlation With Theory, Full Diameter, 1375 rpm, $V = 150$ Knots, $\alpha_s = -8^\circ$.

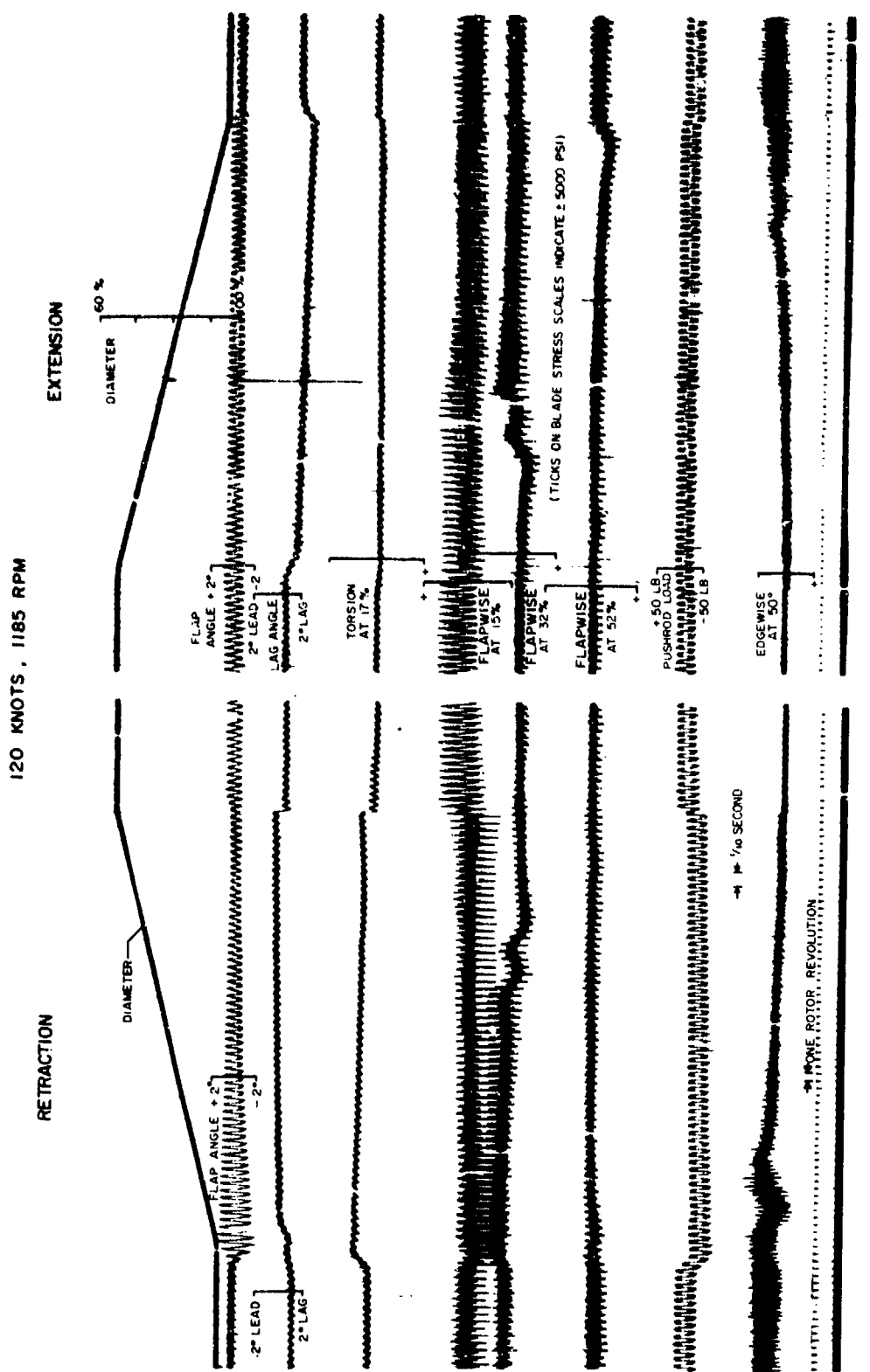


Figure 52. Diameter Change Time History, 1185 rpm, $V = 120$ Knots,
 $\alpha_s = 0^\circ$, $\theta_c = 0^\circ$.

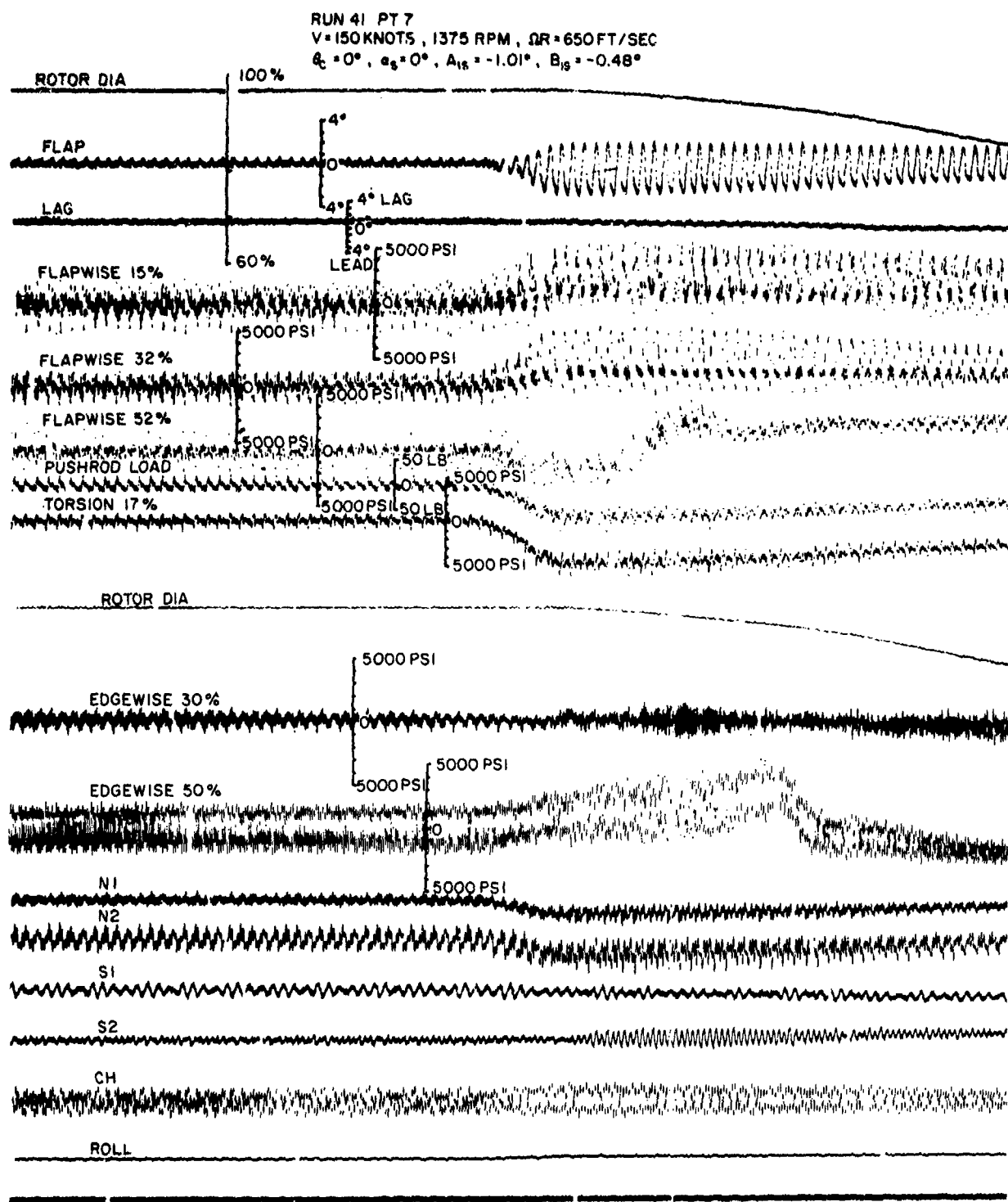
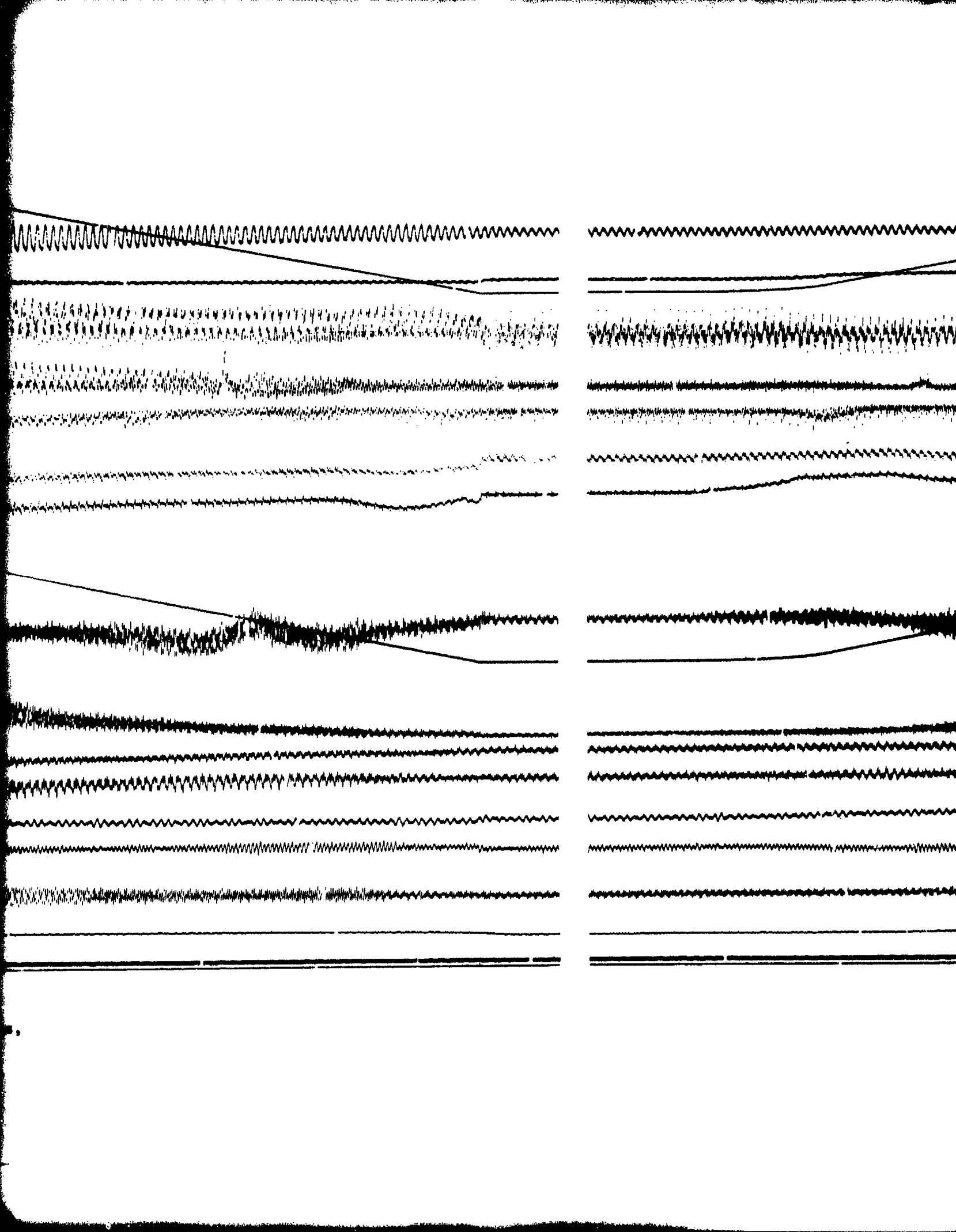
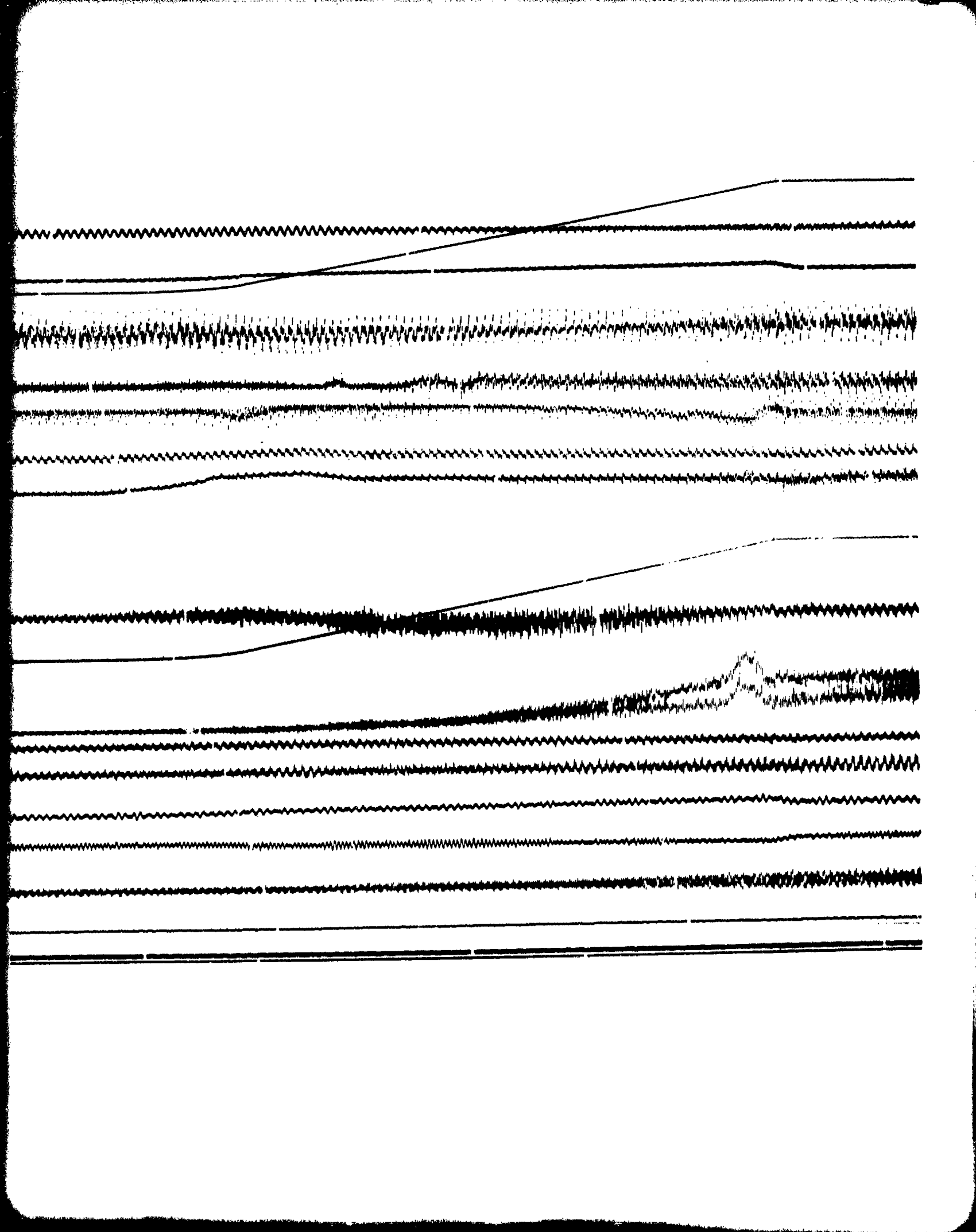


Figure 53. Diameter Change Time History, 1375 rpm, $V = 150$ Knots,
 $\alpha_s = 0^\circ$, $\theta_c = 0^\circ$.





RUN 43 PT 9
 $V = 150$ KNOTS, 1375 RPM, $\Omega R = 650$ FT/SEC
 $\theta_c = 0^\circ$, $\alpha_s = 2^\circ$, $A_{1s} = -0.96^\circ$, $B_{1s} = -0.80^\circ$

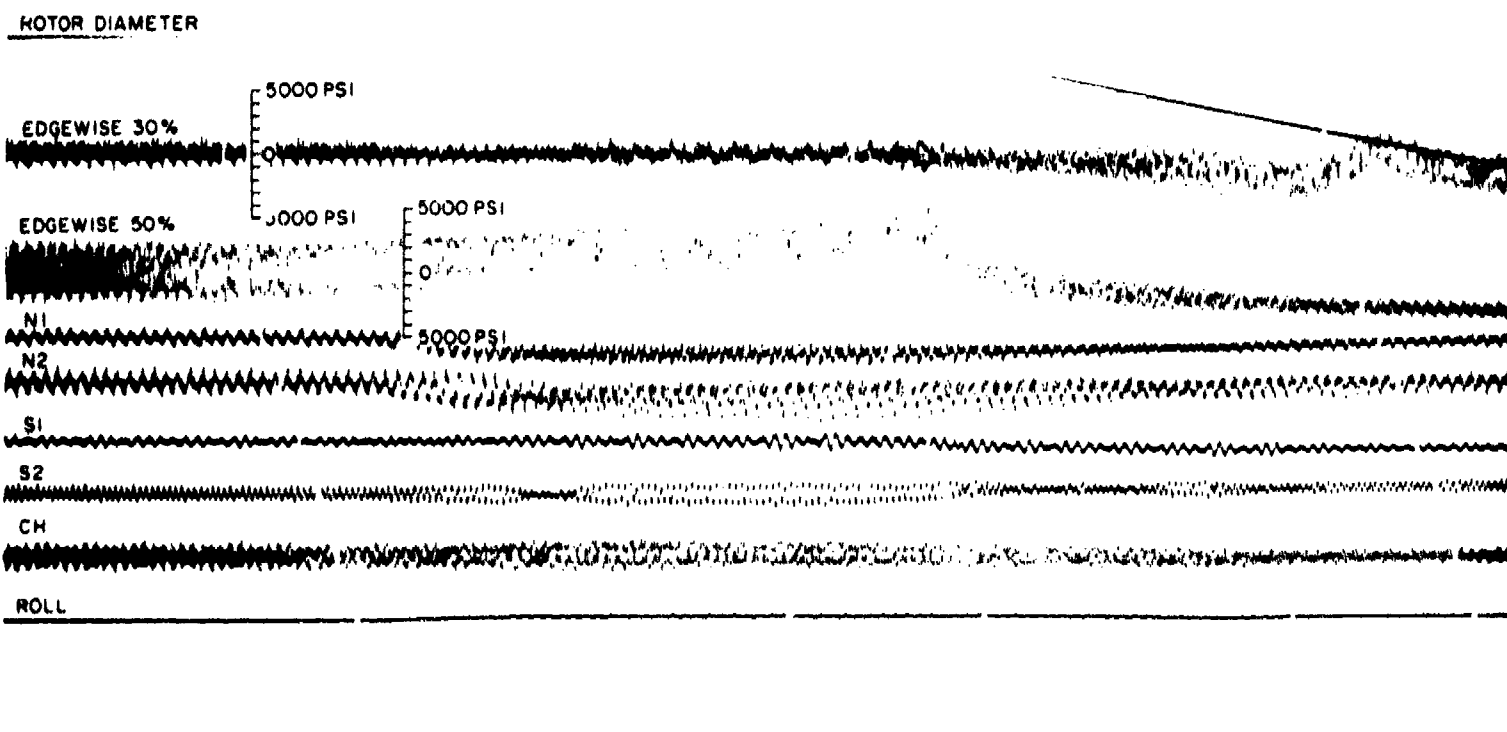
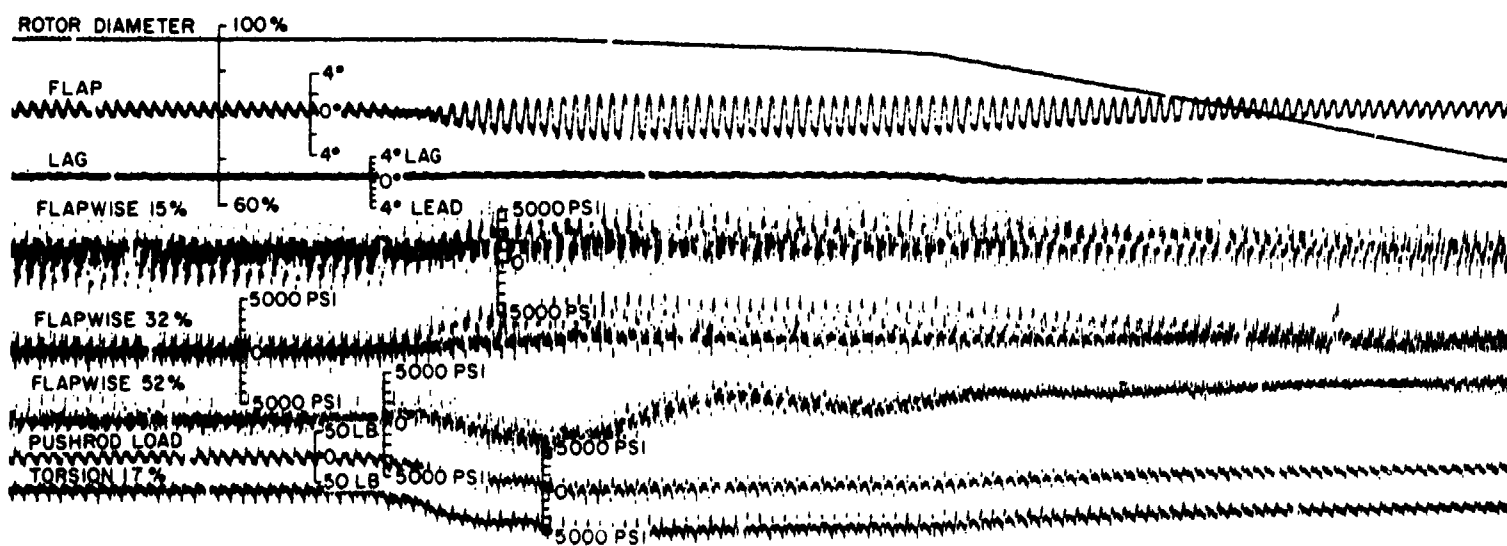
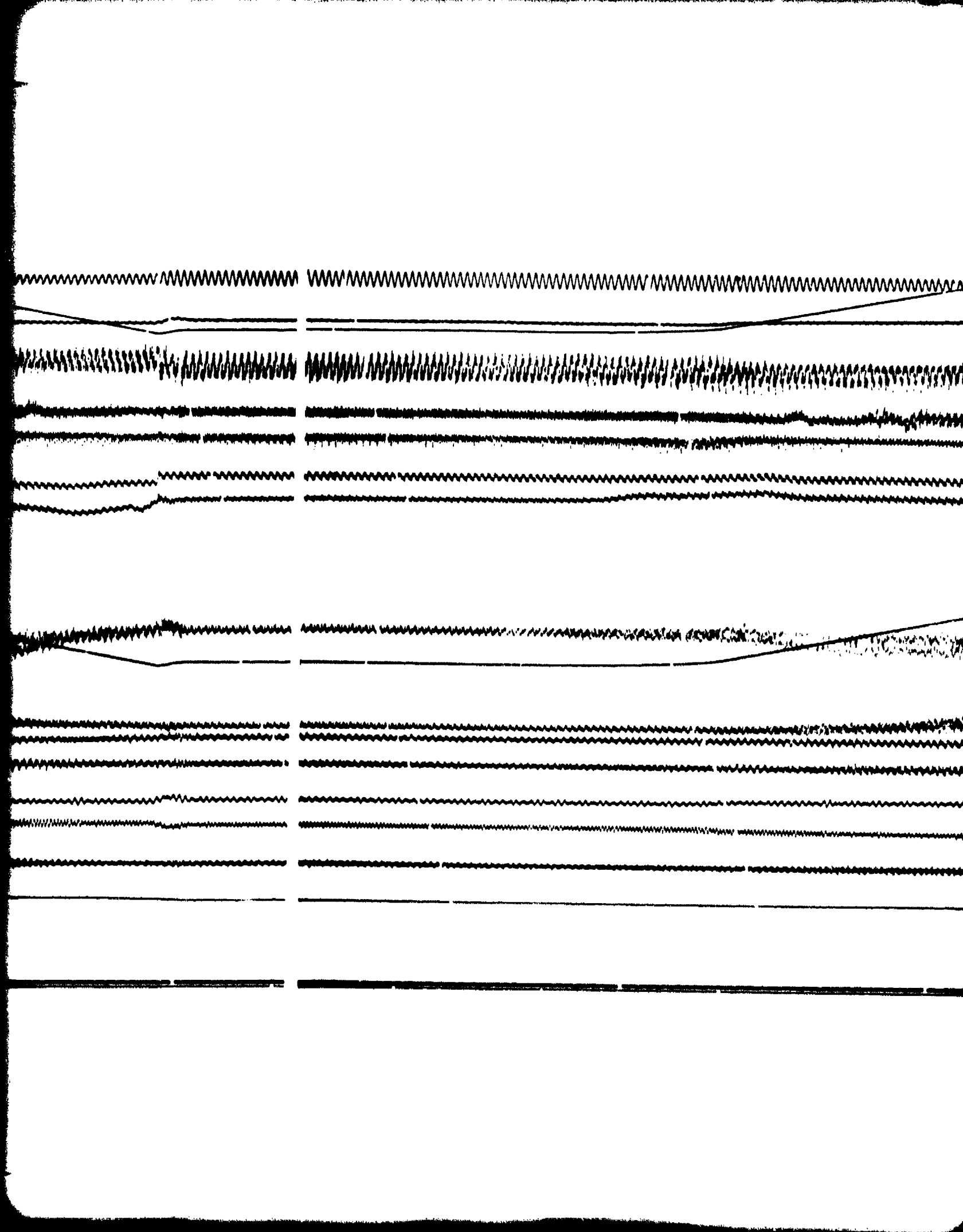
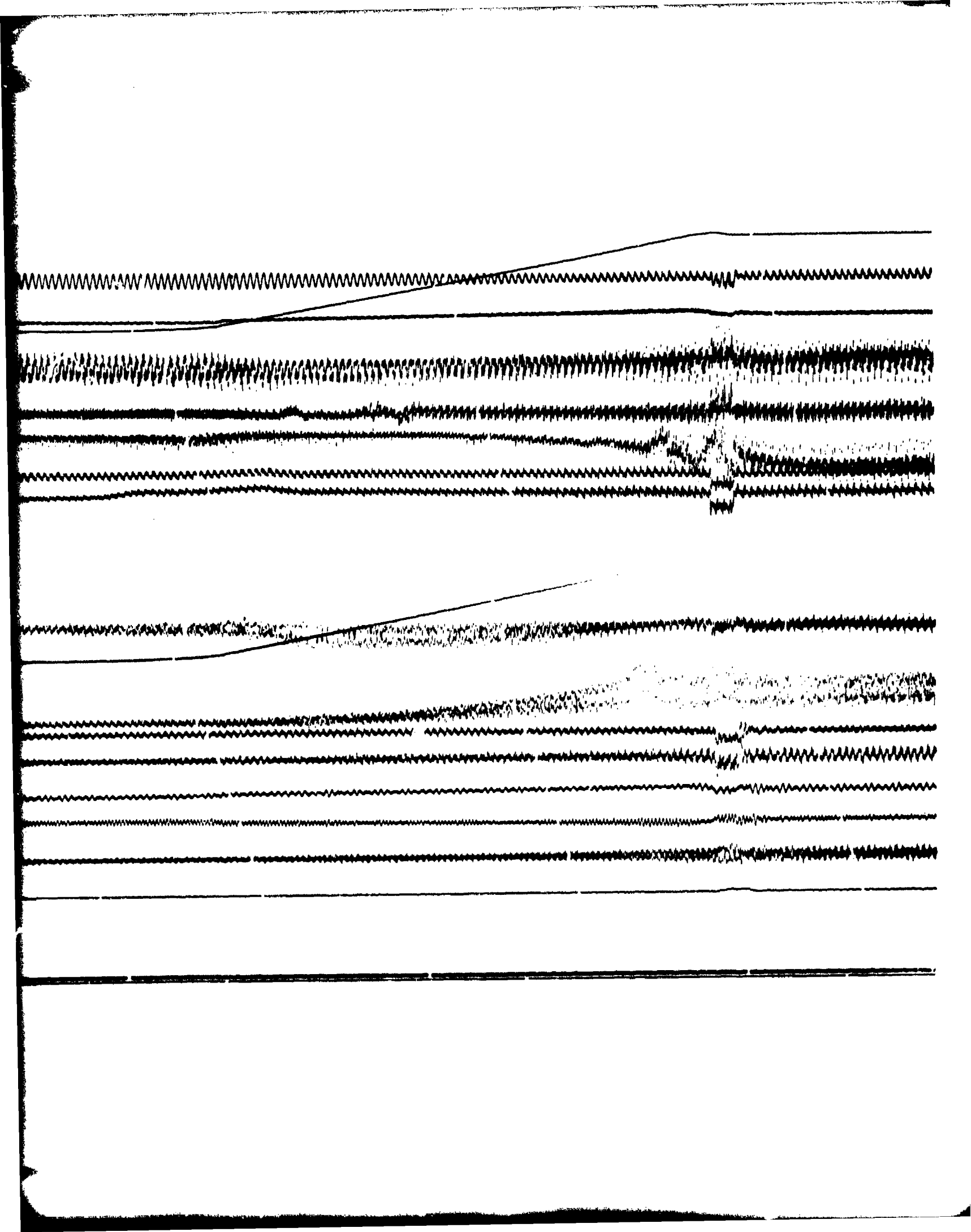


Figure 54. Diameter Change Time History, 1375 rpm, $V = 150$ Knots,
Gust Condition, $\alpha_s = 2^\circ$, $\theta_c = 0^\circ$.





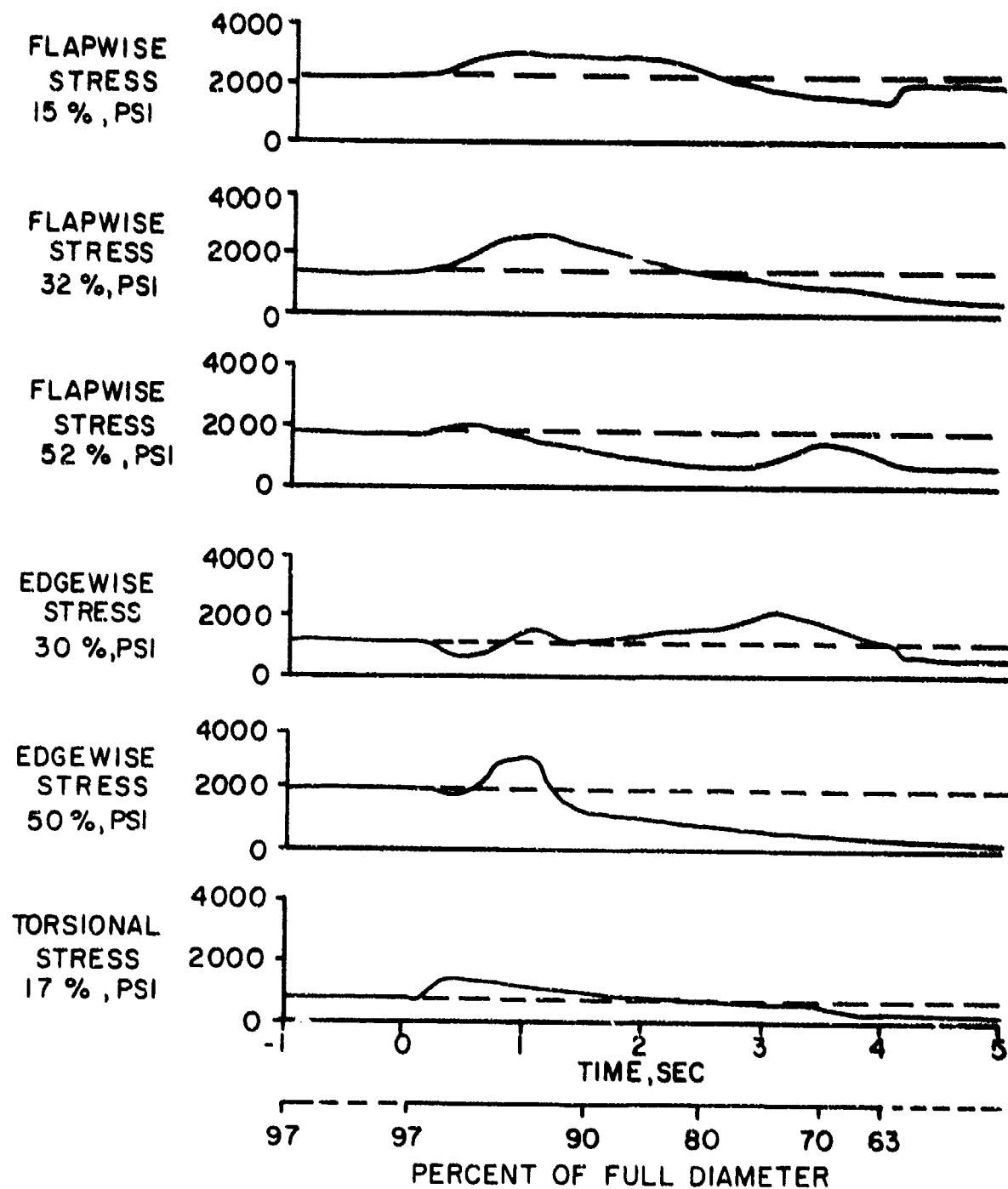
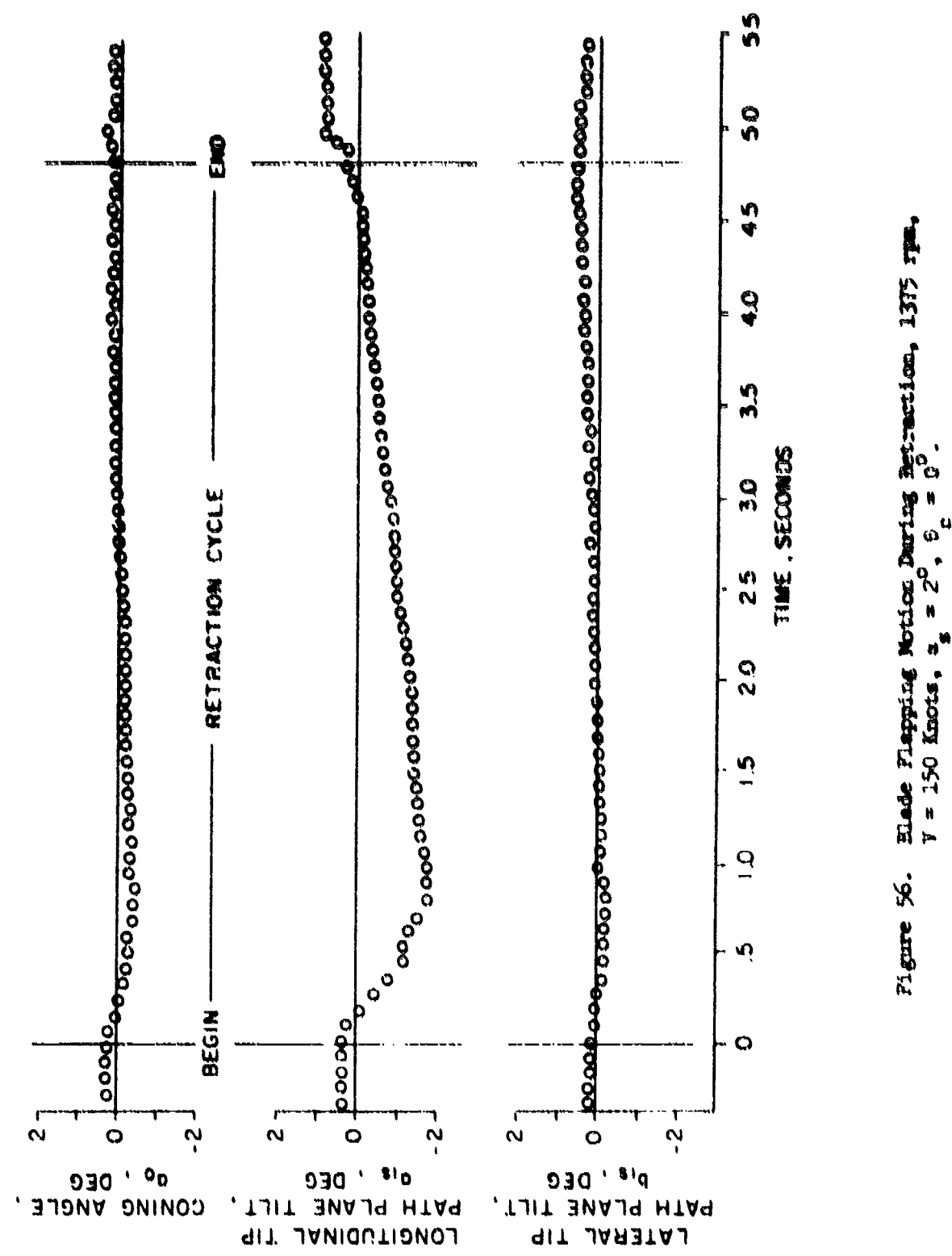


Figure 55. Blade Vibratory Stresses During Retraction,
 1375 rpm , $V = 150 \text{ Knots}$, $\alpha_g = 0^\circ$, $\theta_c = 0^\circ$.



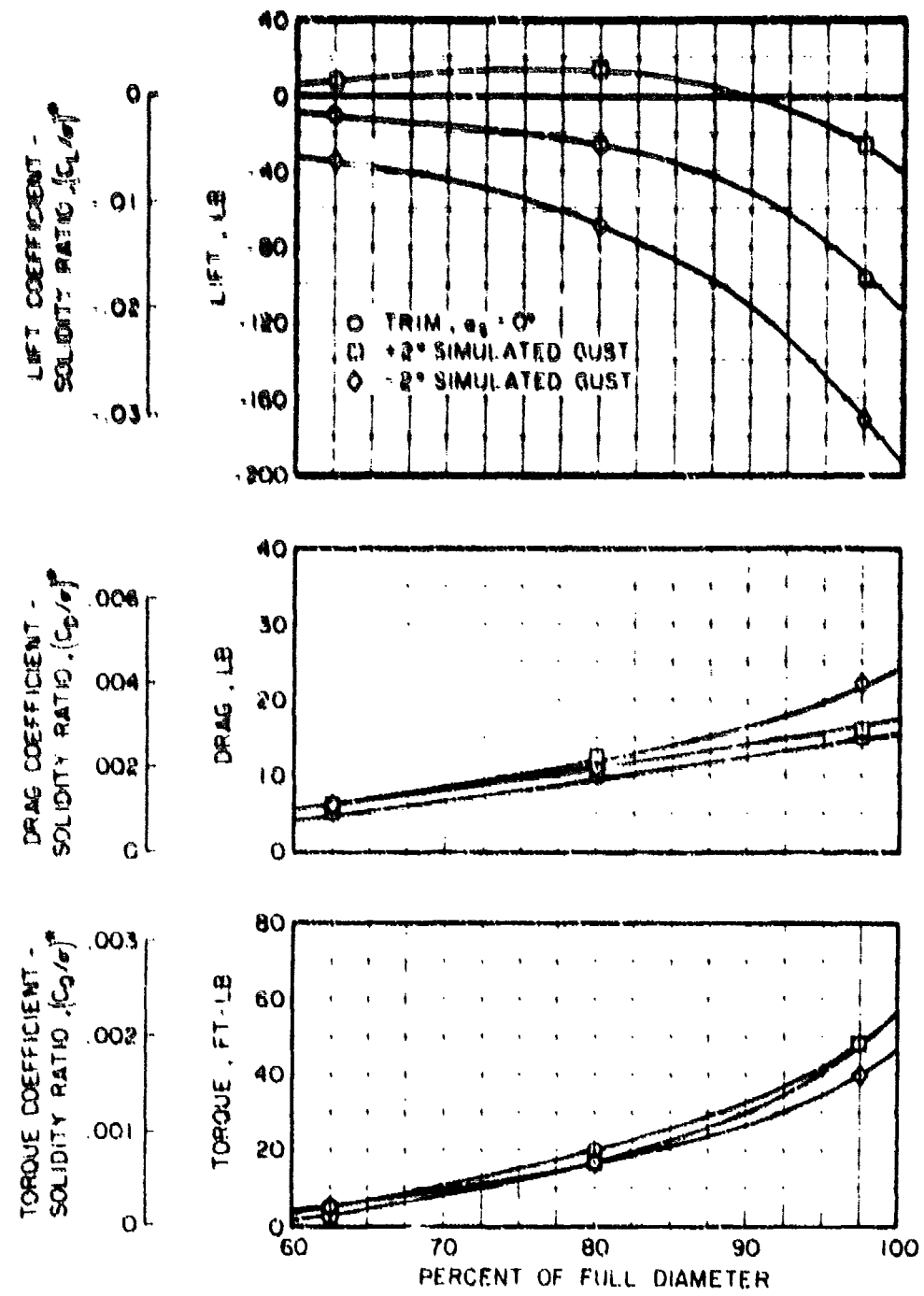


Figure 57. Influence of Rotor Diameter on Performance Parameters,
1375 rpm, $V = 150$ Knots, $\theta_c = 0^\circ$.

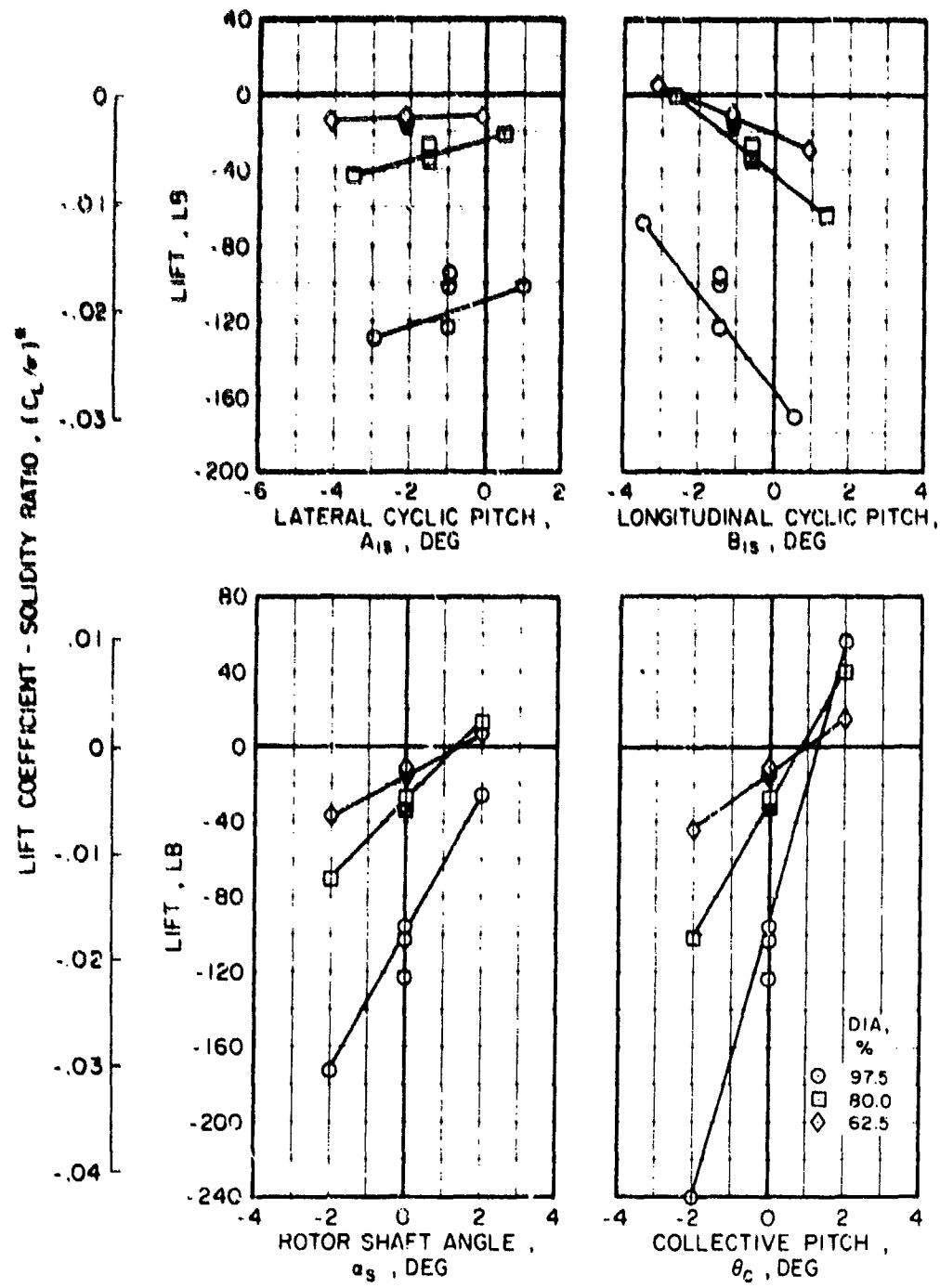


Figure 58. Variation of Rotor Lift With Incremental Angular Inputs, 1375 rpm, $V = 150$ Knots.

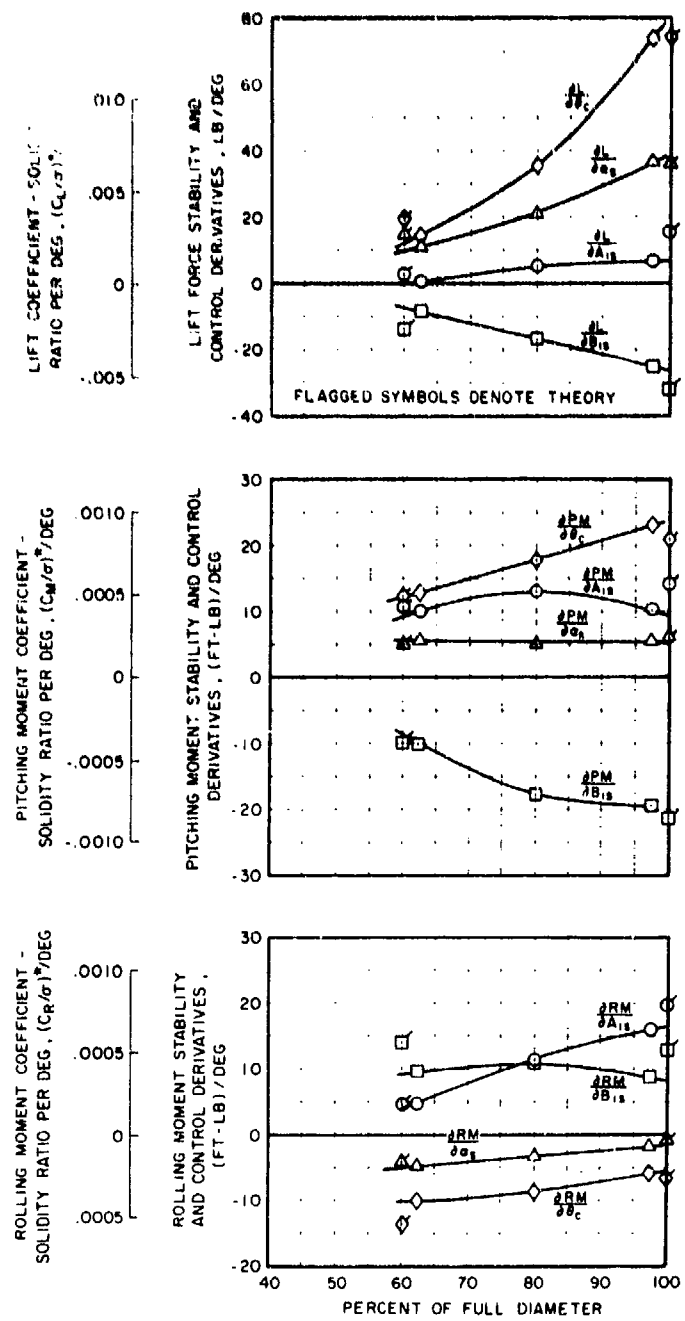


Figure 59. Influence of Rotor Diameter on Stability and Control Derivatives, 1375 rpm, $V = 150$ Knots.

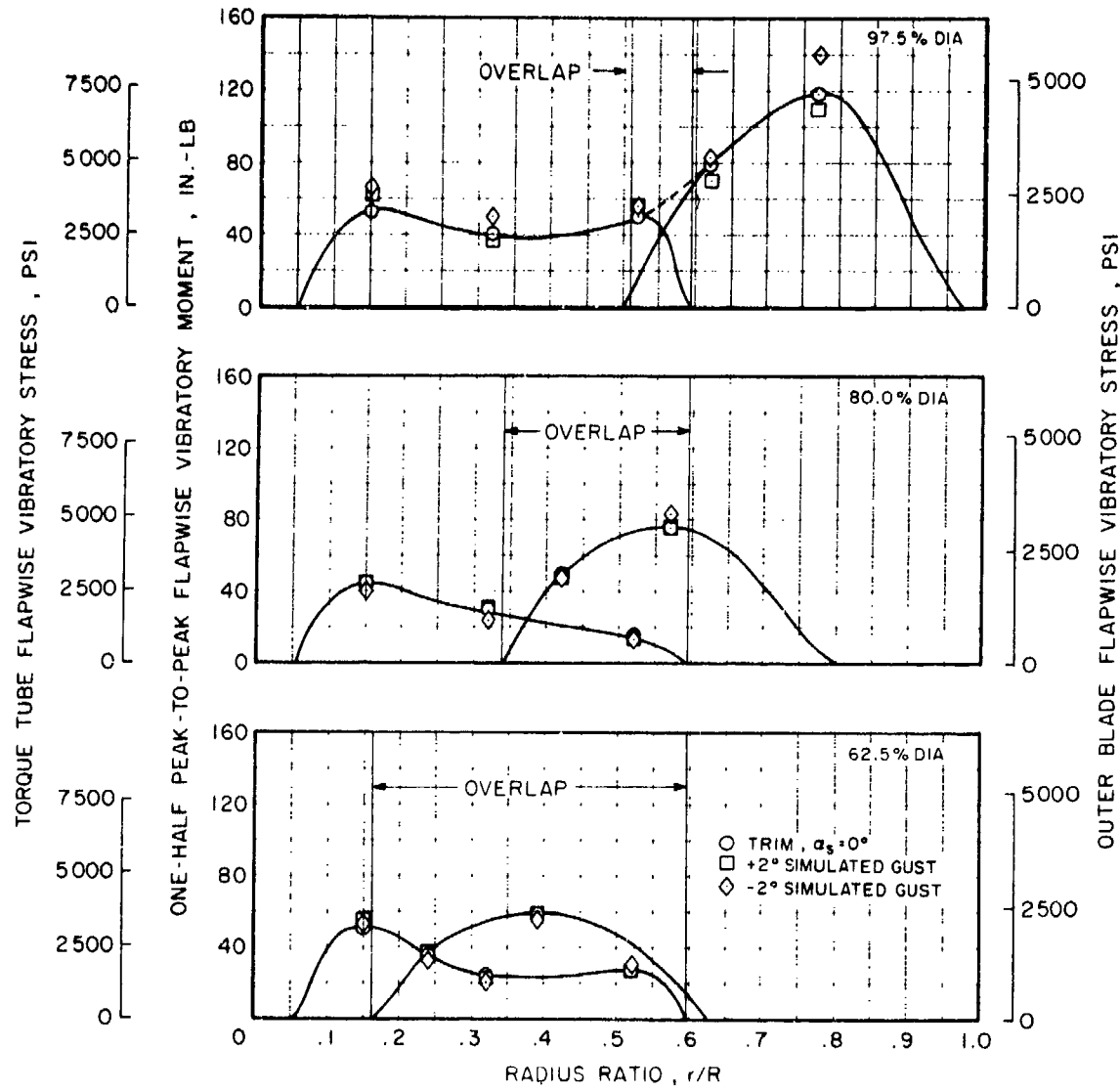


Figure 60. Effect of Diameter and Simulated Gust on Flapwise Stress Distributions, 1375 rpm, $V = 150$ Knots, $\theta_c = 0^\circ$.

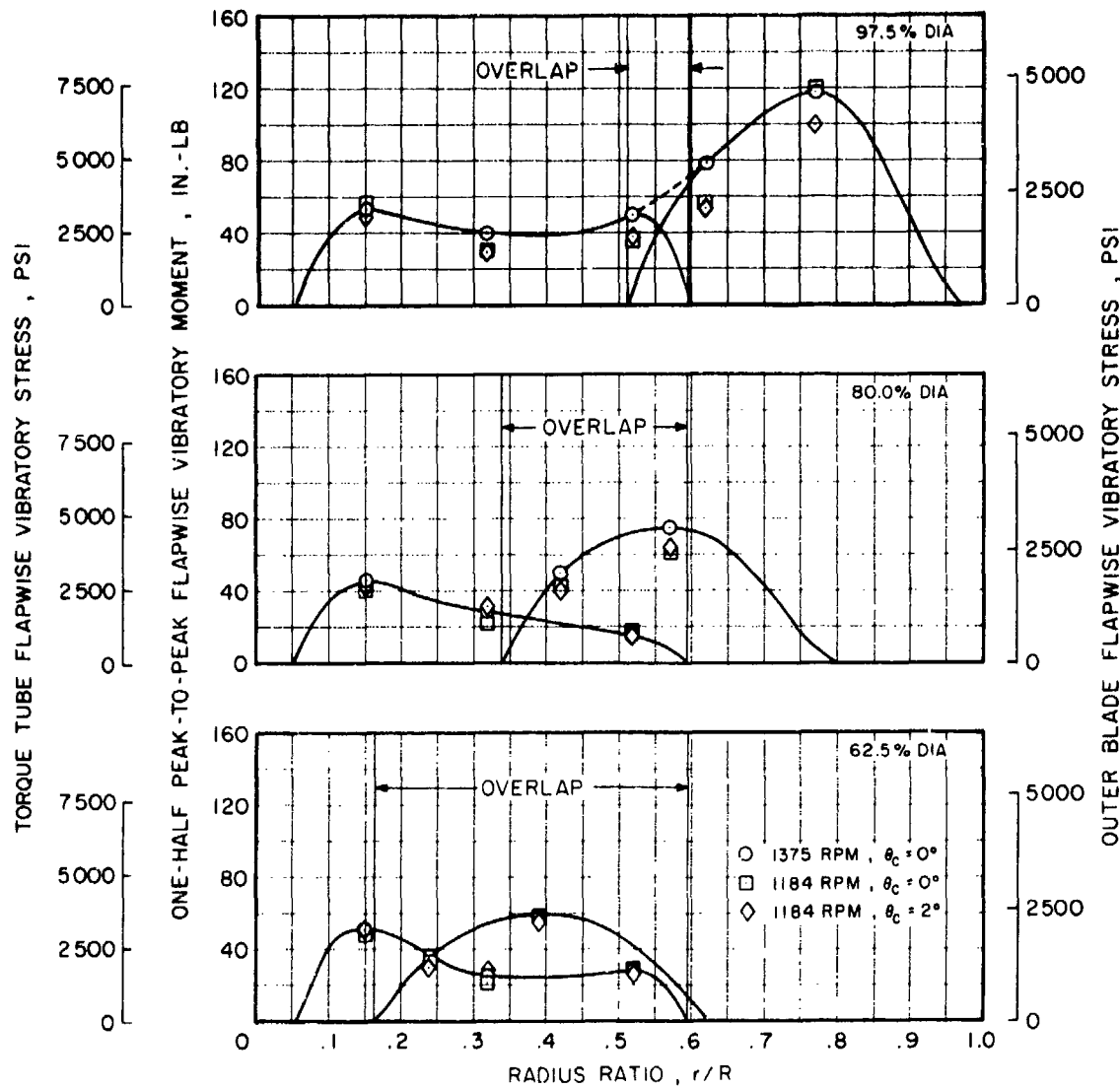


Figure 61. Effect of Diameter, RPM, and Collective Pitch on Flapwise Stress Distributions, $V = 150$ Knots, $\alpha_s = 0^\circ$.

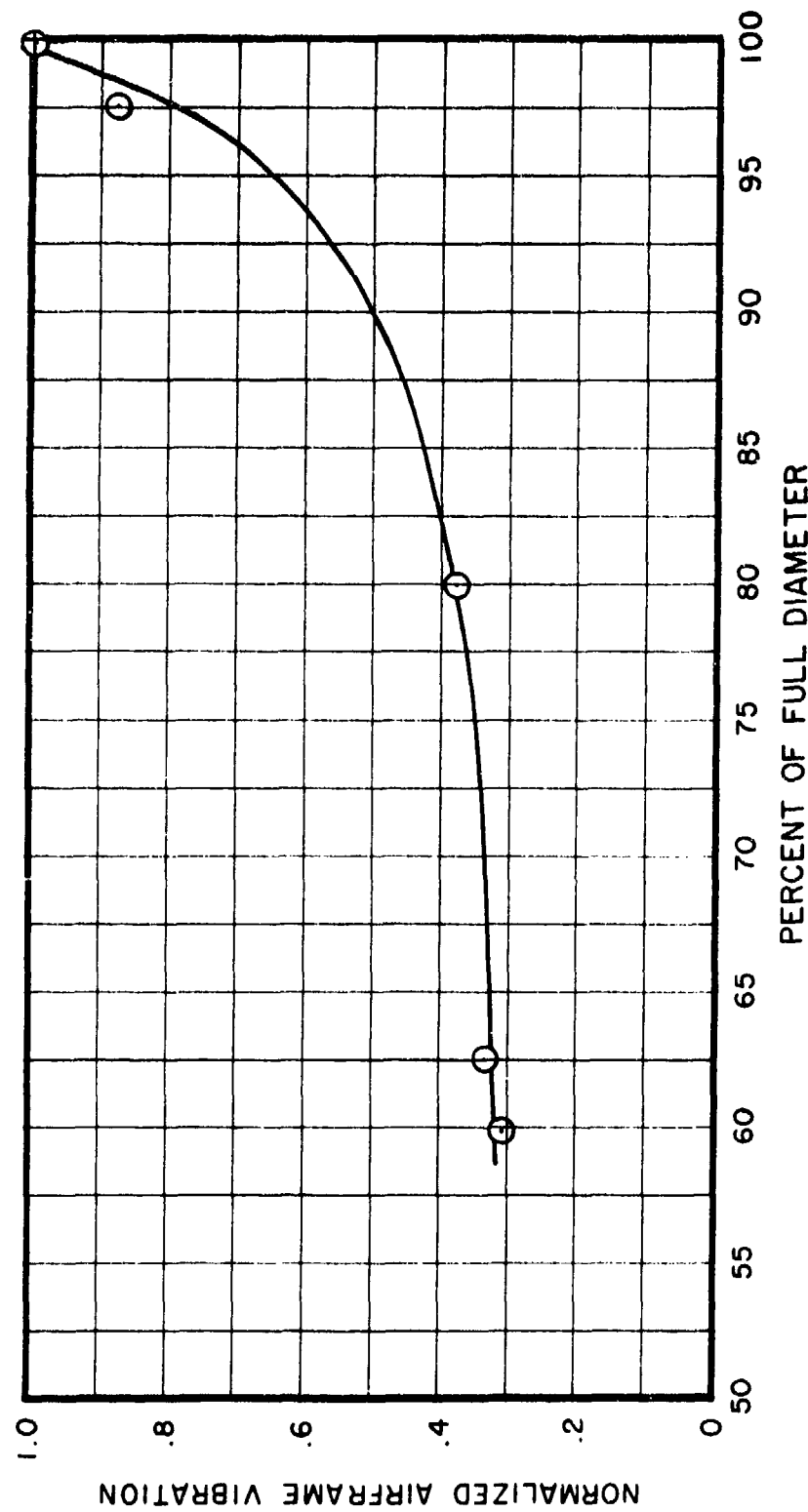
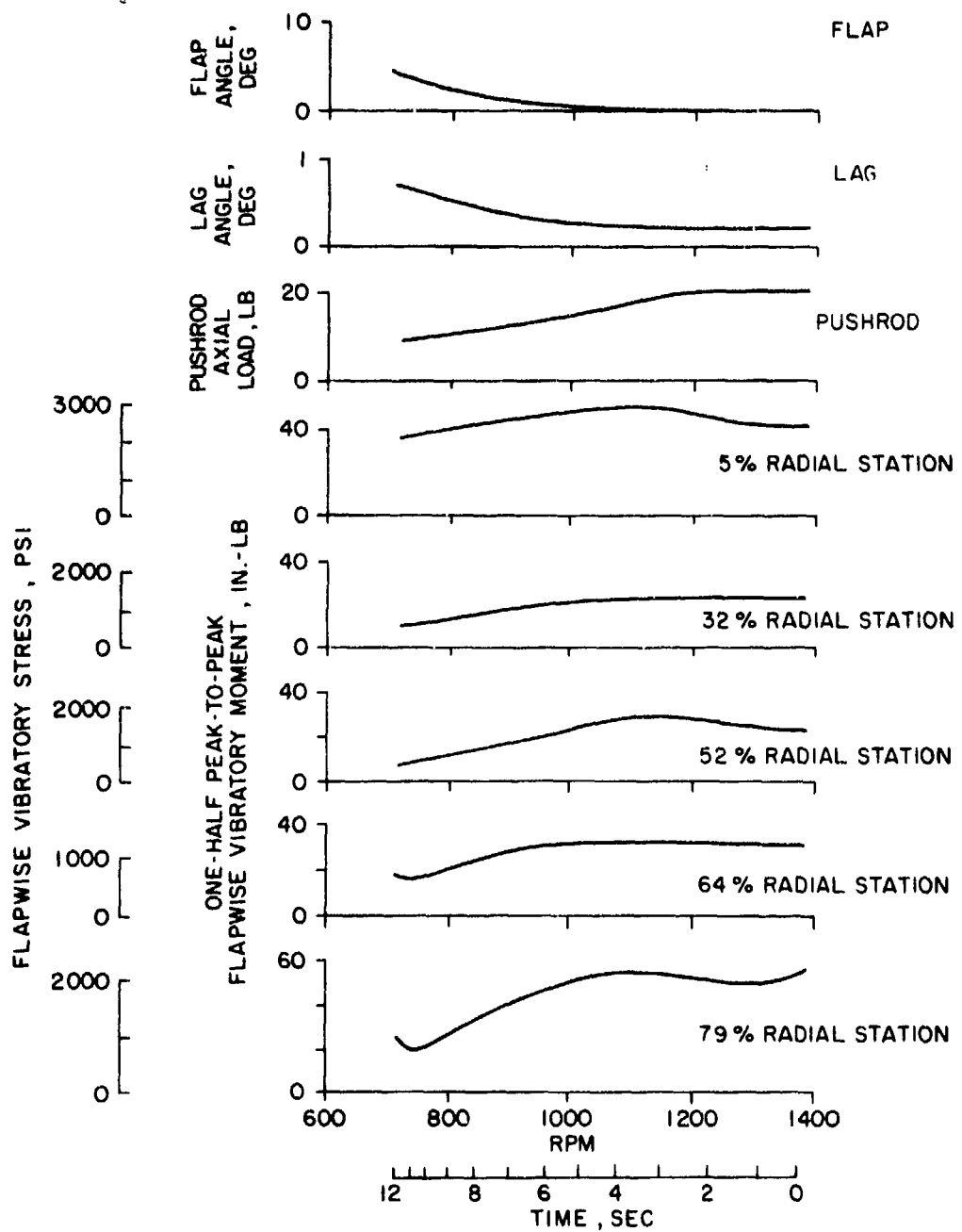
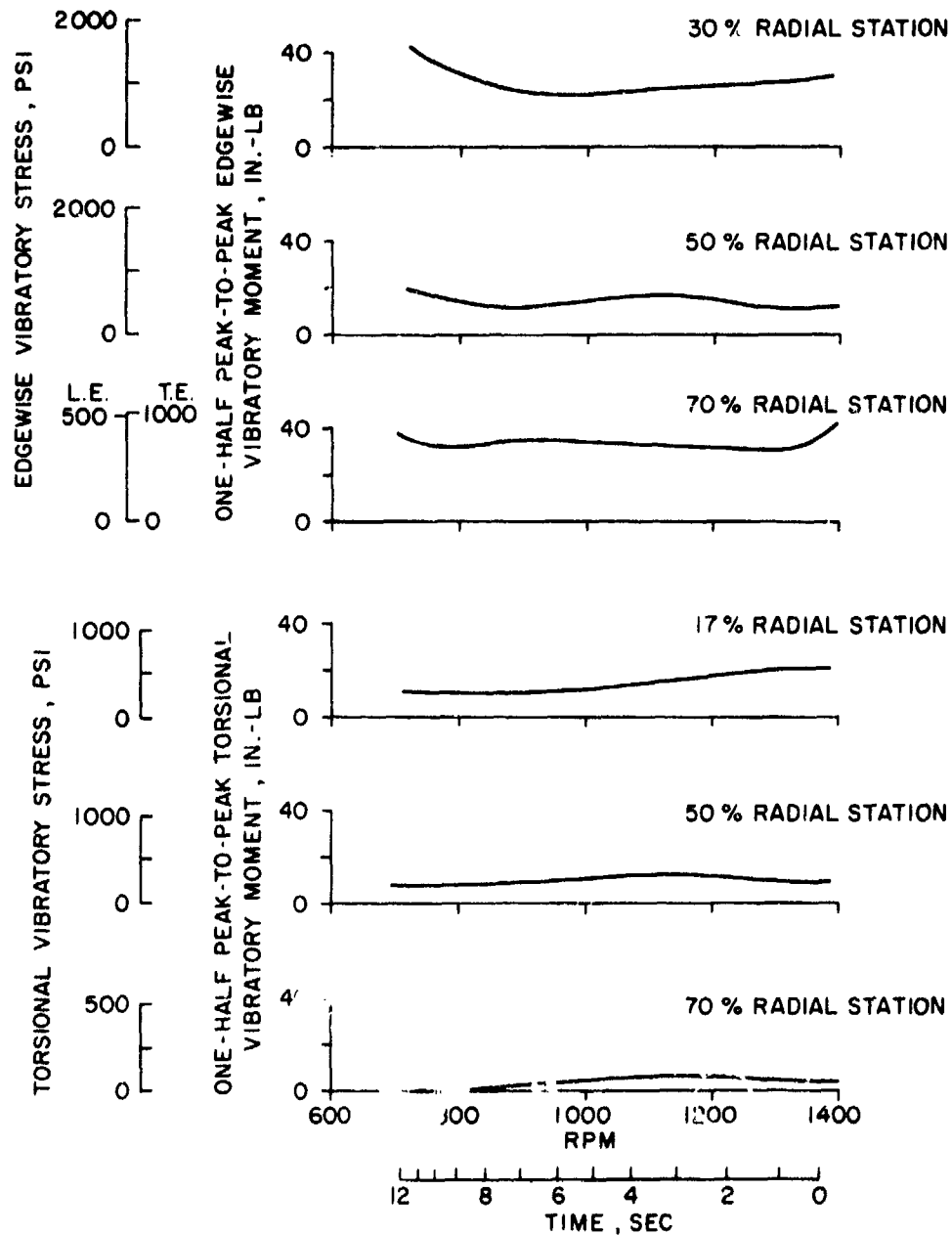


Figure 62. Effect of Diameter on Model Vibration Levels, 1375 rpm,
 $V = 150$ Knots, $\alpha_s = 0^\circ$, $\theta_c = 0^\circ$.



(a) Flapwise Stresses, Pushrod Load, and Blade Motions

Figure 63. Blade Vibratory Response During RPM Reduction,
 62.5% Diameter, $V = 150$ Knots, $\alpha_s = 0^\circ$, $\theta_c = 0^\circ$.



(b) Edgewise and Torsional Stresses

Figure 63. Concluded.

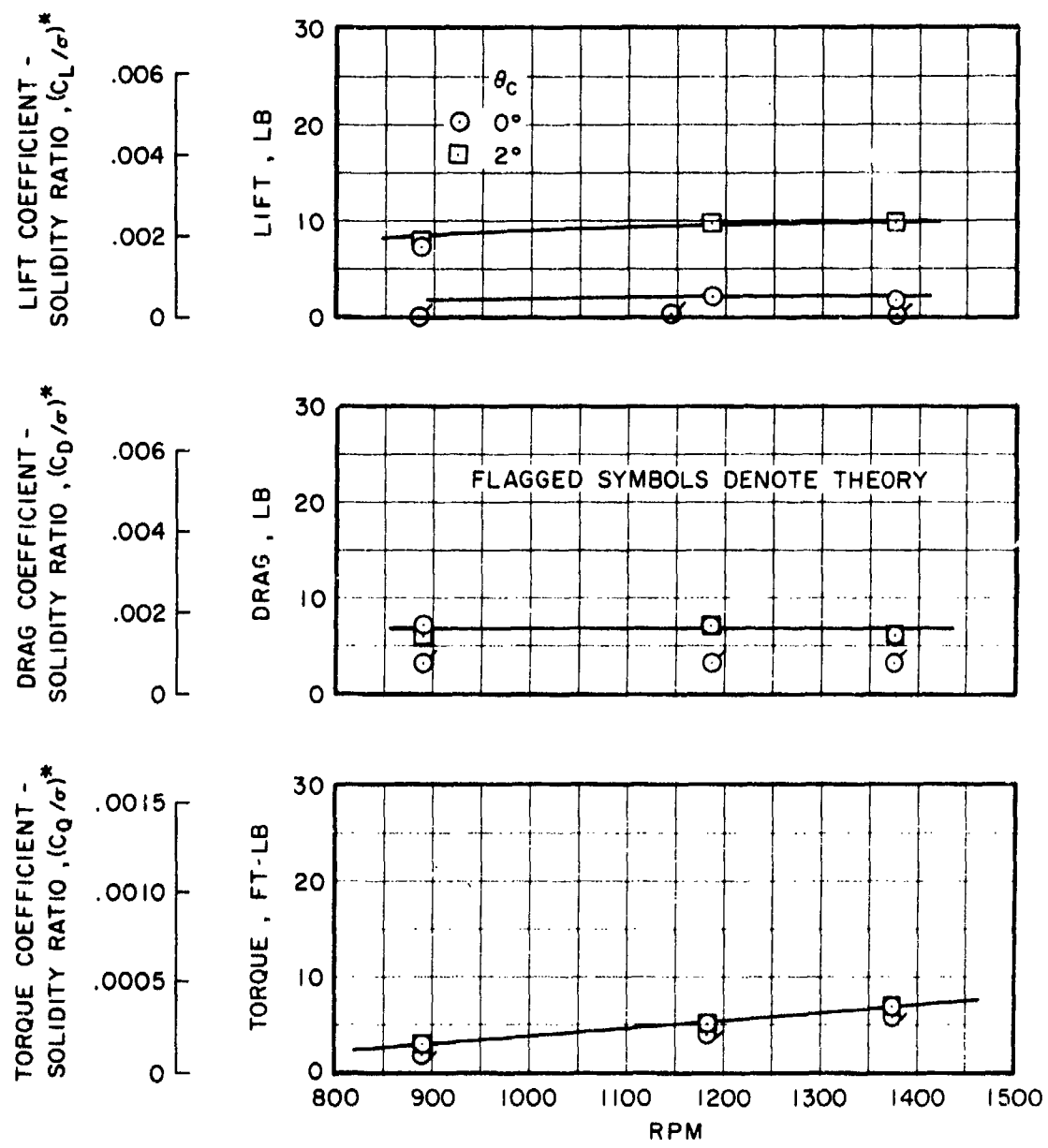


Figure 64. Effect of RPM on Performance Parameters, 60.8% Diameter, $V = 150$ Knots, $\alpha_s = 0^\circ$.

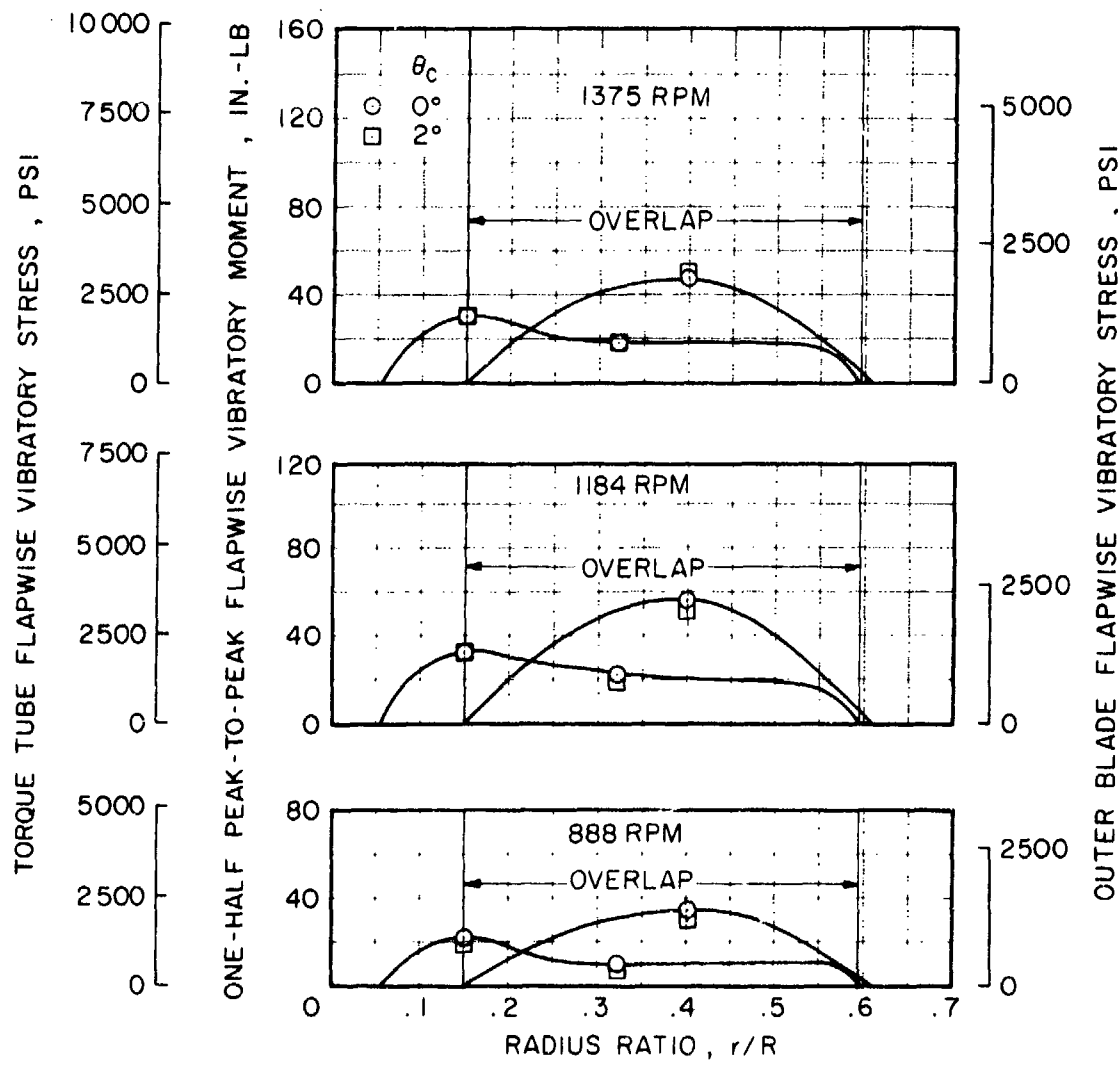


Figure 65. Effect of RPM on Blade Flapwise Stress Distribution, 60.8% Diameter, $V = 150$ Knots, $\alpha_s = 0^\circ$.

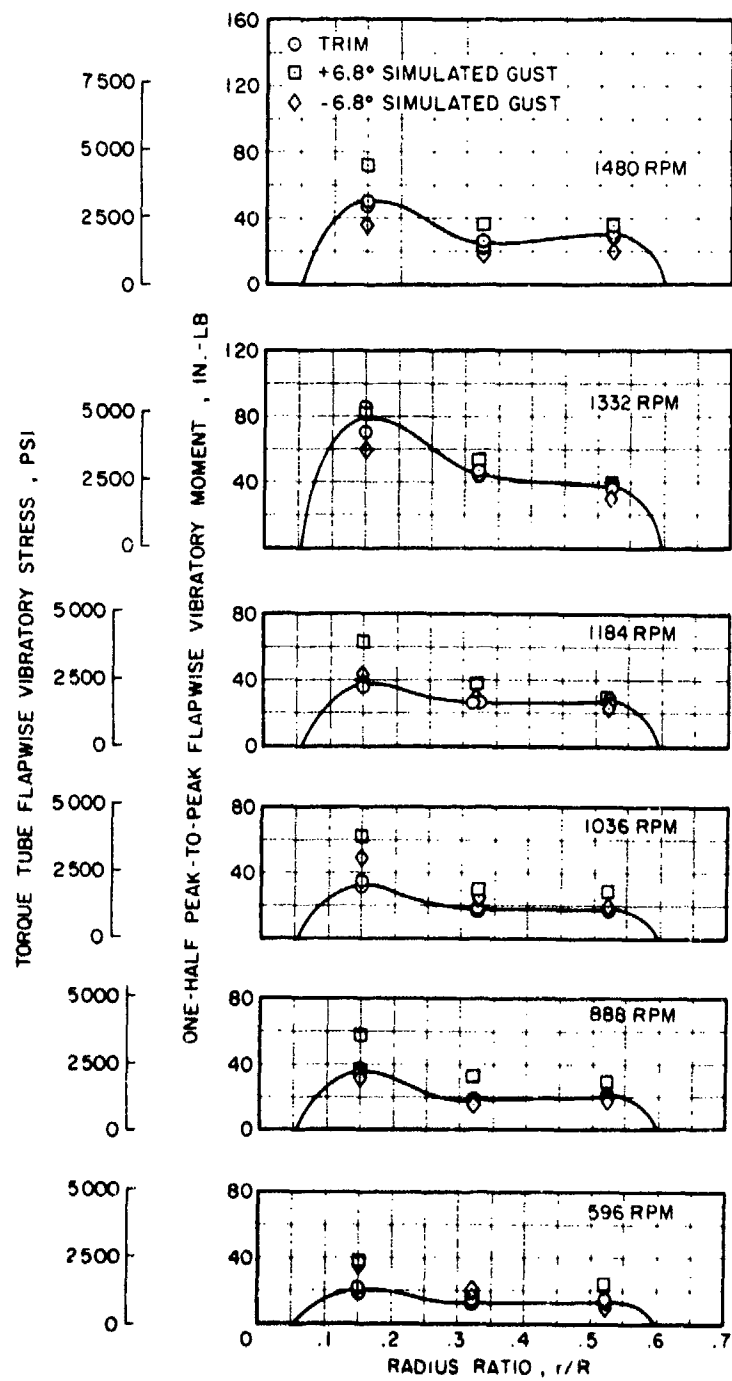


Figure 66. Effect of RPM and Gusts on Torque Tube Flapwise Stress Distribution, 60.5% Diameter, $V = 150$ Knots, $\theta_c = 0^\circ$.

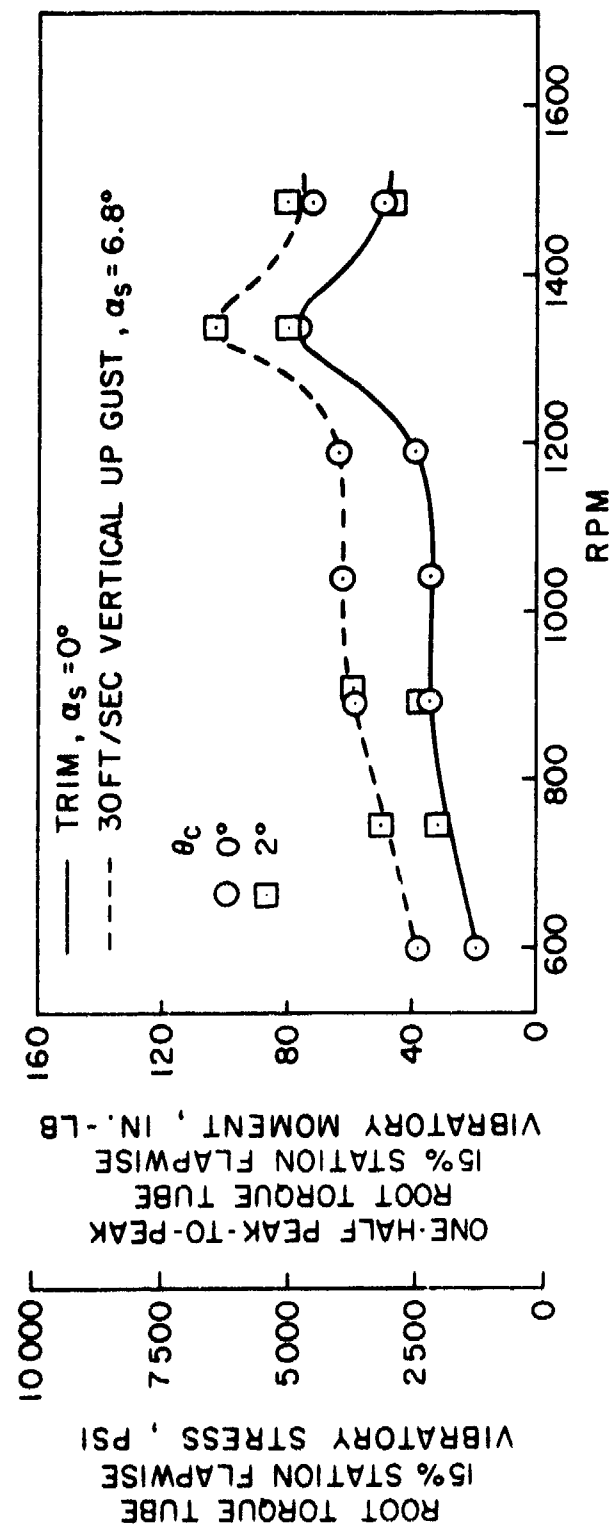
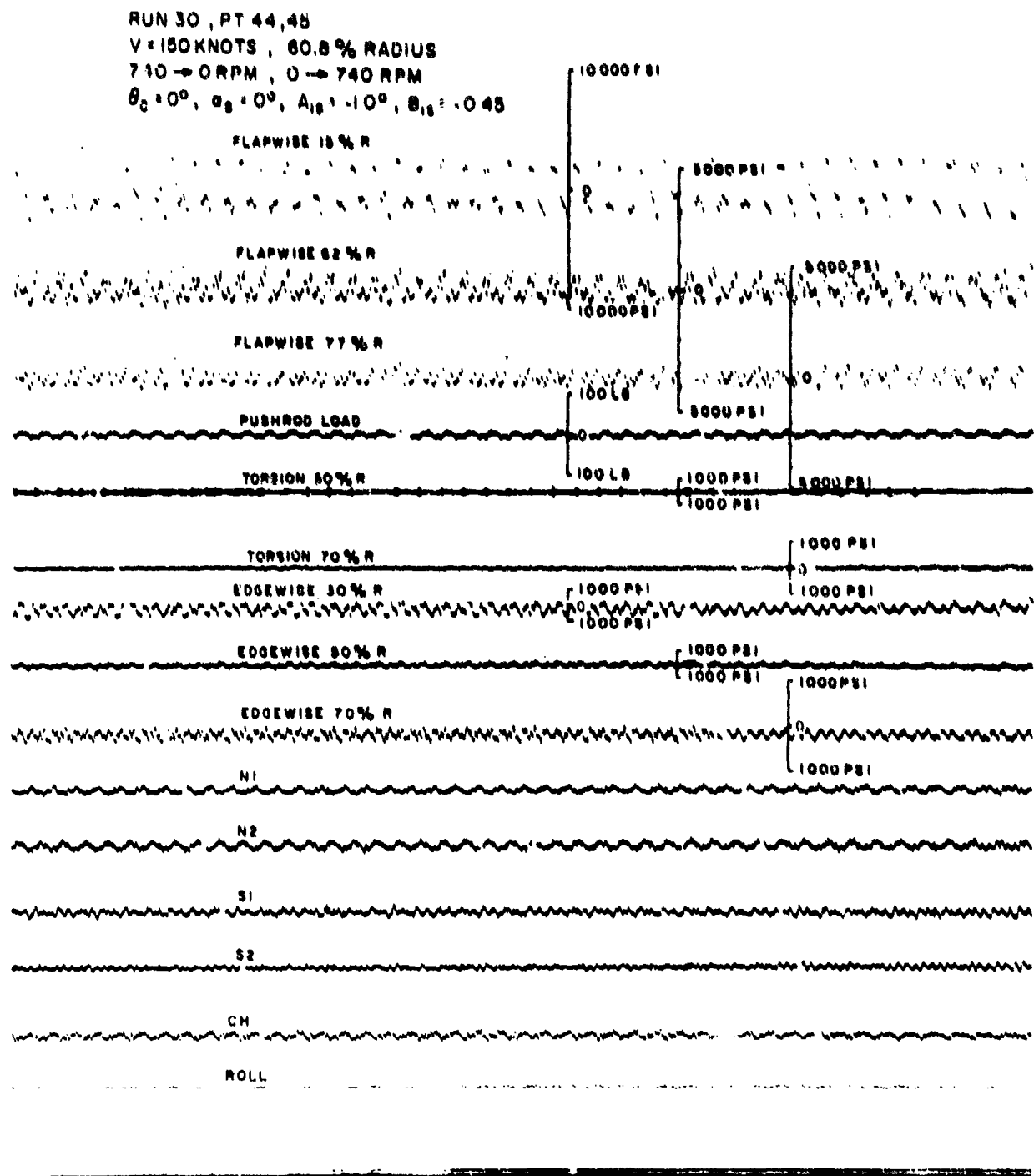
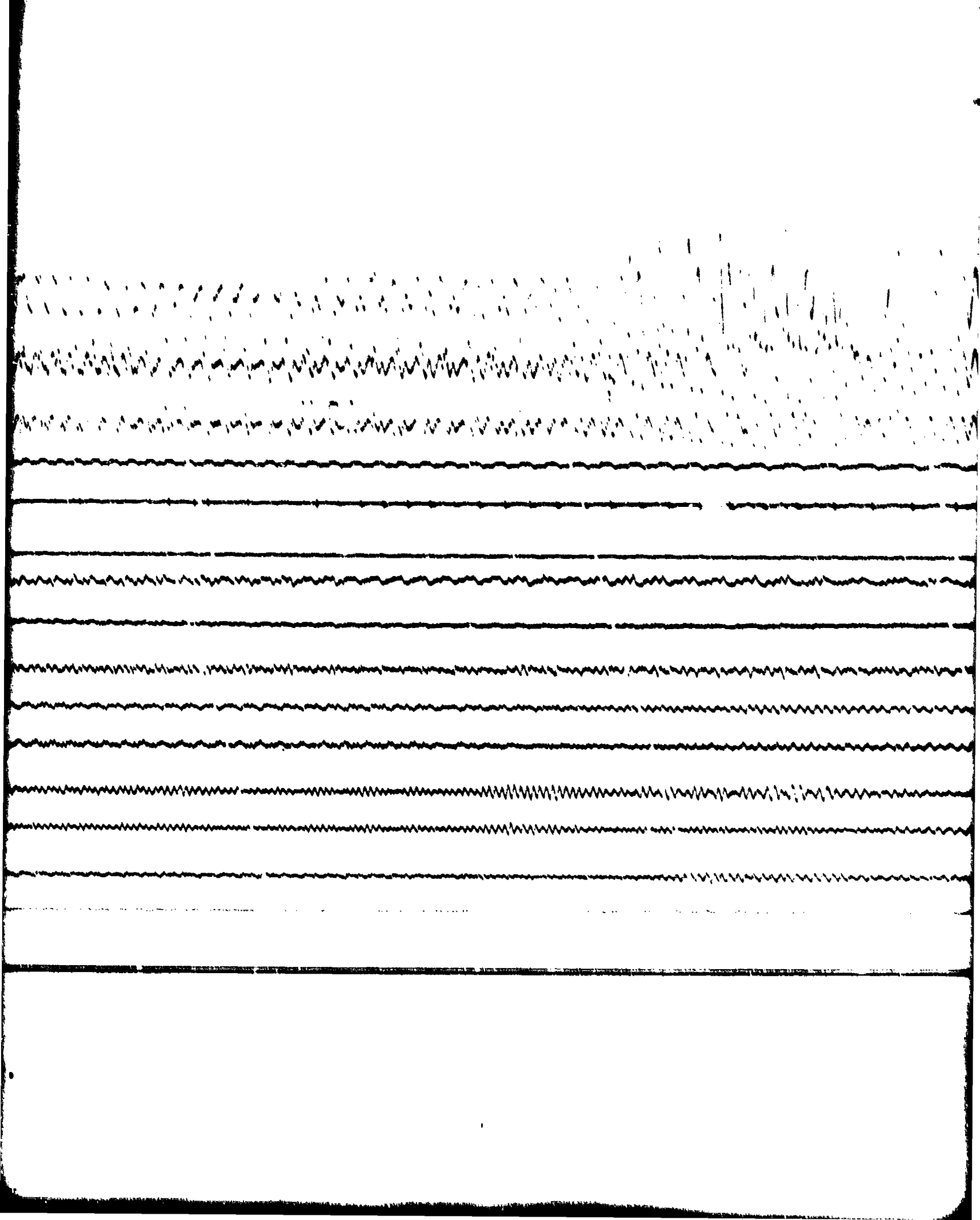


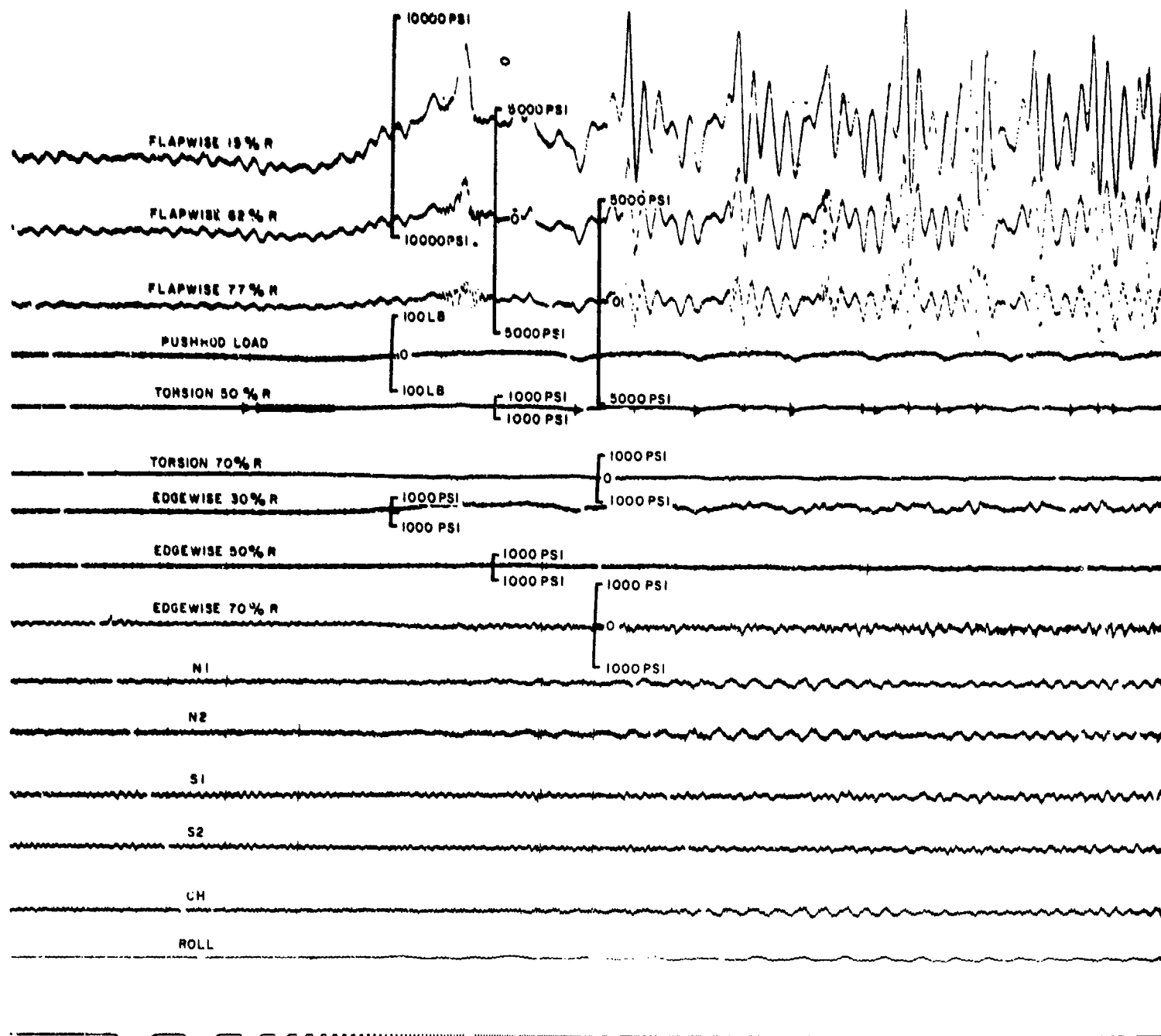
Figure 67. Effect of RPM on Torque Tube Stress Measured at the 15% Station, 60.5% Diameter, $V = 150$ Knots.



(a) Rotor Stop Sequence

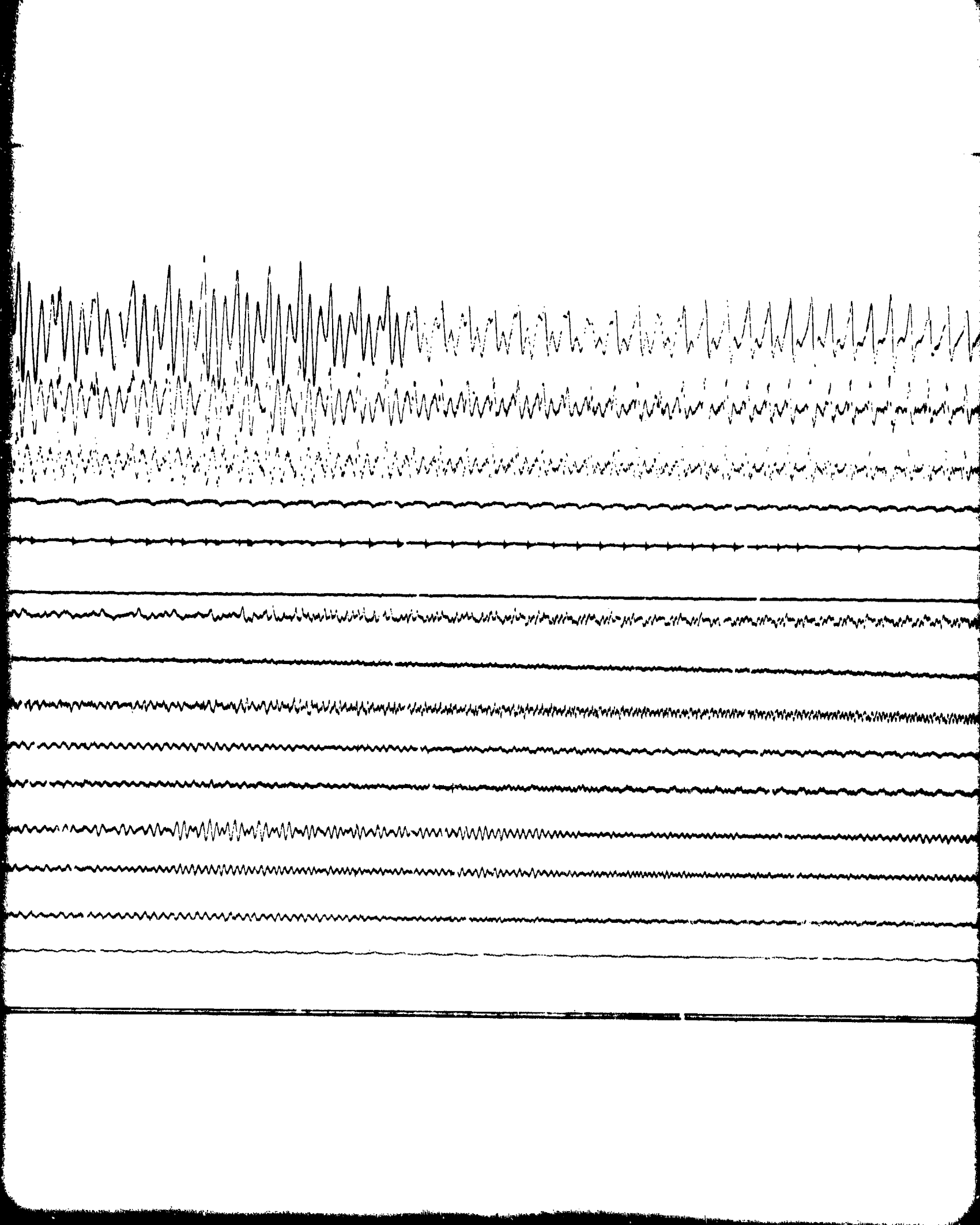
Figure 68. Typical Time History of Stop-Start Sequence, 60.8% Diameter,
 $V = 150$ Knots, $\alpha_s = 0^\circ$, $\theta_c = 0^\circ$.



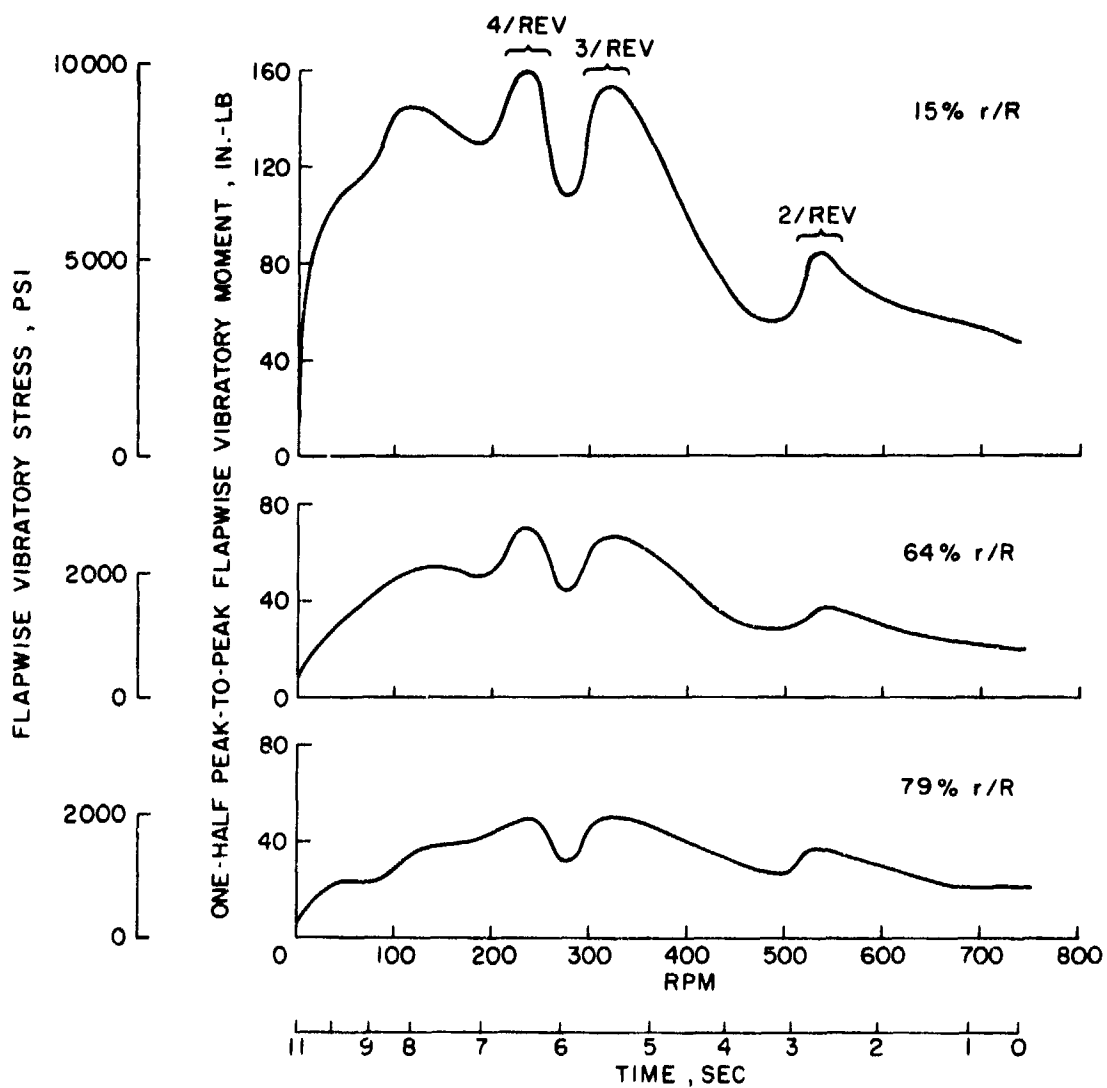


(b) Rotor Start Sequence

Figure 68. Concluded.



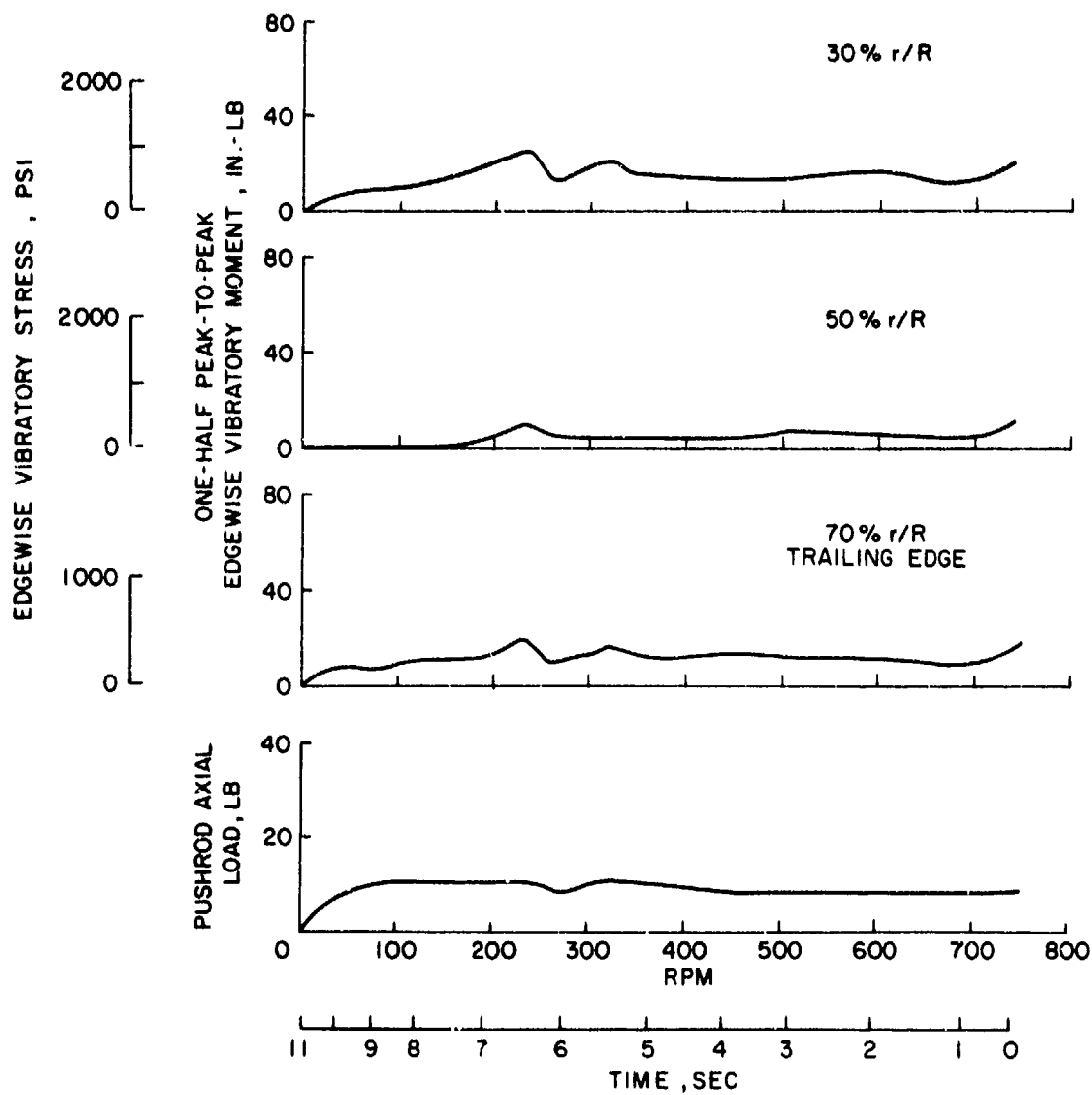
The figure consists of ten horizontal lines, each representing an ECG trace. The top line is characterized by high-frequency, high-amplitude noise, indicating a low-quality or heavily artifacts-contaminated signal. As the lines progress downwards, the noise level decreases significantly, and the underlying signal becomes more clearly visible. The bottom line shows a clean, regular sinusoidal pattern with a period of approximately 0.8 seconds, representing a high-quality ECG signal. A horizontal dashed line is drawn across the middle of the plot, separating the highly noisy top half from the clean bottom half.



(a) Flapwise Stress

Figure 69. Rotor Vibratory Loads During Typical Rotor Stop;
 60.8% Diameter, $V = 150$ Knots, $\alpha_s = 0^\circ$, $\theta_c = 0^\circ$,
 $A_{ls} = -1.0^\circ$, $B_{ls} = -0.45^\circ$.

Preceding page blank



(b) Edgewise Stress and Pushrod Loads

Figure 69. Concluded.

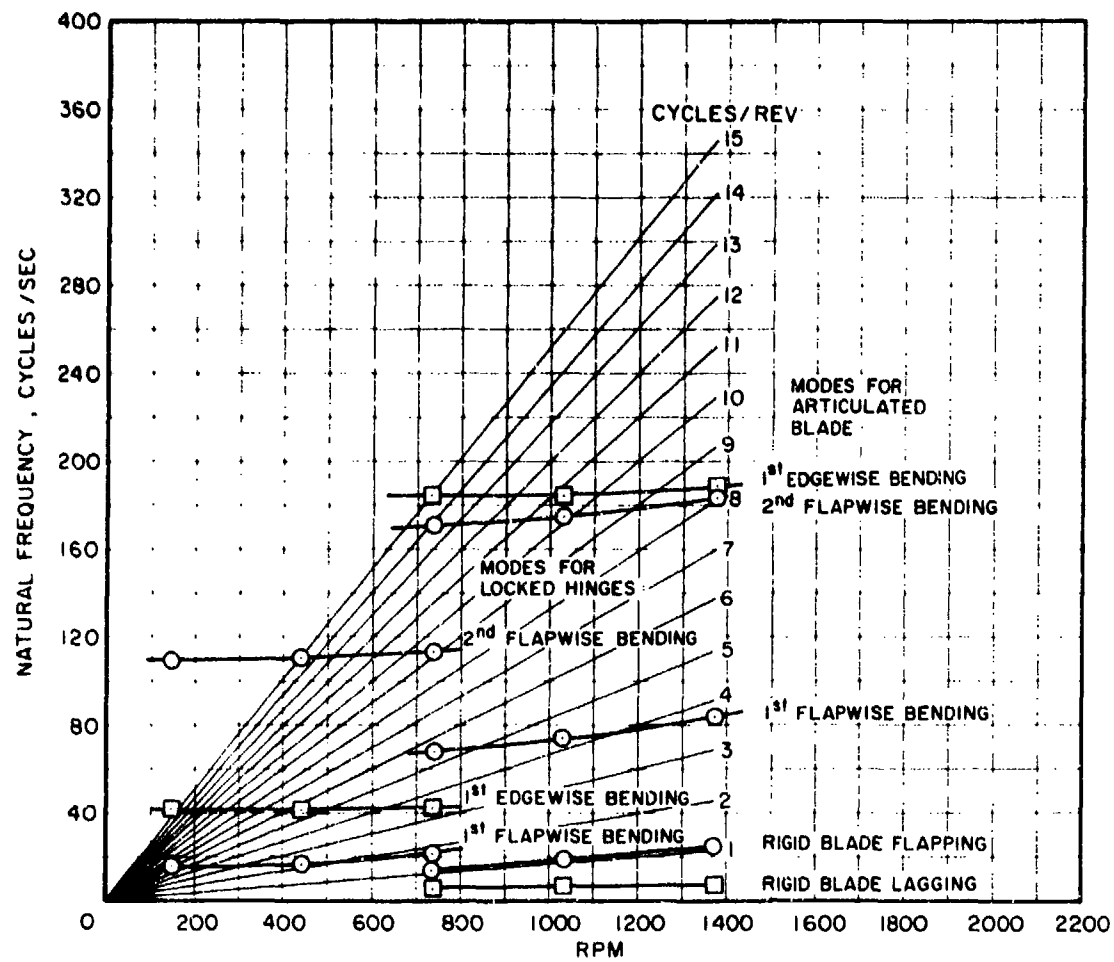


Figure 70. Calculated Natural Frequencies for 60.8% Diameter Conditions.

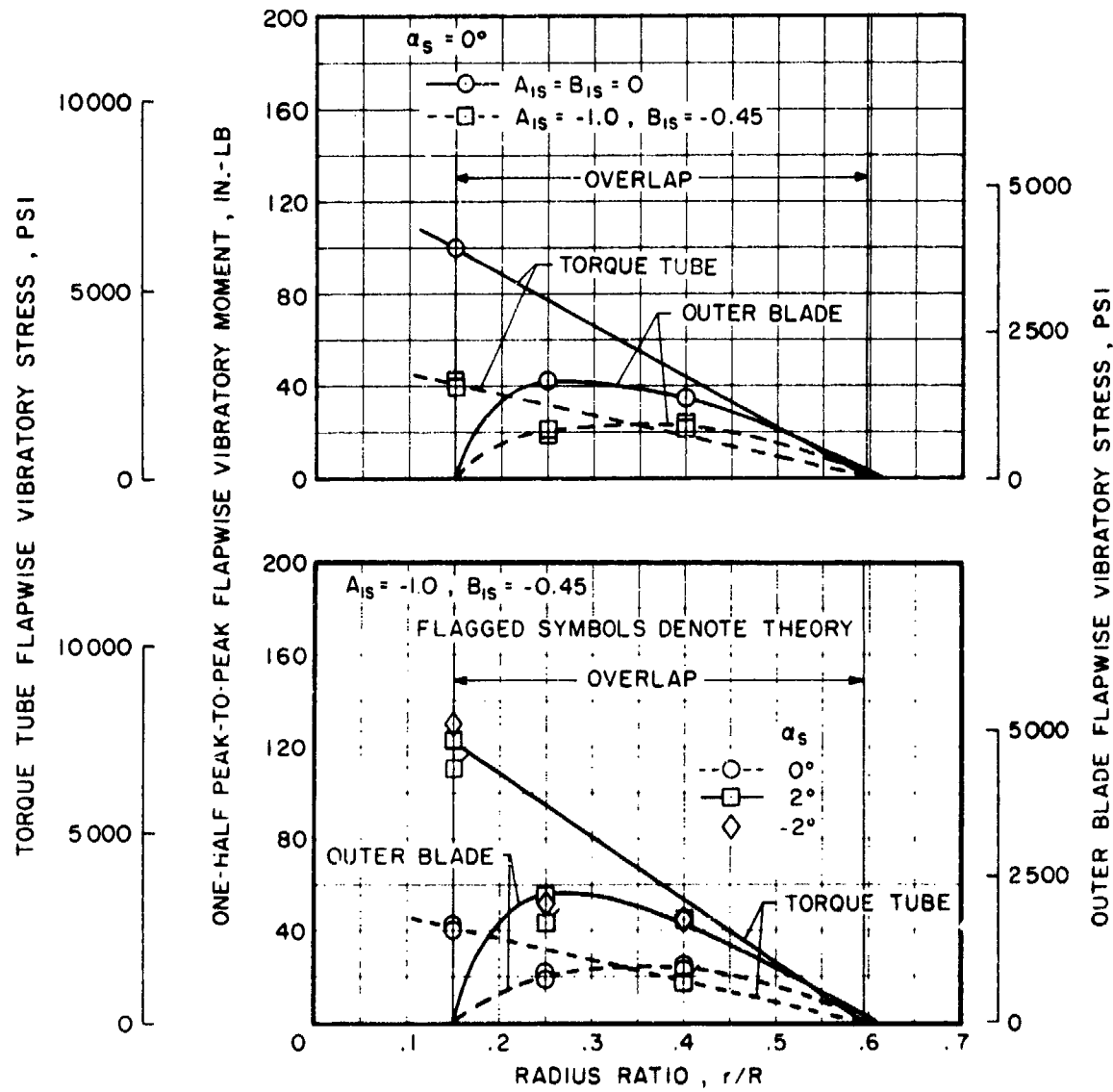


Figure 71. Effect of Cyclic Pitch and Gusts on Blade Flapwise Stress Distribution, Locked Hinge, 60.8% Diameter, 740 rpm, $V = 150$ Knots, $\theta_c = 0^\circ$.

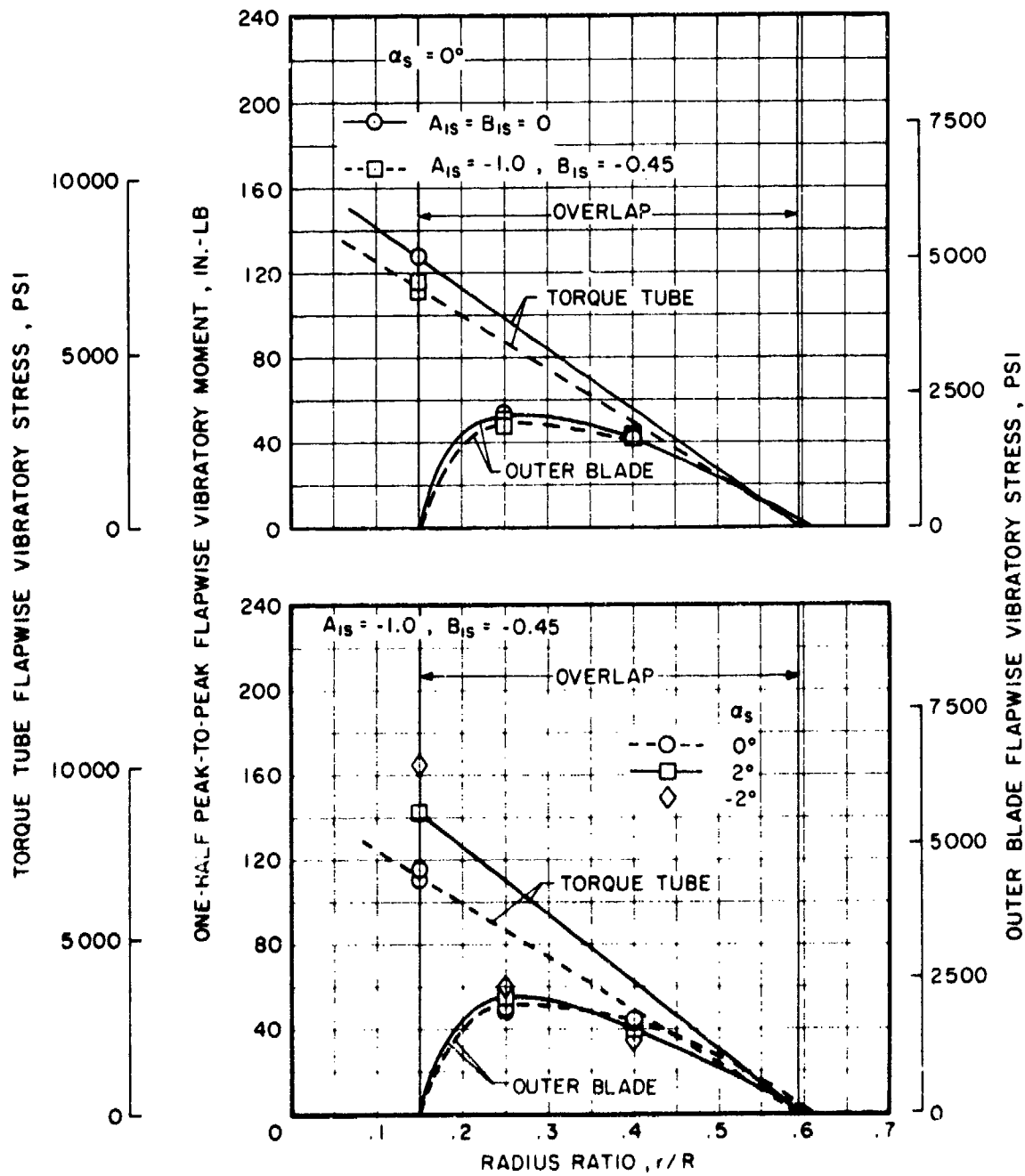


Figure 72. Effect of Cyclic Pitch and Gusts on Blade Flapwise Stress Distribution, Locked Hinge, 60.8% Diameter, 296 rpm, $V = 150$ Knots, $\theta_c = 0^\circ$.

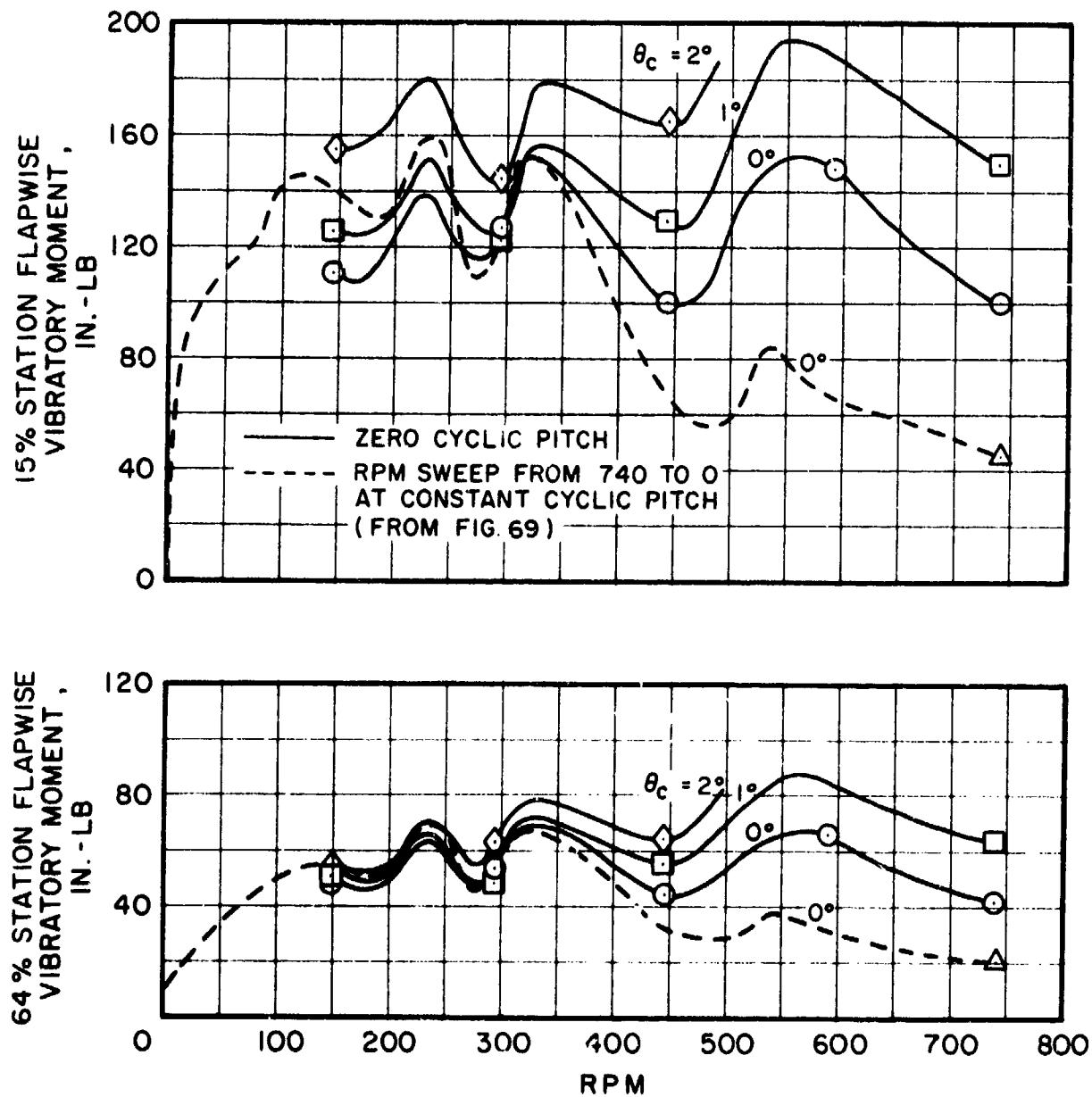


Figure 73. Variation of Blade Stress With RPM and Collective Pitch, 60.8% Diameter, $V = 150$ Knots, $\alpha_s = 0^\circ$.

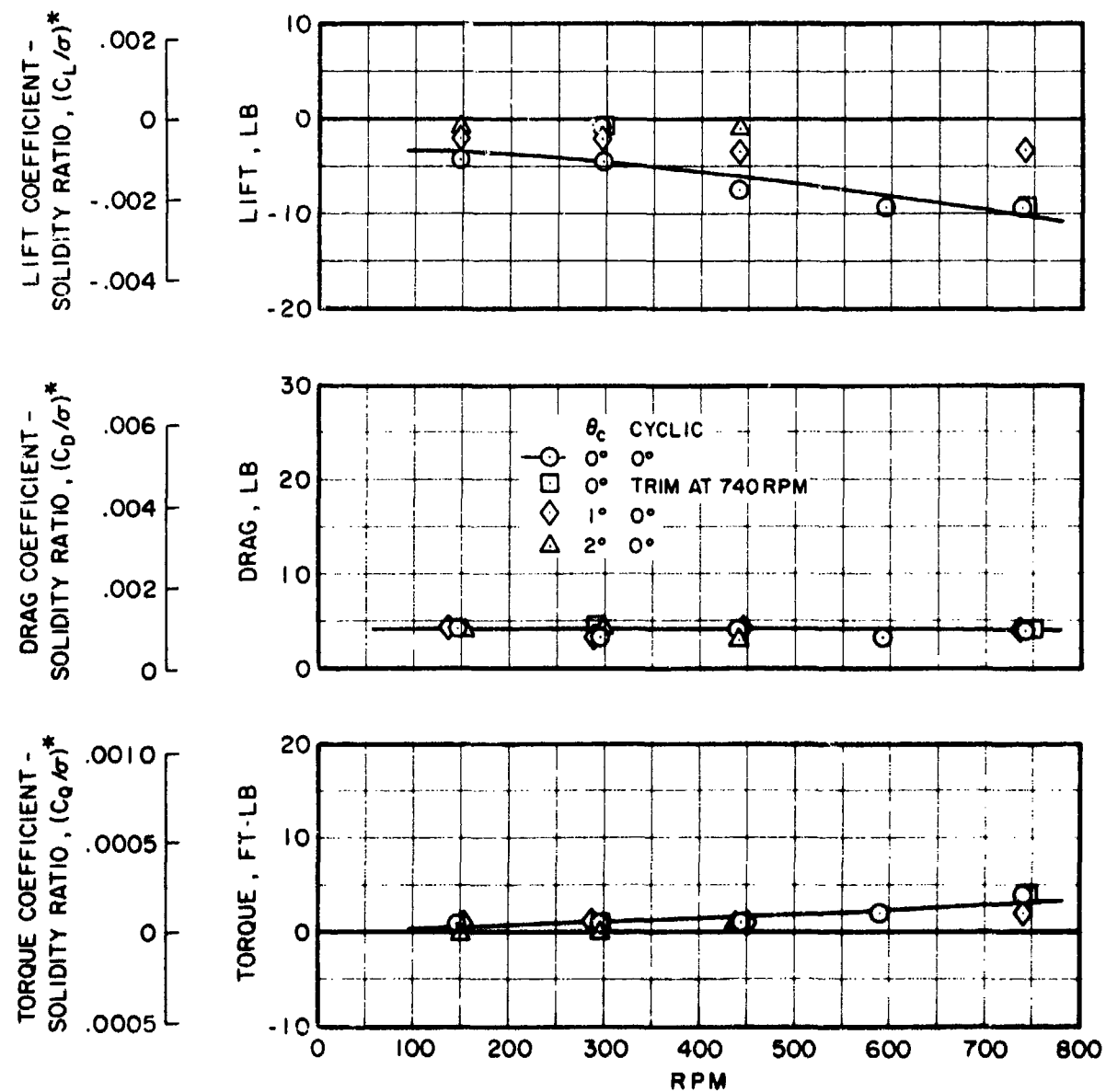


Figure 74. Variation of Rotor Performance Parameters With RPM, Locked Hinge, 60.8% Diameter, $V = 150$ Knots, $\alpha_s = 0^\circ$.

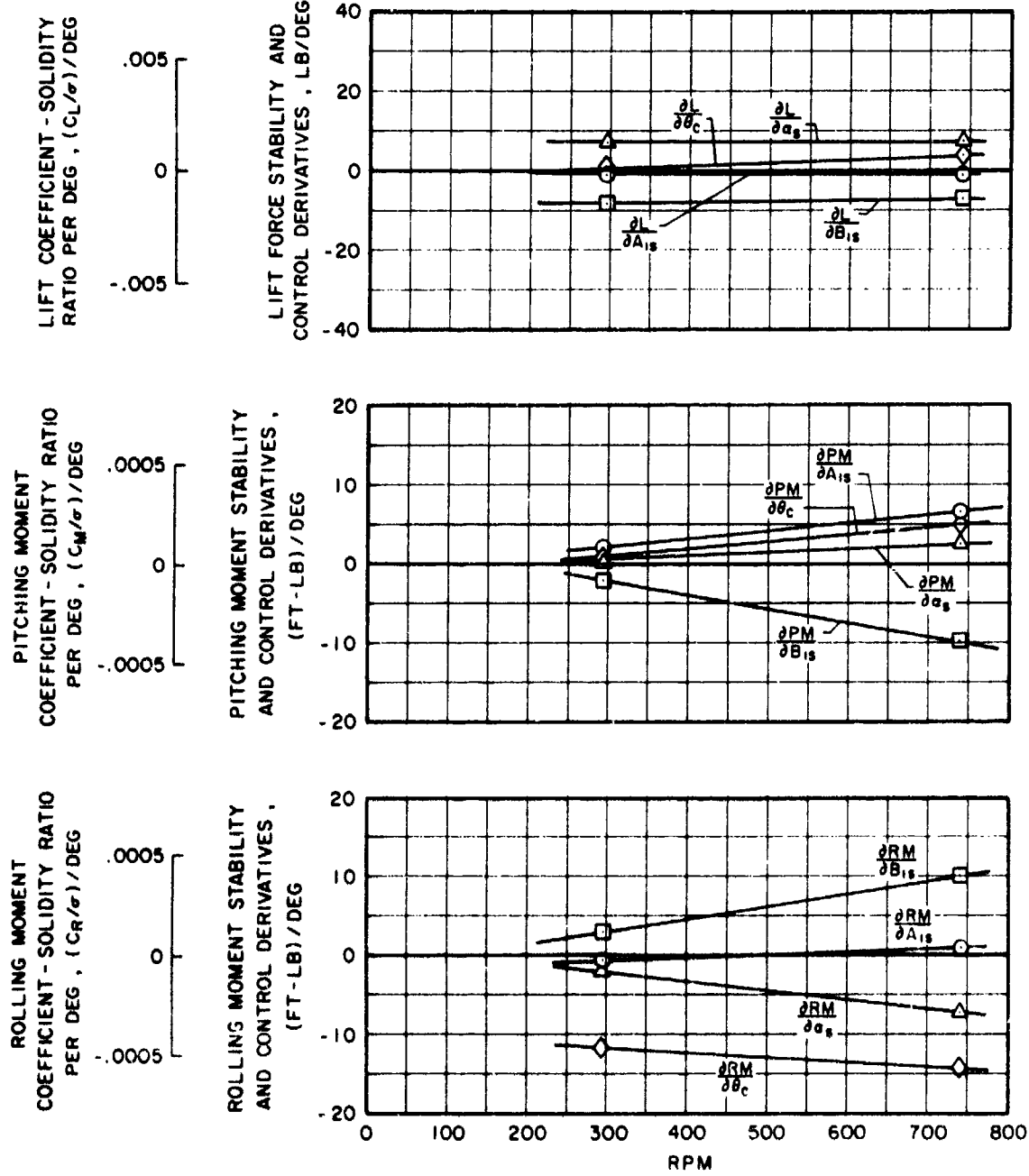


Figure 75. Variation of Stability Derivatives With RPM for Locked Hinge Configuration, 60.8% Diameter, $V = 150$ Knots.

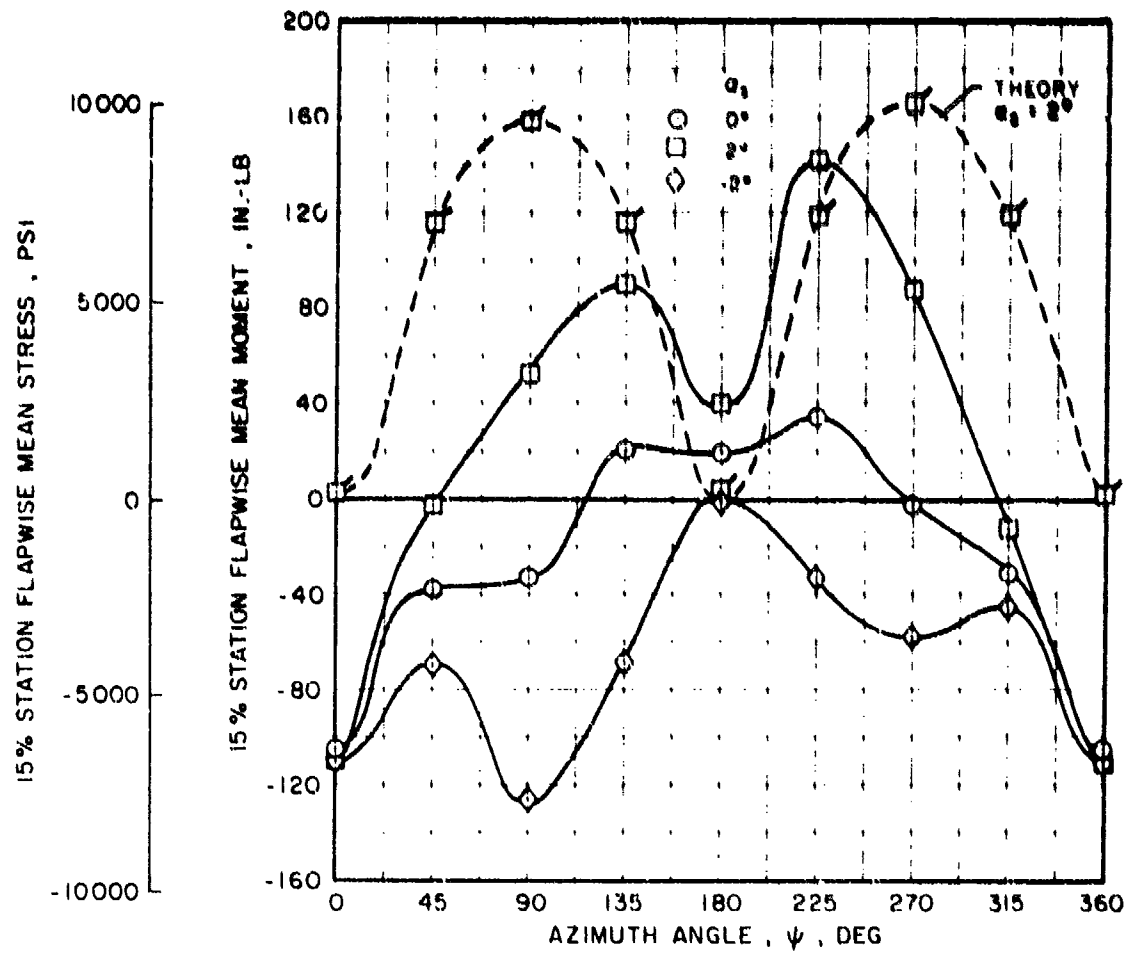


Figure 76. Variation of Blade Root Bending Stress With Azimuth Position, 60.8% Diameter, Stopped Rotor, $V = 150$ Knots, $\theta_c = 0^\circ$.

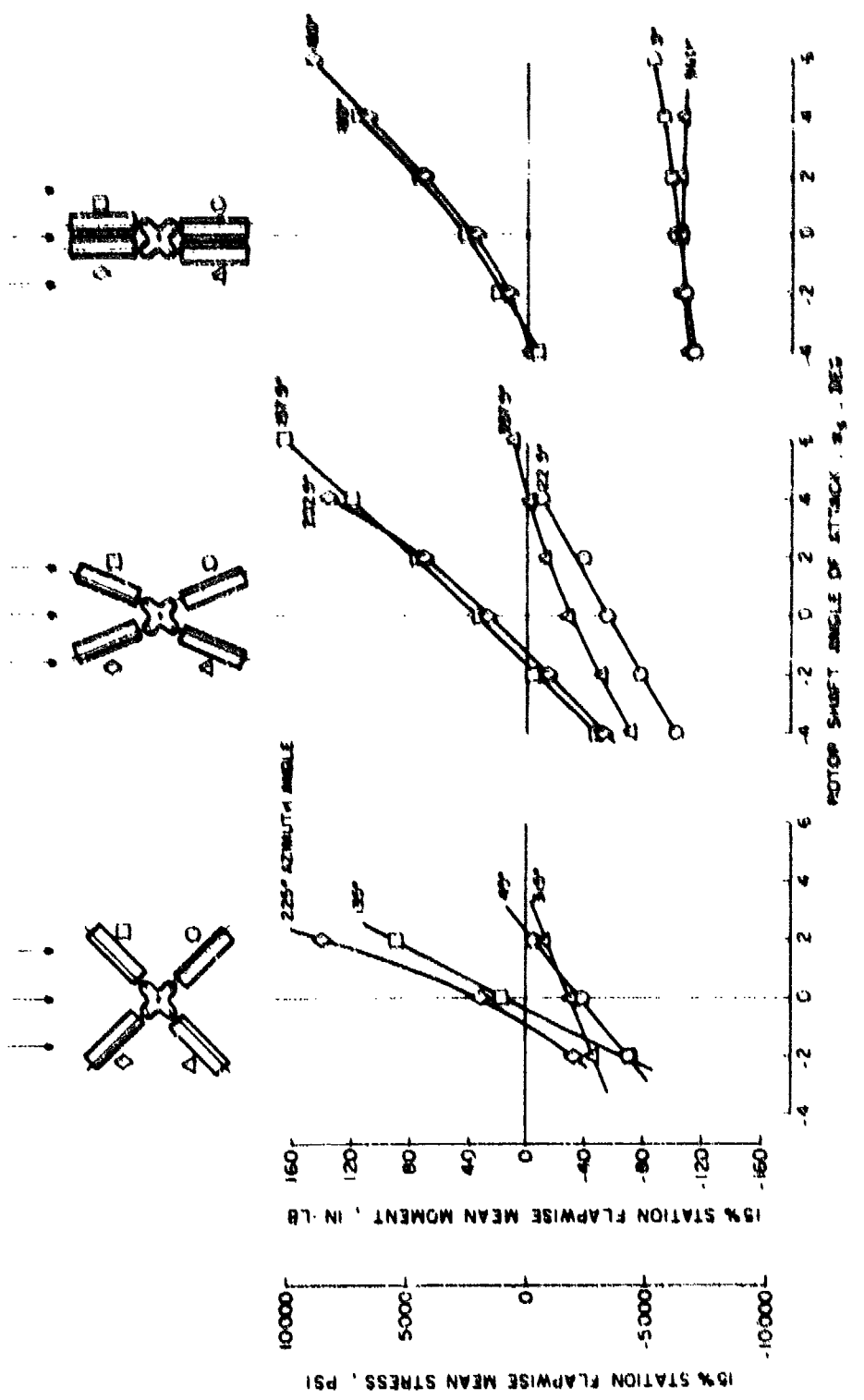


Figure 77. Effect of Fore-and-Aft Folding on Elbow Root Bending Stresses
 Measured at the 15° Radial Station, 60.00 Diameter,
 $V = 150$ Knots, $\theta_c = 0^\circ$.

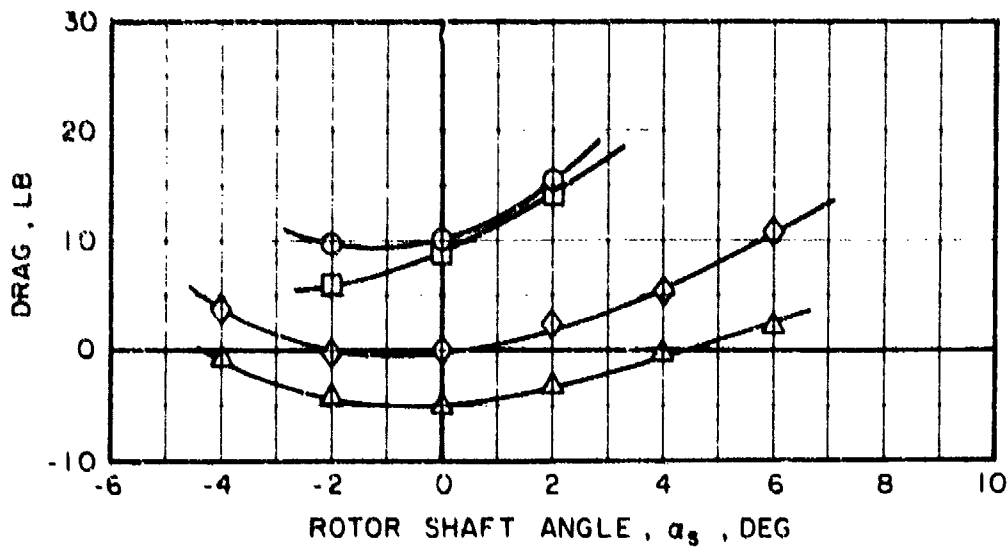
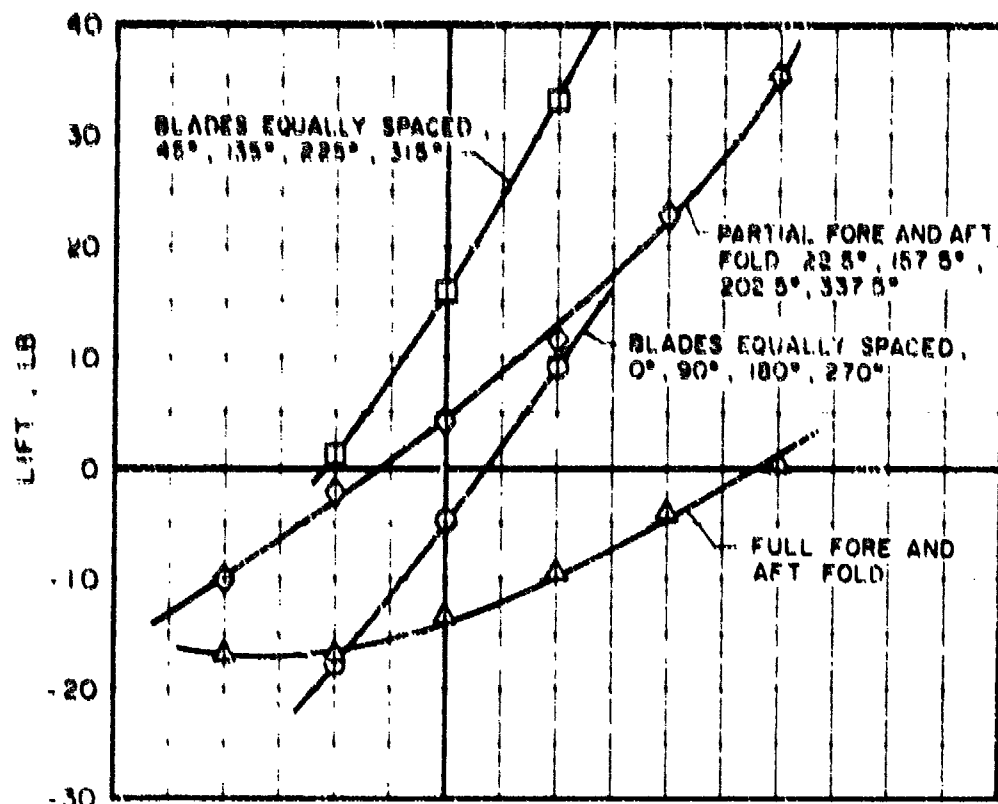


Figure 78. Effect of Rotor Index Position and Folding on Rotor Forces,
60.8% Diameter, $V = 150$ Knots, $\theta_c = 0^\circ$.

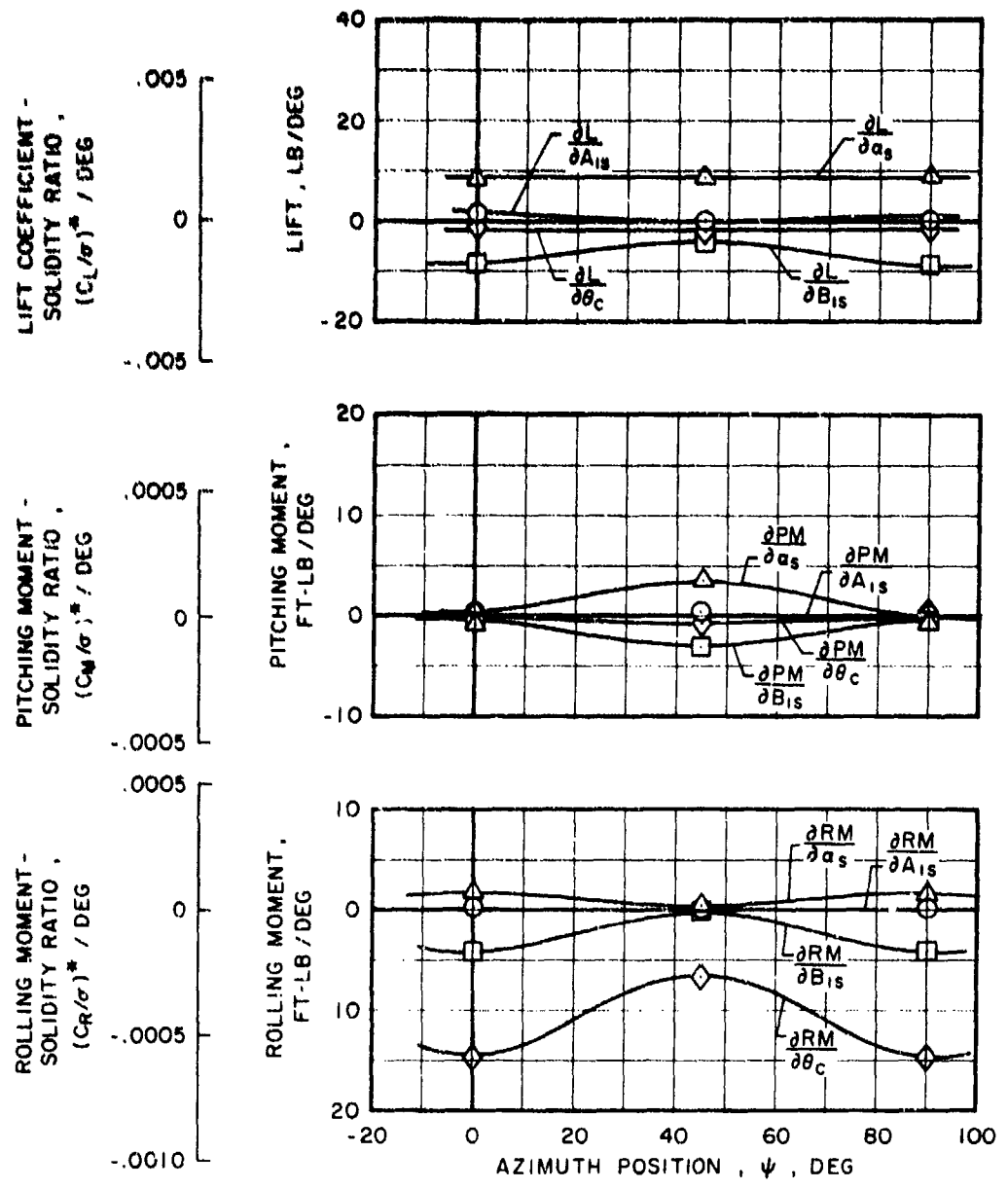


Figure 79. Stability and Control Derivatives for Stopped Rotor, 60.8% Diameter, $V = 150$ Knots.

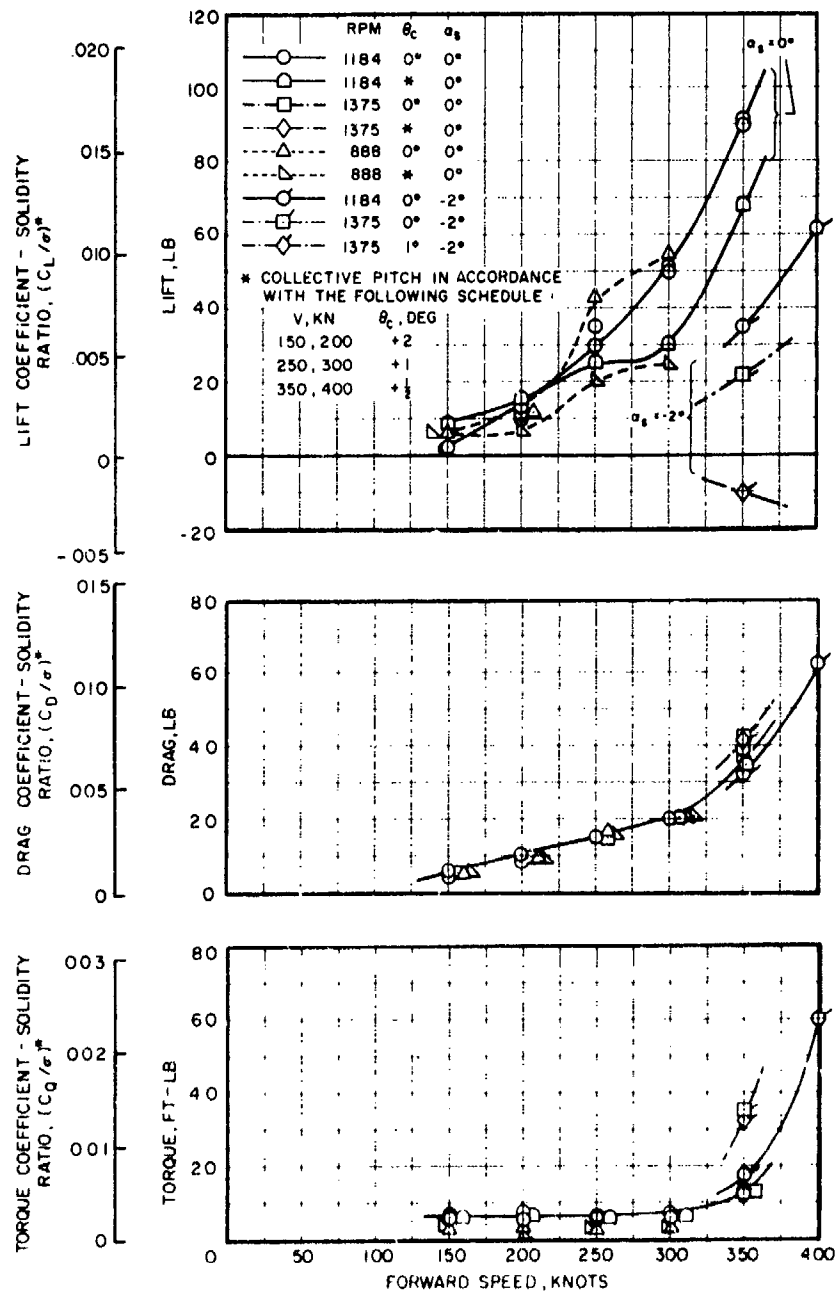


Figure 80. Rotor Performance Parameters at High Forward Speeds, 60.8% Diameter.

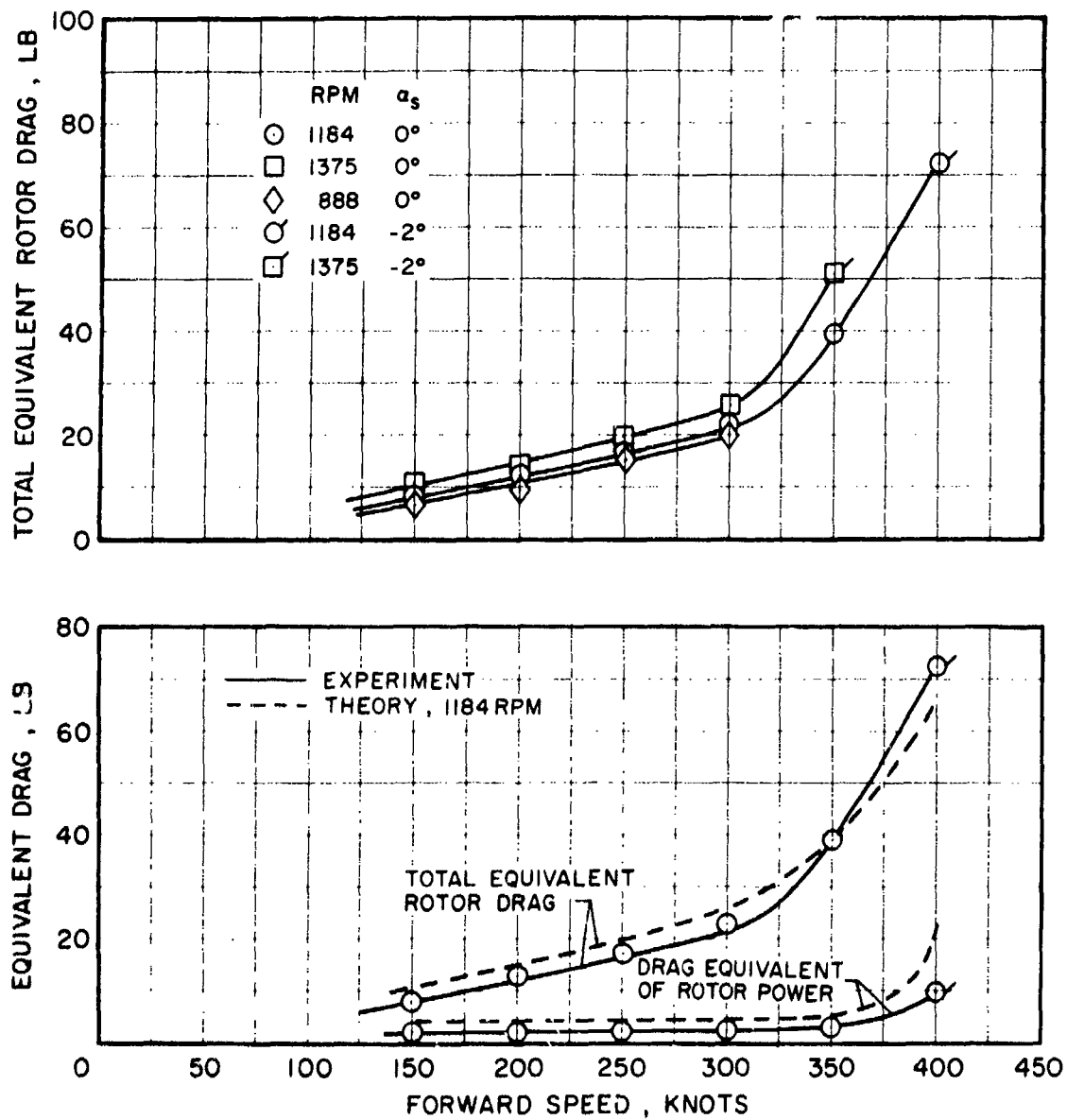


Figure 81. Rotor Equivalent Drag at High Forward Speeds, 60.8% Diameter,
 $\alpha_c = 0^\circ$.

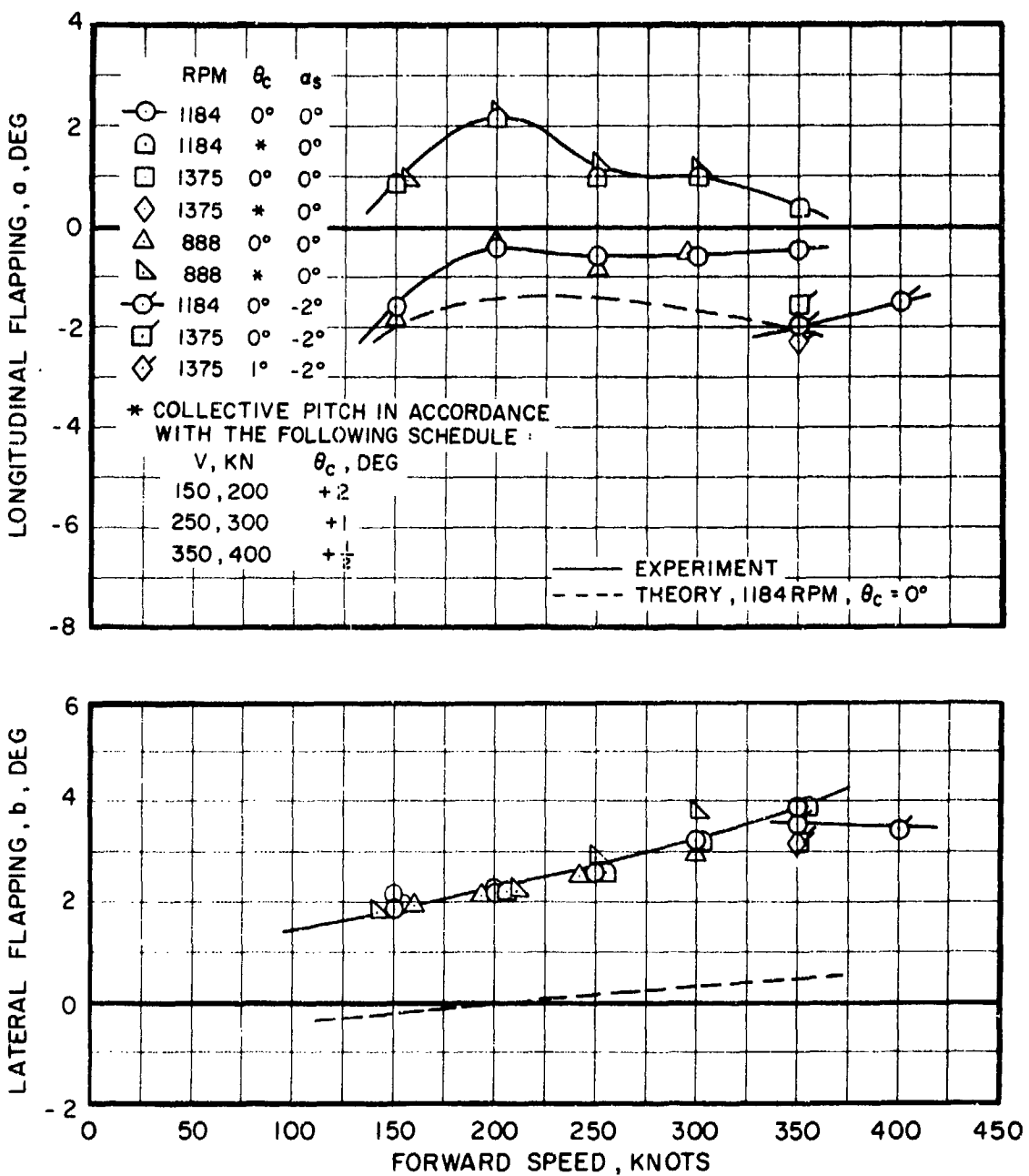


Figure 82. Blade Flapping at High Forward Speeds, 60.8% Diameter.

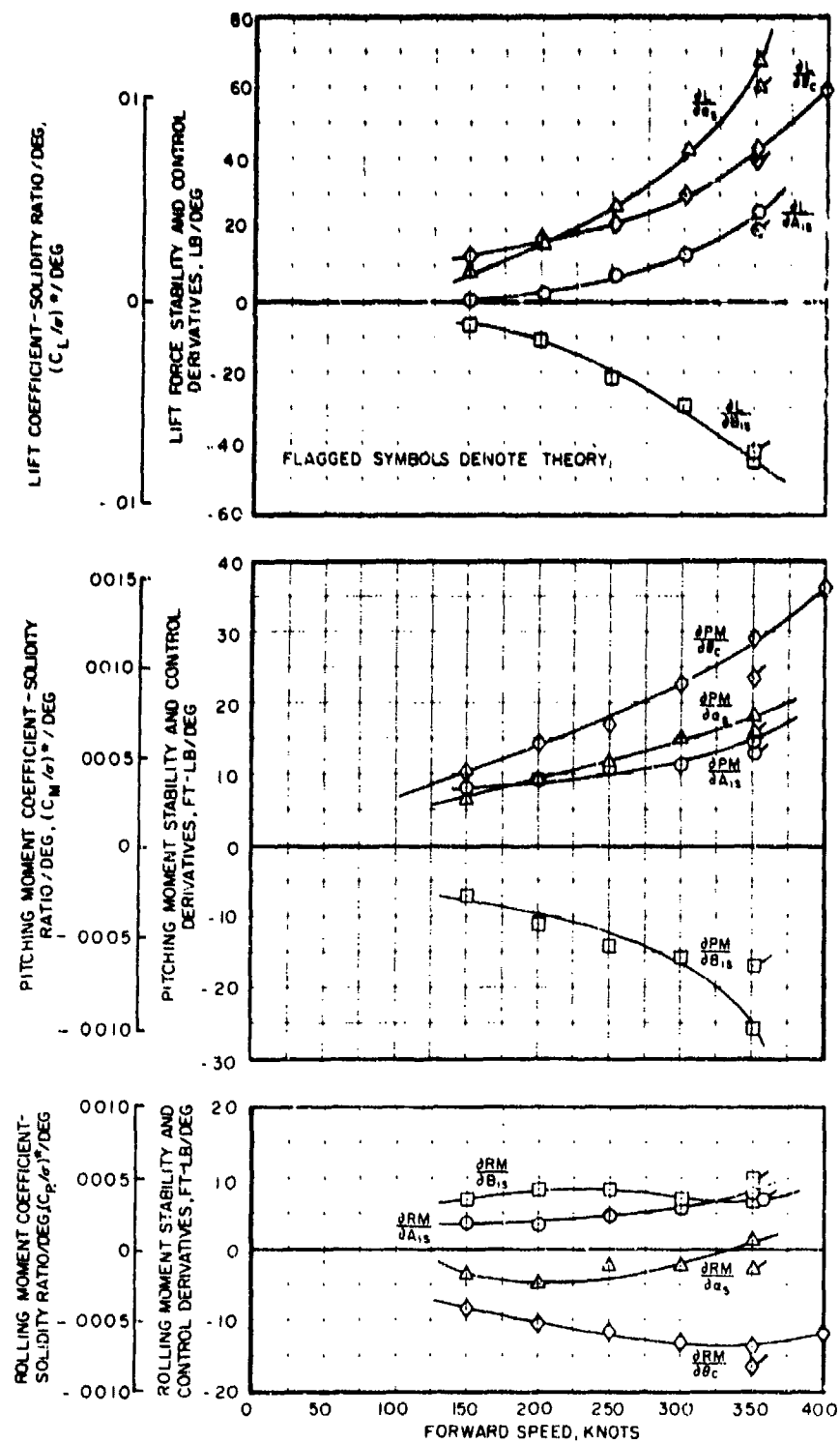


Figure 83. Stability and Control Derivatives at High Forward Speeds,
60.8% Diameter, 1184 rpm.

TEST RESULTS NORMALIZED TO A 10 FT/SEC GUST

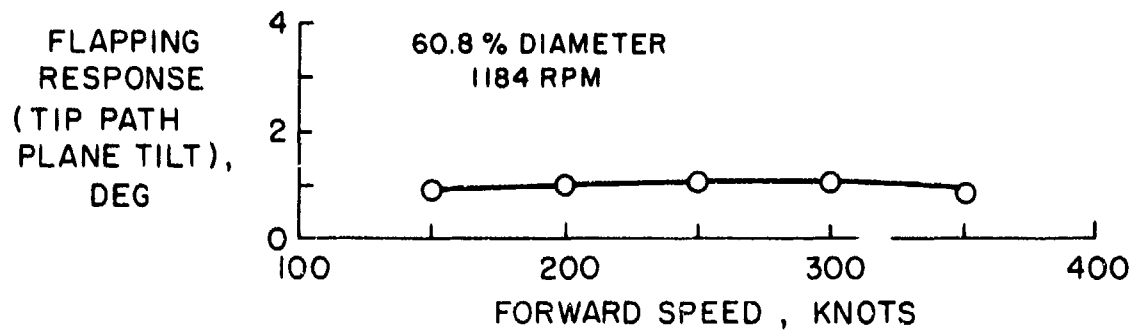
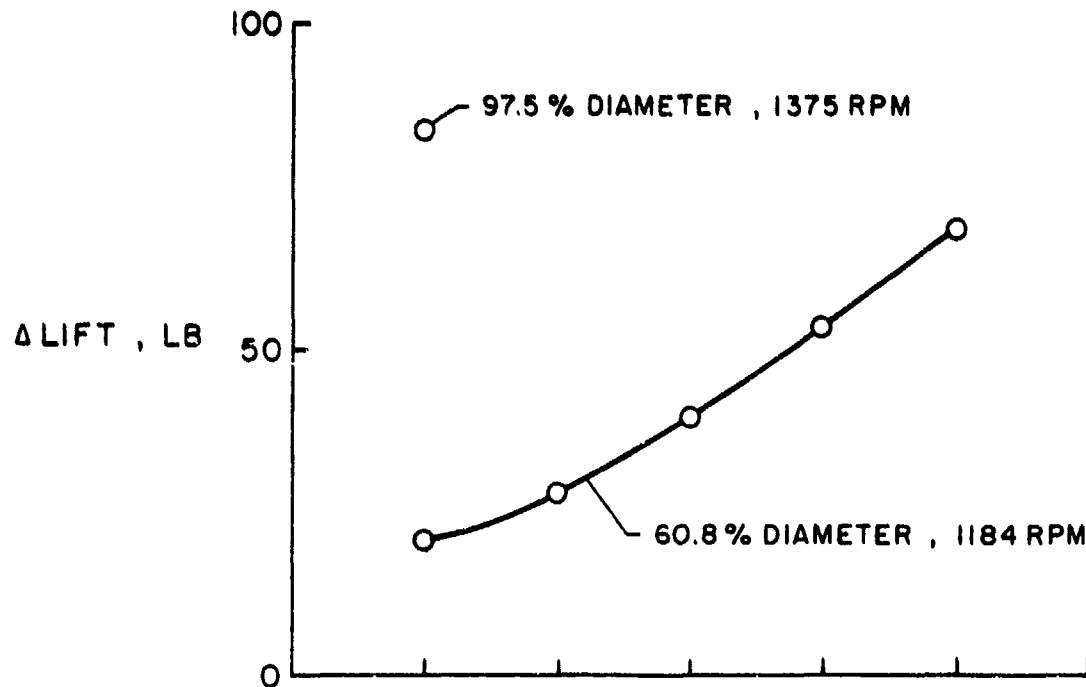


Figure 84. Gust Response Characteristics at High Forward Speeds.

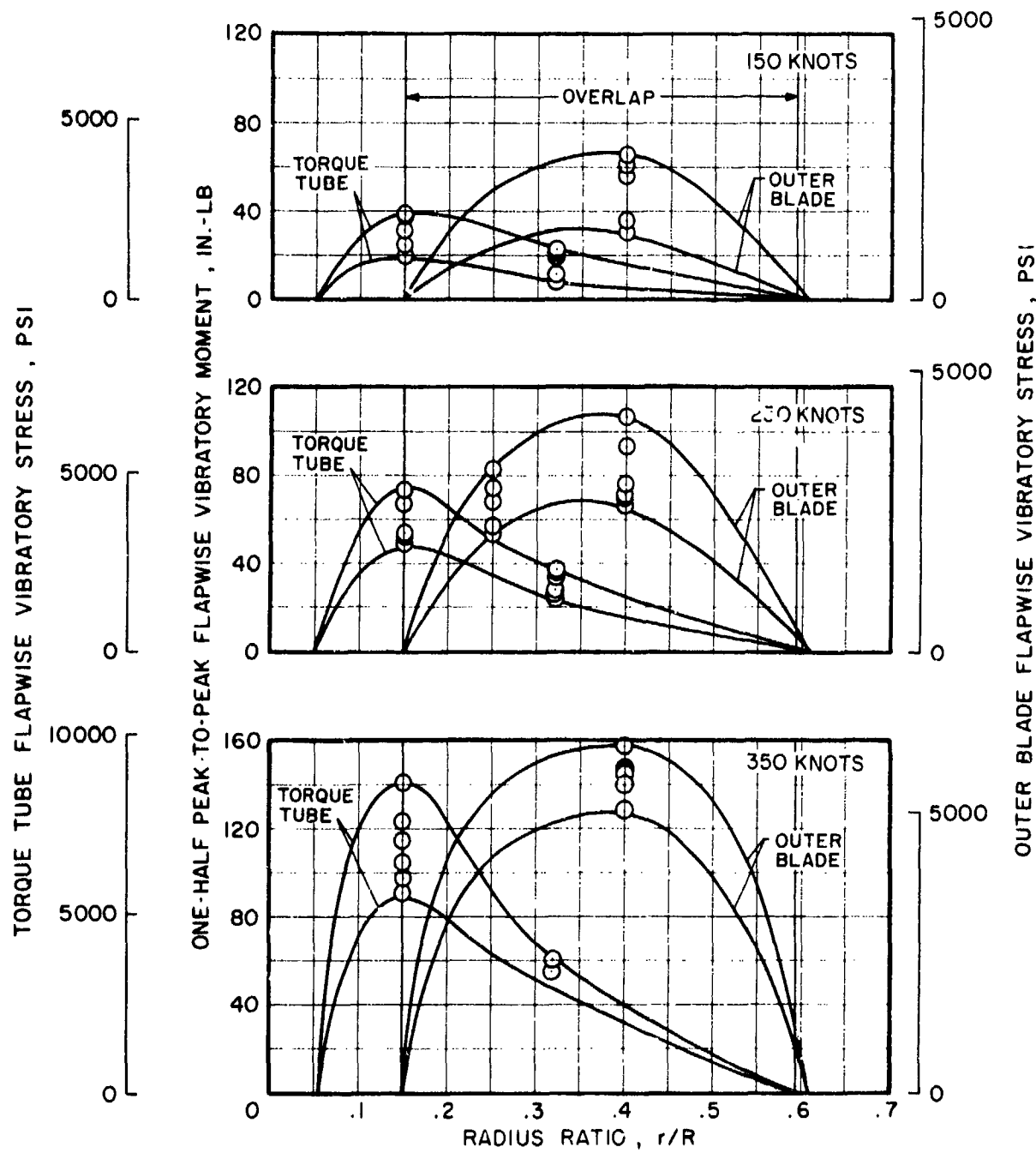


Figure 85. Effect of Forward Speed on Flapwise Vibratory Stress Distributions, 60.8% Diameter.

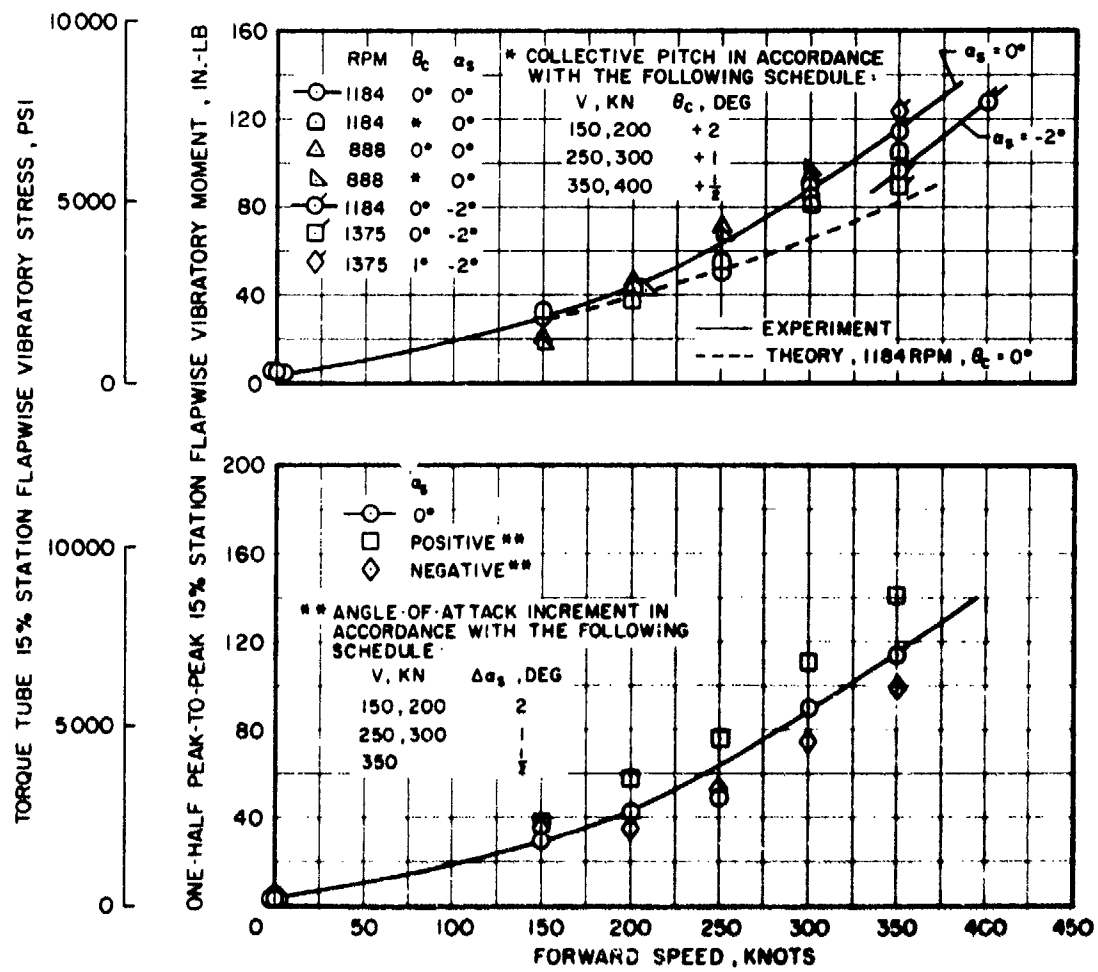


Figure 86. Variation of Torque Tube 15% Station Flapwise Vibratory Stress With Forward Speed, 60.8% Diameter.

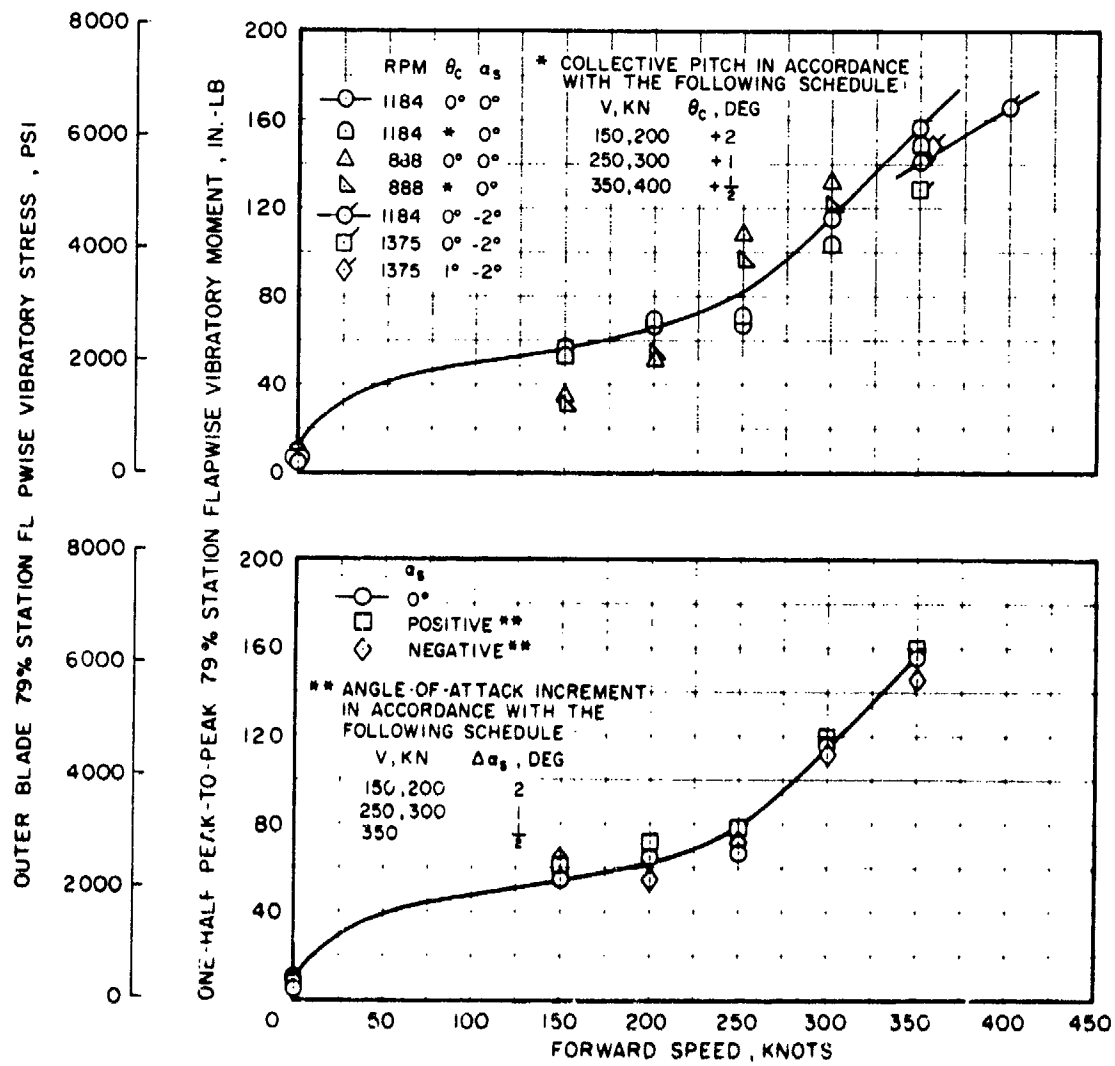


Figure 87. Variation of Outer Blade 79% Station Flapwise Vibratory Stress With Forward Speed, 60.8% Diameter.

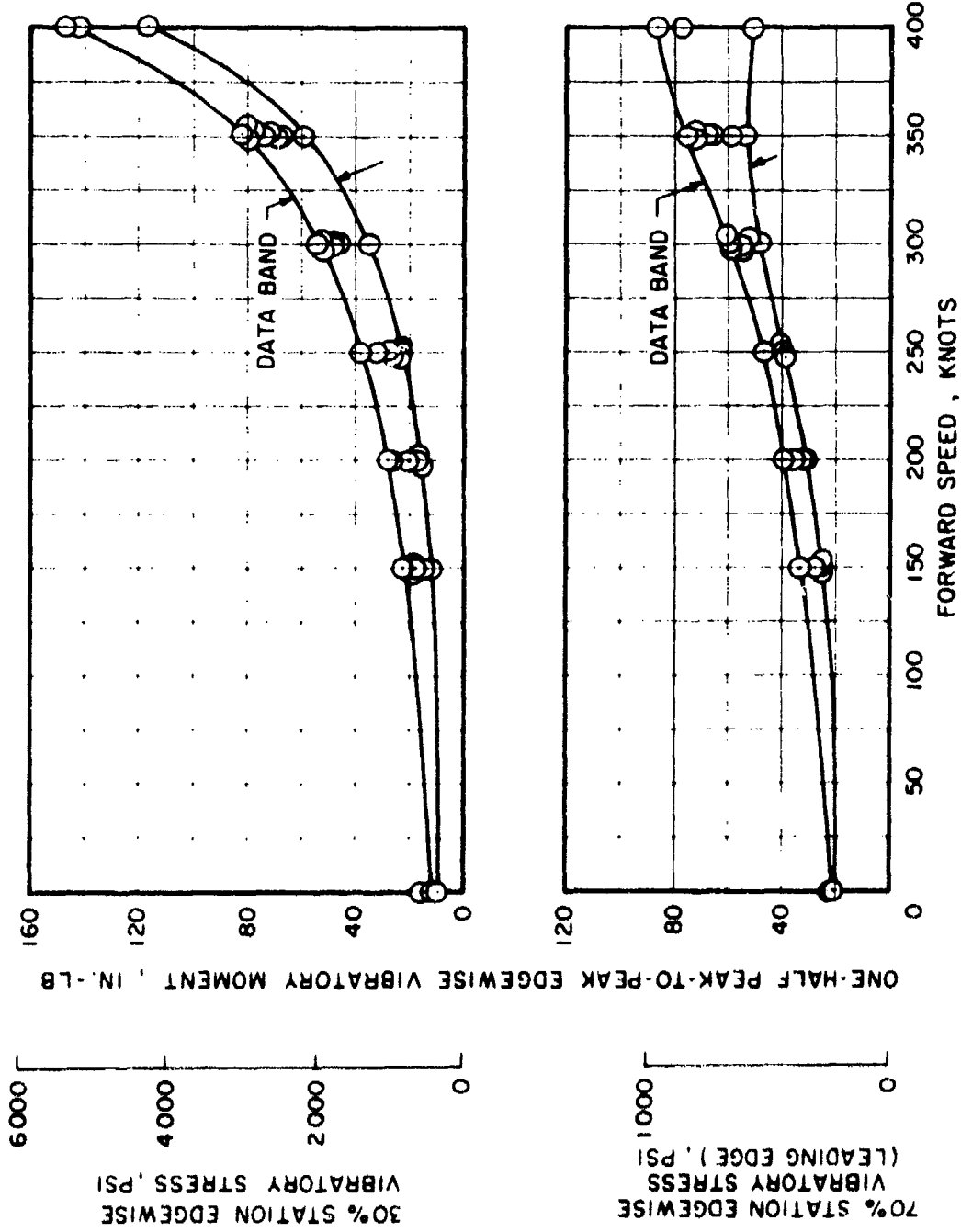


Figure 88. Variation of Edgewise Vibratory Stress With Forward Speed, 60.8% Diameter.

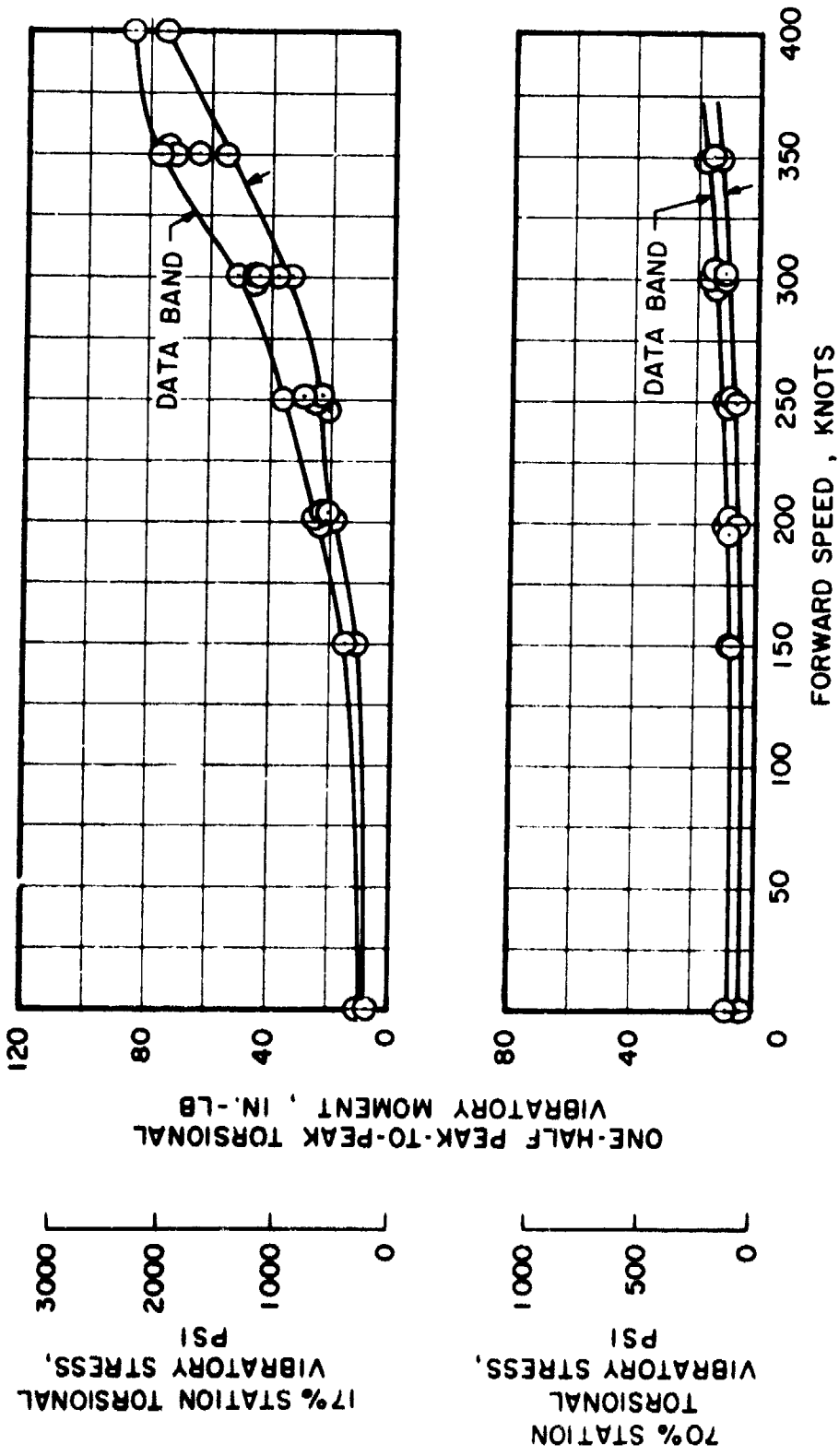


Figure 89. Variation of Torsional Vibratory Stress With Forward Speed, 60.8% Diameter.

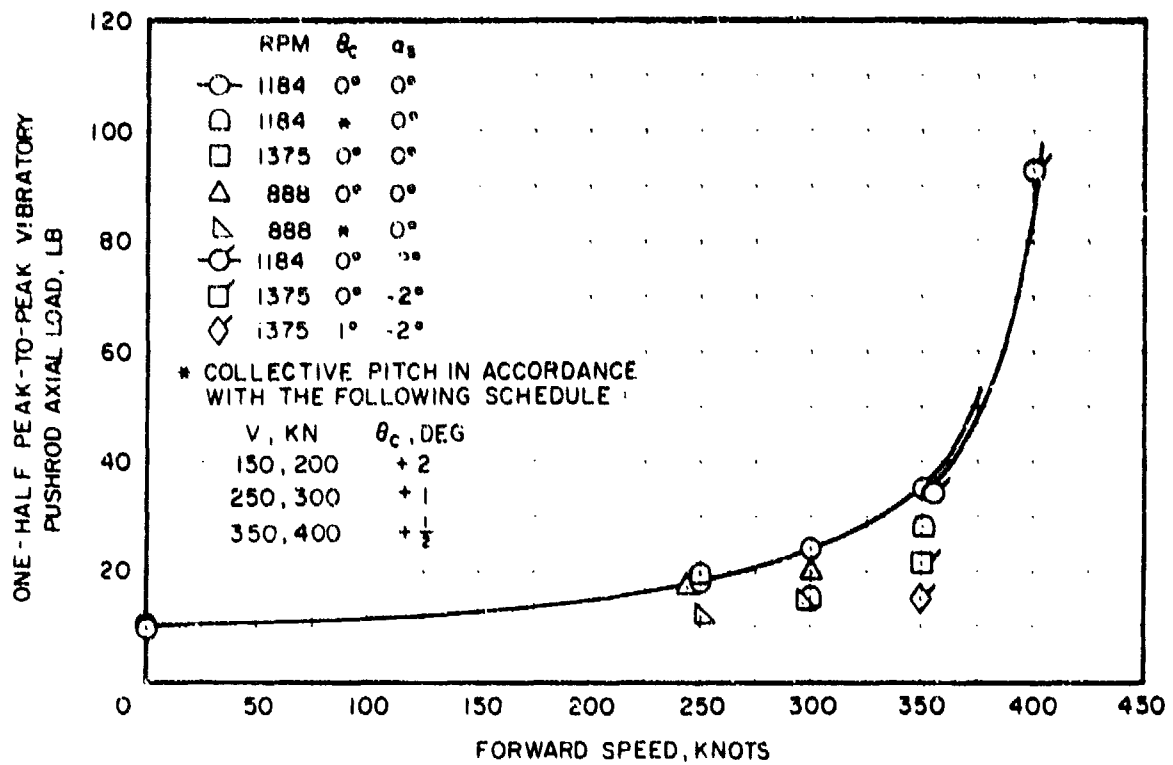


Figure 90. Variation of Pushrod Load With Forward Speed, 60.8% Diameter.

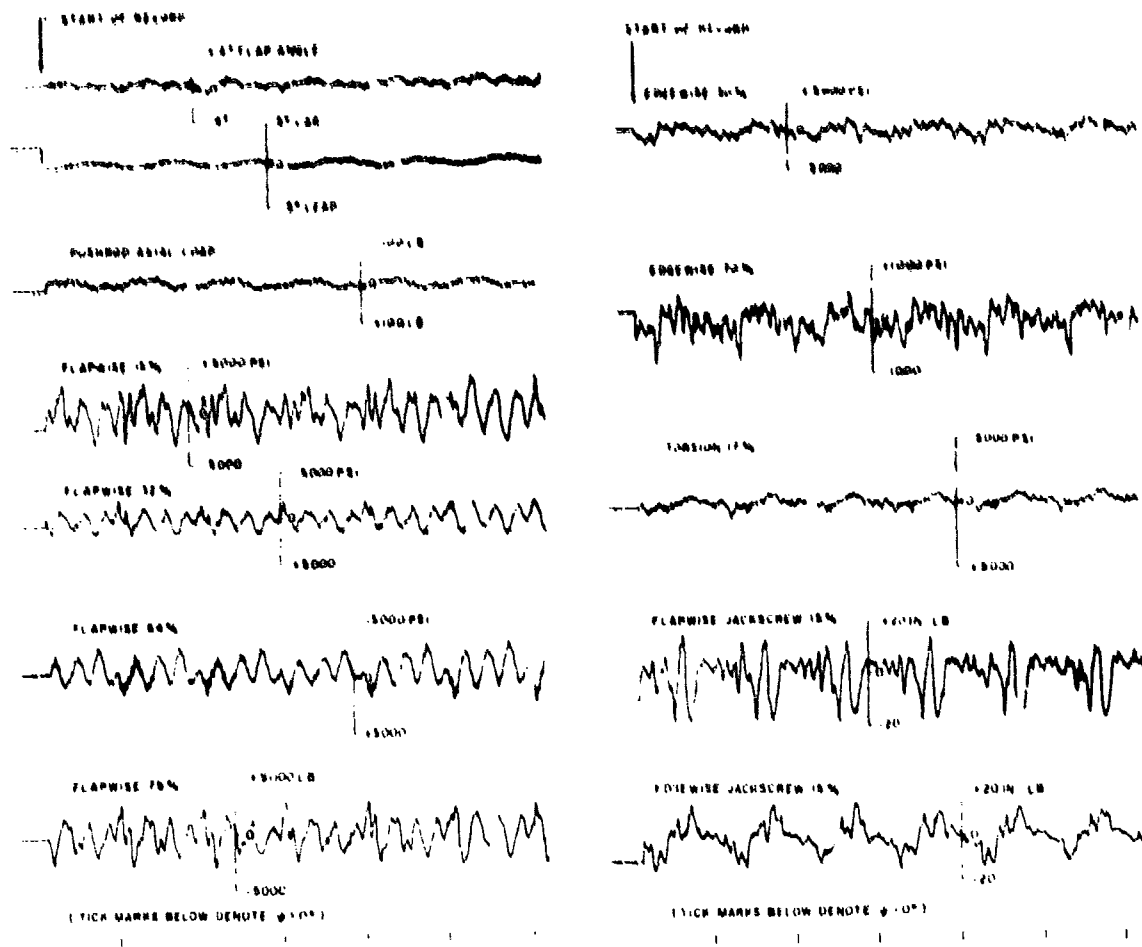


Figure 91. Measured Azimuthal Variation of Blade Stresses and Motion, 60.8% Diameter, 1184 rpm, $V = 250$ Knots,
 $a_s = 0^\circ$, $\theta_c = 0^\circ$, $A_{ls} = -2.6^\circ$, $B_{ls} = -0.6^\circ$.

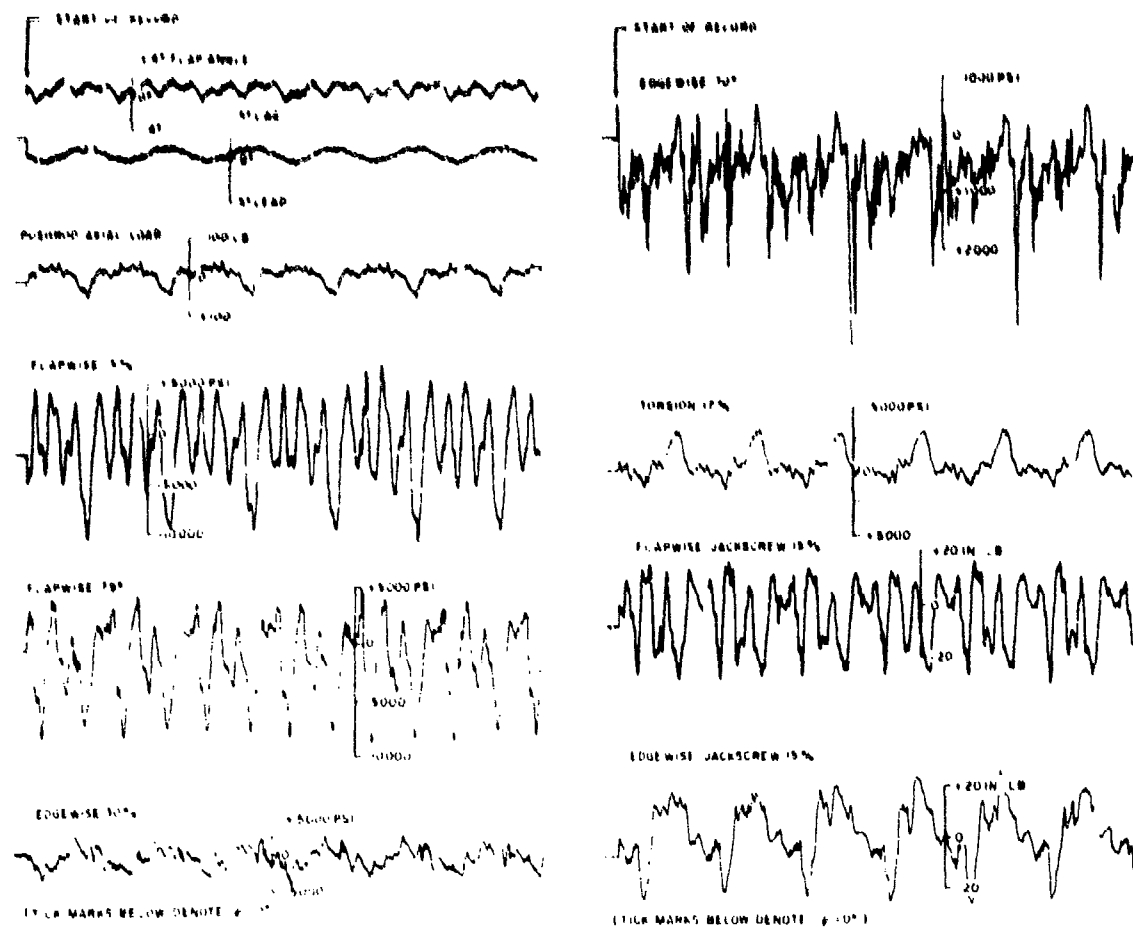


Figure 92. Measured Azimuthal Variation of Blade Stresses and Motion, 60.8% Diameter, 1184 rpm, $V = 350$ Knots,
 $\alpha_s = 0^\circ$, $\theta_c = 0^\circ$, $A_{ls} = -3.9^\circ$, $B_{ls} = -1.0^\circ$.

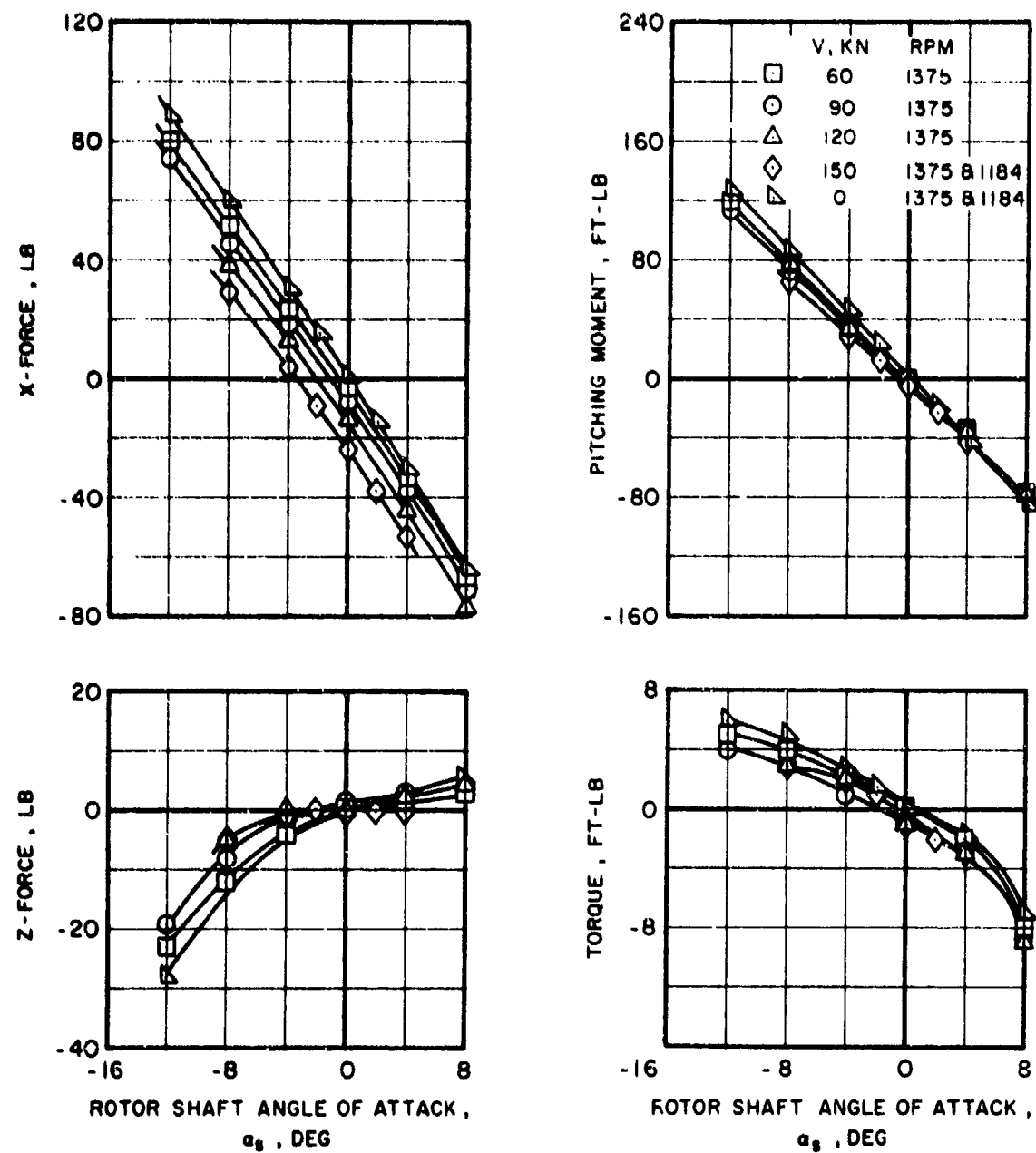


Figure 93. Typical Total Rotor Head Tares (Aerodynamic Plus Gravity).

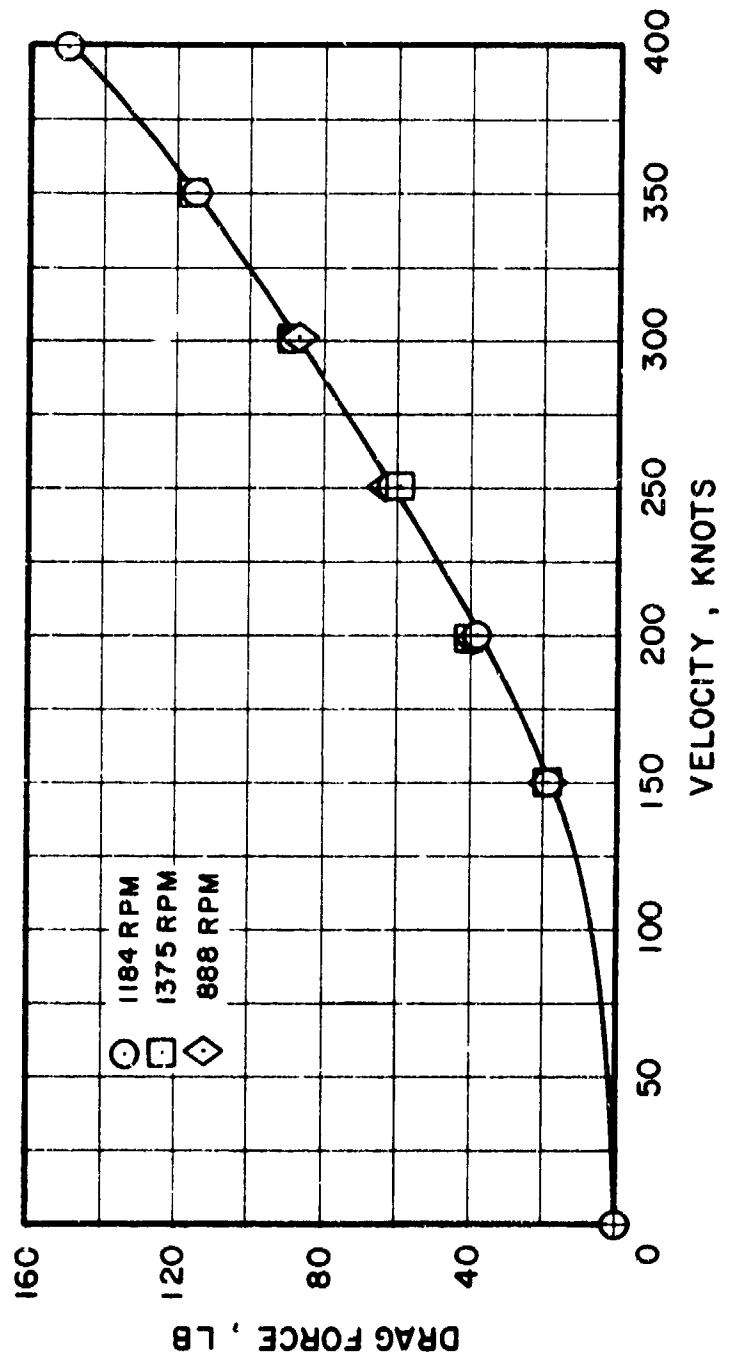


Figure 94. Rotor Head Drag Tare at High Forward Speeds, $\alpha_s = 0^\circ$.

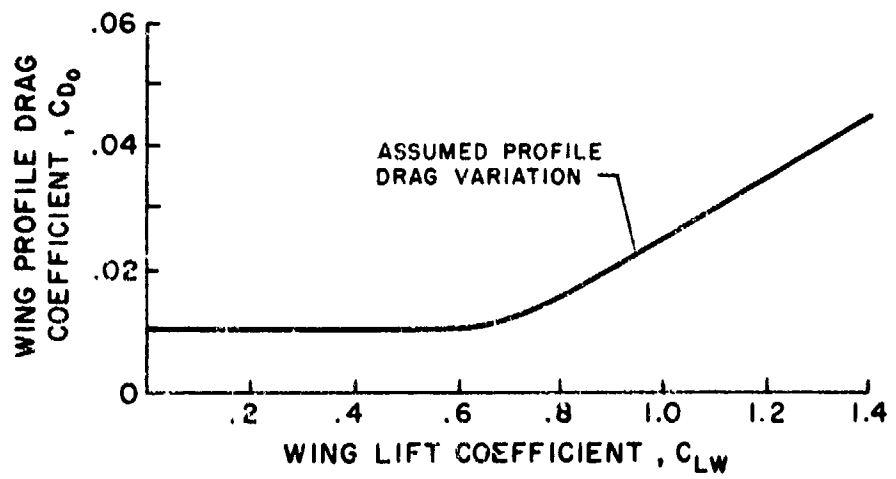
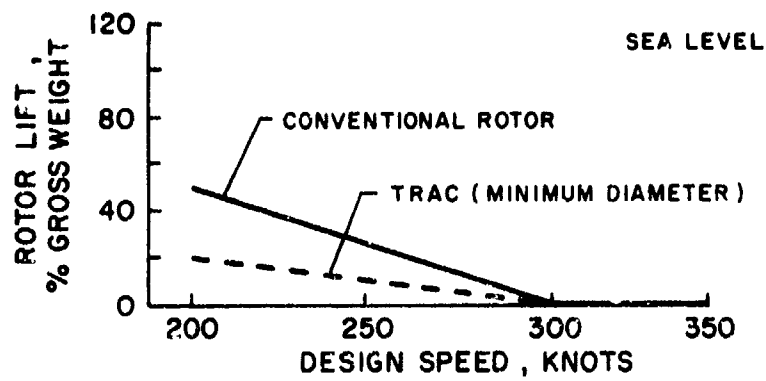


Figure 95. Assumed Rotor Lift Schedule and Wing Profile Drag.

WING AREA FT ²	SPAN FT.	ASPECT RATIO	WING LOADING PSF
207	40	6.0	150
400	49	6.0	100
600	60	6.0	67

EXTENDED DIA 720 FT
 RETRACTED DIA 432 FT
 GROSS WEIGHT 40000 LB.
 HOVER TIP SPEED 700 FT/SEC
 σ (EXTENDED) .095

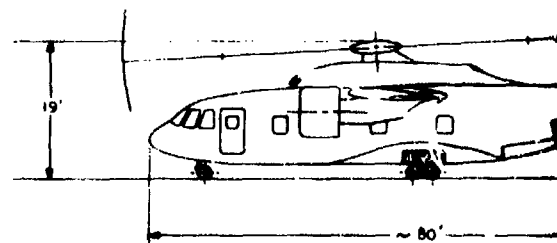
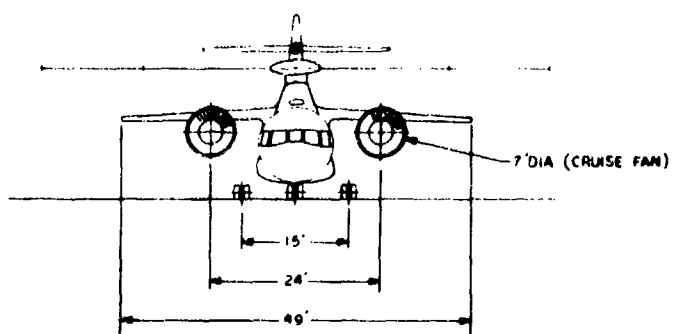
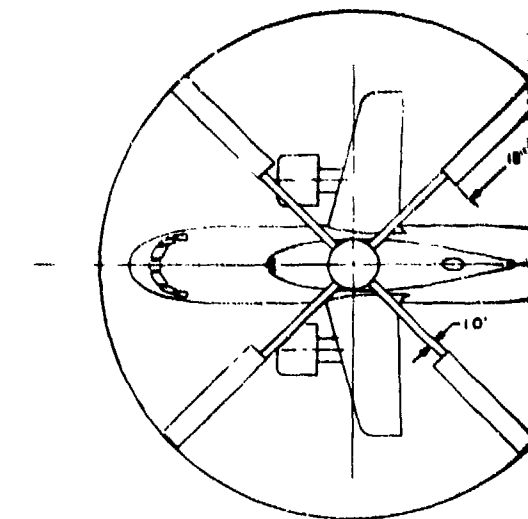
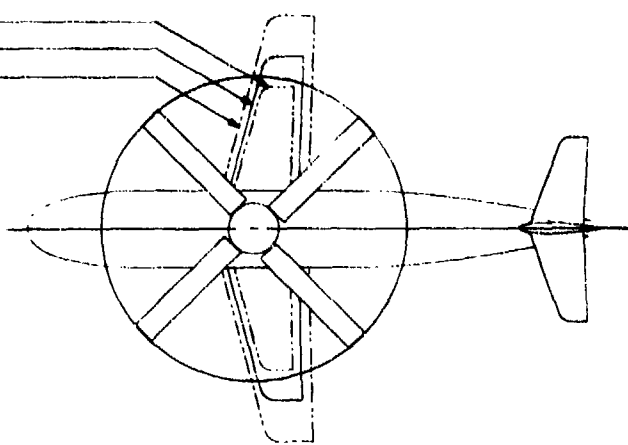
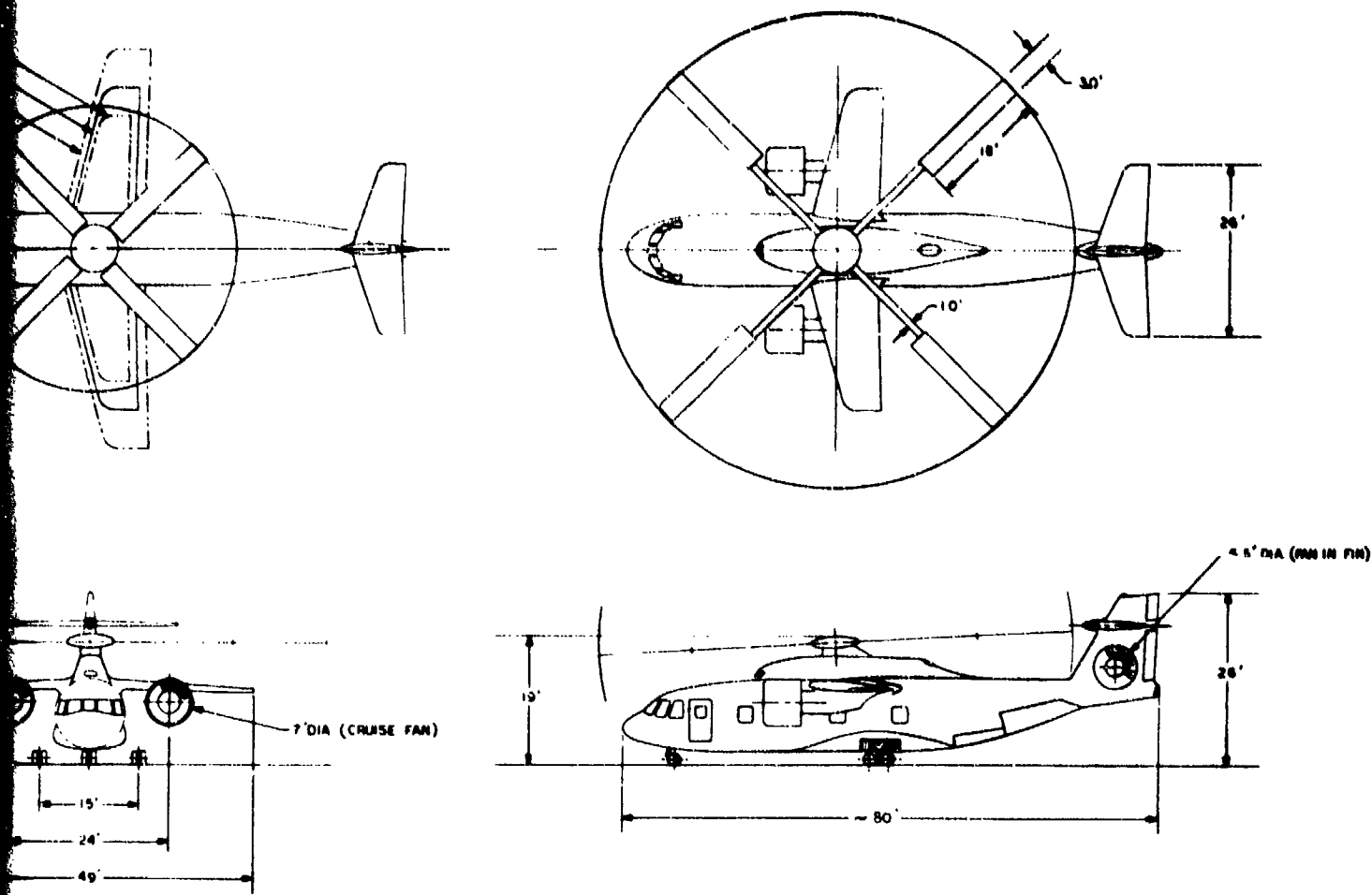


Figure 96. General Arrangement of Typical Compound Helicopter With TRAC Rotor.



Front and Rear View of Typical Compound Helicopter

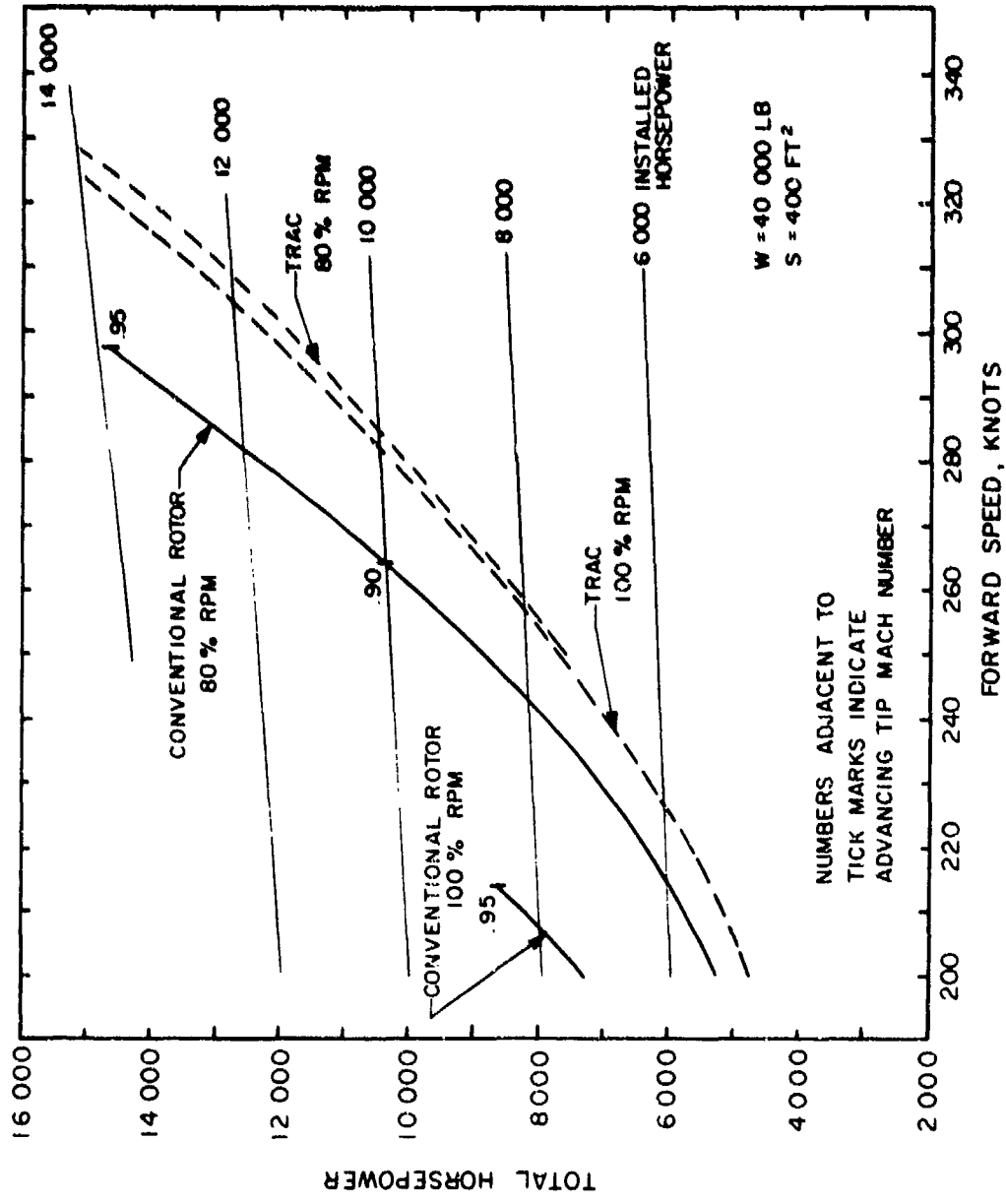


Figure 97. Power Required for Compound Helicopter at Sea Level.

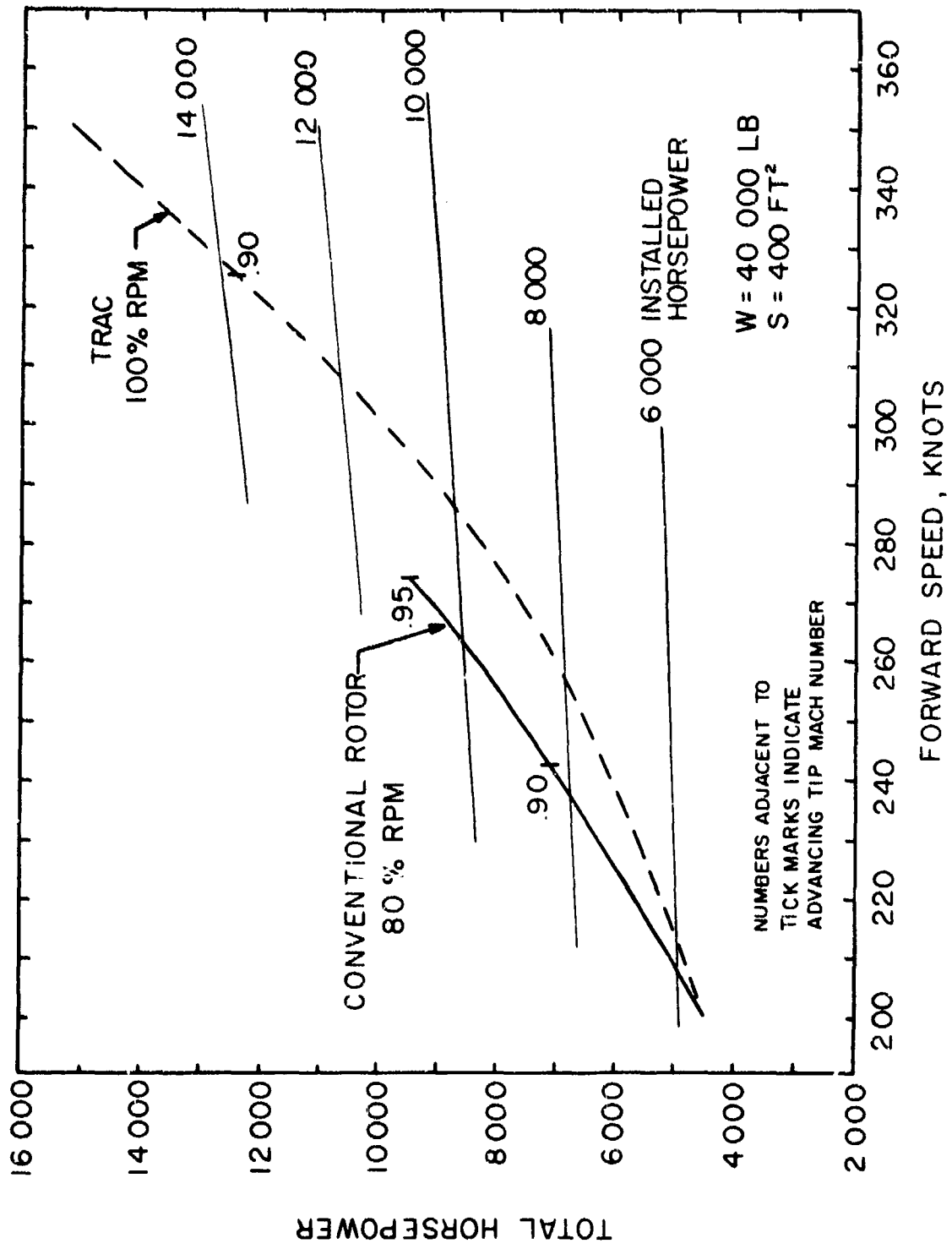


Figure 98. Power Required for Compound Helicopter at 10,000 Feet Altitude.

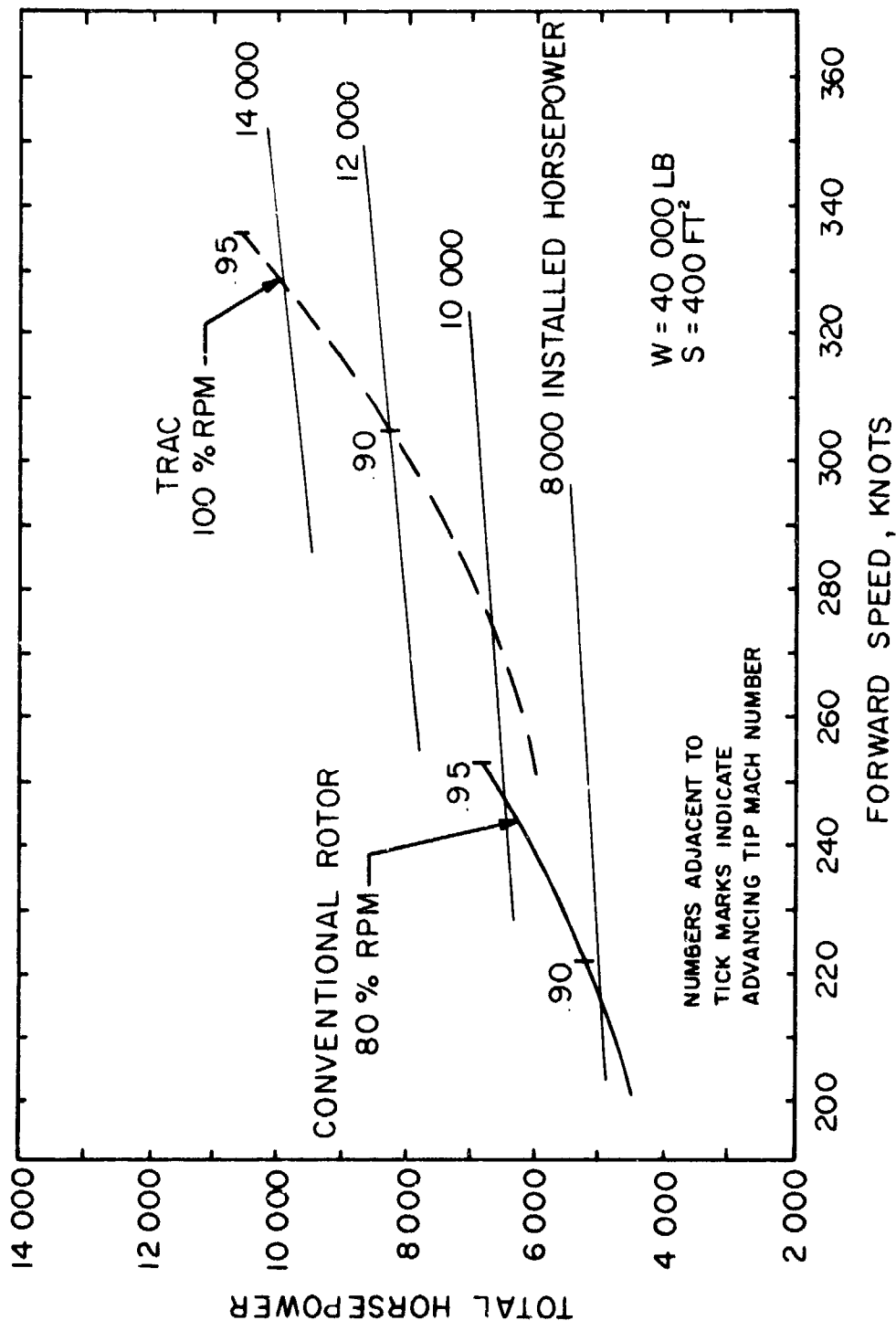


Figure 99. Power Required for Compound Helicopter at 20,000 Feet Altitude.

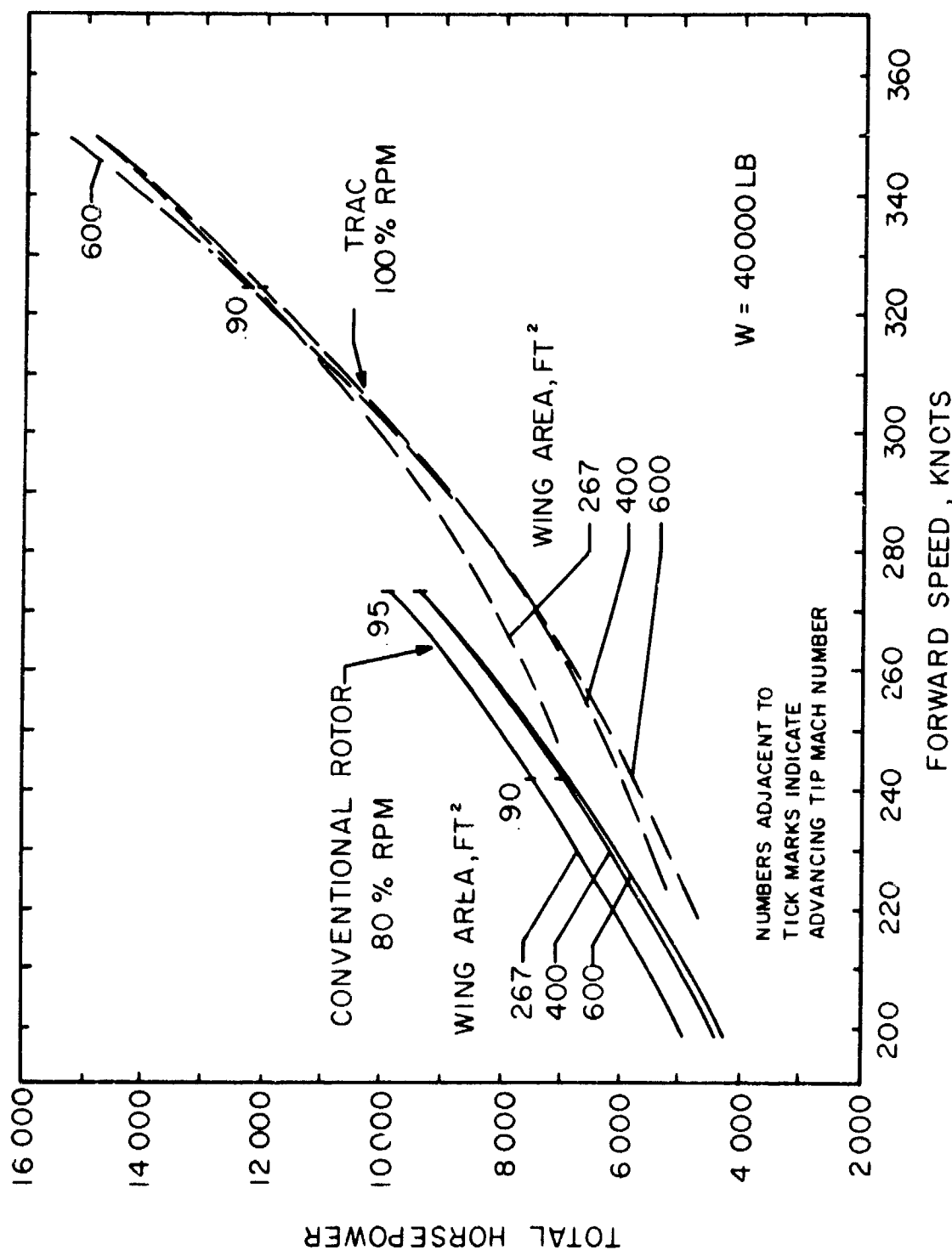


Figure 100. Effect of Wing Area on Performance at 10,000 Feet Altitude.

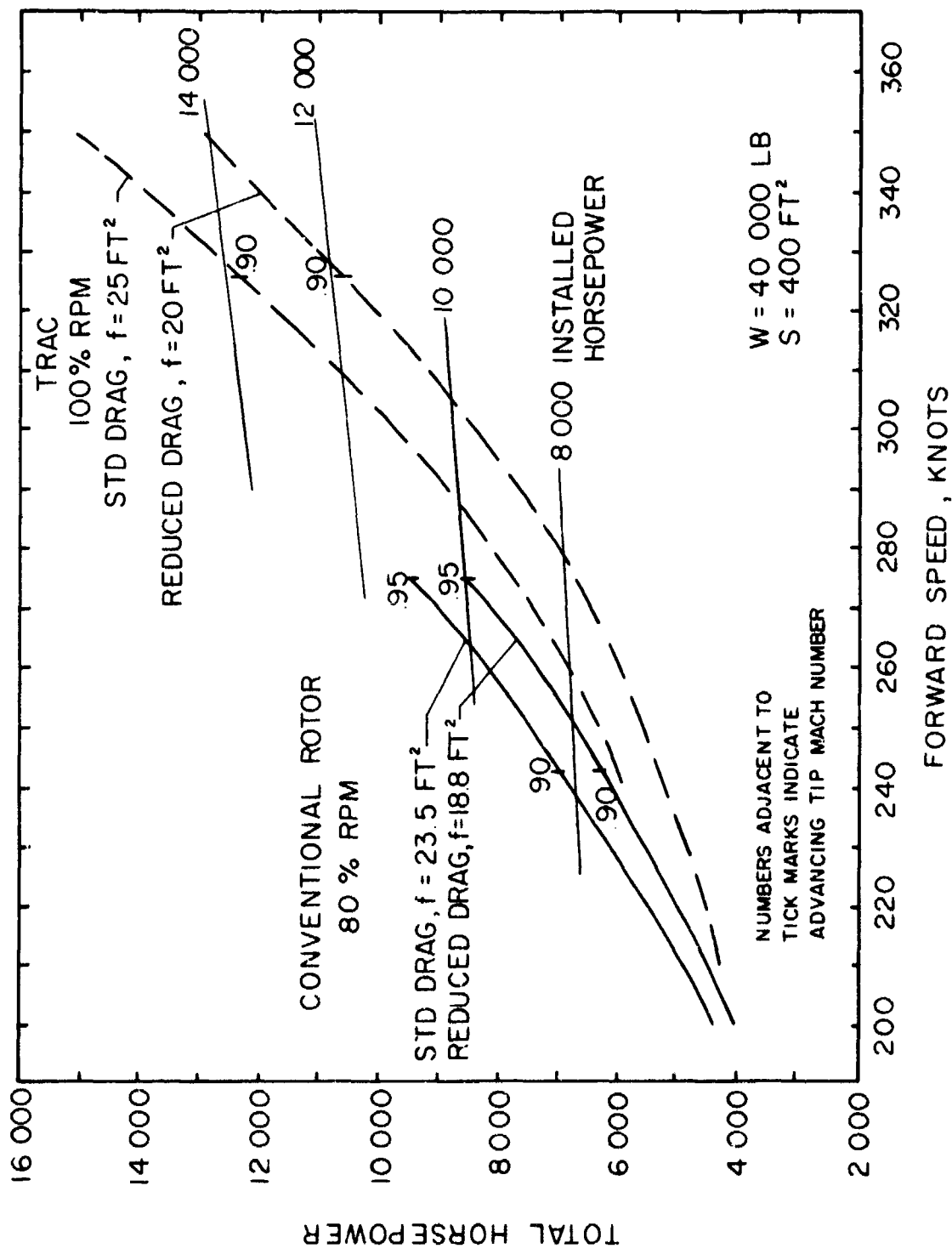
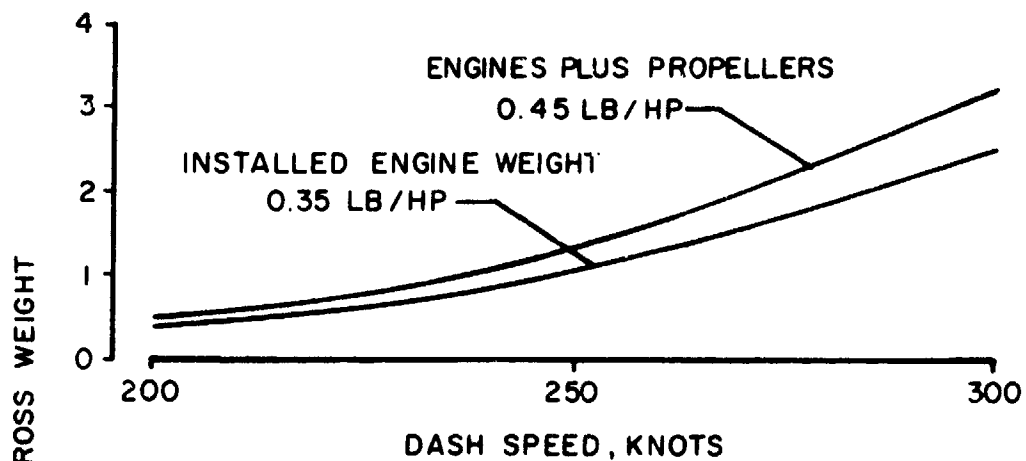


Figure 101. Effect of 20 Percent Drag Reduction on Performance at 10,000 Feet Altitude.

PROPULSION SYSTEM WEIGHT



FUEL WEIGHT

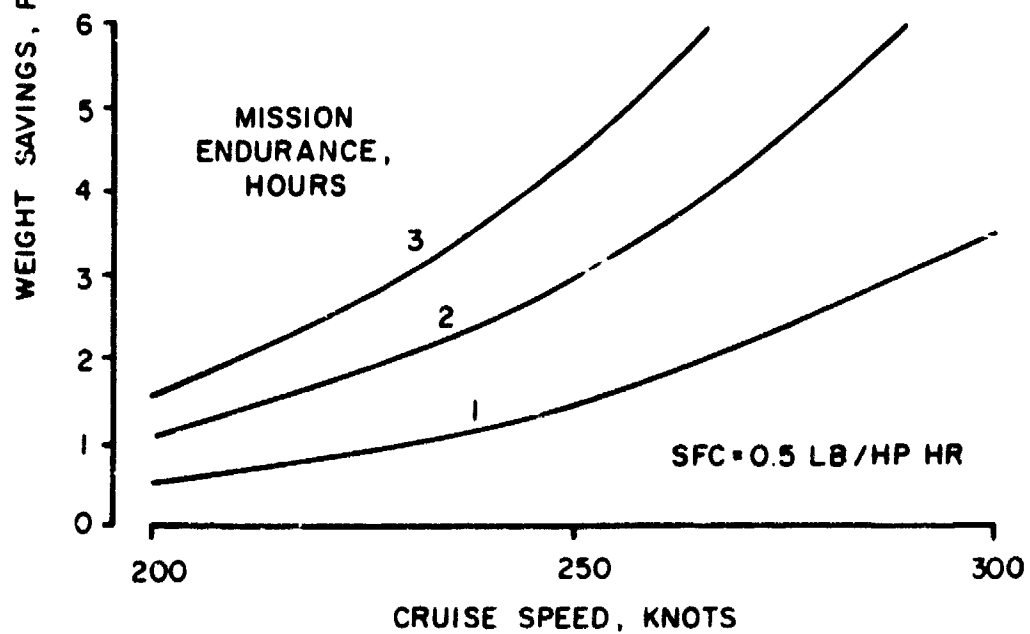


Figure 102. Weight Savings due to Power Reduction With TRAC Rotor, Sea Level.

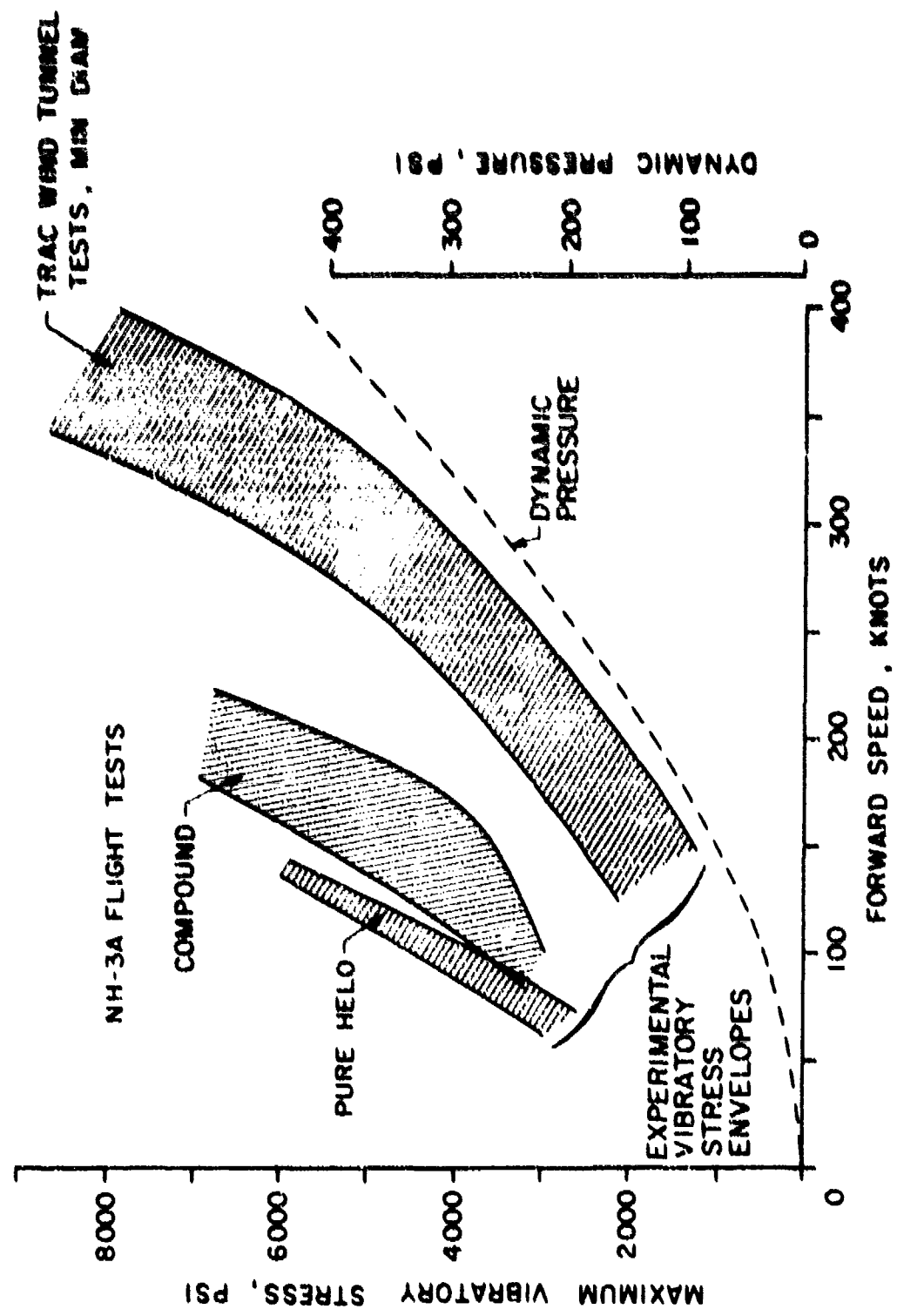


FIGURE 103. Blade Vibratory Stress Comparisons.

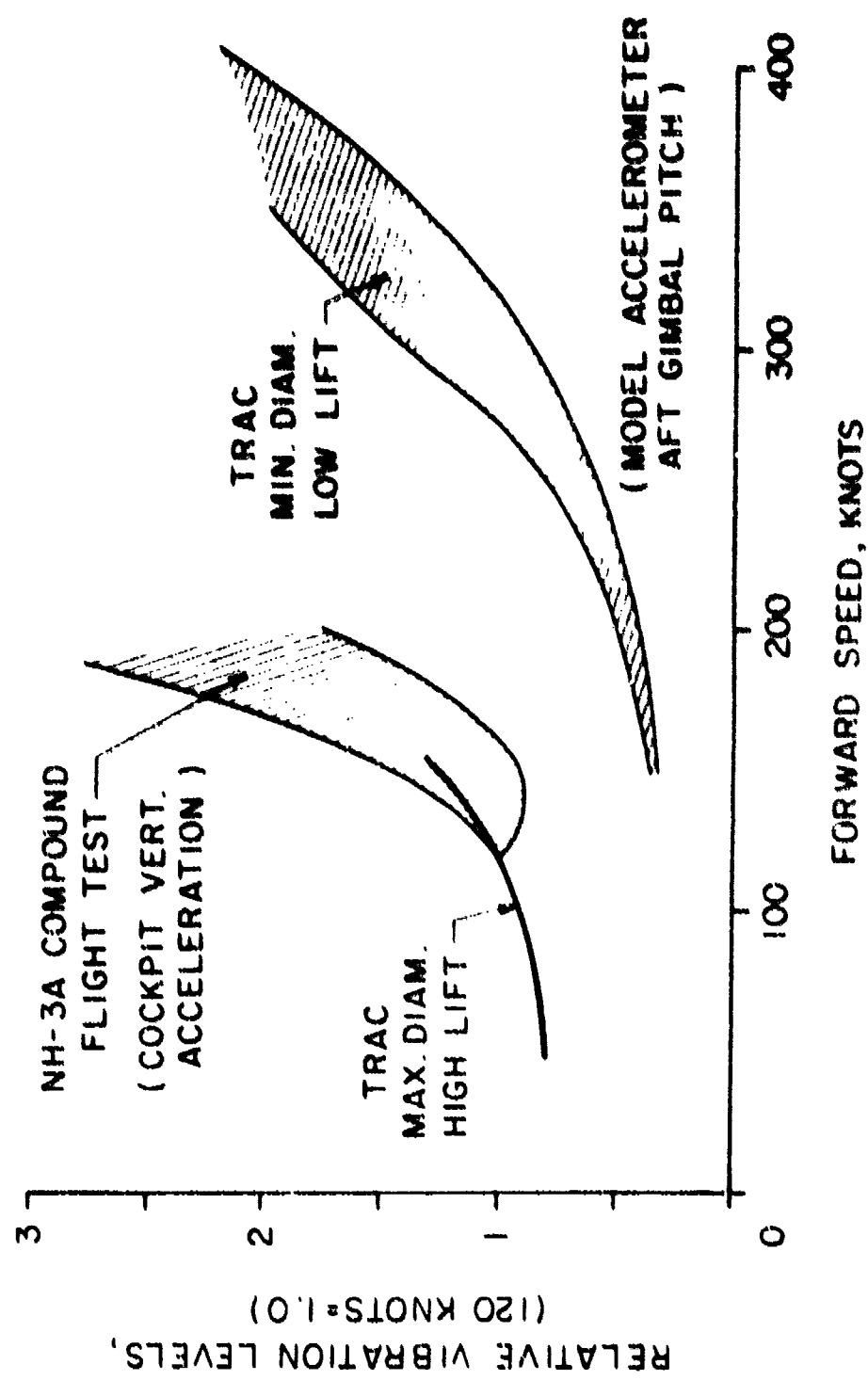


Figure 104. Attitude Vibration Comparison.

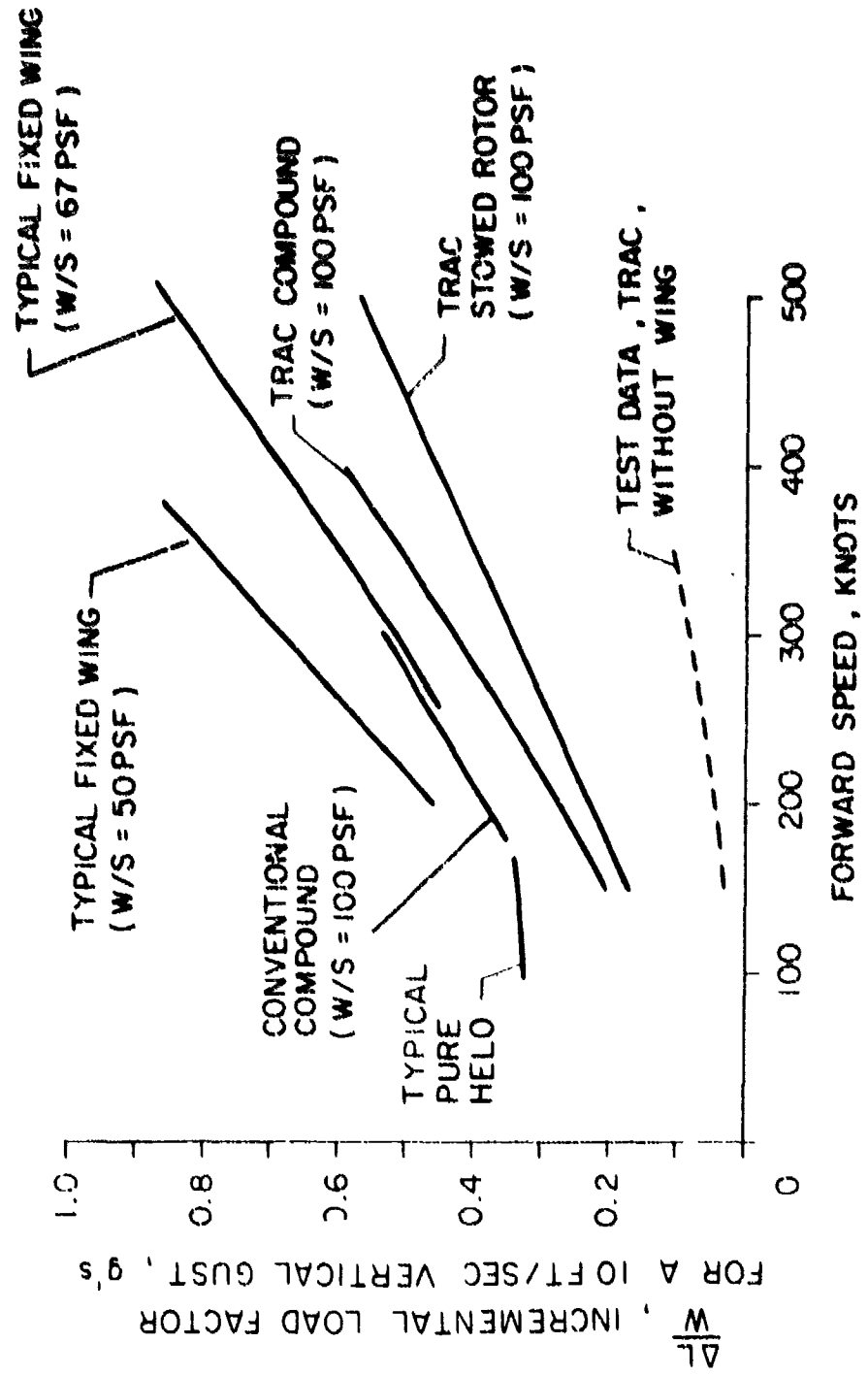


Figure 105. Aircraft Gust Response Comparisons at Sea Level.

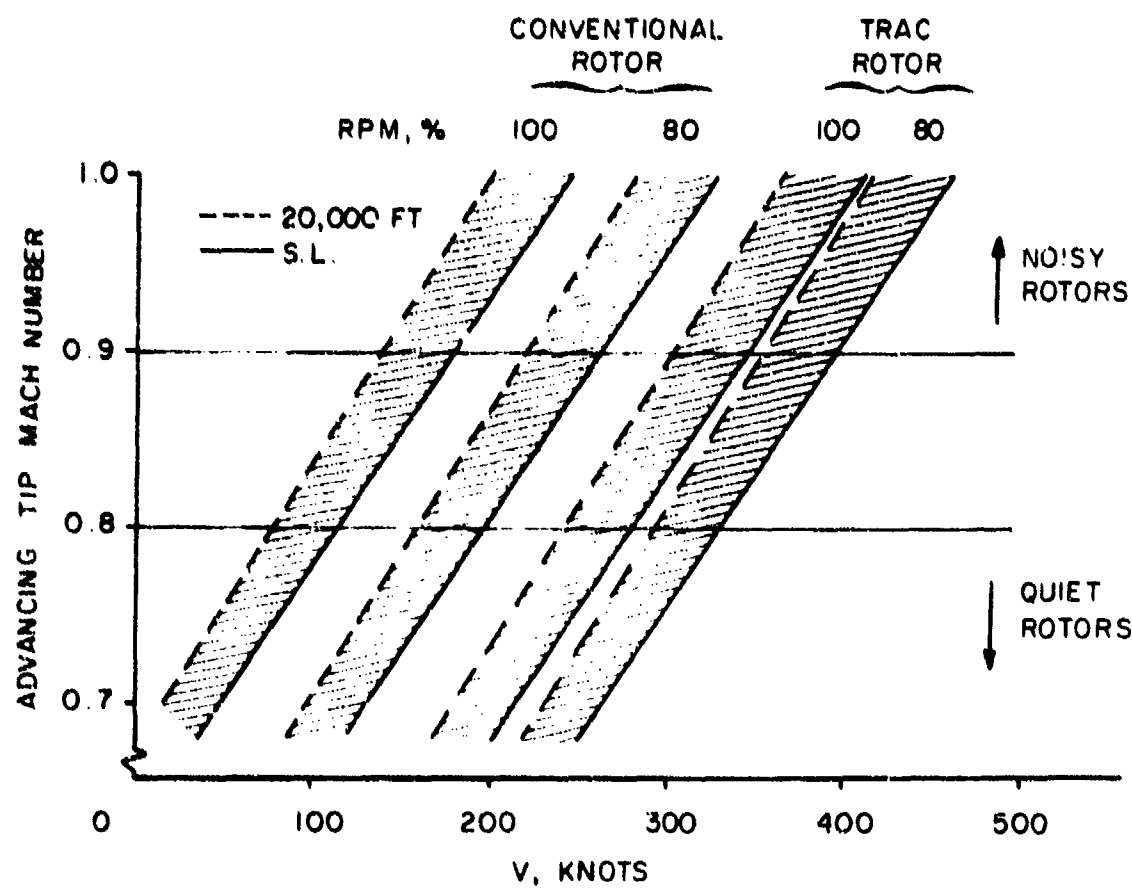


Figure 106. Rotor Advancing Tip Mach Number/Noise Comparison.

APPENDIX I

DETAILS OF FULL-SCALE PRELIMINARY DESIGN STUDY

Data provided in APPENDIX I supplement the information presented under the heading PRELIMINARY DESIGN STUDY OF FULL-SCALE ROTOR, pages 4-6 of this report.

Rotor Hub and Diameter Change Actuation Mechanism

The main rotor is a four-bladed, fully articulated rotor system with co-incident flapping and lag hinge. This configuration, shown in Figure 107, is basically a conventional Sikorsky design, having upper and lower hub plates, vertical hinge member, sleeve and spindle assembly, anti-flapping-droop restrainer, and dampers. Differences between this design and a conventional rotor head include a central hub which houses the differential gear assembly; a special vertical hinge member having conventional bearings mounted vertically on one set of journals and roller bearings mounted horizontally on the other set, thus enabling the universal joint in the jackscrew drive train to pass through a central opening in the hinge member; removable yoke arms, large enough to retain roller bearings to allow blade flapping and necessary for installation to the hinge; and dampers mounted on the top of the rotor head designed to act as blade-fold pistons, which when actuated fold the blades to a maximum of 50°.

The differential gears and coaxial shafts used in actuating diameter changes are of conventional type, and the design analysis was limited to verification that the required actuation torques were within the load capacity of the components selected. A positive mechanical stop system, utilizing a traveling nut between the two coaxial actuation shafts, was devised to prevent excessive blade extensions or retractions; a mechanical diameter lock was also incorporated.

Blade Design

The major components of the blade consist of the outer blade, torque tube, and the internal components (jackscrew, nut, and tension straps). A general arrangement of the blade is shown in Figure 108. Blade loads were determined from the flight conditions below. Condition #1 was used to determine the vibratory stress levels, and conditions #2-#4 were used for the static analysis.

- Condition #1: Max cruise speed as a pure helicopter, $V = 100$ knots, $N = 185$ rpm, $W = 40,000$ lb
- #2: Same as #1 with a 30-fps upward gust
- #3: Pullout maneuver, 120% rotor rpm, rotor load factor 1.4, $V = 100$ knots, $N = 223$ rpm, rotor thrust = 56,000 lb
- #4: Stopped rotor (minimum diameter), $V = 150$ knots, max blade section lift coefficient (1.3) over entire exposed length.

A stress analysis based on the above load conditions was conducted, and wall thicknesses, etc., were adjusted to provide acceptable calculated

stresses for all conditions. A brief description of the blade components follows:

Outer Blade

The outer section of the blade is composed of two major components: the spar assembly and the pocket or trailing edge of the airfoil section. A planform and cross-sectional view of this section are shown in Figure 108. The spar is an aluminum extrusion with a sheet aluminum and honeycomb core sandwich aft section covering most of the length of the spar. Both the extrusion and sandwich facings are 2014-T6 aluminum. The extrusion is similar to the "D" section extrusions used on other Sikorsky blades. To locate both the center of gravity and neutral axis of the blade on the 25% chord position, the aft portion of the extruded spar is removed as shown in Figure 109 and replaced by the sandwich type of structure. The solid "D" section is retained only in the overlap region and at the tip of the blade, where the centrifugal force of the outer blade is transferred to the tension straps.

The trailing-edge pocket is a structural member on the TRAC blade, unlike the nonstructural pockets used on other Sikorsky blades. This structural fairing consists of a honeycomb core with an aluminum facing bonded to the core and to the outer facing of the spar.

Torque Tube

The torque tube, shown in Figure 109, is an elliptical cross-sectional titanium tube which has a constant wall thickness of .125 in. over most of its length. The wall thickness is increased to .250 in. in the blade overlap region on the outboard end and also at the inboard end adjacent to the area where the elliptical shape of the tube begins the transition into the circular cross section for the cuff.

Internal Components

The blade jackscrew and nut were designed to retract or extend the rotor blade in approximately 30 seconds with the main rotor operating at full rpm.

The specifications used in the design analysis for the screw and nut are:

Outside diameter	3.000 in.
Pitch diameter	2.850 in.
Minor diameter	2.690 in.
Internal diameter (bore)	2.050 in.
Pitch	0.500 in.
Lead	1.000 in.
Thread	Modified 10° square stub, double, left hand
Thread thickness	0.242 in.

Material	9317 steel, carburized threads
Screw speed	344 rpm
Length of nut travel	176 in.
Time of travel	31 sec
Number of threads on nut	19
Thread bearing stress	5000 psi
Screw efficiency, dynamic (coeff. of friction 0.10)	0.52
Screw efficiency, static (coeff. of friction 0.13)	0.46

Tension Straps

The tension straps shown in Figure 108 are circular in cross section and taper at the ends to a flat, rectangular cross section for attachment to the tip block and nut.

Bearing Blocks

Two sets of bearing blocks are utilized for the sliding contact between the torque tube and outer blade. One set is attached to the outboard end of the torque tube and one set to the inboard end of the outer blade. Teflon sheet bonded to aluminum contoured blocks was selected for the bearing surface. Figure 108 shows the method of attaching these blocks to their respective member. This method was chosen over a block of solid bearing material because it provides the possibility of shimming to adjust for manufacturing tolerances and wear and can be easily replaced.

Blade Mass Properties

The spanwise mass distribution of the blade is presented in Figure 110. Total weight for one blade, up to and including the cuff attachment and including the internal components, is 760 pounds. The centrifugal force distribution for the various blade components at 185 rpm is shown in Figure 111. All of the components are in tension except for the outer blade, which is in compression. The centrifugal load of the outer blade is zero at the inboard end and reaches a maximum at the tip.

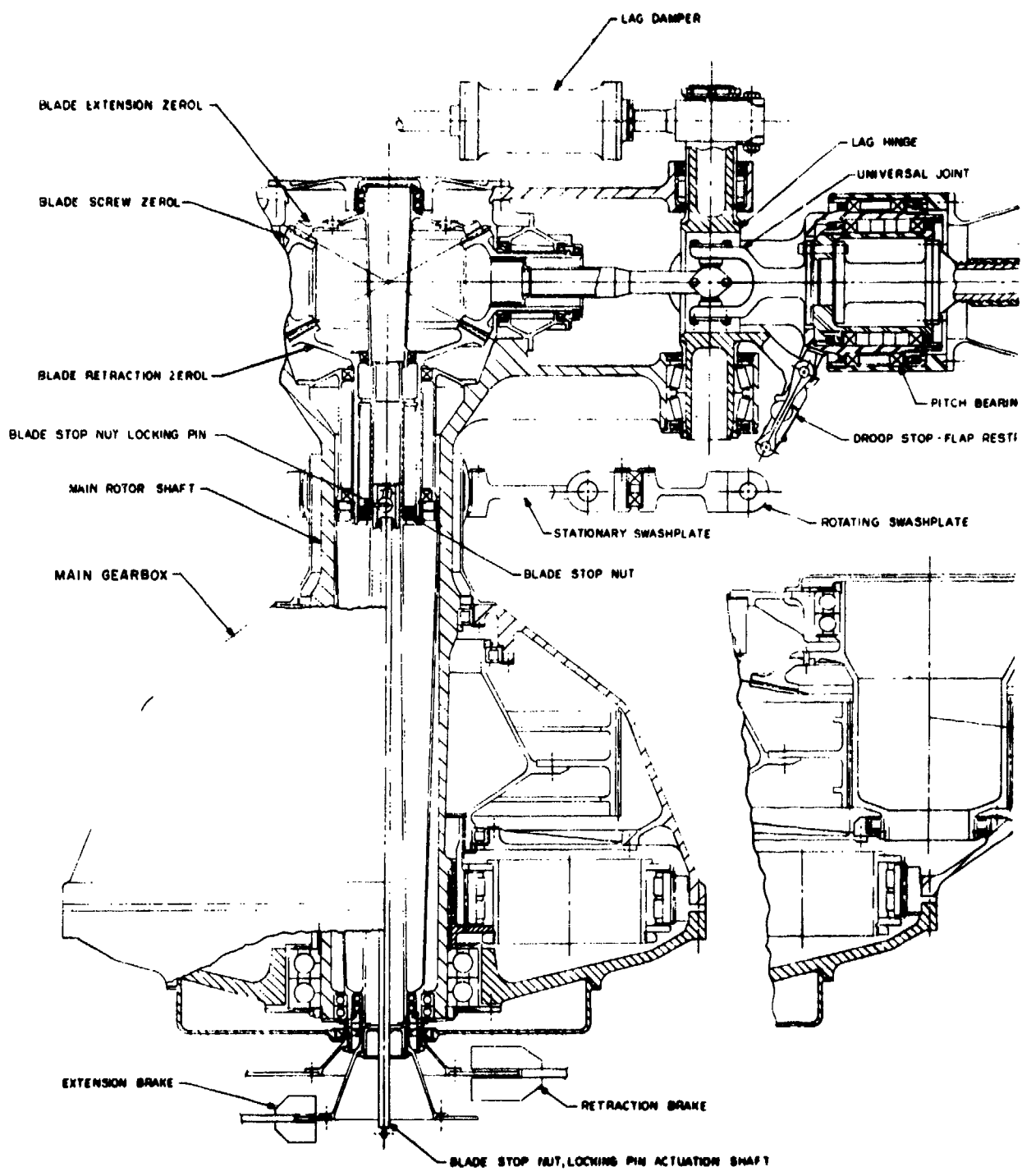
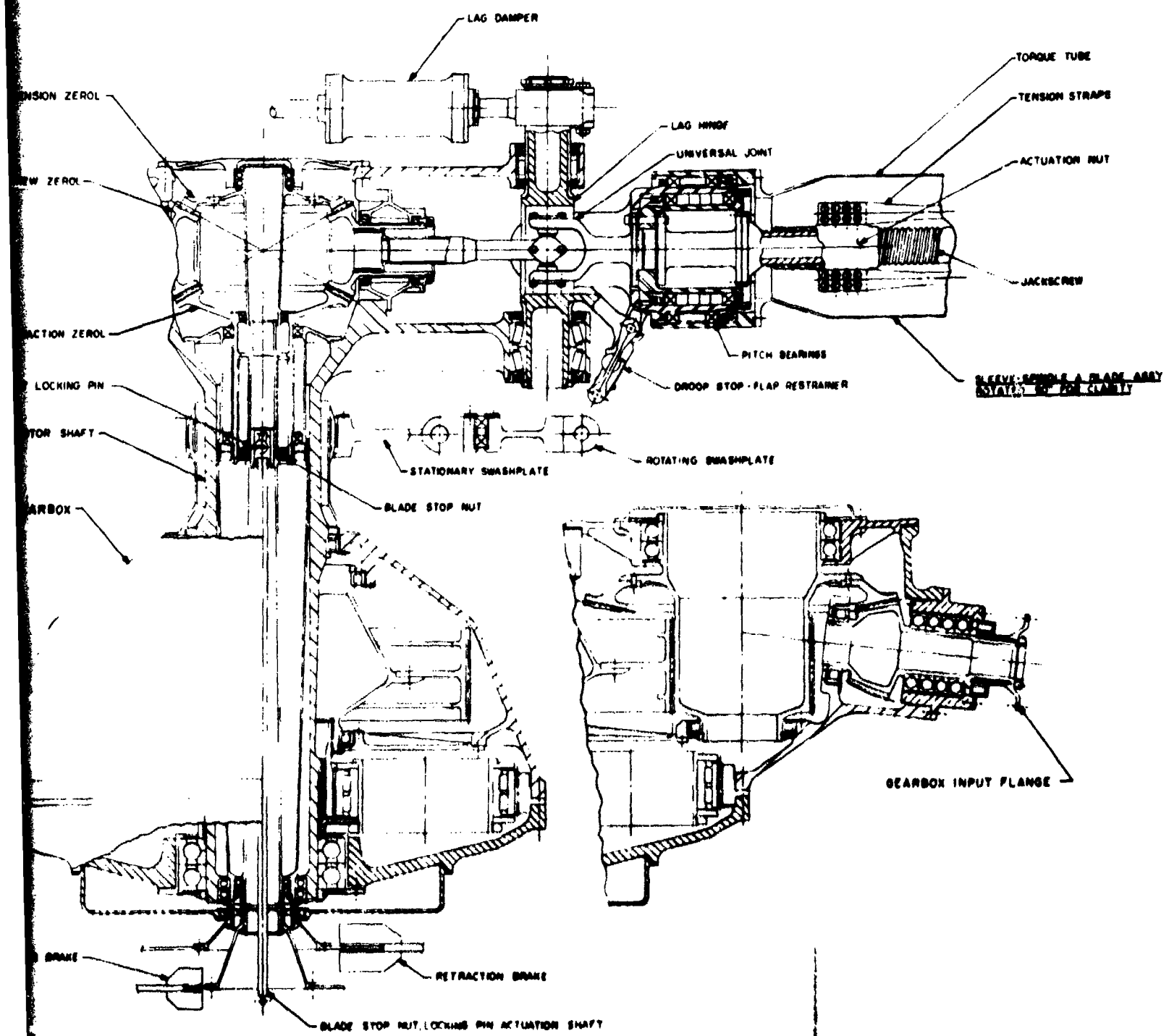


Figure 107. Full-Scale Preliminary Design - TRAC Rotor Head and Retraction Mechanism.



Full-Scale Preliminary Design - TRAC Motor Head and Retraction Mechanism.

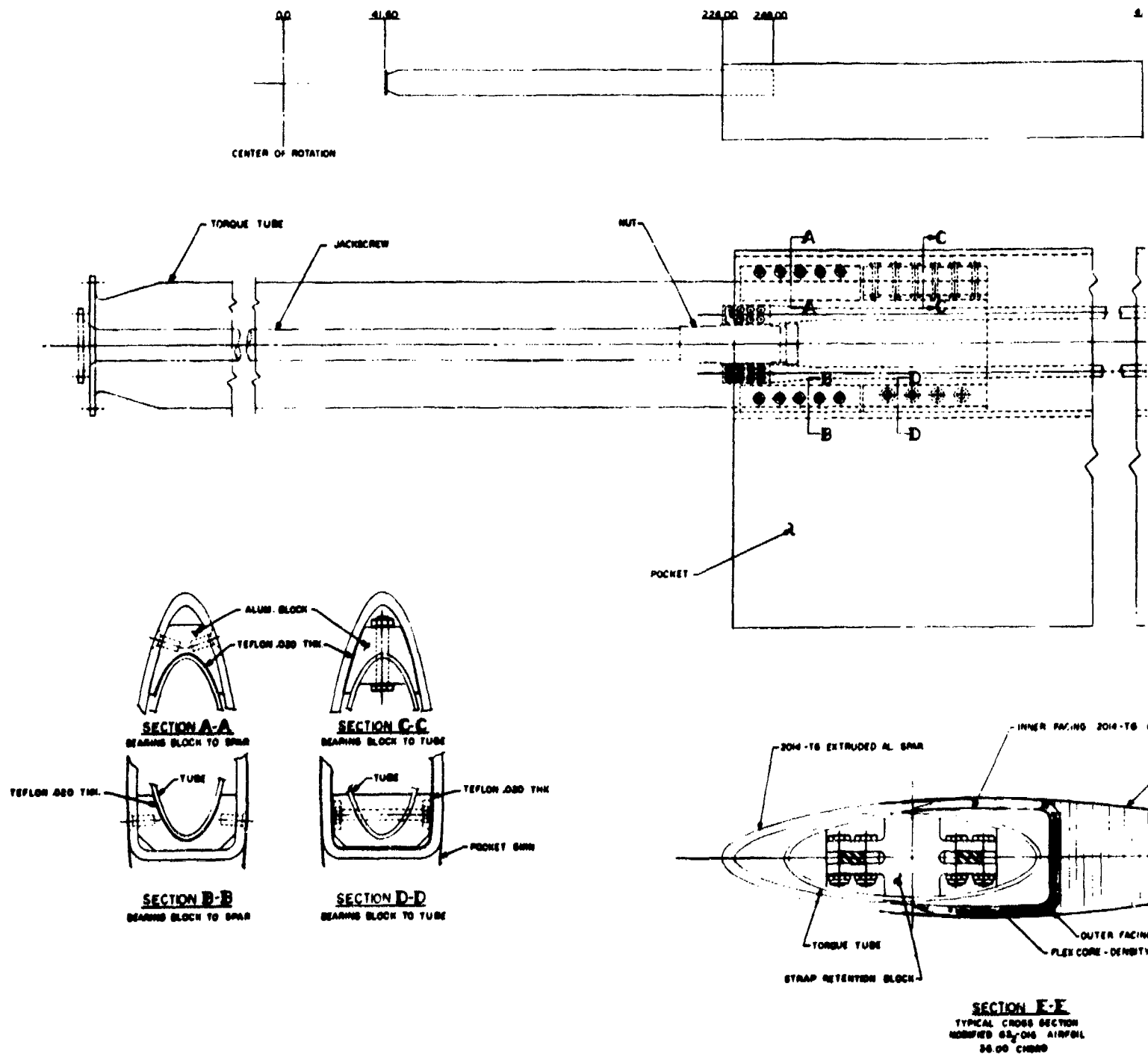
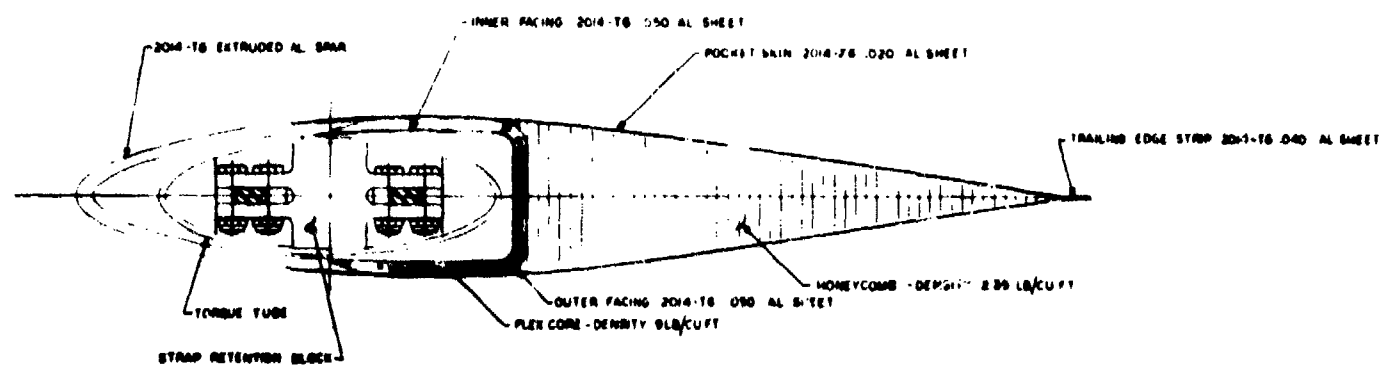
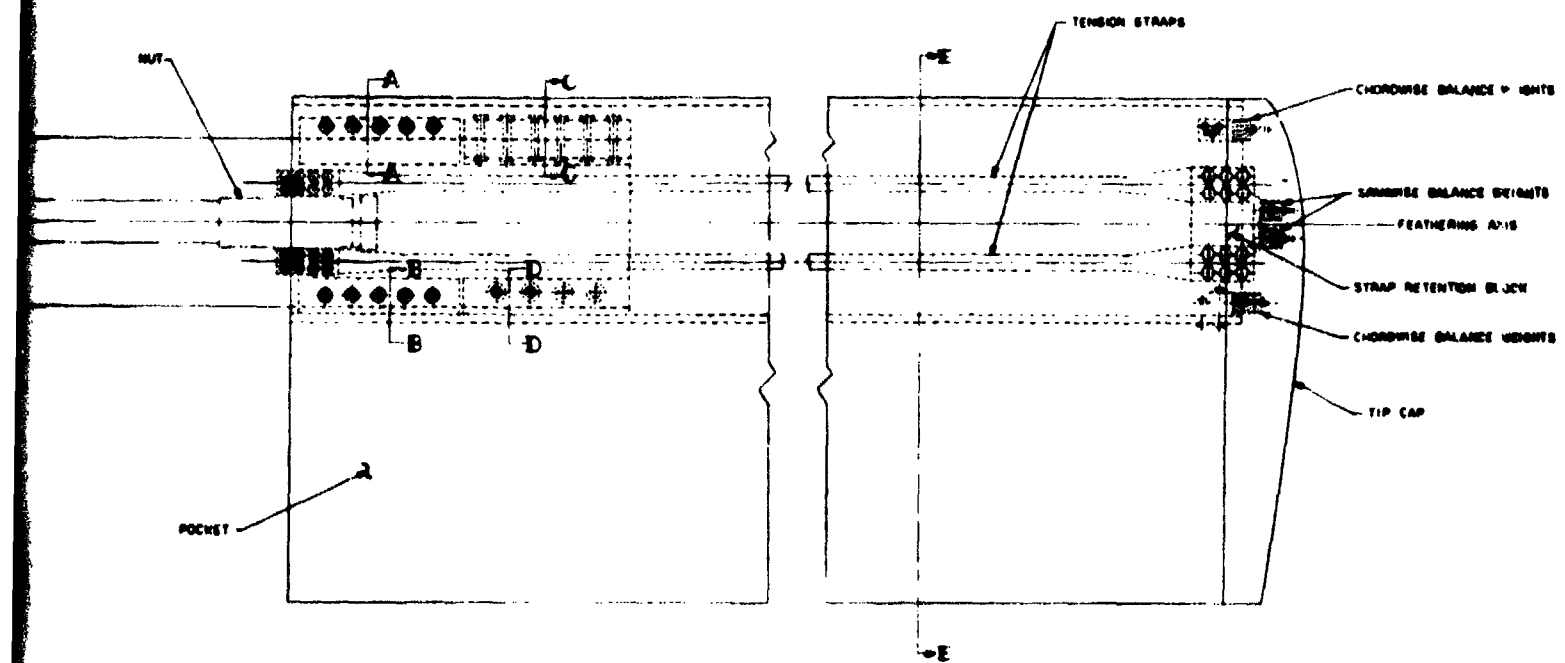
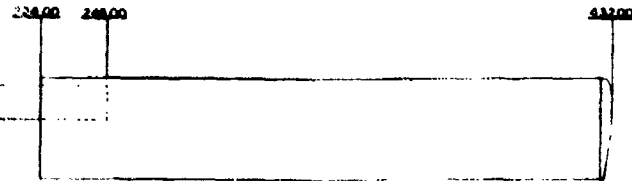
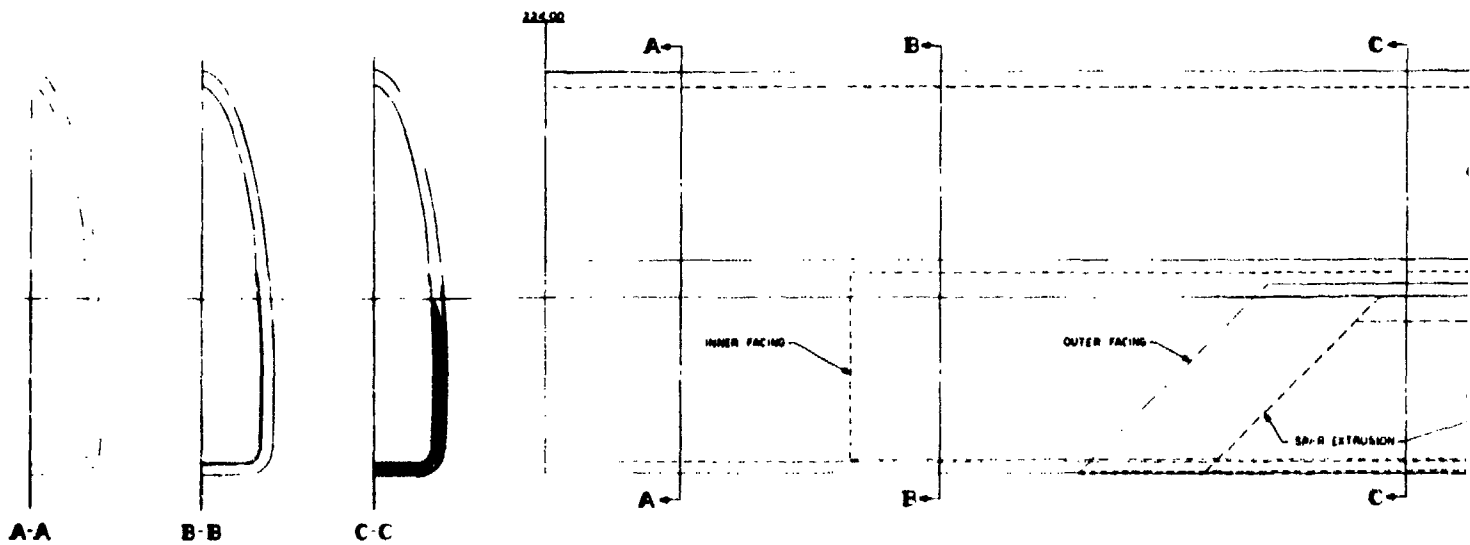


Figure 108. Full-Scale Preliminary Design - TRAC Blade General Arrangement.

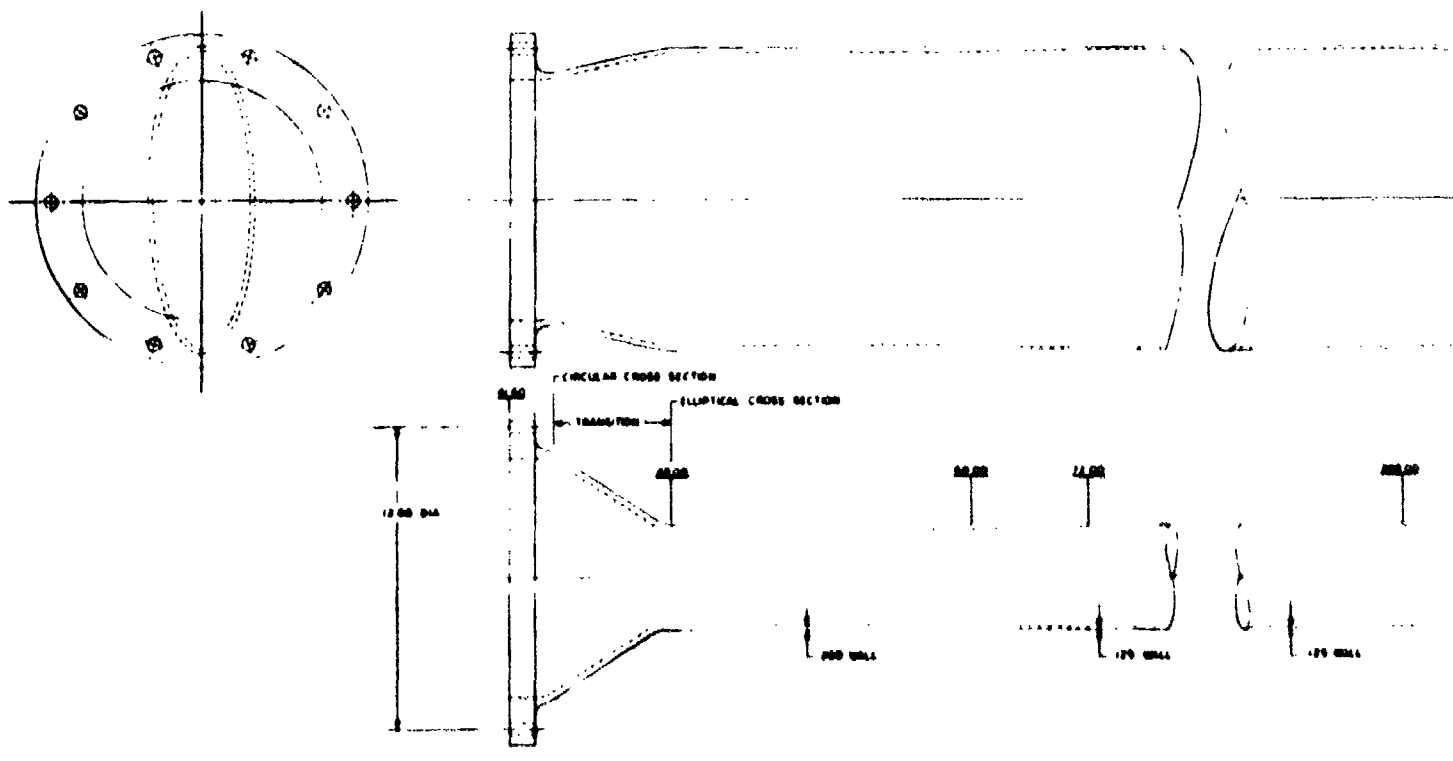


SECTION E-E
TYPICAL CROSS SECTION
REINFORCED BY THE AIRFOIL
50.00 CHORD

TRAC Blade General Arrangement.

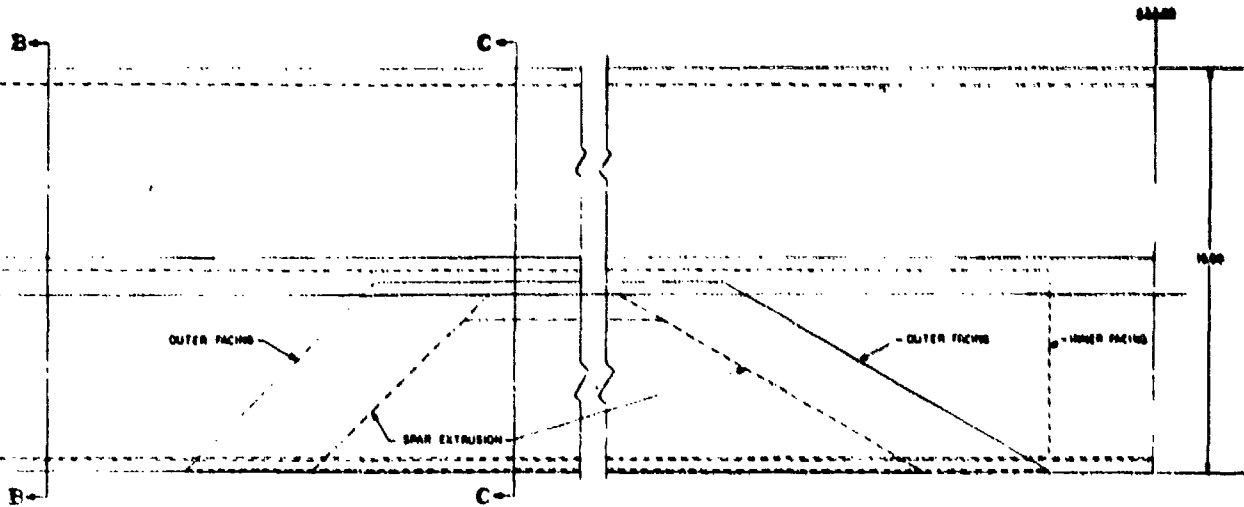


SPAR ASSEMBLY

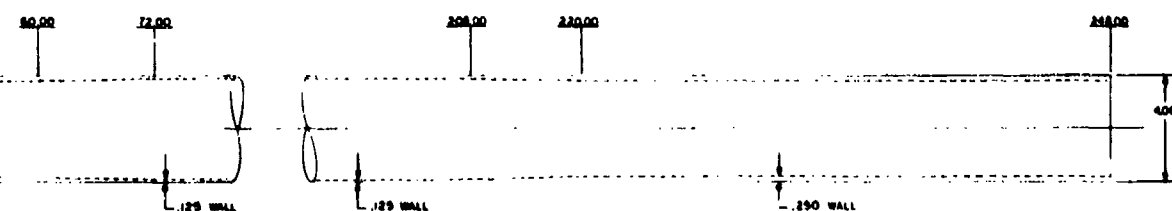
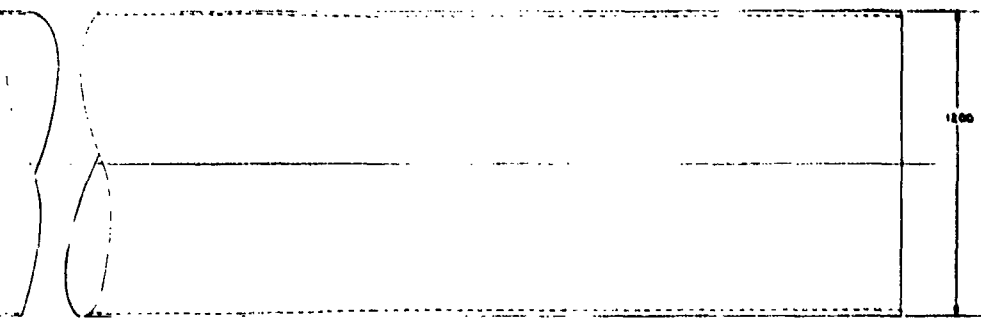


TORQUE TUBE

Figure 109. Full-Scale Preliminary Design - Torque Tube and Spar.



SPAR ASSEMBLY



TORQUE TUBE

Torque Tube and Spar.

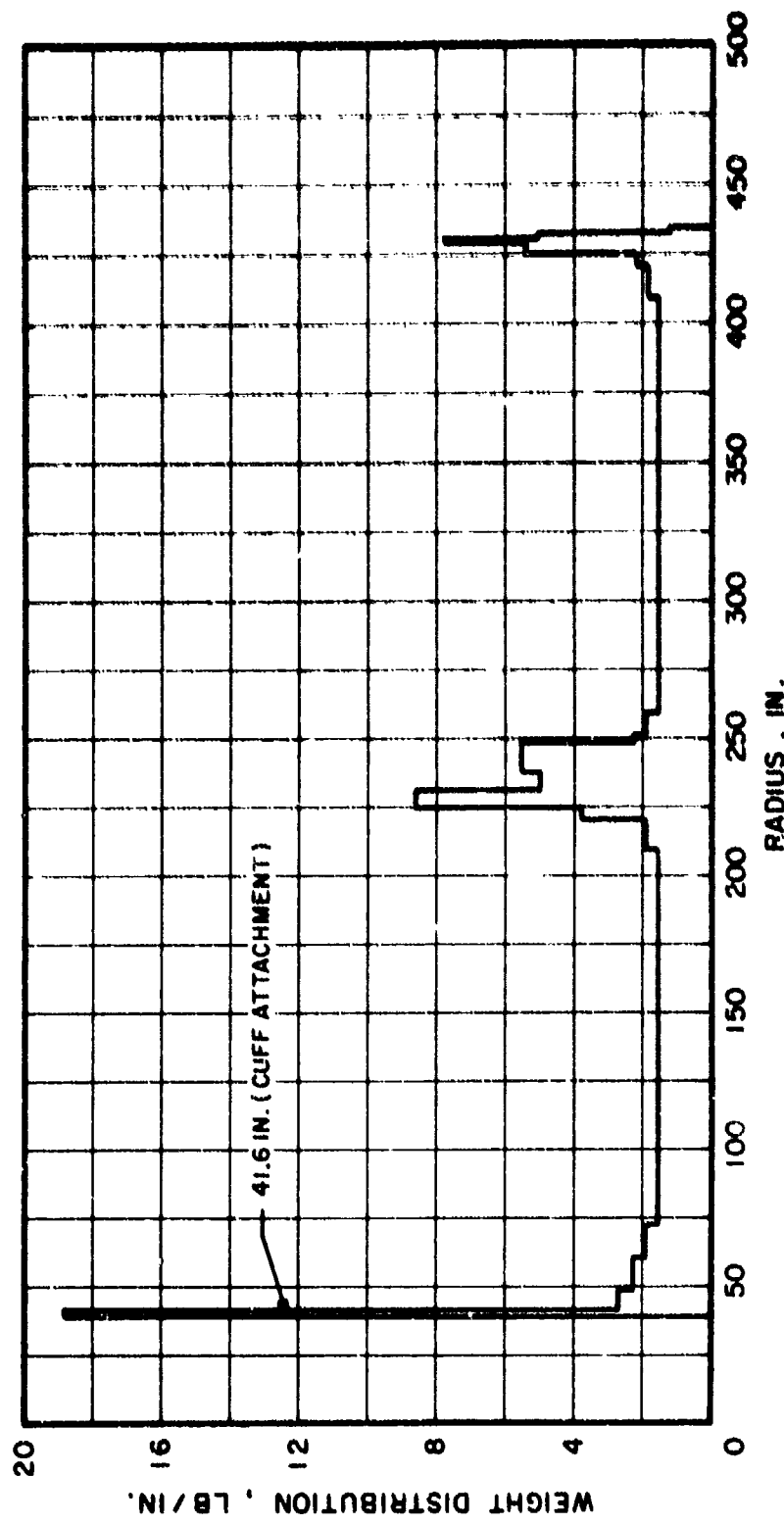


Figure 110. Mass Distribution for Full-Scale Blade Design.

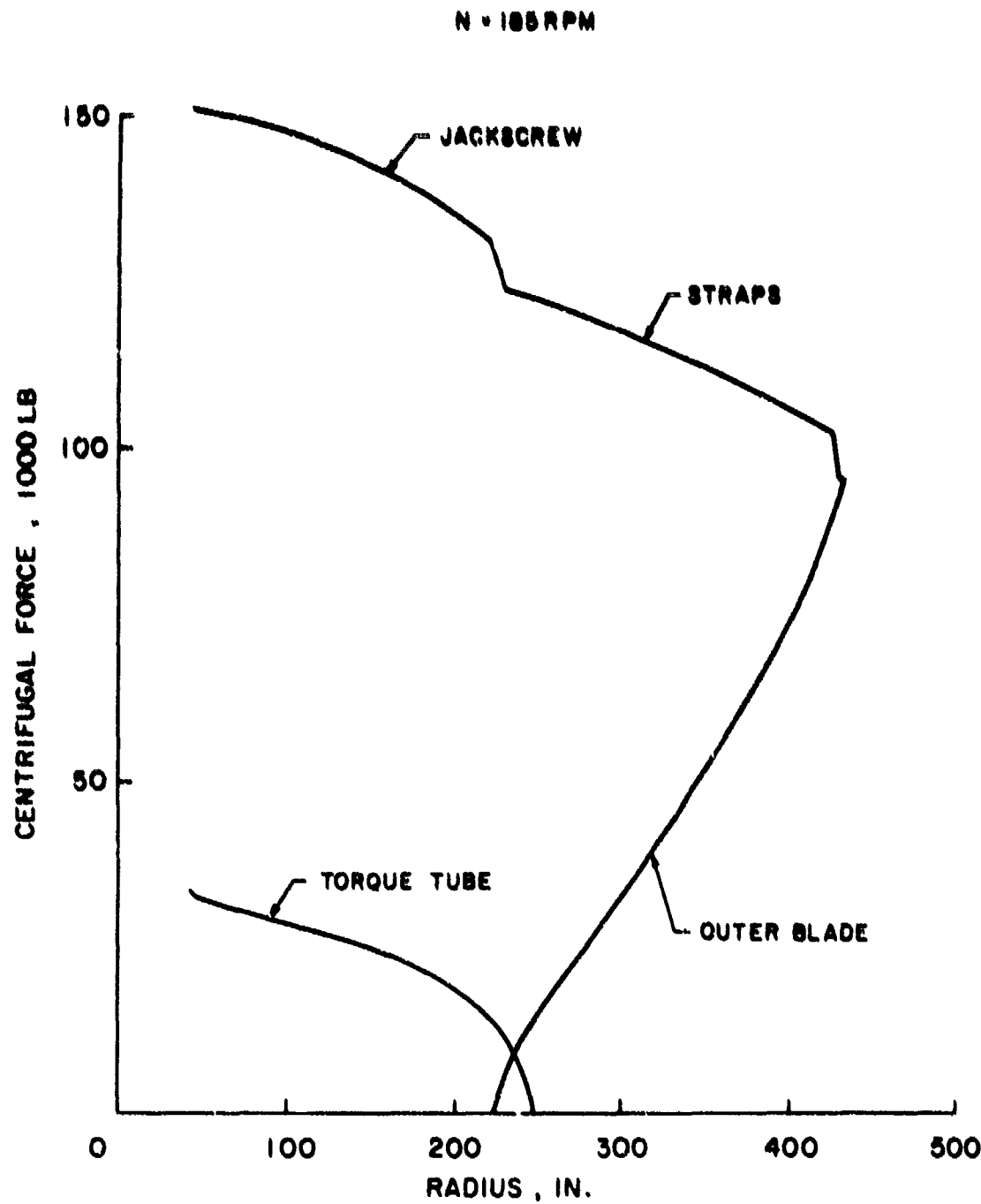


Figure III. Centrifugal Force Distribution for Full-Scale Blade Design.

APPENDIX II

DETAILS OF MODEL BLADE CONSTRUCTION

Data provided in APPENDIX II supplement the information presented under the heading MODEL BLADE DESIGN AND CONSTRUCTION, pages 6 - 7 of this report.

Outer Blade

The outer section of the blade is composed of two major components: the spar assembly and the pocket or trailing edge of the airfoil section. Figure 6 shows a typical cross-sectional view of the blade.

The model spar is built up into a D-section with formed sheet metal, as compared to a conventional extruded aluminum spar. An assembly drawing of the spar is shown in Figure 112. The spar consists of a constant-wall aluminum leading edge and a sandwich type structure which is bonded to the leading edge to complete the D-section. The sandwich consists of two thin-wall channel facings, one aluminum and one magnesium, bonded to the core. The core is solid aluminum at the extreme inboard and outboard ends and an aluminum screening material over most of the length of the spar. Because of the availability of aluminum screening in various thicknesses and densities, it was selected as the best material to approximate the honeycomb core used on the full-scale spar. The increase in weight and stiffness resulting from the screen was compensated for by using magnesium for the outer facing. Two stepped recesses are chemically milled along the length of the spar on both the upper and lower surfaces at approximately 20% chord. These recesses are used as bonding surfaces for the outer facing and pocket assembly to maintain a flush and smooth airfoil contour.

The scaling of the pocket assembly was more difficult than for previous Sikorsky dynamic model blade designs, as it is a full structural member of the blade. Scaling down the prototype pocket utilizing the same materials resulted in parts too flimsy to handle. Furthermore, adjustment of blade chordwise balance, which could be achieved on conventional blades by adjusting leading-edge counterweights, was not possible here since the TRAC blade design eliminated the use of counterweights. The result of a number of trials was a pocket composed of a .004-inch magnesium skin bonded to a comb-like balsa wood core. A cutaway view of the pocket is shown in Figure 6.

Since the overlap region of the full-scale design spar is an extrusion and the model spar a built-up section, a loop strap was bonded over the inboard end of the model outboard blade to eliminate the possibility of the bond separating when the joint was fully loaded.

Torque Tube

Steel rather than titanium was originally selected for the model torque tube because of procurement and fabrication complexities associated with titanium. The elliptical shaped tubes were drawn through contoured dies from thin-wall tubing and then chemically milled to the required thickness of .010 inch. Sheet steel doublers were bonded to the inside of the torque tube at each end to match the increased torque tube thickness called for in the preliminary design of the full-scale blade. These doublers extended around the entire inside of the torque tube, and were .010 inch thick and approximately 3.5 inches long. Aluminum cuffs were machined in two halves and then bonded to the inboard end of the torque tube.

The quality control of overall dimensions and wall thickness for the steel torque tubes, although acceptable, was not as good as desired and therefore was reviewed after the first series of wind tunnel tests to determine better manufacturing approaches or new materials. Drawing of the steel tubes with the correct wall thickness was unsatisfactory due to inability to control overall straightness. However, sample aluminum torque tubes were drawn through the same contoured dies used for the steel tubes, with excellent results. Therefore, aluminum was selected for the new torque tubes. It should be noted that although the material is different from that used initially, dynamic similarity was maintained by adjustment in wall thickness to .030 inch so that bending stiffness (EI) of the tube remained the same. The only exception to this is that the increased thickness did not allow space for internal doublers at the ends of the torque tube, so that at these points the tubes were under design stiffness and strength. The root end cuffs were again bonded to the inboard end of the torque tube. Thin stainless steel abrasion strips (.005 inch thick) were bonded internally along the full length of the tubes, as shown in Figure 6, to prevent excessive wear by the translation of the nut during the retraction or extension cycles.

Bearing Blocks

Nylatron G. S., a molybdenum disulphide filled nylon, was selected for the bearing slide blocks because of its good mechanical and bearing properties. As the fit between the inside of the blade spar and the outside of the torque tube is critical, molds were fabricated using actual blade components as masters. As a result the molded parts required minimum hand fitting during assembly. The molded blocks were first attached to the torque tube by a series of screws which go through the blocks and tube wall and are secured in a contoured nut plate inside the tube. The assembly is then inserted in the outer blade, fitted, and then positioned in a fixture to provide proper alignment for installing the remaining blocks. These blocks are held in place by a series of screws which go through the spar wall and are threaded into the blocks.

Jackscrews

The Jackscrews were fabricated from Veeocomax 300, a high-strength, 18% nickel maraging steel. The 0.250-inch hole in the center of each Jackscrew was gun-bored. The threads, which were double and left-hand as in the full-scale design, were ground and then lapped against the nuts which were used in the blades. After lapping, the Jackscrews were coated with Vitrolube dry film lubricant, which incorporates molybdenum disulphide as the primary lubricating element in a vitreous base material.

A redundant structure was incorporated in the Jackscrew design. A high-strength maraging steel strap, 0.125 inch in diameter, was mounted in the center of the Jackscrew, anchored by means of a shoulder on the strap and a counterbore in the Jackscrew at the root end, and by means of a nut at the tip of the Jackscrew. The redundant strap, which was preloaded in tension by approximately 100 pounds, was more than strong enough to carry the entire centrifugal load of the blade.

Nut

Beryllium copper was selected for the retraction nut because of its excellent bearing and heat dissipation properties. Threads were tapped prior to the material hardening cycle. Each nut and corresponding Jackscrew was lapped and burnished as a set.

Tension Straps

Strap material selection and method of attachment to the nut and tip of the blade required a unique solution, as conventional means could not be employed because of the severe space restriction. During the development of the blades, several strap designs and retention techniques were investigated. The final design utilized music wire for the straps, centerless ground to the desired diameter but with a shoulder on one end to fit in counterbored holes in the nut. After the straps were installed through the nut and the blade tip block, the diameter of the outer end of the straps was increased by a nickel sulphamate plating process which increased the diameter to the same dimension as the machined shoulder at the other end. The plated shoulder was then snugly fitted into the counterbore provided in the tip block. Static tests demonstrated that full strap strength was developed with this connection technique.

It should be noted that certain details of the nut-strap assembly differ from those indicated in Figure 6, which, for these components only, should be considered as a schematic drawing. The exact details are not shown because of a restriction which was imposed by the U. S. Patent Office.

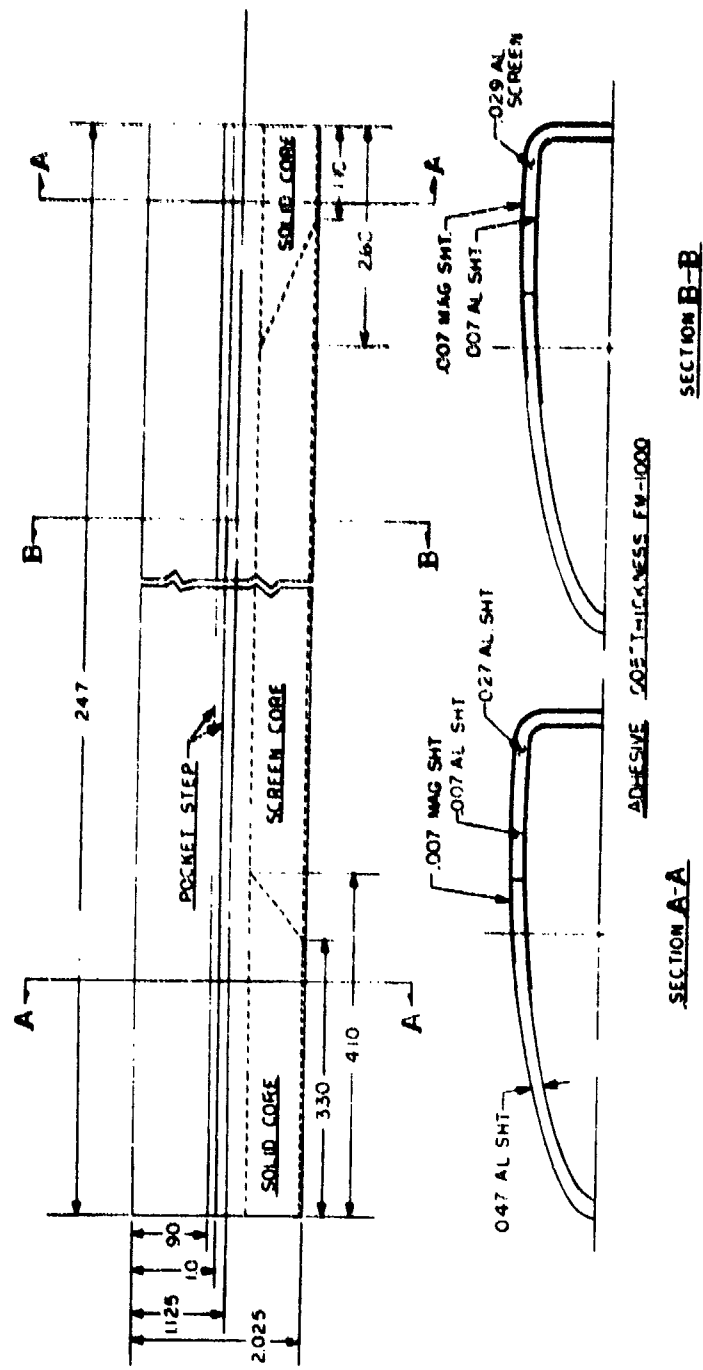


Figure 112. Model Blade Spar Assembly.

APPENDIX III

DETAILS OF WIND TUNNEL MODEL

Data provided in APPENDIX III supplement the information presented under the heading WIND TUNNEL MODEL, pages 8 - 9 of this report.

Diameter Change System

Two concentric shafts inside the main rotor shaft connect the rotorhead differential and clutch assembly used to actuate the telescoping mechanism. With both clutches free the internal shafts rotate with the rotor shaft, resulting in no relative motion between the bevel gears and no rotation imparted to the jackscrews. Actuation of either the extend or retract clutch causes the respective shaft to stop relative to ground. The other shaft rotates at twice rotor speed and the pinions and jackscrews turn to extend or retract the blades. Both the extension and retraction clutch on the model are of the dry, multiple-disc type. Actuation of the clutch was accomplished with a small position-feedback hydraulic cylinder controlled from the rotor control console. The feedback circuit included signals from limit switches incorporated in the mechanical portion of the diameter measurement system. When the diameter control knob on the model control console was held in the extend or retract position, the limit switches served to neutralize the clutch position when essentially full diameter or minimum diameter was reached. When the diameter control knob was returned to the neutral position, the circuit automatically drove the clutch actuator away from the limit switches, with a corresponding blade length change of approximately one-half inch. This latter feature served as a safety device to prevent excessive travel in case some unforeseen factor caused a diameter change not noticed by the control console operator.

Diameter Measurement

Rotor diameter was measured by determining the relative rotation of the coaxial shafts in the rotor drive system. Any two of the three shafts could be used for this purpose; the pair selected for convenience consisted of the main drive shaft and the inner (extension) shaft of the diameter change mechanism. The rotational motions of each of these shafts were transmitted through appropriate mechanical means to a miniature differential gearset located below the model gearbox. Rotation of the lower bevel gear of this differential was directly proportional to the rotation of the inner shaft of the diameter change mechanism, and the rotation of the upper bevel gear of the miniature differential was proportional to the rotation of the main rotor shaft, except that the direction of rotation was reversed by an intervening garmesh. When the rotor diameter is held constant, the coaxial shafts all turn at the same speed, and the upper and lower bevels of the miniature differential turn at equal but opposite speeds. Under these conditions the pinion gear connecting the two bevels spins on its own axis but does not rotate circumferentially about the bevels. Thus the centerbody to which the pinion is mounted does not rotate. When the rotor diameter is changed, however, there is a relative rotation between the coaxial shafts, with the result that the bevels of the

miniature differential do not turn at equal and opposite speeds. Under these circumstances the centerbody of the differential, which always turns at the average speed of the upper and lower bevels, will rotate in one direction or other depending on whether the diameter is being increased or decreased, with the number of turns proportional to the magnitude of the diameter change. The rotation of the centerbody was geared to a multiple-turn rotary potentiometer which supplied the electrical signal for the rotor diameter measurement. This centerbody rotation was also used to provide a linear mechanical motion, by means of a screw and traveling nut, to actuate the limit switches in the diameter-control electrical circuit.

Blade Pitch Control System

Blade pitch control was achieved with an electromechanical swashplate control system in the most recent test series. The system used three independent electric motors, controlled from the rotor control console, to provide pure collective and cyclic control inputs to the swashplate. Required mixing is accomplished mechanically with three intermeshed differential gearsets. Mixed outputs are transferred to three conventionally positioned mechanical actuators by means of flexible shafts. The actuators transfer the rotary motion of the shafts into linear motion by a worm gear and jackscrew. Control angles are measured with geared potentiometers which effectively count the number of turns of the input electric motors. The collective and cyclic pitch angles are displayed on three digital meters in the control console. Earlier test series had utilized a hydraulic control system consisting of pumps, reservoirs, filters, servo valves and hydraulic actuators. The system used electrical mixing with position feedback.

Rotor Drive and Gimbal Mounting Systems

The rotor system is powered by a water-cooled variable-frequency electric motor, nominally rated at 80 horsepower. Power is transmitted to the rotor shaft by a 5.25:1 reduction, two-stage gearbox. Gearbox lubrication and cooling are provided by an oil spray and scavenge system.

The blades, rotorhead, shafts, clutches, clutch servo, motor, gearbox, blade pitch control system, diameter measurement system, and instrumentation slipring comprise the internal model assembly. This portion of the model is metric. It is mounted on a six-component strain gage balance for measurements of rotor forces and moments. The ground side of the balance is supported in a soft damped gimbal.

The gimbal mounting was incorporated as part of the system to eliminate the ground resonance type of instability which had previously prevented testing of the model on the wind tunnel struts at full diameter and rpm. This instability was not associated with the TRAC rotor, but would have existed for any conventional rotor configuration operating at comparable rotational speeds. The analysis, development, and verification of the gimbal mounting system are described in detail in Reference 5. The wind tunnel tests to verify the system are summarized in this report under TEST PLANS AND PROCEDURES. The gimbal provides a pitch and roll freedom

for the internal model about axes which intersect at the centerline of the strain gage balance. Spring restraint is provided between the internal model and the fuselage by means of cantilever springs in the pitch direction and a torsion bar in the roll direction. Damping is provided by rotary viscous dampers with mechanical linkages to increase their effective output for small gimbal motions. One set of dampers was connected directly between the model fuselage and metric balance case for damping about the roll axis. It was found experimentally that this soft grounding of the balance did not affect the steady-state force and moment measurements. The gimbal mounting system permitted the internal model assembly to respond to destabilizing forces by rotating at the gimbal axis rather than storing the energy as elastic deformations in the structure. The dampers dissipated the energy as the gimbal deflected, resulting in a stable system.

Fuselage and Support Struts

The model fuselage consists of a nonstructural fiberglass and aluminum outer shell mounted on a steel frame. Overall length is 123 inches and maximum diameter is 17.3 inches. During the high-speed portion of the test only, an inverted V-tail, shown in Figure 12, was used to increase the lateral static stability margin of the fuselage. The basic fuselage, including the V-tail, is the same as that utilized in the high-speed rotorcraft drag investigation reported in Reference 11. A photograph of the model with the side panels and nose section removed is shown in Figure 113.

The struts for mounting the model in the wind tunnel were developed in conjunction with the soft damped gimbal system to provide, as nearly as possible, a rigid support for the external fuselage. The struts used for the low-speed portions of the test are shown in Figure 114. Both the longitudinal and lateral bracing were bolted to the tunnel framework. The main struts were mounted on the wind tunnel balance frame, which was grounded for these tests. Blockage effects from the struts did not appreciably disturb the rotor inflow, as most components were located in a vertical plane well below the model. The strut installation for the high-speed portion of the test was similar, except that the bracing struts were attached below the level of the test section floor.

Portions of the TRAC program completed during the first test series utilized a different fuselage than described above, and both the first and second test series employed different support strut hardware. However, all important components of the dynamically scaled TRAC rotor have remained similar. The model test installations utilized in the first and second test series are shown in Figure 115. Both of these models were mounted on a single main support strut and were not equipped with the gimbal. The model tested in the first test series utilized the Sikorsky compound helicopter fuselage described in Reference 12.

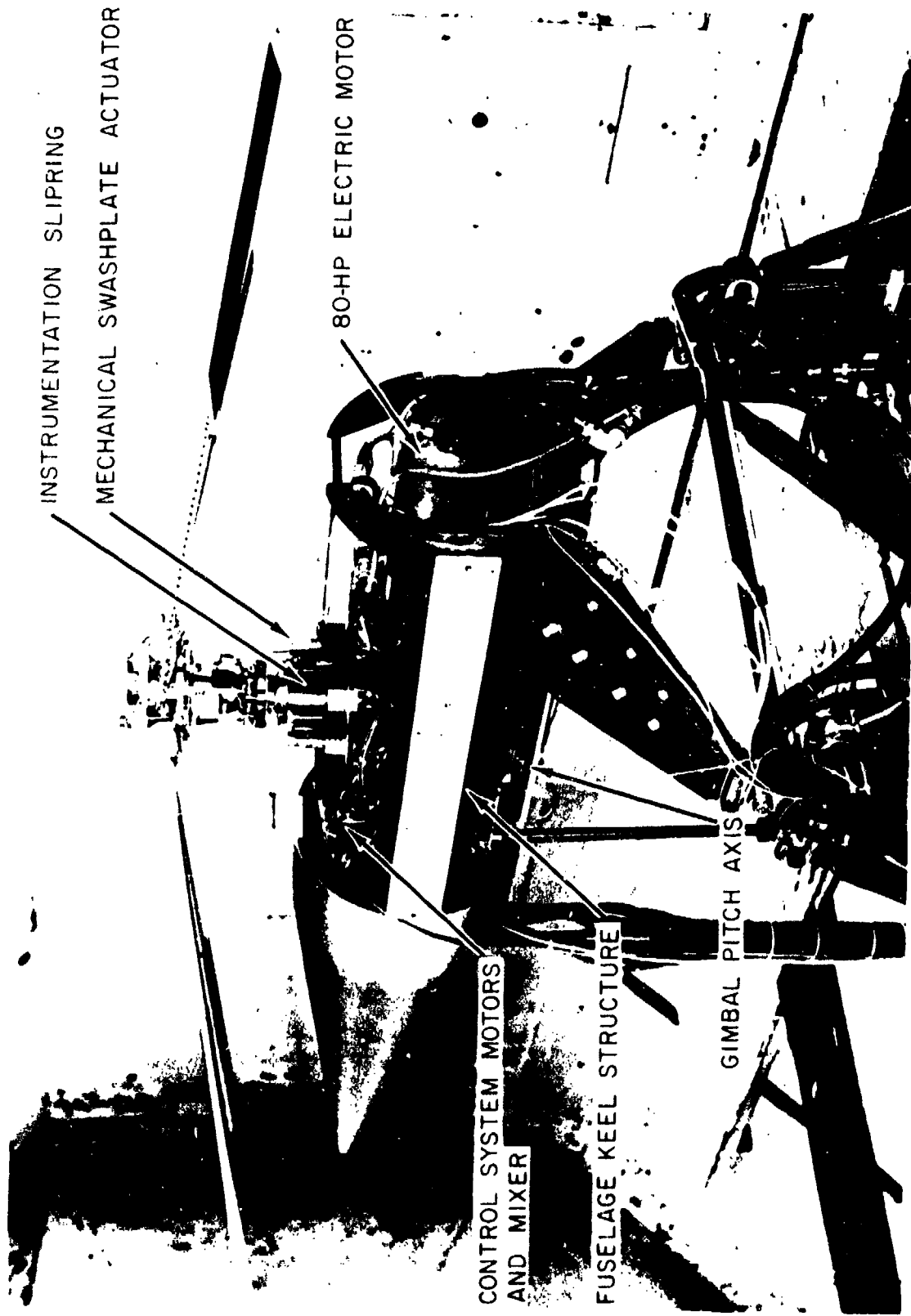
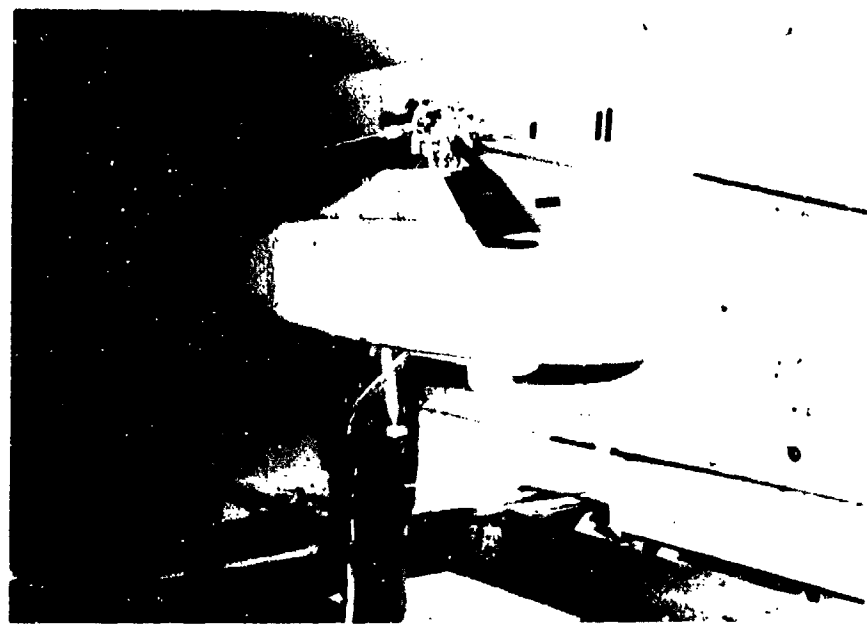


Figure 113. Fuselage with Outer Shell Partially Removed.



Figure 114. Model Support Strut System in 18-Foot Wind Tunnel.



(a) Test Series One



(b) Test Series Two

Figure 1.5. Model, telescope and target, (a) and (b) utilized in first two test series.